UNIVERSITY OF CRETE

GEORGIOS SURLANTZIS

THE MAGNETOHYDRODYNAMIC NATURE OF THE SOLAR ATMOSPHERE

Models for Magnetized Plasma Loops with Flows

Ph.D THESIS
SUBMITTED TO PHYSICS DEPARTMENT
AT THE UNIVERSITY OF CRETE

HRAKLION 1994

ΠΑΝΕΠΙΣΤΗΜΙΟ ΚΡΗΤΗΣ

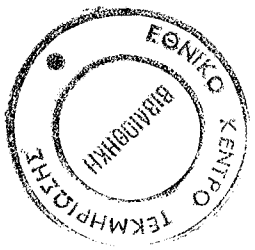

ΣΟΥΡΛΑΝΤΖΗ ΓΕΩΡΓΙΟΥ

Η ΜΑΓΝΗΤΟΔΡΟΔΥΝΑΜΙΚΗ ΔΟΜΗ ΤΗΣ ΗΛΙΑΚΗΣ ΑΤΜΟΣΦΑΙΡΑΣ

Πρότυπα για Μαγνητικούς Βρόγχους Πλάσματος με Ροές

ΔΙΔΑΚΤΟΡΙΚΗ ΔΙΑΤΡΙΒΗ
ΠΟΥ ΥΠΟΒΛΗΘΗΚΕ ΣΤΟ ΤΜΗΜΑ ΦΥΣΙΚΗΣ
ΤΟΥ ΠΑΝΕΠΙΣΤΗΜΙΟΥ ΚΡΗΤΗΣ

ΗΡΑΚΛΕΙΟ 1994

Αυτή η διδακτορική διατριβή εκπονήθηκε στο Τμήμα Φυσικής του Πανεπιστημίου Κρήτης υπό την επίβλεψη του Αναπληρωτή Καθηγητή κ. Κανάρη Τσίγκανου.
Η αντίστοιχη τριμελής συμβουλευτική επιτροπή αποτελείτο από τους κκ.

Ι. Βεντούρα, Καθηγητή Τμήματος Φυσικής Πανεπιστημίου Κρήτης,
Κ. Τσίγκανο, Αναπληρωτή Καθηγητή Τμήματος Φυσικής Πανεπιστημίου Κρήτης,
Ν. Κυλάφη, Αναπληρωτή Καθηγητή Τμήματος Φυσικής Πανεπιστημίου Κρήτης,

ενώ η επταμελής εξεταστική επιτροπή περιελάμβανε, επιπλέον τους

J. Heyvaerts, Professeur, Observatoire de Strasbourg, France,
Ν. Παπανικολάου, Καθηγητή Τμήματος Φυσικής Πανεπιστημίου Κρήτης,
Ι. Παπαμαστοράκη, Αναπληρωτή Καθηγητή Τμήματος Φυσικής Πανεπιστημίου Κρήτης,
Ε. Σαρρή, Καθηγητή Πολυτεχνικής Σχολής του Δημοκρίτειου Πανεπιστημίου Θράκης.

Στην Θεανώ

Πρόλογος

Η ανακάλυψη ότι ένα σημαντικό τμήμα της εκπεμπόμενης ενέργειας από το Ηλιακό στέμμα προέρχεται από μαγνητισμένους βρόγχους πλάσματος ήταν από τις πιο θεμελιώδεις για την κατανόηση του Ηλιου. Οι βρόγχοι αυτοί είναι οι δομικοί λίθοι του Ηλιακού στέμματος, ιδιαίτερα στις ενεργές περιοχές του Ηλιου. Η μελέτη τους έχει παρουσιάσει αξιοσημείωτη αύξηση τα τελευταία χρόνια, τόσο απο παρατηρησιακής όσο και από θεωρητικής σκοπιάς.

Η διατριβή αυτή, το αντικείμενο της οποίας εντάσσεται στην Ηλιακή μαγνητοϋδροδυναμική, έχει σκοπό αφενώς στη θεωρητική μελέτη των μαγνητισμένων βρόγχων με έμφαση την επίδραση ροών σε αυτούς, των οποίων η ύπαρξη σε αρκετές περιπτώσεις είναι αδιαμφισβήτητη, και αφετέρου την δυνατότητα εύρεσης λύσεων των χρονοανεξάρτητων εξισώσεων της ιδανικής μαγνητοϋδροδυναμικής, εφαρμόσιμες σε διάφορες δομές της Ηλιακής ατμόσφαιρας.

Το περιεχόμενο της διατριβής αυτής διαιρείται σε επτά κεφάλαια. Στο πρώτο παρατίθενται, γενικά παρατηρησιακά δεδομένα για την δομή της ατμόσφαιρας του Ηλιου, με έμφαση στους μαγνητικούς βρόγχους, ενώ στο δεύτερο και τρίτο αντίστοιχα αναπτύσσεται το θεωρητικό πλαισίο για την θεωρητική περιγραφή τους, όπως επίσης και τα κυριώτερα προταθέντα μέχρι σήμερα πρότυπα για αυτούς. Στα υπόλοιπα τέσσερα περιγράφονται λεπτομεριακά κλάσεις προτύπων που αποτελούν και την πρωτότυπη συνεισφορά της διατριβής καθώς και ερευνητικές ιδέες για το μέλλον.

Η εκπόνηση του μεγαλύτερου τμήματος της διατριβής, που πραγματοποιήθηκε την περίοδο 1990-94, έγινε στο Πανεπιστήμιο Κρήτης, εκτός από ένα μέρος της που έγινε στο Observatoire de Meudon, στο Παρίσι, την χρονική περίοδο 1991-92.

Θεωρώ υποχρέωση μου να ευχαριστήσω το Φυσικό τμήμα του Πανεπιστήμιου Κρήτης που μου έδωσε την δυνατότητα εκπονήσης διδακτορικής διατριβής παρέχοντάς μου υποδομή διεθνών προδιαγραφών, καθώς επίσης καιτην ομάδα αστροφυσικής για τις συζητήσεις που είχα μαζί τους σε όλο αυτό το διάστημα. Ευχαριστώ τους φίλους και συνεργάτες μου στην Γαλλία Jean Heyvaerts και Pascal Demoulin για το ατέλεωτες ώρες που αφιέρωσαν σε

μένα, μεταδίδοντας μου τις γνώσεις και την πείρα τους, όπως επίσης και την φιλοξενία του Observatoire de Meudon. Τον καλό μου φίλο και συνεργάτη Christophe Sauty με τον όποιο περάσαμε πολλές όμορφες στιγμές, επιστημονικές και μη, τόσο στην Κρήτη όσο και στο Παρίσι, ο οποίος επωμίστηκε το βάρος όλων των επαφών και των συνθηκών ζωής μου στις πρώτες μέρες μου στο Παρίσι. Αφησα τελευταίο, τον επιβλέποντα αυτής της διατριβής Κανάρη Τσίγκανο, για τον οποίο όσες και ευχαριστίες να παραθέσω θα είναι λίγες. Θα πω μόνο ότι στάθηκε κοντά μου σαν δεύτερος πατέρας σε όλα τα προβλήματα που αντιμετώπισα στο διάστημα αυτό, επιστημονικά ή μη, καθοδηγώντας με σαν νέο ερευνητή και άνθρωπο. Κλείνοντας, ευχαριστώ θερμά την σύζυγό μου Θεανώ Μαρινοπούλου για την υπομονή και συμπαράσταση που έδειξε σε όλη αυτή την προσπάθεια, στην οποία και αφιερώνω αυτήν την διατριβή.

Ηράκλειο, Αύγουστος 1994

Contents

CONTENTS

Chapter 1

THE SOLAR ATMOSPHERE

1.1 General Properties of the Sun

The Sun is an ordinary star with an absolute stellar magnitude 4.8, and it is of spectral type G2 V. But its short distance from the Earth makes it unique object. Thus its study is of central importance for understanding the behavior of stars and of cosmical plasmas in general. The overall properties of the Sun are summarized in Table 1.1.

In comparison to the Earth, the Sun has similar mean density but is 330,000 times more massive. The solar radius is 109 times larger, while its surface gravity is 27 times greater. The received solar radiation in Earth, is about 1 KW/m^2. Furthermore the Sun's equator is inclined at about 7^o to the plane of the Earth's orbit and the solar equatorial velocity is comparable to the terrestrial one.

In a first approximation, solar atmospheric phenomena can divided into two broad classes, quiet and active. The *quiet Sun* is viewed as a static, spherically symmetric ball of plasma, whose properties depend on a first approximation on the radial distance from the center and whose magnetic field is negligible. The *active Sun* consists of transient phenomena, such as sunspots, loops, prominences and flares, which are superimposed on the quiet atmosphere and most of which owe their existence to the magnetic field. But in many cases this division does not apply. For example the quiet atmosphere is influenced markedly by the magnetic field; it is structured by the magnetic network above and around evolving supergranule cells and the normal heating of the outer atmosphere may well be due to the magnetic field.

In this chapter we shall present a general description of the Sun from the ob-

Age: 4.5×10^9 $yr.$
Mass: $M_\odot = 1.99 \times 10^{33}$ $g.$
Radius: $R_\odot = 696,000$ $km.$
Mean density: 1.4 $g/cm^3.$
Mean distance from Earth: 1 $AU = 150,000,000$ $km = 215 R_\odot.$
Surface gravity: $g = 274$ $m/sec^2.$
Escape velocity at surface: 618 $km/sec.$
Luminosity: $L_\odot = 3.86 \times 10^{26}$ $W.$
Equatorial rotation period: 26 $days.$
Polar rotation period: 34 $days.$
Angular momentum: 1.7×10^{41} $kg\,m^2/sec.$
Mass loss rate: 10^9 $kg/sec.$
Effective temperature: 5785 $K.$
1 $arc\ sec (\equiv 1'') = 726$ $km.$

Table 1.1: *Characteristic quantities in the Sun (Priest 1984).*

servational point of view which is based on the first chapter of Priest's book "*Solar Magnetohydrodynamics*". At the end of this chapter, the emphasis will be given on the presence of various types of systematic flows in the solar atmosphere, for which the models in the following chapters refer.

1.2 Solar photosphere, chromosphere and corona

The solar atmosphere (Priest 1984) consists of three regions with different physical properties. The lowest is an extremely thin layer of plasma, called *photosphere*, which is relatively dense and opaque and emits most of the solar radiation. Above it lies the rarer and most transparent *chromosphere* while the *corona* extends from the top of a narrow *transition region* to the Earth and beyond. Hydrogen is almost totally ionized in the upper chromosphere, but neutrals are important in the lower chromosphere and photosphere. The density decrease rather rapidly with height above the solar surface, starting from 10^{23} m^{-3} at the photosphere, becoming 10^{15} m^{-3} at the transition region and 10^{12} m^{-3} at a height of 1 $R_\odot$.

Before 1940 it was thought, quite naturally, that the temperature decreases as one goes away from the solar surface. But, since then, it has been realized that, after falling from about 6600 K (at the bottom of the photosphere), to a minimum value of about 4400 K (at the top of the photosphere), the temperature rises slowly through the lower chromosphere and then dramatically through the transition region to a few 10^6 K in the corona (Fig.1.1). Thereafter, the temperature falls slowly in the outer corona, which

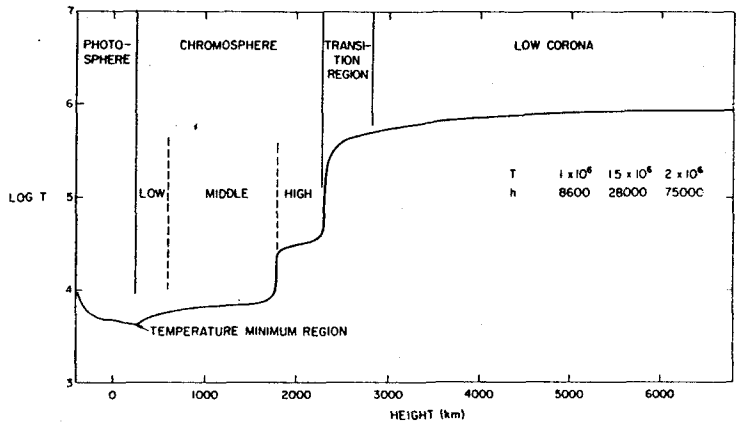

Figure 1.1: *The variation of the temperature with height in the solar atmosphere (Athay 1976).*

is expanding outwards as the *solar wind*, to a value of 10^5 K at 1 AU. The reason for the temperature rise above the photosphere has been one of the major problems in solar physics and is not yet fully answered; The low chromosphere is probably heated by sound waves that are generated in the noisy convection zone, propagate outwards and then dump their energy after steepening to form shocks; higher levels may well be heated by several magnetic mechanisms. In coronal temperatures of order a few million degrees the hydrogen and the lighter atoms are completely ionized.

Most of the solar radiation comes from the *photosphere* (its name comes from the Greek word "φως" which means light), which emits a continuous spectrum with superimposed dark absorption lines. These lines have to do with the absorption of the light by the atoms in the overlying atmosphere. Most lines are formed in the upper photosphere, but some, such as Hα, come from the chromosphere. Thus, when the Sun is observed through filters of different wavelengths, pictures can be obtained of the Sun's structure at a variety of levels (Fig.1.2). For example, the *lower chromosphere* is shown up by using an Hα filter, which is the most important for following the evolution of *active regions*, and *prominences* and for observing the lower part of a *solar flare*. In the beginning of an eclipse we can see light that has emitted from the photosphere and is then scattered towards us at the chromospheric levels as well as the intrinsic chromospheric emission. This colourful effect, led Young in 1870 to give the chromosphere its name (from the Greek word "χρώμα" which means colour). The chromosphere has sometimes been modelled as a static plane-parallel region, but in reality is highly non-uniform.

In more detail, the photosphere is the Sun's extremely thin visible surface layer

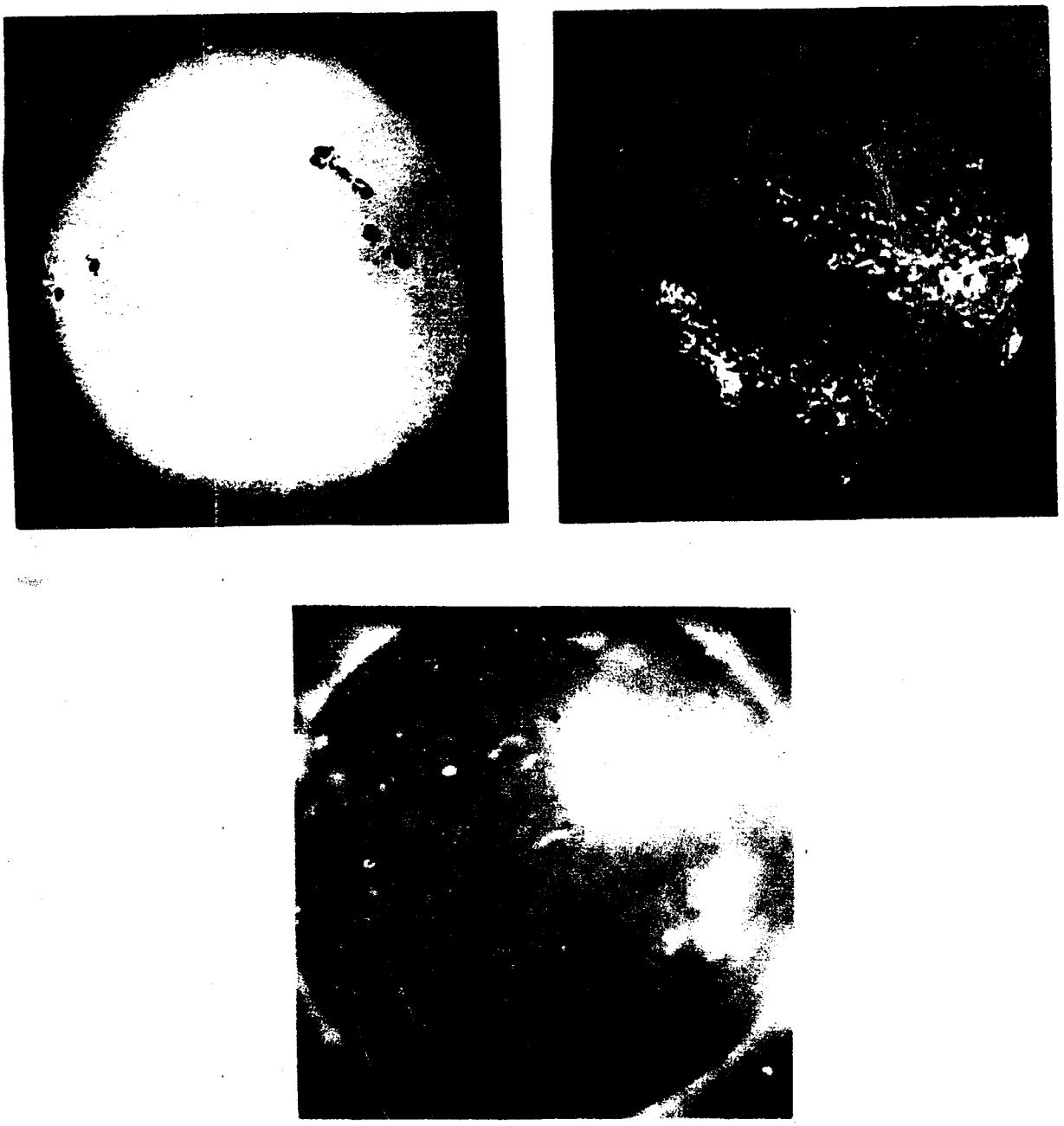

Figure 1.2: *The appearance of the Sun at various wavelengths which reflect to different levels in atmosphere. (a) photosphere at white light (BBSO), (b) chromosphere in Hα (BBSO), and (c) corona in soft X-rays (AS&E).*

about 500 km thick from which most solar light escapes. It is not uniformly bright; in high-resolution it appears covered with irregularly shaped bright granules of size of order 1000 km which are in continual motion with speeds about 0.5 km/sec. This structure called *granulation*, covers the whole Sun (there are about 10^6 granules present) and is an evidence of the presence of the convection zone (Fig.1.3). In addition to the granular pattern, there are also *mesogranulation* and *supergranulation* which their typical scale size and velocities are $5000 - 10000$ km and 60 km/sec for mesogranules (which their origin still unknown) and $20000 - 40000$ km and about 0.3 km/sec for supergranules which are the tops of large convection cells. These supergranules appears very clearly in chromosphere as a network of supergranulation boundaries with an irregular bright pattern. This is the basic reason for the high non-uniformly of the chromosphere (Fig.1.4) which at the limb one sees it as a mass of plasma jets, temperature 10^4 K, known as *spicules*; they are ejected up from the high chromospheric part of supergranule boundaries (probably along magnetic field lines) and reach speeds of 20 to 30 km/sec and heights of about 11000 km before fading, although most show no sings of falling (their typical lifetimes are $5 - 10$ min). A surprising feature is that after the initial acceleration, the velocity of a spicule remains fairly constant over a long distance, despite the strong gravitational field. In polar regions, where the magnetic field lines are open, there are larger jets of plasma, called *macrospicules* which reach to heights 4000 to 40000 km, and their typical velocities are 10 to 150 km/sec.

The *corona* (from the Latin for "crown") is known from many centuries and in white light is observed at eclipses as a faint halo of very low density and high temperature (Fig.1.5). Because the eclipses are rare Lyot in 1930 prompted to create artificial eclipses by means of a *coronograph*. This is a telescope containing an occulting disc to eliminate the glare of the photosphere, which is about a million times brighter than the corona. Many weeks of observation have now been made as well from Earth and from broad satellites.

In the quiet inner corona, the average electron density is several times 10^{14} m^{-3}, but this is enhanced by factors of 5 to 20 in many of the structures seen in Fig.1.5. The density rapidly falls off with the distance from the solar surface, it is about 10^{12} m^{-3} at 1 $R_\odot$ above it, 10^{11} m^{-3} at $4R_\odot$ and less than 10^{10} m^{-3} at $10R_\odot$. The overall shape of the corona varies with the solar cycle, near sunspot maximum, bright features called *streamers* extend out in all directions; near sunspot minimum, streamers are present only in the equatorial region and *polar plumes* are seen to fan out from the poles. *Coronal streamers* are roughly radial structures extending from heights of 0.5 to 1 $R_\odot$ up to 10 $R_\odot$, with a density enhancement of 3 to 10. In particular, *helmet streamers* lie above prominences and *active-region streamers* above active regions. A streamer consist of a round base (or arcade) of closed field lines surrounded with open

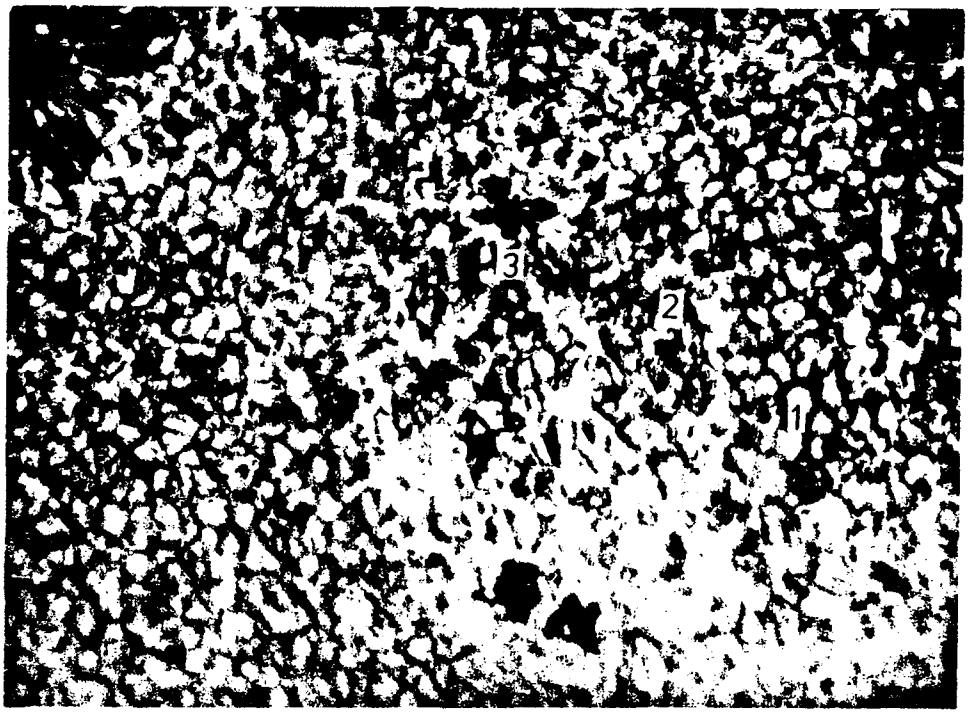

Figure 1.3: *A high resolution picture of the photosphere close to a spot (upper-left). It is evident the granulation pattern while in some cases, dark structures called pores are seen (J. P. Mehltretter; SPO).*

Figure 1.4: *Spicules as seen near the limb in the wing of Hα outlining the network (SPO).*

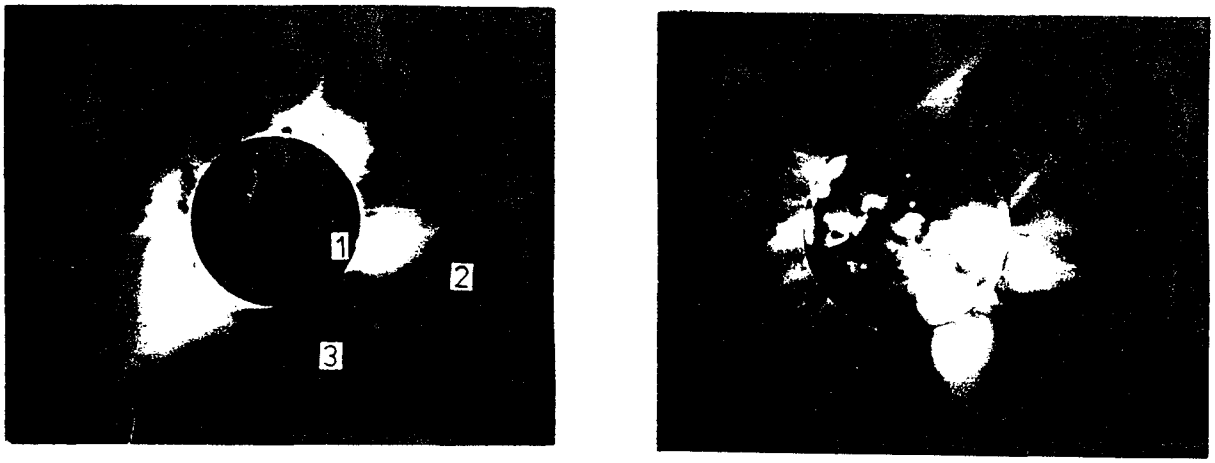

Figure 1.5: *(a) White-light eclipse (12 November 1966) photographs of the corona showing (1) prominence, (2) streamer, (3) coronal hole (G. Newkirk; HAO). (b) Eclipse photograph (7 March 1970) with superimposition of a soft X-ray photograph of the inner corona from Skylab (A. S. Krieger; AS&E).*

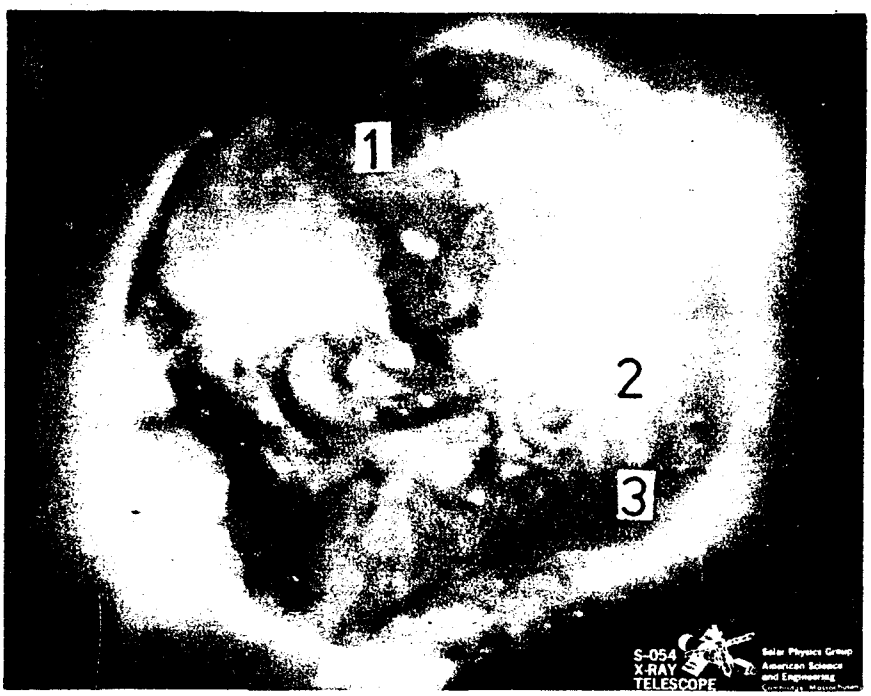

Figure 1.6: *A soft X-ray image of the corona from Skylab, showing (1) coronal hole, (2) active region, and (3) X-ray bright point (A. S. Krieger; AS&E).*

field lines; from the end it looks like a helmet and from the side like a fan. *Polar plumes* are ray-like structures near the poles, especially noticeable at times of sunspot minimum; they last for only about 15 h and presumably outline the local magnetic field. Plumes are also seen in coronal holes.

In soft X-rays, the corona emits thermally and so may be viewed directly, since the contribution from the lower atmosphere is negligible. The disadvantage of observing in soft X-rays is that such wavelengths are normally absorbed by the Earth's atmosphere. But the resulting images from satellites such as Skylab and YOHKOH are truly spectacular, and show the corona in a completely new guise (Fig.1.6). There are regions of two distinct types. Those in which the magnetic field is predominantly open appear relatively dark and are known as *coronal holes*; here the plasma is flowing outwards to give the solar wind. Those in which the magnetic field is mainly closed consist of myriads of *coronal loops*. Also, small intense features called *X-ray bright points* are scattered over the whole disc.

In open field regions, the solar corona is not in hydrostatic equilibrium, but is continuously expanding outwards as the *solar wind*. Most of it probably escapes along open field lines from coronal holes, especially the two polar coronal holes that are normally present, but small, open regions above active regions may also exist. The

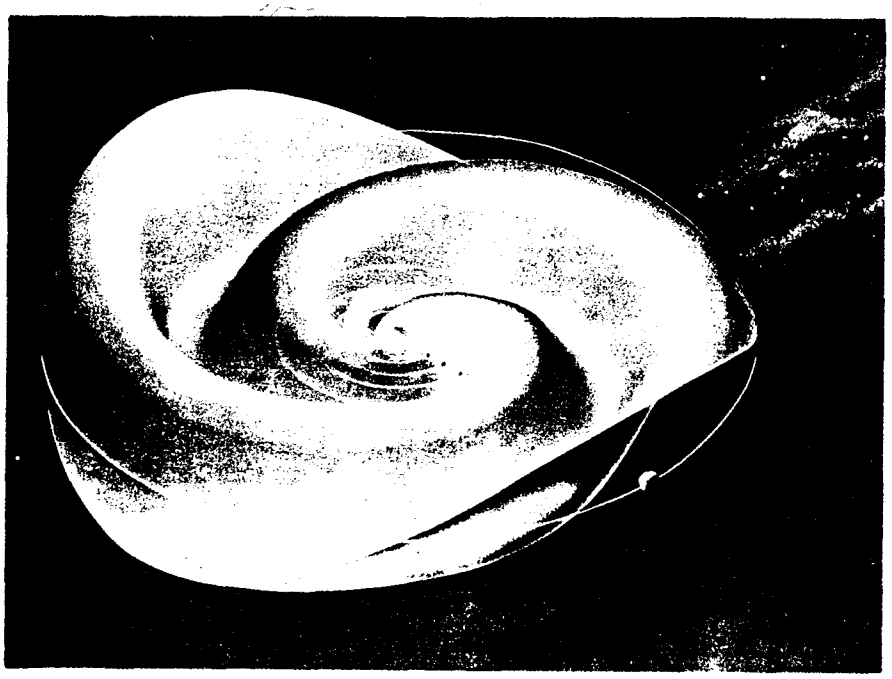

Figure 1.7: *An illustration due to (Hoeksema) of the warped heliospheric current sheet, drawn to scale with some planetary orbits. As the Sun rotates, an observer above the solar equator sees a sequence of alternating polarities (typically four in number), successively from one side or the other of the current sheet (Foukal 1990).*

two polar holes with their oppositely directed magnetic fields are, at small distances from the solar surface, separated by the closed magnetic configuration typical of active regions. But beyond one or two solar radii above the solar surface they come into contact at a *neutral current sheet.* In an idealized solar atmosphere, this current sheet would lie along the magnetic equator, but the presence of large-scale photospheric fields causes the sheet to be *warped* (Fig.1.7).

The flow speed increases monotonically from very low values in the inner corona and eventually becomes supersonic and superalfvénic. Close the Sun the magnetic field dominates the plasma dynamics while the opposite far away. In the Earth distance the average plasma wind velocity is 400 km/sec (from 200 to 900 km/sec), the density $6.5 \times 10^6\ m^{-3}$ (from 4×10^5 to $10^8\ m^{-3}$), the temperature $10^5\ K$ (from $4 \times 10^3\ K$ to $10^6\ K$) and the magnetic field $6 \times 10^{-5}\ G$ (from $2 \times 10^{-6}\ G$ to $8 \times 10^{-4}\ G$). The large variation of the above parameters related directly to the solar cycle (the maximum of solar activity the strongest solar wind). Also the solar wind plasma does not quite flow radially from the Sun; its velocity is inclined at about 1.5^o to the radius vector. This means that angular momentum is being transferred from the Sun to the solar wind and the Sun is being braked in the process; this effect is sufficient to slow the Sun down

significantly over its lifetime. The solar wind is far from uniform. It consist of a series of *high speed streams* related with the appearance of open field regions on the Sun. On a small scale the solar wind is highly irregular as a result of propagation of various magnetohydrodynamic waves and discontinuities on it.

1.3 Transient Features in the Solar Atmosphere

When viewed at low resolution in white light, the Sun appears rather simple, but a closer look at the photosphere and the overlying atmosphere reveals a complex structure, which changes dynamically in a rich variety of ways. For example, an Ha photograph such as Fig.1.7 shows up many features superimposed on the quiet atmosphere. *Active regions* appear as bright *plages* of emission in the equatorial belt within $\pm 30^o$ of the equator; they represent moderate concentrations of magnetic flux with mean fields of 100 G or so. Within an active region one finds dark regions of intense magnetic field called *sunspots*, and near sunspots there is occasionally a brilliant region of intense emission, called a *solar flare*, which represents the violent instability of part of an active region magnetic field and the resulting energy release. Furthermore, around and far away from active regions there are thin, dark ribbons called *filaments* (or *prominences*). It is interesting to compare the appearance of all these features at different levels in the atmosphere, as for instance in Fig.1.2; in white light, sunspots represent the dominant departure from uniformity, whereas in soft X-rays the active regions as a whole are most prominent (Fig.1.6). Furthermore, the eclipse photograph in Fig.1.5 shows clearly the streamers that lie above prominences and active regions, while a magnetic field map shows intense magnetic flux concentrations in sunspots and, to a lesser extent, in active regions (Priest 1984).

All the above forms of activity owe their existence to the *magnetic field.* Rather than being distinct, they simply represent different ways in which the solar plasma is responding to the underlying magnetic field development. They evolve on a variety of time scales. The distribution of sunspots varies with an 11-year periodicity known as the *solar cycle.* Prominences, the most stable of all surface features, may endure for 200 days, whereas a large sunspot group may last half that time and a solar flare is usually over in an hour or so.

1.3.1 Active Regions

When new magnetic flux rise up from below at the photosphere as an *emerging flux region*, the atmosphere is heated and produces an X-ray bright point. The mean lifetime of those is less than a day but sometimes magnetic flux near the equator continues to

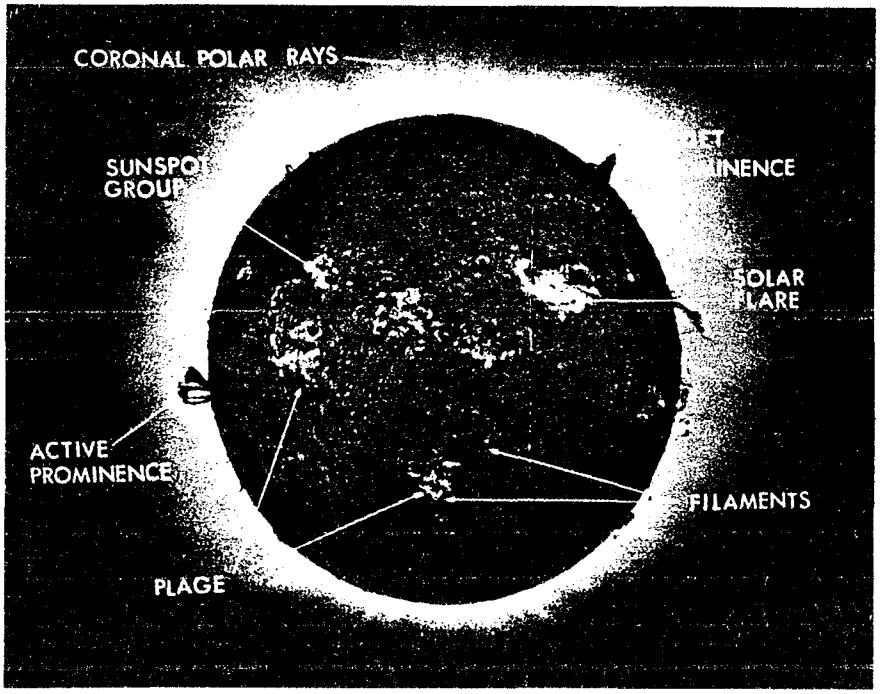

Figure 1.8: *A composite photograph of the Sun, showing several forms of activity. It includes the solar disc in Hα and the corona during an eclipse (S. Martin; LSO).*

emerge and a bright point grows into an active region. Most active regions are bipolar with the flux well-ordered into two islands of opposite polarity, but occasionally a magnetically complex region forms as new flux emerges with a different orientation or as a new region appears within an existing one. In the photosphere the most intense concentrations of magnetic flux called *sunspots* which form during the emergence of flux in one day or so. They decay away during the slow dispersal of the magnetic flux which marks the decay of an active region, but the region may remain active with an enhanced magnetic field for weeks or months after the disappearance of sunspots. Typical well-developed active regions (Fig.1.9) have a single sunspot; its preceding flux is concentrated there and its following flux is much more diffuse. The long, thin, dark rope-like structure are called *fibrils* and probably follow magnetic field lines, some connecting opposite polarities. They have widths 700 to 2200 km, an averaged length of 11000 km and life times of 10 to 20 min, although their overall pattern remains constant for hours. During the emergence of new flux the active region typically consists of a pair of sunspots joined by a system of dark loops calling an *arch filament system* which subsequently replaced by fibrils called *field transition arches*, which continue to join opposite polarity areas (Priest 1984).

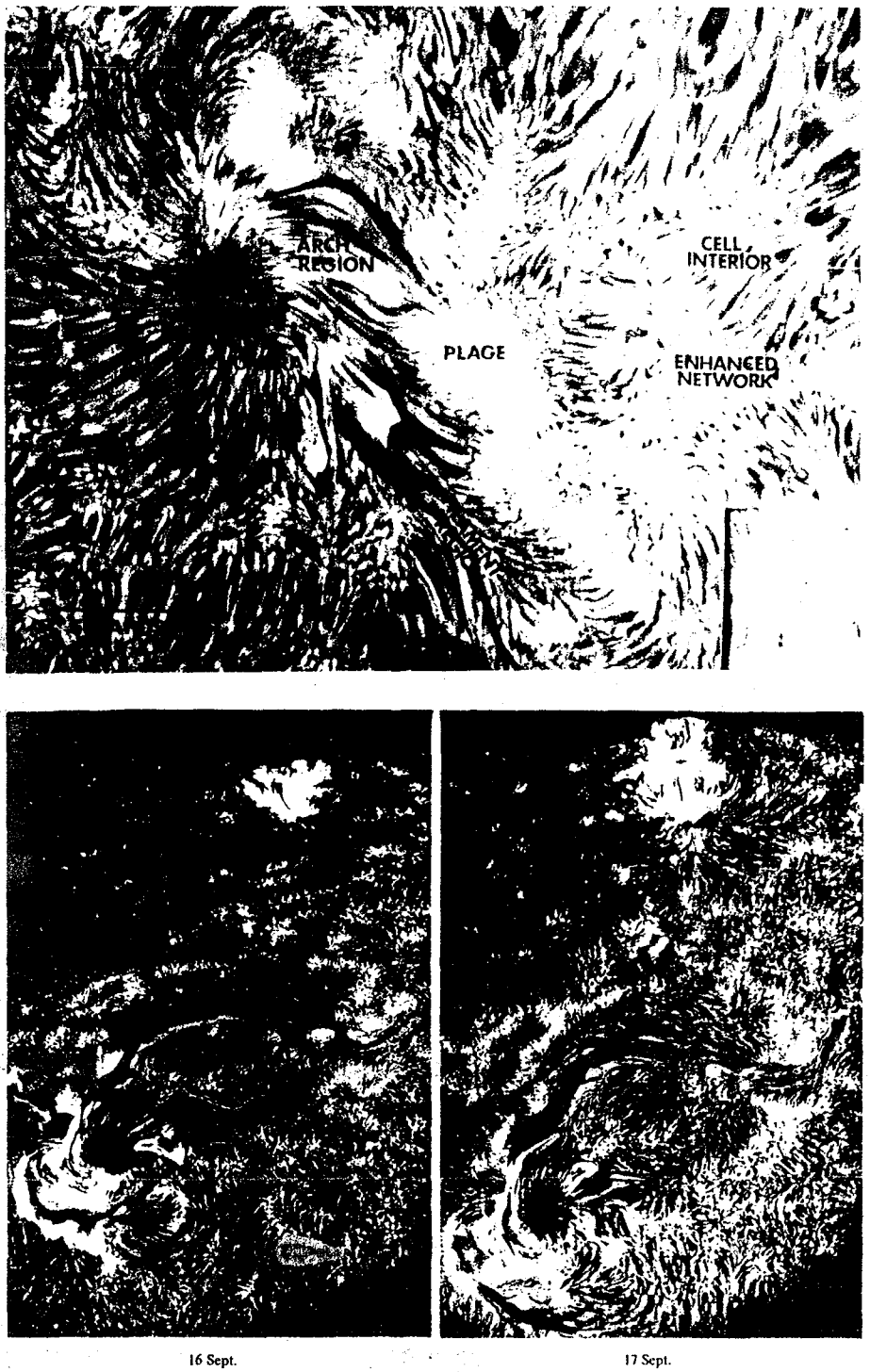

Figure 1.9: *(a) A typical active region in Hα (K. Marsh & H. Zirin; BBO). (b) A new growing active region (top right) together with an older one (bottom left) containing a single sunspot above which stretches a filament (S. Martin; LSO).*

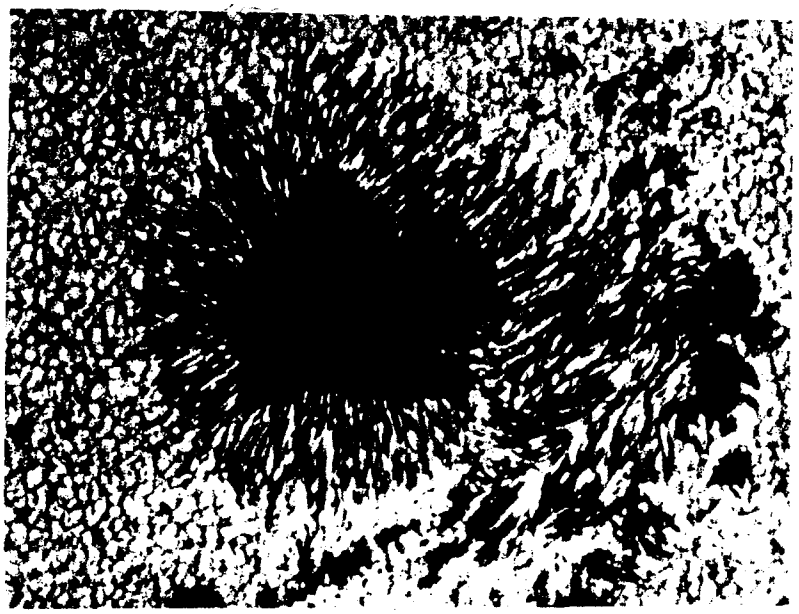

Figure 1.10: *A large sunspot (Muller 1973).*

The density and the temperature are enhanced in the corona above an active region ($10^{16}\ m^{-3}$ and $3{\times}10^{6}\ K$) which makes it visible in white light at the limb during eclipses (Fig.1.5) and also in EUV, X-ray and radio wavelengths against the disc. Above an active region is found an *active region streamer* (Fig.1.5) extending outwards for 3 to 4 $R_{\odot}$ as a series of fans or rays; the most conspicuous ones narrow to a throat or neck at 2 to 3 $R_{\odot}$ above the base and then diverge slightly.

1.3.2 Sunspots

The most intense phase of an active region is characterized by the presence in the photosphere of sunspots (Gurman 1992, Priest 1984, Thomas 1981), which are cooler than their surroundings and represent exceptionally strong concentrations of magnetic flux. They form when the magnetic flux appears at the center of a supergranulation cell, seeing in Hα as an arch filament system, forming eventually a pore in about 5-6 hours. Pores (Fig.1.3) are darker than the surrounding photosphere and have no penumbra; they have diameters of 700 to 4000 km, and magnetic field greater than 1500 G. Often they last for hours or days, but sometimes one develops into a small sunspot. During the growth-phase of the sunspot, lasting between 3 and 10 days, more and more magnetic flux is added to it. Most sunspots disappear within a few days of forming, but some large ones last much longer, slowly decaying over a few months (Fig.1.9).

The central dark area of a sunspot (Fig.1.10) is known as the *umbra*, with a typical diameter of 10000 to 20000 km, about 0.4 of the total spot diameter. The magnetic field strength of about 2000 to 3000 G, and temperature of only 3700 K, in comparison with the 5800 K temperature of the ambient photosphere, are fairly uniform and the intensity in visible light is only 5 to 15% of the photospheric value. But at high resolution one may find 20 or so *umbral dots*, with a diameter of only 150 to 200 km and a normal photospheric brightness; they have depths of about 100 km and are moving upwards at 0.5 km/sec with a lifetime of 1500 sec and a temperature of 5700 K. It appears that the magnetic field in umbral dots is the same as in umbra. At lower resolution, umbral dots are described as *umbral granulation.* Umbral granules resemble ordinary photospheric granules, but they are fainter, more closely packed and have substantially longer lifetimes.

Outside the umbra is found the *penumbra*, which consists of light and dark radial filaments that are typically 5000 to 7000 km long and 300 to 400 km in width. Individual penumbral filaments endure typically 0.5 to 6 hours, by comparison with a lifetime of days or months for the sunspot as a whole. The intensity of a bright filament is typically 95% that of the photosphere, while that in a dark filament is only 60%. *Running penumbral waves* start at the umbral boundary of a regular spot and propagate outwards at about 10 to 20 km/sec, with a velocity amplitude 1 km/sec and periods of 260 to 280 sec. Also continuous plasma *outflow* with speed of 6 to 7 km/sec is observed along the dark penumbral filaments, called *Evershed effect.* It seems that the field lines spread out as one moves outwards from the center of the spot, as indicated in Fig.(1.9). Nearly all the magnetic flux from a sunspot probably returns to the photosphere.

The appearance of a sunspot changes as it passes from the east to the west limb of the Sun, the east side of penumbra being thinner than the west side when the spot is located near the west limb and vice versa, as shown in Fig.1.11. This is known as the *Wilson effect* and implies that the sunspot is a saucer-like depression of about 500 to 700 km below the photosphere. The effect is caused by the fact that the sunspot is more transparent than the surrounding photosphere (because of its lower temperature and density) and so the observed light comes from a greater depth.

The 53% of the sunspots groups are bipolar, with the spots concentrated at the preceding and following sides of a group and having opposite polarity. The 46% are unipolar and only 1% are complex in their polarity.

Of course the most known about sunspots is their cycle which is remarkable in its complexity and regularity. The major aspects of the cycle are, the 11-year period of sunspot number and their spatial distribution (Fig.1.12), (ii) the Hale-Nicholson law of sunspot polarity; the polarity of the leading spots in the northern hemisphere is the same and reverses its sense at the start of a new cycle (also leading spots in the southern

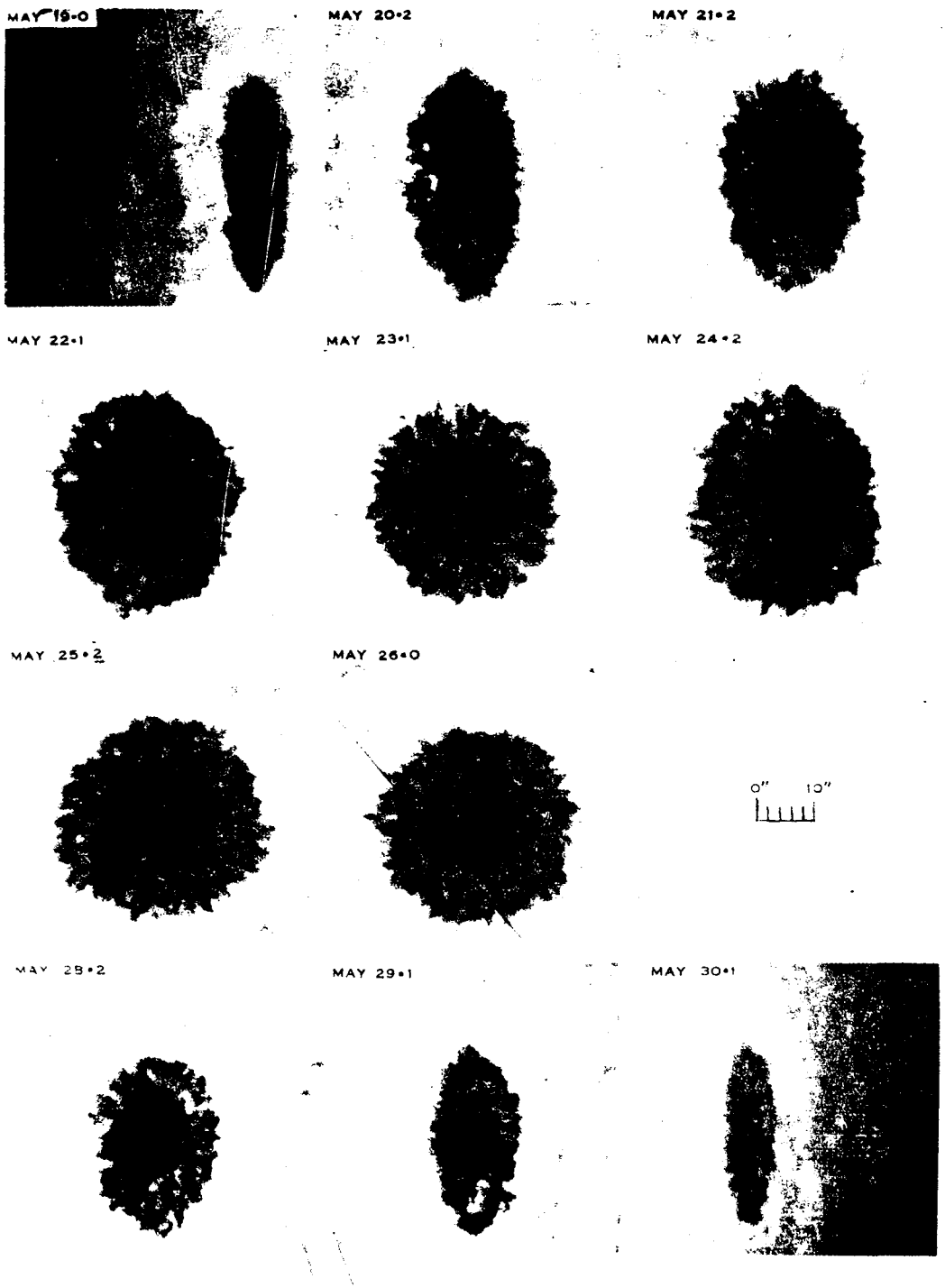

Figure 1.11: *The Wilson effect in a sunspot, showing the changing appearance of the spot as it passes from the east to the west limb of the Sun (Bray & Loughhead 1964).*

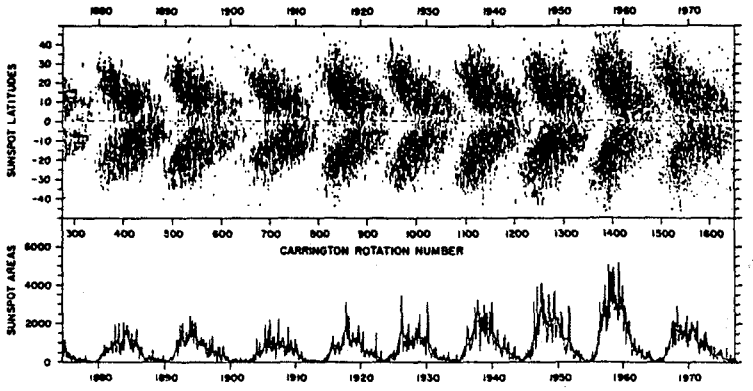

Figure 1.12: *The butterfly diagram, with a single dot for each spot group. The new cycle spots form at high latitudes before the old cycle spots disappear. The lower panel shows the sunspot number in each cycle (B. Yallop; GO).*

hemisphere have opposite polarity to those in the north), and, (iii) the reversal of the general field.

1.3.3 Prominences

Prominences are the most impressive objects on the Sun because they are located in the corona but possess temperatures a hundred times lower and densities a hundred or a thousand times greater than the coronal values. In eclipses they appear bright at the limb, but in Hα-photographs of the disc they show up as thin, dark, meandering ribbons called *filaments* (Fig.1.13).

The observations suggested that prominences are supported against gravity by horizontal magnetic fields. In fact the term prominence is used to describe a variety of objects ranging from relatively stable structures with lifetimes of many months, to transient phenomena that last a few hours or less. Prominences have been classified morphologically in several ways, but there appear to be of two basic types.

(i) *Quiescent prominences* (Figs.1.13, 1.14) are exceedingly stable structures and may last for many months. They are located outside active regions and they migrate towards latitudes higher than 45°; then they are called polar prominences. Their spatial dimensions are 60000-600000 km long, 15000-100000 km high and 4000-15000 km thick. They are anchored in the photosphere at footpoints periodically distant of about 30000 km. Their densities and temperatures are of order 10^{16}-10^{17} m^{-3} and 5000-8000 K, respectively. The magnetic field is found to be 5-10 G. The average angle between the direction of the magnetic field and the long axis of prominence is about 15° (Demoulin 1991, Priest 1984, Zirker 1989).

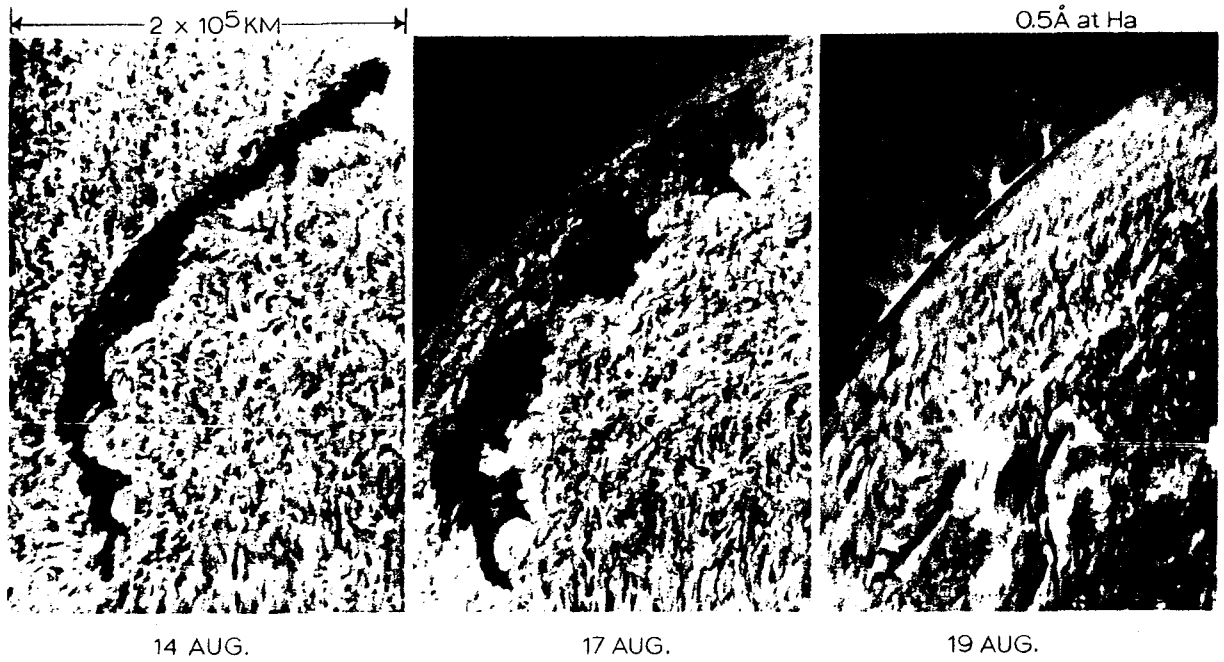

Figure 1.13: *The migration of a quiescent prominence to the limb seen in Hα due to solar rotation (S. Martin; LSO).*

Figure 1.14: *A prominence 70000 km high seen in Hα (H. Zirin; BBSO).*

Figure 1.15: *A small limb flare and surge, typical of what is seen as a modest active region goes over the limb (H. Zirin; BBSO).*

A quiescent prominence forms at a relatively small *active region* (or *plage*) *filament*, which is located either along the magnetic inversion line of an active region or an active region where it meets a surrounding region of opposite polarity. Sometimes it may enter a sunspot from one side. As the active region disperses, the prominence grows thicker and longer. Often continue growing for many months up to 10^6 km in length, and in the process it moves slowly towards the nearest pole and becomes a polar prominence.

(ii) *Active prominences* are located in active regions and are usually associated with solar flares. They are dynamic structures with violent motions and have lifetimes of only minutes or hours. There are various types, such as *surges* (Fig.1.15), *sprays* (Fig.1.16) and *loop prominences* (Fig.1.17). They have magnetic fields of order 100 G and it appears that may be aligned approximately with the filament, whereas for quiescent ones the field run across the filament. The spatial dimensions are typically three or four time smaller compare to the quiescent one, but the temperature is much higher. The density is rather larger ($\geq 10^{17}$ m^{-3}). Although it seems that their support may be hydrostatic or ballistic.

Often a prominence reaches downwards towards the chromosphere in a series of regularly spaced *feet*, which resemble great tree trunks. These feet are located at supergranule boundaries and are joined by huge arches (Fig.1.12). Within a prominence there is much *fine structure* in the form of vertical *threads* of length 5000 km and

Figure 1.16: *A limb spay. These are associated with larger flares and less dominant fields than surges (H. Zirin; BBSO).*

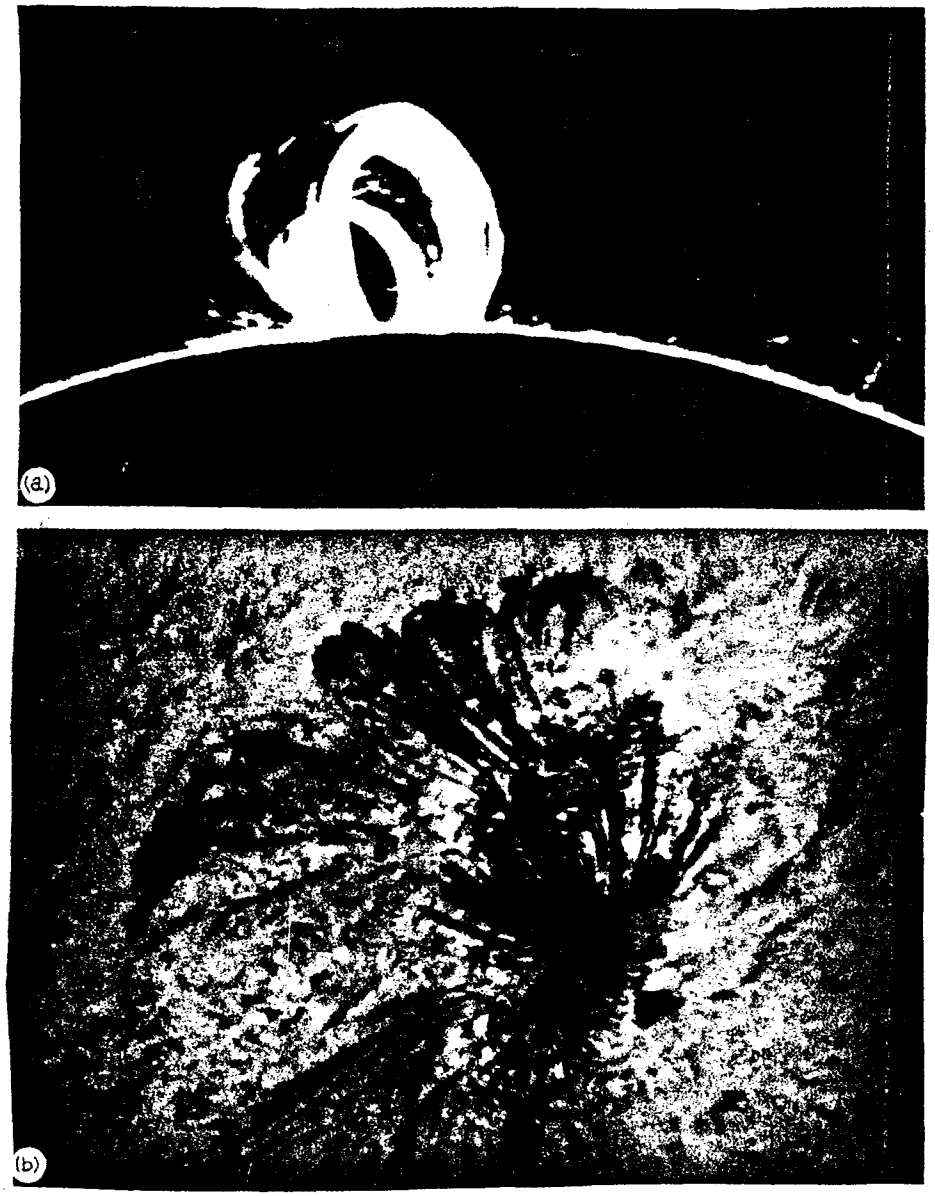

Figure 1.17: *Loop prominences observed in Hα, (a) at limb (Bumba & Kleczek 1961) and (b) at disc (Svestka 1976). These loops go higher and higher in the thermal cooling of the flare.*

diameter about 300 km or less (Fig.1.12); material continually streams slowly down these threads and down the arches into the chromosphere at speeds of only 1 km/sec, which is much less than the free-fall speed. The resulting loss of mass is immense and would drain the prominence in a day or so if it were not being replenished somehow. Hardly any motion along the axis of a quit quiescent filament is observed, unless it interacts with a sunspot, but active region filaments often show matter flowing along the axis into a sunspot.

Active region and quiescent prominences can became *activated* and exhibit several types of large scale motion, such as growing in size and varying their brightness. At this time, there may be an increase in turbulent or helical motion or flow along the filament. This type of activation sometimes fades away after an hour, but sometimes leads to an *eruption* if the filament become completely unstable, especially for those exceed about 50000 km in height. Thus we have an *erupting prominence* (Fig.1.18) which eventually disappears; some of the material escapes from the Sun altogether while some descends to the chromosphere along helical arches. Also at some cases the prominence material may drain away from the summit along a curved arc at speeds of 100 km/sec.

Erupting prominences are related to the 70% of it coronal transients which have been observed in the outer corona by Skylab (Fig.1.19). The rest are associated with large flares. They represent outward-moving loops or clouds with speeds of 100-1200 km/sec; the material probably originates in the low corona above the prominence, rather than from its interior. These loops had similar orientations to those of the original filaments.

1.3.4 Loops

One of the most exciting realizations of the past 15 years is that the solar corona is filled with myriads of loop structures. Today it is quite acceptable that *the loops that we see is the solar corona.* These loops relate with closed magnetic structures, on a relatively large scale in quiet regions and a smaller scale inside active regions. The only exception are the coronal holes where the field lines are open and are the source of the solar wind. There is a wide range of different types of loops (Priest 1978):

(i) *Interconnecting loops* join different active regions and seem to form either when two loops stretch from separate active regions and recconect or when one loop recconects with some newly emerging flux (Fig.1.20). They may be up to 700000 km long and in soft X-rays have a temperature of typically 2 to 3×10^6 K and a density of 3×10^{14} m^{-3}. Their ends are rooted in regions of strong magnetic field near the edges of active regions. A single loop lasts about a day, but the whole system may endure for

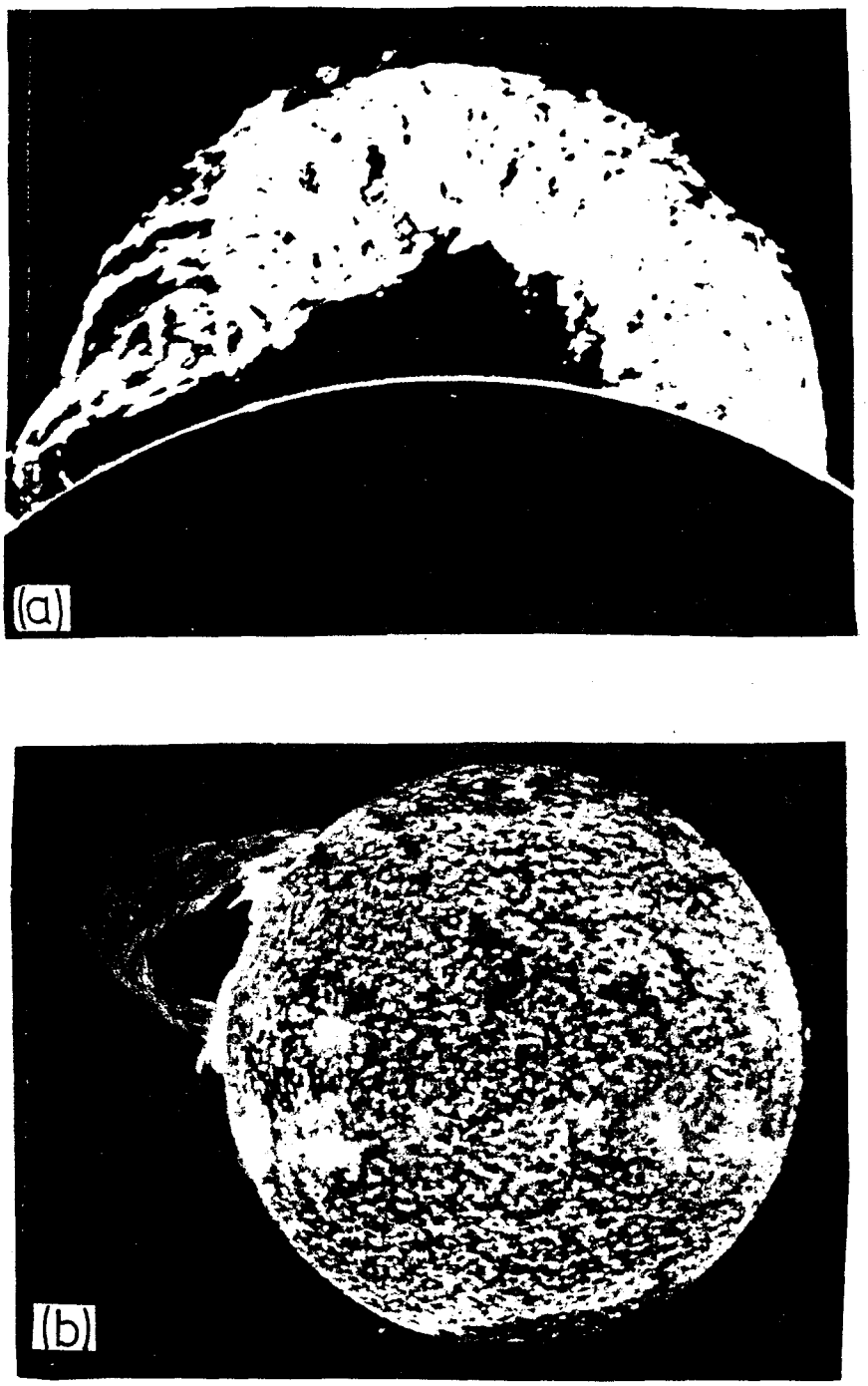

Figure 1.18: *Examples of erupting prominences. The left photograph is in Hα (G. Newkirk; HAO) and the right in HeII (R. Tousey; NRL).*

Figure 1.19: *A coronal transient associated with a prominence eruption observed by Skylab (R. MacQueen; HAO).*

many rotations. Loops that connect fully developed active regions have an intermittent visibility, but those that join an active region to an old remnant change little in shape and brightness for up to 12 days. Interconnecting loops sometimes brighten suddenly (exhibiting higher temperatures and densities by factor two), which may be associated with a twisting of the foot points.

(ii) *Quit region loops* do not connect active regions, and in soft X-rays are somewhat cooler than interconnecting loops with a temperature of 1.5 to 2.1 $\times$ 10^6 K. This, surprisingly, is independent of the density, which may range from 2×10^{14} m^{-3} to 10^{15} m^{-3}

(iii) *Active region loops* are found inside active regions. In soft X-rays, only a few are distinguishable with temperatures 2.2 to 2.8 $\times$ 10^6 K for a wide range of density, from 5×10^{14} m^{-3} to 5×10^{15} m^{-3} and their lengths lie typically between 10000 km and 100000 km, the sorter loops appearing brighter in X-rays. But in 1975 Foukal was found that exist also extremely cool loops, with temperatures at least an order magnitude lower than the surrounding corona. Usually these loops connect sunspots, so may be called also *sunspot loops*. Most are about 100000 km long and 10000 km wide and have cool cores with a temperature lower than 2×10^5 K (Fig.1.21) The core density is lees certain but is probably the same as the surrounding density, so that the core pressure is about a tenth of the coronal pressure. Also, there may be a sheath

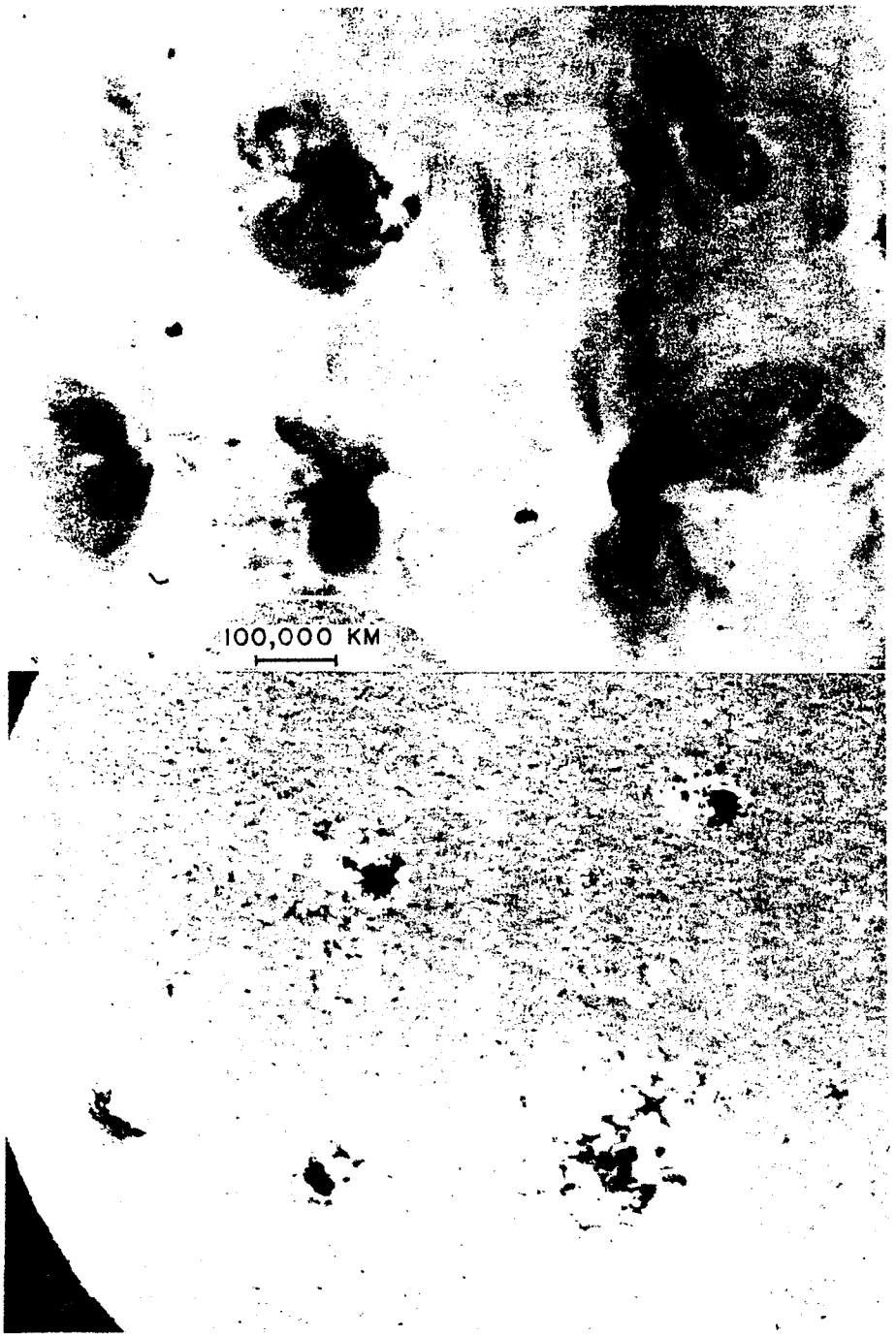

Figure 1.20: *Comparison between a (negative) picture in the EUV line of FeXV (above) and a photospheric magnetogram, showing several active regions and their interconnecting loops (Sheeley et al 1975).*

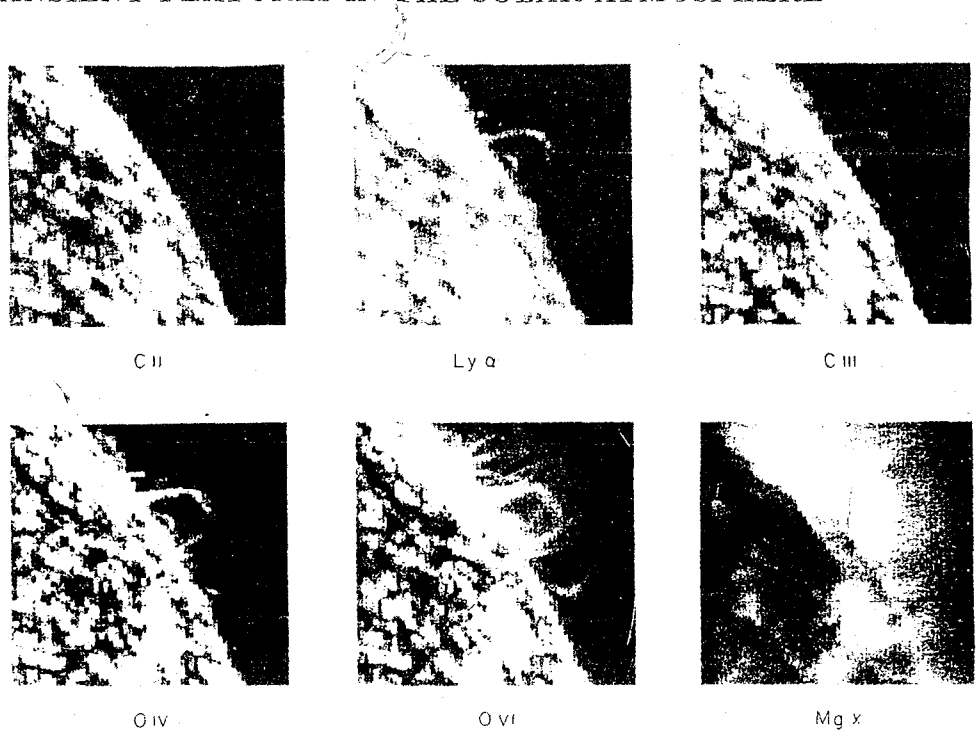

Figure 1.21: *An active region sunspot loop about 60000 km high in the EUV lines of CII (3×10^4 K), Ly α (10^4 K), CIII (7×10^4 K), OVI (1.8×10^5 K), MgX (1.5×10^6 K). Hotter emission comes from progressively thicker co-axial shells (Foukal 1976).*

around the core with a plasma density three or four times bigger than the ambient value. The low core-temperature accounts for its visibility in EUV lines, whereas the sheath density-enhancement shows up the loop in X-rays against the background emission. The pressure and energy balance are steady over several hours, much larger than the free-fall time, and their intensities are not directly related to umbral area; large loops can be rooted in insignificant spots and some large spots may have no bright loops at all.

(iv) *Post-flare loops* (Fig.1.22) relate with solar flares as it observed in EUV and X-rays. These loops may be up to 100000 km high, have bright tops (as hot as 4×10^6 K), densities 10^{17} m^{-3} and follow a filament eruption. They link the two Hα ribbons and form an arcade (visible in both Hα and X-rays) that increases in height as the main phase of the flare proceeds and the Hα ribbons move apart. Post-flare loops are evolving in a manner that may arise from the closing down of a magnetic field that has previously blown open during the stages of a two-ribbon flare. Also an enormous material downflow is observed in Hα.

(v) *Simple-flare loops* (Fig.1.23) are usually smaller than the post-flare loops, with typical size between 5000 and 50000 km, and are extremely hot and dense, with tem-

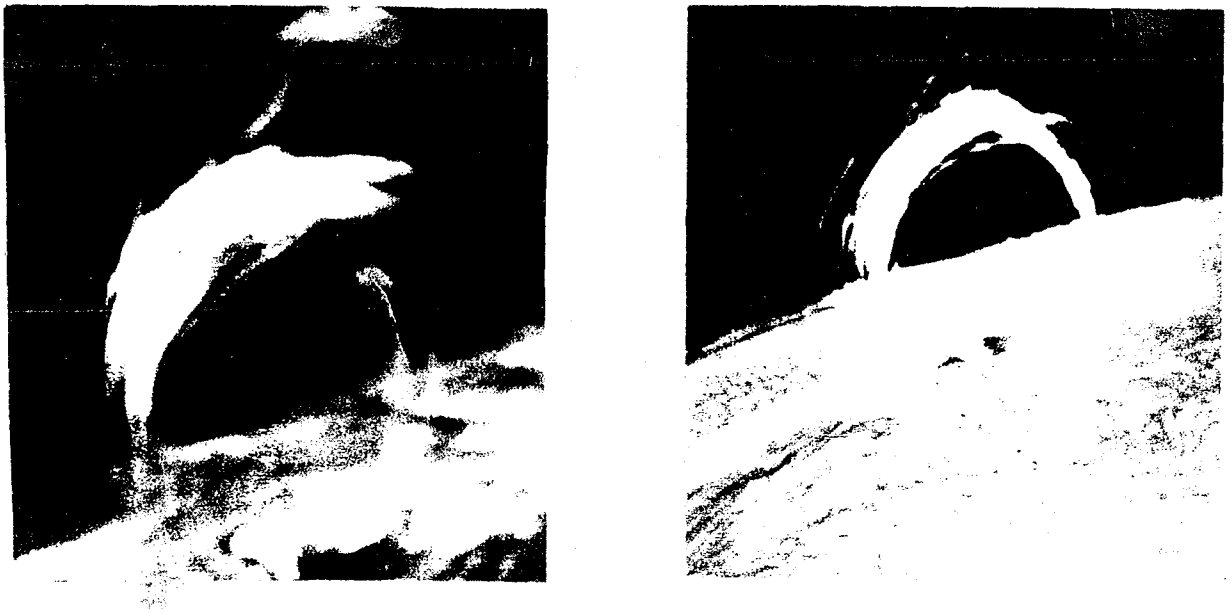

Figure 1.22: *Post-flare loops ending in the flare ribbons inside the limb. The soft X-ray emission comes from loop tops (H. Zirin; BBSO).*

peratures as high as 4×10^7 K and densities up to 10^{17} or 10^{18} m^{-3}. Simple flare loops must contain some dramatic heat source and are far from steady; they may have emerged from below the photosphere during the previous few hours (or a day) or they may be pre-existing loops that have became unstable.

Finally we must note the existance of interplanetary magnetic loops (with dimensions ≥ 1 AU) which are connected bipolar active regions. They are dued to the flare activity, and can be acted like magnetic bottles trapping energetic particles (Sarris & Krimigis 1982).

1.3.5 Flares

The solar flare is the most violent event in the solar system. It varies from being a simple, localized brightening to a very complex violent structure. A solar flare consists of three phases. During the *preflare phase* a large flux tube (a prominence) starts to rise slowly, and there is a gradual brightening in soft X-rays, EUV and microwaves for several minutes. In the *flash phase* which lasts typically 5 min the flux tube suddenly starts to erupt much more rapidly and there is a steep increasing in Hα, EUV, and soft X-rays, while they appear radio bursts in the form of electron beams. At the same time nonthermal particles are evidenced by the appearance of hard X-rays spikes and impulsive EUV and microwave bursts, with shock waves sometimes initiated. Also, Hα knots of emission become joined up to form two ribbons in the chromosphere. During

Figure 1.23: *Two views of a flare near the limb which ejects a loop (H. Zirin; BBSO).*

the *main phase* the intensity declines slowly over about an hour, while the ribbons separate with velocities 2 to 10 km/sec and are joined by a rising arcade of post-flare loops (Fig.1.24).

When a large flare occurs near a quiescent prominence, where the magnetic field is weak, the flare tends to be slow, long-lived and thermal, sometimes with no Hα brightening at all, thought the basic magnetic instability is probably the same. When it occurs instead near an active-region prominence, where the magnetic field is strong and complex, the flare is violent, short-lived and nonthermal (Priest 1984).

Near the polarity inversion line one often finds small pores and transient weak X-ray sources. Many other precursors in the corona can be seen up to an hour preflare, while prominence activation may sometimes begin even earlier. Soft X-ray and EUV brightening occurs often around the prominence or in the form of loops or kernels close to the subsequent flare site. In microwaves sometimes there is an increase in intensity because of heating and a change in polarization due to changes in the coronal magnetic field. Also radio bursts can occur before a large event, possibly because of the preaccelaration of electrons (Priest 1988).

Since flares invariably occur in active regions and the other sources of energy seem inadequate, it has usually assumed that it is the magnetic field which supplies the energy of 10^{22} to 3×10^{25} J for a flare (Priest 1984).

1.3.6 Modern view of solar corona

It is now known that the old magnetohydrodynamic, steady picture of an active region and the background corona based on the previous low cadence images is not correct. Instead, recent observations from YOHKOH (Ogawara et al 1992) revealed that steady mass from below supply at least a certain fraction, if not all, of the mass and energy of the active region corona which is almost continually expanding (Ushida 1992, Ushida et al 1992). The injected mass itself is confined in flux tubes inside the active regions (Klimchuk et al 1992). The mass injections may turn out to be the cause of destabilization of such coronal active regions, and they may turn bring a new component (magnetically driven mass loss) into the solar mass loss problem (Shibata et al 1992).

The background general corona turns out not to be an isolated quiet entity, but is rather a system closely linked with the active region corona. Changes in the active regions can affect the environment corona. In some cases propagating '*magnetic reconnection waves*', caused by changes in the magnetic field connectivity in the stronger magnetic field regions, can propagate further away from an active region in cascade. In some other cases magnetohydrodynamic disturbances may simply perturb distant magnetic structures transiently in the form of simple waves, but in some other cases

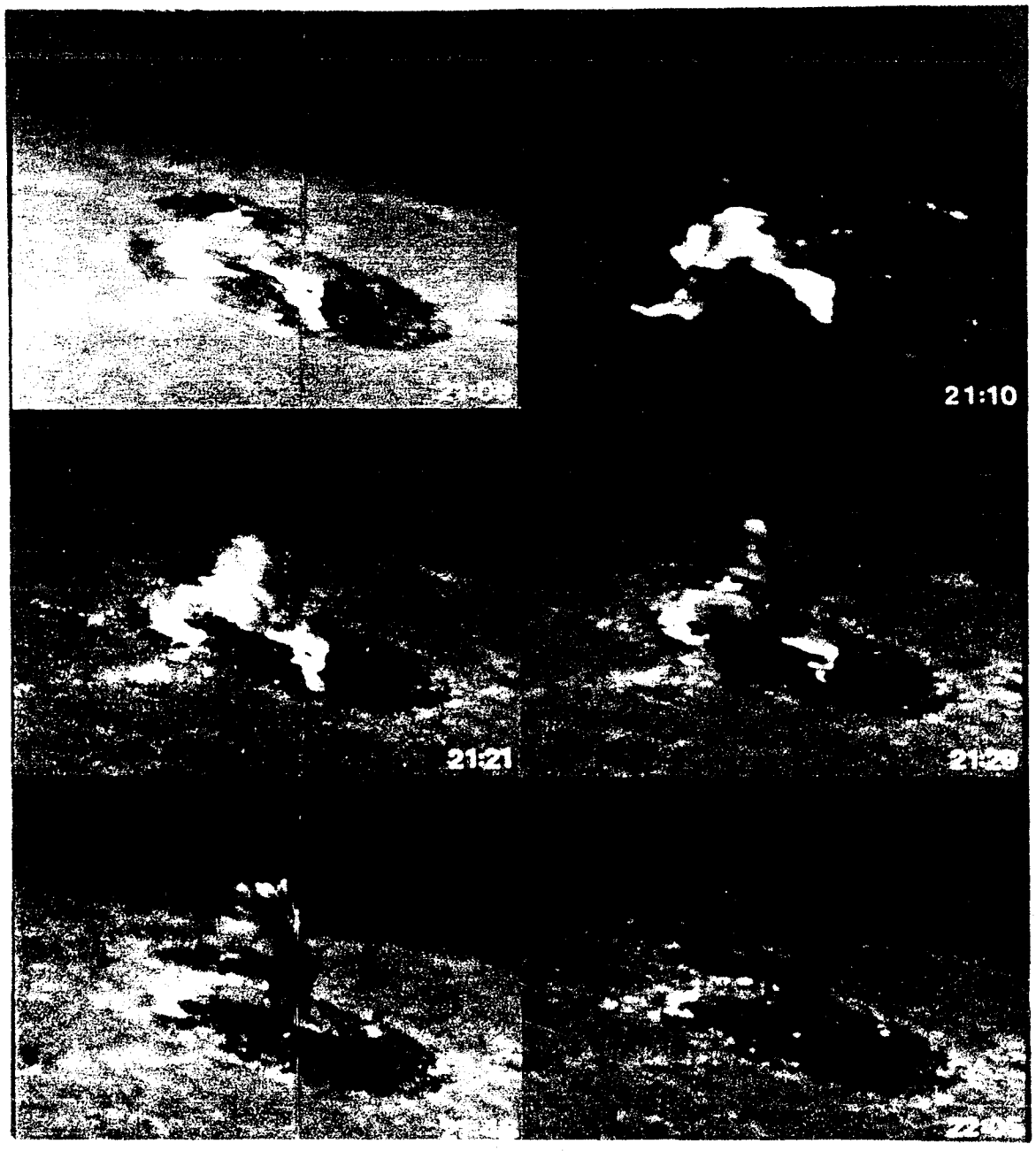

Figure 1.24: *An excellent view of a flare near the limb, showing the development of loop prominences. The first frame is after the flare peak. Bright loops is seen two sunspots. As they develop, the loops rotate, become darker, but the tops are always brightest and densest. In all loops the material rains down in two branches (H. Zirin; BBSO).*

they may influence distant structures permanently either stimulating some instabilities, or through such magnetic reconnection waves (McAllister et al 1992, Ushida 1993, Shimizu at al 1992).

Dynamical changes in the general background corona itself, either spontaneous or by stimulation, often occur at the same time as disappearances of Hα dark filaments. Coronal mass ejections may, in this way, either be related to a flare occurring at a distance from the site of coronal mass ejections, or be unrelated to a flare but related to a much less energetic phenomenon, an active region transient loop brightening that can greatly affect the magnetic structure in the surroundings. The required energy may come from the release of the magnetic buoyancy of the structure anchored by the magnetic ties. It is possible that the dark filament disappearance itself in these events is merely a passive feature, not a driver of the energy liberation, but one of the results of an instability of the field structure as a whole, which can be triggered by a small disturbance at a distance (Hara et al 1992, McAllister et al 1992).

An interesting point is that various phenomena in the solar corona, such as *arcade formation* in relation to the disappearing dark filament, seem to have examples or analogues with scales ranging from very large in the polar region to small inside active regions. These may correspond to the weak field case and the strong field case, respectively, with similar field configurations. Thus the large and faint arcade above a disappearing polar dark filament, the medium scale hotter arcade, and the relatively quiet version of flares with Hα double-ribbon structures in active regions may all belong to the same physical class and occur in similar magnetic field configurations but with different magnetic field strengths and different scales (Ushida 1993).

1.4 Coronal plasma loops

The discovery that a significant part of the energy emission from the solar corona is concentrated along well-defined curved paths – called *loops* – represents a major advance in our understanding of the Sun. Such plasma loops are the basic structural elements of the corona, particularly in and over active regions. Moreover, they play a decisive role in the origin and physics of solar flares. Our new insight is due largely to the wealth of space observations of the Sun obtained, in particular, firstly from the satellite Skylab (1973-1974) and the Solar Maximum Mission, Hinotory and YOHKOH satellites which followed. Ground-based observations in the visible and microwave regions of the electromagnetic spectrum have also play a vital role. The literature on coronal plasma loops is vast and includes not only hundreds of research papers but also the proceedings of numerous symposia and workshops. In this section we shall cover briefly the observational part of coronal loops, while in chapter 3, we shall present a

magnetohydrodynamical analysis of them. In the rest of this thesis they are described in detail our proposed models for the structure of coronal loops and the solar corona in general.

1.4.1 Introduction

Coronal loops are a phenomenon of active regions and there is significant evidence that they are in fact the dominant structures in higher levels (inner corona) of the whole atmosphere of the Sun. Although that our knowledge of loops has greatly expanded in recent years because of the space observations in the far ultraviolet and X-rays, we must not ignore the fact that a considerable amount of quantitative information on the morphological, dynamical, and physical properties of coronal loops has been derived from ground based observations in the visible and near-visible regions. in fact, observations at these wavelengths have achieved significantly higher spatial resolution (better than $1''$) than almost all the space observations so far obtained.

Observations show that coronal loops, depending on their temperature, can be divided into two distinct categories. The properties of the two types differ radically. Loops formed at temperatures in excess of $\approx 10^6$ K are conventionally referred to as *hot loops*, while those formed at lower temperatures are termed *cool loops*. We shall consider the two types separately.

1.4.2 Cool loops

The range of temperature covered by the category of cool loops extends from $\approx 10^6$ K down to ≈ 20000 K; the Fig.1.17 represents a temperature characteristic of loops observed in Hα. Taken as a whole, the observations described in this section show that, with the exception of temperature, all cool loops appear to have similar properties and, in fact, can be regarded as manifestations of the same basic physical nature.

When cool loops observed in the limb in Hα and other visible region lines, appear to be anchored to underlying sunspots. In Fig.1.17 is shown a particular fine example of an active region loop system beyond the limb (Bumba & Kleczek 1961). In general, photographs of active region loops (Lategan & Jarrett 1982, Foukal 1978) showing a single neat loop and the characteristic condensations or knots often present in Hα loop systems. The number of loops in a single system may range from just one up to perhaps ten or so; an upper limit is hard to establish from limb observations because loops overlap each other. The apparent, projected heights measured by various authors range from 26400 km (Lategan & Jarrett, 1982), through 50000 km (Tandberg-Hanssen 1977, Makhmudov et al 1980), to 57000 km (Kleczek 1963). However, true heights cannot be determined from limb observations unless the loop geometry is known. Observations

did not say anything about loop lifetimes, but Tandberg-Hanssen (1977) quotes a typical value of 15 *min*. Active region cool loops are found to be in *dynamical stage with flows*. It has long been known that there are three types of motion associated with them (de Jager, 1959), (i) a downflow in both legs, starting at the top of the loop (Kleczek 1963, Lategan & Jarrett 1982), (ii) a flow up one leg and down the other (Martin 1973), and, (iii) a mainly horizontal back-and-forth oscillation of the whole loop (Vrsnak 1984). Bodily upward motions of the whole loop have also observed (Kleczek 1963, Vrsnak 1984). The majority of the velocities are inferrent either from Doppler shifts (Foukal 1978, Lategan & Jarrett 1982) or from the proper motion of knots (Kleczek 1963, Foukal 1978, Makhmudov et al 1980) lie in the range 20-150 km/sec. The upflow accelerations are sometimes greater than $g_\odot$ (absolute values), while the downflow ones are always less. These values are also consistent with values derived from measurements of loops observed on the disc. Finally, the magnetic field in active region loops is found to be in the range 7-100 G (Bray et al 1991). Measurements have been done using either the Zeeman effect (Tandberg-Hanssen 1974, Tandberg-Hanssen & Malville 1974) in order to find the line of sight field component, or, the Hanle effect (Bommier et al 1981, Athay et al 1983) in order to find all the field components. It is possible that the typical value of ≈ 50 G for the magnetic field in active region loops, is probably represent lower limit to the true field along the axis of loops. However, the limb measurements are valuable since no disc measurements have yet been attempted. Not have any measurements so far been attempted in the EUV spectral region.

On the disc an active region loop appears in the Hα line as a thin, curved, dark feature linking a sunspot with another spot or area of opposite magnetic polarity (Ellison 1944, Tandberg-Hanssen 1974). The actual location of the footpoints with respect to the associated sunspot or spots is seems to be the umbra/penumbra boundary. Also according to Ellison (1944) single or double loops are quite common, but complex formations of loops are rare. By contrast, post-flare loop systems commonly contain a large number of loops in the form of an arcade (Fig.1.22). The lifetimes of Hα loops observed in the disk are found to be less than 1 h (Bray et al 1991). Often, the planes in which lie Hα loops are inclined at fairly large angles (30^o to 40^o) to the solar vertical; this is also the case for cool loops observed in the EUV. The axes of symmetry, are tilted at only small angles (-6^o to 6^o) to the perpendicular bisector of the line joining the footpoints, while the highest points lie some 40000-50000 km above the solar surface, in agreement with the estimates of the heights of cool Hα loops observed at the limb (Loughhead et al 1984, Loughhead & Bray 1984). Note also that these heights are comparable to those found for cool EUV loops. Finally, two types of flow are observed; (i) a unidirectional flow along the axis of a loop, in other words an ascent in one leg

and a descent in the other (Ellison 1944, Tandberg-Hanssen 1977, Bray & Loughhead 1983), and (ii) a downflow from from the top towards both footpoints (Martin 1973, Chen & Loughhead 1983). The first type of flow is a commonly observed characteristic of loops in new and complex active regions. Only few velocity measurements in Hα loops on the disk are available (Loughhead & Bray 1984). In one studied case (Loughhead & Bray 1984) they show high (supersonic) velocities almost throughout the loop (Fig.1.25), with the material to be accelerated fastly as it rises and descends from and in the solar surface. This means that upflow is driven by a strong accelareting mechanism (larger than $g_{\odot}$ at this particular case) despite the presence of gravity, while downflow is subject to a retarding force since the acceleration which found is less than the solar gravitational one.

Below 150 nm the contribution of the photospheric layers to the solar spectrum vanishes and the radiation comes from overlying material at chromospheric or coronal temperatures. When this wavelength is reached, the character of the emission has changed from that of familiar dark line spectrum in the visible and near ultraviolet to that of a bright-line spectrum (Fig.1.26). The far ultraviolet extends down to about 10 nm, below which it is customary to categorize the emission as soft X-ray radiation. The solar EUV spectrum is dominated by emission from resonance lines of HI (Lyman series), HeI, and HeII, of intermediate stages of ionization of C, N, O, Si, and S, and of highly-ionized stages of Si, Ne, Mg, and Fe. Other distinctive features are the Lyman continuum at $\lambda < 91.2\ nm$, and the HeI and HeII continua at $\lambda < 50.4\ nm$ and $\lambda < 22.8$ nm respectively. Under the conditions of formation normally assumed to apply, the intensity of any given line is a sensitive function of the electron temperature, peaking at some particular value and falling off sharply on either side. The presence of this line in the spectrum of a feature under study thus indicates that the temperature in the emitting region must be close to the resulting electron temperature. For this reason this temperature is often termed the *formation temperature* of the line. EUV lines characterized by electron temperature values of $\approx 10^6\ K$ or less are conventionally reffered to as *cool lines*, whereas lines with electron temperatures greater that $\approx 10^6$ K are described as *hot lines*. In the case of coronal loops this distinction is more than a matter of convention, cool loops observed in EUV lines in temperatures $<< 10^6\ K$ differ in their properties from hot loops observed in lines with electron temperatures $\geq 10^6\ K$.

Usually, when an active region is observed in EUV lines it is found that the emission is centered on two bright areas overlying the regions of opposite magnetic polarity in the photosphere; not surprisingly, the outlines of the bright areas follow the contours of the underlying Hα faculae (Cheng et al 1980, Schmahl et al 1982). With the best available resolution the central bright areas are resolved into aggregates of small, very bright

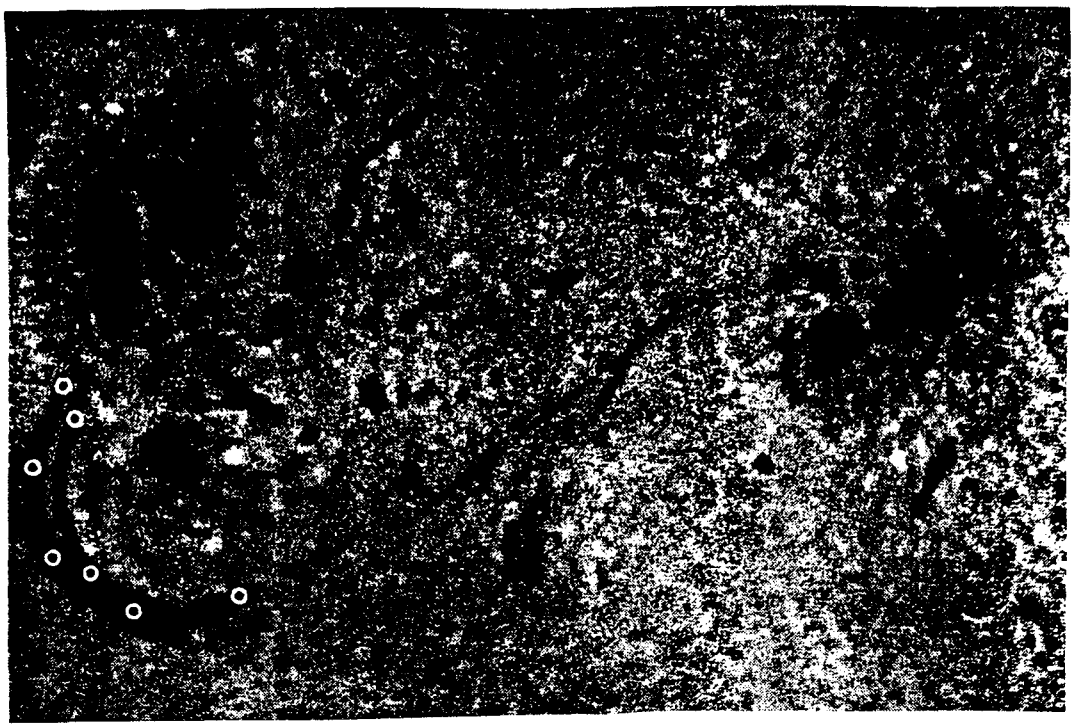

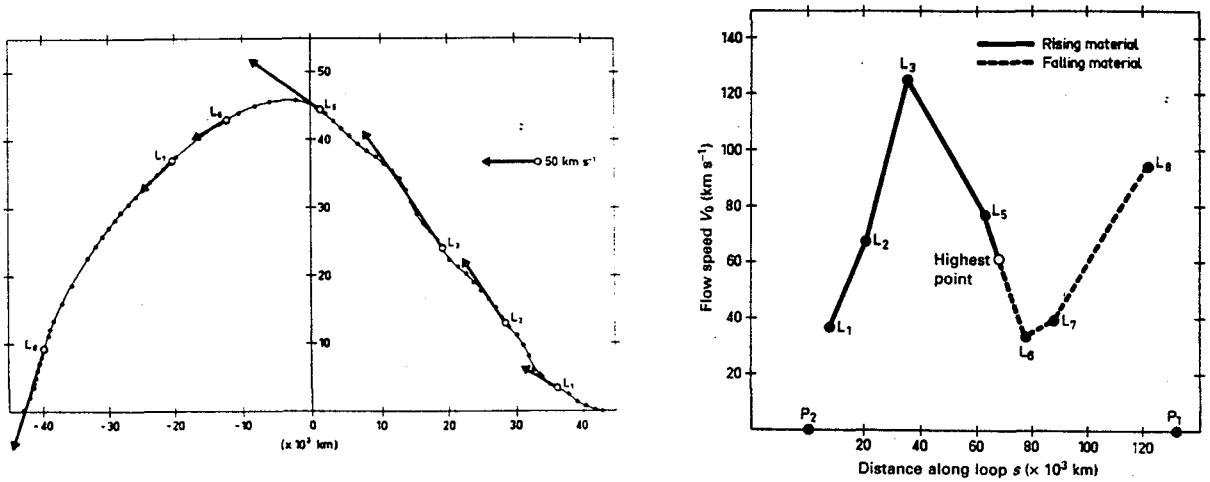

Figure 1.25: (a) Active region loop of 6 June 1980 photograph at Hα (Bray & Loughhead 1983). The small white circles identify the points of the loop using for its geometrical reconstruction seeing in (b). The arrows at these points represent the magnitudes and directions of the true flow speed V along the central axis of the loop, which is seen in (c), and is supersonic at all locations. Note that between L_2 and L_3 the speed of the rising material almost doubles, despite the retarding effect of gravity. On the downward leg the material speeds up as it approaches L_8, and the footpoint P_1, but it does not attain the velocity of free-fall ($\approx$ 150 km/sec) from the highest point above the surface (39800 km).

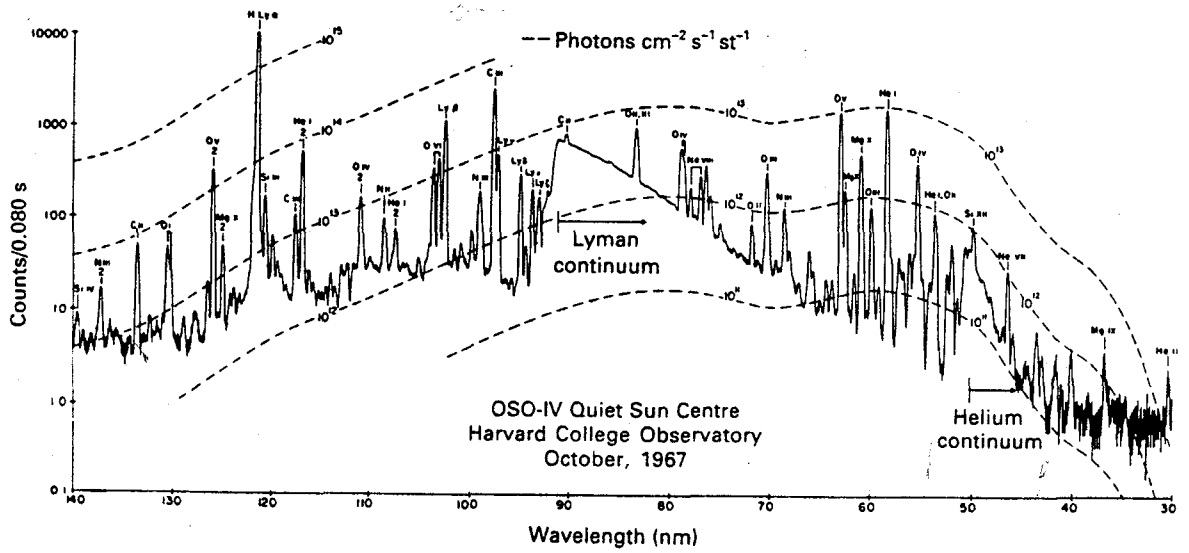

Figure 1.26: Prominent EUV emission lines at the center of the solar disc.

kernels, some of which are noticeably elogated. But, just outside, a number of bright loop-like features are seen pointing more or less radially outwards. Limb observations demonstrate that these features represents portions of coronal loops, which may extend up to heights of tens of thousands of kilometers.

In common with all other solar features, cool EUV loops are always observed in projection against the plane of the solar disk or of the sky beyond. Consequently, in the absence of geometrical reconstructions of individual loops along the lines of those accomplished for Hα loops, relatively little can be said about the true shapes and sizes of cool EUV loops. Nevertheless, limb observations such that in Fig.(1.27) do show that most loops are essentially *planar*. The inclination of the planes containing the loops may vary from nearly vertical to nearly horizontal. Moreover, there is some indication that the preferred inclination of a loop may become more vertical as the region grows older (Levine 1976, Bray et al 1991). Limb observations also yield estimates of the heights attained by the loops. Usually there are found to be in the range 50000 to 60000 km (Cheng 1980, Chiuderi 1981) while sometimes reach 110000 km (Athay et al 1983). The widths of cool EUV loops seem to increase only slowly with height by a factor less than two (Foukal 1976, Cheng 1980), and lie in the region from <2000 to 5000 km (Foukal 1975). But Dere (1982) gives larger estimates, ranging from 6000 to 22000 km. For Lα loops observed at the limb, Tsiropoula et al (1986) have measured diameters, constant with height, of 2000 to 3500 km. However, it is important to say that the loop width increases with temperature (Foukal 1976, Sheeley 1980); an example is seen in Fig.(1.21). The *aspect ratio* parameter, which sometimes arises in

Figure 1.27: An active region cool loop system in the EUV line OVI (3×10^5 K). Despite the obscuration at low heights caused by overlapping, the region consists basically of a number of separate loops lying in planes inclined at widely differing angles to the solar vertical. Individual loops may reach heights of tens of thousands of kilometers (Levine 1976).

studies of loop stability, defined as the ratio of the cross-section loop radius to its length, is found to be 0.006 (Cheng et al 1980), an order magnitude smaller than that found in hot EUV loops. The footpoints of cool EUV loops are generally located on the peripheries of the two areas of opposite magnetic polarity in a bipolar active region (Cheng et al 1980). On the other hand, there is an important class of cool coronal loops which have at least one end anchored in bright EUV emission over a sunspot (Foukal 1976). The former ones possibly may be more stable than the others cool EUV loops. Despite of this, there are no quantitative informations about the lifetimes and the evolution of them, although that cool loops observed in the EUV regime are found to have flows. The line of sight velocities in the CIV (Athay et al 1982, 1983) are found to range from ±5 to ±10 km/sec near disk center and from ±9 to ±18 km/sec near the limb, a negative (positive) sign denoting redshift (blueshift). In most cases the flow was directed downwards in both legs of the loop, but there were others showing a unidirectional flow from one end of the loop to the other. This pattern is analogous to that observed in the Hα active region loops discussed previously.

To end this section, we give in Table 1.2 the known quantitative data concerning the morphological, dynamical and physical properties of cool loops (Bray et al 1991). From the data presented it is evident that, over the temperature characterizing cool coronal

Quantity	Value	Wavelength	Disk (D) or Limb (L)
Height, true (km)	40000–53000	Hα	D
Height, projected (km)	26000–57000	Hα	L
	50000–67000	EUV	L
Length (km)	130000	Hα	D
	22000–109000	EUV	D
Separation of the footpoints(km)	71000–86000	Hα	D
Diameter (km)	1600 ('normal' loop)	Hα	D
	< 2000–22000 ('normal' loop)	EUV	D,L
	1300–580 ('very thin' loop)	Hα	D
Aspect ratio	0.006	EUV	D
Inclination of loop plane to vertical	30^o–40^o	Hα	D
Tilt of axis of symmetry	4^o–6^o	Hα	D
Lifetime	3–6 hr (loop system)	Hα	D
	< 15 min (single loop)	Hα	D
Axial flow speed (km/sec)	34–125	Hα	D
	20–150	Hα	L
	95	EUV	D
Mach number	1.6–6	Hα	D
Temperature (K)	21000	Hα	D
	7000–25000	Visible	L
	6×10^4–10^6	EUV	D,L
Electron density (cm^{-3})	5.6×10^{10}	Hα	D
	3–6000×10^9	Visible	L
Gas pressure ($dyne/cm^2$)	0.36	Hα	D
	0.14–0.58	Visible	L
Gas density (g/cm^3)	1.3×10^{-13}	Hα	D
Degree of hydrogen ionization	0.996	Hα	D
Sound speed (km/sec)	21	Hα	D
Nonthermal velocity (km/sec)	26	Hα	D
	10–30	EUV	D
Line-of-sight magnetic field (G)	7–100	Visible	L
Total magnetic field (G)	4–45	Visible	L

Table 1.2: *Properties of cool loops (Bray et al 1991).*

loops ($20000 - 10^6$ K), both the heights and lengths of the loops are comparable. On the other hand, there is a small but apparently real increase in diameter with temperature. the inferred values of the electron density in cool loops observed in both the visible and EUV regions of the spectrum extend over a wide range of several orders of magnitude. despite this, the values of the gas pressure listed in Table 1.2 are restricted to a much smaller range of one order of magnitude. This may reflect the circumstance that the stability of a loop, whatever its temperature, depends on the maintenance of approximate pressure equilibrium with the surrounding coronal medium. Taken as a whole, the presented data show that, with the exception of temperature, all cool loops appear to have similar properties and can be regarded as manifestations of the same basic physical structure.

1.4.3 Hot loops

As we have seen, observations made in cool visible and EUV lines have provided extensive information on the large-scale systems of loops which dominate the structure of the lower corona above active regions. The loops are believed to trace out closed field lines of force of the magnetic field which protrude up from beneath the photosphere and expand to fill the whole coronal volume above an active region. Hence a picture of the loop systems gives us some insight into the three-dimensional configuration of the

magnetic field. But the picture obtained from observations of cool loops is far from complete. For more detail we have to turn to observations of hot loops, filled with material at coronal temperatures of a million degrees or more. Emission from material at that temperatures dominates the EUV and the soft X-ray regions of the solar spectrum. The lack of any appreciable photospheric or chromospheric emission at these wavelengths enables the corona to be viewed directly against the disk and, in fact, most of the available information on hot loops has been obtained from such (space) observations. In addition, other important contributions to our knowledge have come from the visible and the radio regions of the spectrum. The line and the continuum radiation emitted by the corona in the visible region is many orders of magnitude too faint to be detected on the disk against the glare of the underlying photosphere. Nevertheless, it can be observed beyond the limb both during and, with the aid of coronograph, out side of a solar eclipse.

Before we are reffered to EUV and X-ray observations of hot coronal loops, we shall cover briefly the observation in visible and radio wavelengths. From many decades ago, it is known that the solar corona emission in the visible (wavelengths in the range 500-700 nm) consist of three components, conventionally denoted by the the letters K, F and L. The K component originates from the Thomson scattering of the photospheric light by free electrons and is thus proportional to their number density. The F component is due to scattering by interplanetary dust. Finally, the L component is due to the emission of spectral lines, and is termed the *monochromatic* corona; it is visible only in the inner corona. Hot coronal loops usually observed in FeX, FeXIV, FeXV, NiXV, CaXV visible lines, because they are very bright in the Sun and they have high ionization potential, which is a direct indication of the temperature of hot loops which must be of order of 1-2 $\times$ 10^6 K. Thus active regions observed in this spectrum regime (Kleczek 1963, Dunn 1971) are seen to consist from a system of loops with typical heights of up 50000 to 100000 km. The systems appear to be rooted in sunspot groups or in plage areas. But the larger loops may connect two active regions and extend up to heights of 200000 to 250000 km. Also the larger loops are generally uniform in intensity and have diameter of 8000 to 12000 km, while the smaller loops are less uniform, particularly in their earlier stages, and they have a diameter of 3000 to 8000 km. Hot loops are planar structures and they are more active when they are small, they tend to grow *in situ*, then fade, in a couple of hours and others grow at a higher elevation, while large loops are very stable lasting for days.

Centimeter and low decimetre observations of the Sun with a spatial resolution comparable to that achieved for EUV and X-ray loops are a relatively recent development. This advance has largely been brought about by construction of large array type radio telescopes (i.e., Very Large Array, Westerbork Synthesis Radio Telescope)

employing the method of aperture synthesis. As we have seen thermal radiation from the Sun is detectable over a vast range of electromagnetic spectrum, from the soft X-rays to metric radio waves. But two factors combine to make the thermal radio radiation from the Sun observed at the Earth's surface peak in the centimetric region. One is the onset of strong tropospheric absorption at wavelengths below about one centimetre, while the other is the intrinsic decrease in the density of the radiation at longer wavelengths. The two processes which contribute to the thermal emission from active regions are bremsstrahlung (free-free emission by electrons) and gyroresonance radiation by electrons spiraling around magnetic field lines. Until today the more extensive radio observations are referred to active regions generally than of individual loops. These observations have studied the magnetic field distribution in the low corona above active regions and the correlation between the distribution of the radio emission and chromospheric features and the photospheric field pattern. Only few observations existed for individual radio loops of temperature of order 10^6 K giving lengths in the range 70000 to 100000 km and widths typically of 15000 km. As we will see in the following the aspect radio (loop width over its length) which is around 0.075 is comparable to those found for active regions hot loops observed in the EUV and soft X-rays (Bray et al 1991, and references therein).

Going now to the high temperature regime, the EUV emission from the Sun is confined very largely to active regions and the loops emanating from them (Tousey et al 1973, Sheeley at al 1975). This contracts strongly with the case of the cool EUV emission, which comes from all parts of the disk. When photographed in hot EUV lines well-developed bipolar active regions on the disk often present a characteristic 'butterfly' appearance (Levine 1976), so called because most of the emission comes from two extended lobes of rather diffuse bright material shaped like the wings of a butterfly. In some cases any detail discernible within the lobes tends to be in the form of blobs or streaks rather than loops. Recognizable loops are readily seen, however, outside the lobes. These may be grouped together to form systems of loops curving around the outside parts of the active region. Where individual hot EUV loops can be distinguished they are found to be broad and irregular and, overall, appear less loop-like than those visible in the cool EUV. Sheeley (1980) remarks that, unlike cool EUV loops, the hot loops are never observed to brighten progressively along lengths, but appear to brighten and fade in situ. The exact location of the loops footpoints is not known, since hot EUV loops, unlike the cool ones, tends to fade out towards the footpoints; they appear to join regions of opposite magnetic polarity in the underlying magnetic field.

However, not all of the loops extending outwards from an active region necessarily return to the same vicinity. Frequently loops arch across the disk for distances of the

order of 100000 km to link two or more active regions into a huge magnetic complex (Tousey et al 1973, Sheeley et al 1975, Sakurai & Uchida 1977). Such linkages are not confined to active regions located in the same hemisphere, i.e. north or south, but may involve regions lying on both sides of the equator (Sheeley et al 1977). From the other hand interconnecting loops are generally fainter than those with both ends terminating in or on the outskirts of the same active region. Habbal et al (1985) have examined the geometry of the hot and cool EUV loops in an active region near the limb. They find that some of the cool loops appear to extend further out from the limb than the hot loops, which may reflects differences in the heights of the hot and cool loops or could imply that the hot loops tend to lie in planes making greater angles to the solar vertical than those of the cool loops. Clearly a reconstruction of the true geometry of individual loops is required to distinguish between the two possibilities. At that time one information is available about the true shapes and sizes of hot EUV loops (Berton & Sakurai 1985). They studied two long-lived interconnecting loops which was asymmetrical and had inclinations 25^o and 7^o and heights 119000 and 131000 km respectively. However, loops associated with a single active region do not rise to the great heights as the interconnecting ones. Typically they reach up to 5000 to 11000 km above the solar surface and their widths is in the range 11000 to 18000 km (Gerassimenko 1980), or according to Cheng (1980) and Foukal (1975) the widths are range from 4800 to 6500 km and from 3000 to 12000 km respectively. Thus, hot EUV loops may be significally thicker than the cool ones, and so the aspect ratio is found to be typically 0.03 for loops at the outer parts of an active region (Cheng et al 1980), which is an order of magnitude greater than that found for cool EUV loops, while Cheng (1980) found even larger aspect ratios ranging from 0.09 to 0.18 for small loops observed on the disk. About the spatial relationship between hot and cool EUV loops we must note that these structures, which although obviously related, must be regarded separately, since they form in quite separate locations (Dere et al 1982, Cheng et al 1980). On the other hand, as Cheng (1980) has remarked, the existence of hot and cool loops side by side in active regions without any obvious direct spatial relationship to one another intriguing questions about the mechanism of formation and dynamical stability of coronal loops.

Below about 10 nm we leave what is conventionally termed the EUV portion of the spectrum and enter the region of soft X-rays which terminates near to 0.1 nm; below this we speak for hard X-rays observing only during and in aftermath of solar flares. In appearance the solar X-ray spectrum resembles the EUV spectrum. It is dominated by the presence of emission lines of highly ionized stages of the elements N, O, Si, S, Ne, Mg and Fe, superimposed on a continuum background. Three processes contribute significantly to the X-ray continuum, thermal bremsstrahlung (free-free emission by

electrons), radiative recombinations of electrons and ions (free-bound emission), and two-photon decay of certain metastable states of helium-like and hydrogen-like ions. Their relative contributions depend on the temperature and density of the emitting plasma. The region of the solar X-ray spectrum below 2.5 nm is of special interest because it embraces the resonance transitions of many highly ionized ions formed at temperatures truly representative of the conditions in the Sun's inner corona in temperatures of order 2×10^6 K or greater (Walker 1972, Culhane & Acton 1974).

As in the EUV, active regions seen in soft X-rays are believed to be composed basically of bright coronal loops arching between areas of opposite magnetic polarity. However, since the X-rays brightness of an active region may exceed that of 'quit' parts of the corona by some three orders of magnitude (Vaiana et al 1976), the actual appearance of the region on a broad-band photograph depends very much on the exposure time. It is also influenced by the spectral bandpass. While intermediate density exposures, for example, serve to show details of the loop structures associated with active regions, very short exposures are required to reveal the small cores of intense X-ray emission to be found at the hearts of some of them. Thus, it is found that X-ray active regions overlie regions of strong bipolar magnetic fields in the photosphere (Vaiana et al 1973, Poletto et al 1975, Zombeck et al 1978, Pallavicini et al 1979, Golub et al 1982). The most intense X-ray emission from each active region comes from the vicinity of the magnetic neutral line. Also, if the field gradient across the neutral line is large, there is frequently a small bright core connecting the two areas of opposite polarity. The spectrum of the core is harder than that of the rest of the active region, implying that, if the emission is thermal in origin, the hot is hotter. Observations of high spatial resolution resolve the core into a small cluster of densely packed, compact loops. According to Howard & Svestka (1977) older active regions do not have compact cores. the X-ray loops associated with an active region are similar in general appearance to those seen in hot EUV lines (Kundu et al 1980, Pallavicini at al 1981). They have been classified by Davis & Krieger (1982) on the basis of their location into three classes. *Class I loops* which occurring in the core of the active region and joining the areas of opposite polarity on either side of the neutral line. *Class II loops* which surrounding the core and occupying an area somewhat large in size than the associated Ha faculae, and *class III loops* which extending outwards from the active region and connecting it to magnetic areas in the surrounding photosphere. Loops of class III sometimes occur in arcades spanning active region Hα filaments or they may link adjacent active regions, which together form a huge magnetic complex. When interconnecting loops join active regions on opposite of the equator they are referred to as *trans-equatorial* loops. Also many quit region loops seem to occur in association with the final type of solar X-ray filament cavities. These appear as elogated patches of reduced emission

directly overlying quit region Hα filaments. Filament cavities which are observed both on the disk and at the limb cover a (projected) area much larger than that of the Hα filament itself and may persist for some time after the filament disappears (Bray et al 1991).

As we have mentioned above, loops of class I are found in the bright central cores of X-ray active regions. They are small, density packed features which connect areas of opposite magnetic polarity on either side of the neutral line through the active region. according to Davis & Krieger (1982) the widths of such loops range from 700 to 5000 km and their lengths from 7000 to 20000 km, implying an aspect ratio of the order of 0.1. This accords with the estimate of 0.1 to 0.2 given by Cheng et al (1980) for core loops observed in the EUV. On the other hand, the latter authors give the larger values of 7300 to 11000 km and 29000 to 44000 km for the widths and lengths of such loops respectively. The loops that they observed showed little change over a period of about 10 hours.

Loops of class II are seen in the outer parts of an active region. At the limb they appear as giant structures rising to heights of 100000 km or more. In fact, Howard & Svestka (1977) observed loops with heights exceeding 200000 km reaching in one case 260000 km (nearly 0.4 times the solar radius). Davis & Krieger (1982) quote a range of 5000 to 15000 km for the widths of class II active region loops and a range of 10000 to 100000 km for their lengths, which correspond to an aspect ration of order of 0.1. But Gerassimenko et al (1978) give the somewhat larger widths of 20000 km.

Class III loops extend outwards from an active region and terminate either in another or in a surrounding magnetic area. The former case corresponds to interconnecting loops and they will discussed later. Frequently the loops form bright arcades spanning Hα filaments associated with the active region. Measurements made by Davis & Krieger (1982) indicate that this class of loops have widths in the range 10000 to 30000 km and lengths in the range 50000 to 500000 km, yielding an aspect ratio of order of 0.04. Such loops therefore tend to be winder and longer than the class I and II loops. Apart from occasional localized brightenings, individual loops show no evidence of internal structure. Class III loops appear to be connected to localized areas on the outskirts of an active region where the magnetic field and gradients are relatively high. Their other ends are anchored to the bright chromospheric network outlining the boundaries of supergranulation cells (Davis & Krieger 1982). Finally, the brightness of individual loops seems to vary in a slow and continuous manner throughout their lives, presumably in response to changes in the underlying photospheric magnetic field (Krieger et al 1976). More sudden enhancements of the loop are observed, but they are generally associated with Hα flares or filament eruptions (Rust & Webb 1977).

Interconnecting loops appear when a new active region is born in the neighborhood

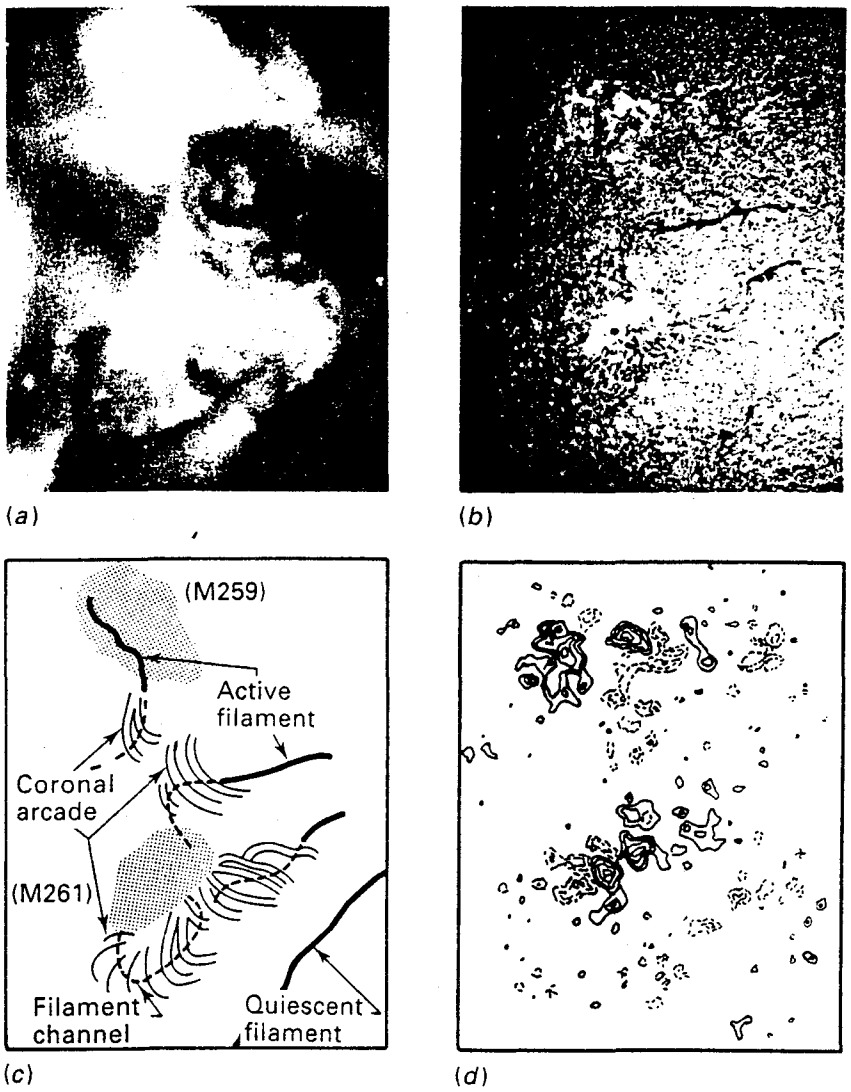

Figure 1.28: (a) X-ray image, taken from the AS&E telescope on Skylab, showing arcades of active region loops over filament cavities. (b) Simultaneous Hα photograph showing the locations of chromospheric filaments and filament channels. (c) Schematic drawing depicting the arcade loops above active region Hα filaments and filament channels. (d) Map of the underlying longitunal photospheric magnetic field (Davis & Krieger 1982).

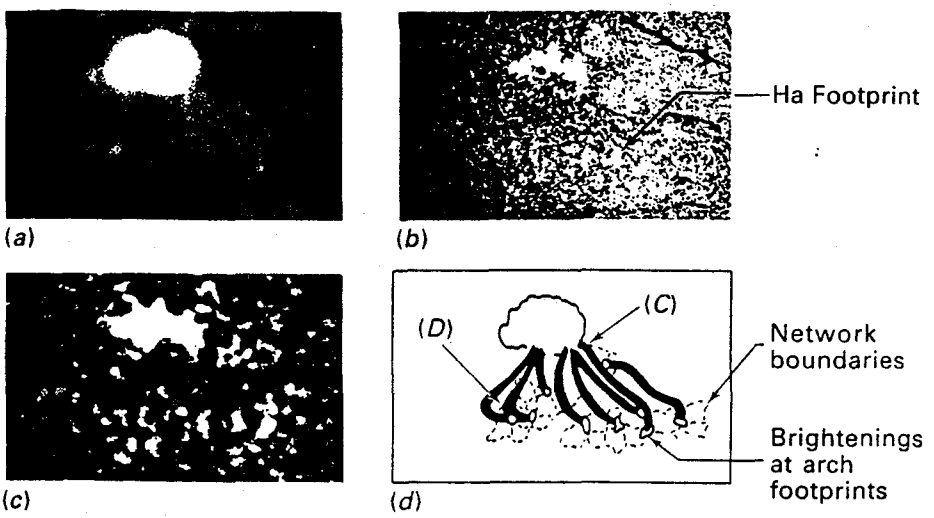

Figure 1.29: Soft X-ray loops linking the outer parts of an active region to points in the surrounding bright chromospheric network (Davis & Krieger 1982). (a) X-ray image of the active region and its surroundings. (b,c) Hα and CaII k line photographs respectively. (d) Schematic drawing showing the relationship between the loops and the network. Note the localized brightenings in the network marking the outer footpoints of the loops.

of an existing region. The birth of one short interconnecting loop took less than 12 hours, and seems to relate with the emergence of new magnetic flux which tends to trigger the appearance of interconnecting loops or to make existing ones brighten. Once magnetic field linkages have established between active regions these connections tent to last at least as long as the interconnecting regions exist as distinct entities. At this stage, the appearance of interconnecting loops against the disk is similar to that of the loops associated with individual active regions but they have heights in the range 25000 to 110000, so they are smaller than the loops internal to active regions. Their lifetimes are typically few days or even hours. During their lifetimes, the shapes of loops changes and sometimes are related directly to variations in the photospheric magnetic field. Also growth of brightening of X-ray interconnecting loops in the absence of flares is observed quite often in old active regions (Howard & Svestka 1977, Chase et al 1976, Bray et al 1991).

Little information is available on quit region loops pertains to those associated with filaments cavities. Ray & van Hoven (1982), and McIntosh et al (1976) demonstrated that their heights can be reached at 500000 km, while Serio et al (1978) found that filament cavities are enclosed by a series of loops with heights greater than 50000 km. The emission from such loops is generally faint, so it is not surprising that their tops are not always visible when they are observed on the disk. Serio et al 1978 point out that

the X-ray loops seen oven filament cavities appear to be related to the large-scale loop systems observed above quiescent Hα prominences in white light and visible coronal lines. Also, isolated loops sometimes accompany the transient X-ray enhancements in the lower corona associated with the disappearance of Hα filaments (Webb et al 1976). But not all neutral lines in the longitudinal magnetic field outside active regions are associated with either existing or recently dissolved filaments. Most of the solar surface is in fact covered with the dispersed remnant fields of long vanished active regions, in which are embedded neutral lines spaced less than 30 heliographic degrees apart. Thus, loops, when present, appear as isolated structures rather than as the components of long arcades spanning the neutral lines. these loops are somewhat smaller than those over filament cavities, having heights of 200000 to 350000 km (McIntosh et al 1976). Finally, since the photospheric magnetic field is concentrated in the bright network outlining the boundaries of the supergranulation cells, one might expect quit region loops to be rooted in the network (Davis & Krieger 1982).

Thus we have described what at first sight might appear to be a bewildering variety of X-ray loops distributed over the solar surface. Closer examination, however, reveals that they all form part of an evolving pattern which begins with the appearance of an active region. As we have seen in section 1.3.1, when first born, an X-ray active region is relatively small ad compact and so must be the loops comprising it. Within hours other loops appear which link the region to other active regions in its vicinity. These inter-region links, but not the individual connecting loops, last at least as long as the regions concerned survive as distinct entities. As the region grows older, it expands and becomes more diffuse and large peripheral loops appear. Some of these are anchored within the active region at both ends, while others terminate in magnetic areas outside. Of particular interest are the peripheral loops which form arcades spanning channels in the corona which represent extensions of dark Hα filaments associated with the active region. Eventually the region dissolves but leaves behind the filaments, each with its associated arcade of X-ray loops. During this final stage of their lives the filaments are termed quiescent filaments. After some 100 to 250 days these filaments too disappear, but still their associated arcades of loops linger on, spanning the neutral lines in the longitudinal magnetic field over which the filaments had formally lain. With the further passage of time the loops in the arcade increase in number and become fainter until, the magnetic field of the original active is fragmented and dispersed and no apparent X-ray trace of its presence remains (Bray et al 1991, Zhang et al 1992).

Little information is available about the detailed relationships between hot loops observed in different regions of the spectrum. As we have seen X-ray loops associated with an active region are similar in general appearance to those seen in hot EUV lines, but systematic comparisons are lacking. More attention has been paid to the complex

relationship between radio and X-ray loops. Lang et al 1982, Lang & Wilson (1982), Webb et al (1983), Dulk & Gary (1983) found that in general, the areas of microwave emission on their maps were not associated with X-ray emission, although several of them were found to coincide with the apparent bases of short coronal X-ray loops and few of them with the tops of X-rays loops. Webb et al (1983) explain this apparent lack of association as a consequence of the strong dependence of the gyroresonance opacity on variations in the strength and direction of the magnetic field pervading the active region. Thus, a radio loop and an X-ray loop could coincide in space but look very different on maps depicting the emission which escapes.

We shall end this section, giving first in Table 1.3 the known quantitative data concerning the morphological, dynamical and physical properties of hot loops and second a comparison between cool and hot ones (Bray et al 1991). By contrast with cool loops, where the data comes almost exclusively from Hα and various EUV lines, here we are able to draw upon data from no less than four regions of the spectrum. When we examine the tabulated figures for the various morphological and physical quantities, we see that – despite the rather large of values in many cases – the picture is a consistent one. In fact, all hot loops appear to be basically similar in their properties regardless of the wavelength region in which they are observed. Also, by contrast with cool loops, dynamical information is not available for hot loops. The inferred temperatures and electron densities cover the ranges 10^6 to 3×10^6 K and 1.5×10^8 to 2×10^{10} cm^{-3} respectively, whereas the gas pressures cover a range of, at most, a single order of magnitude. This parallels a similar situation for cool loops and in fact, the actual values for pressure appear to be much the same for cool and hot loops. Once again, this suggest that, regardless of its temperature, a loop is in approximate pressure equilibrium with its surroundings.

Comparing the two kinds of loops, it is found that hot loops, especially some of those observed in X-rays, can attain much greater heights than cool ones. Both hot and cool loops exhibit a wide range of lengths, but certain classes of X-ray loops (interconnecting) are much longer than cool loops observed in Hα or the cool EUV lines. Hot and cool EUV have much the same diameter, but cool Hα and Lα loops appear to be much than any other class. measurements of the inclinations of the loops planes to the vertical are sparse, but both hot and cool loops may be inclined at significant angles. In general, hot loops last longer than cool ones, and there appear to be no hot counterparts to the sorted-lived Hα loops, which last for only a few minutes. from the other hand however, it is difficult to compare the electron densities in hot and cool loops, since both cover a large range, with considerable overlap. The gas pressures show a much smaller range, as pointed out above, and the values for hot and cool loops are much the same. this also applies to the non-thermal velocity, but there are

Quantity	Value	Wavelength	Disk (D) or Limb (L)
Height, true (km)	110000–130000 (interconnecting)	EUV	D
	45000	radiowave	D
Height, projected (km)	50000–100000	visible	L
	200000–250000 (interconnecting)	visible	L
	5000–70000	EUV	D
	100000–200000 (class II)	X-ray	L
	50000–100000 (class III)	X-ray	D,L
	25000–110000 (interconnecting)	X-ray	D,L
	200000–500000 (quiet region)	X-ray	L
Length (km)	18000–29000	EUV	D
	7000–44000 (class I)	X-ray	D
	10000–100000 (class II)	X-ray	D
	50000–500000 (class III)	X-ray	D
	70000–100000	radiowave	D
Separation of the footpoints(km)	250000–500000 (quiet region)	X-ray	L
Diameter (km)	3000–22000	visible	L
	3000–18000	EUV	D,L
	5000–11000 (class I)	X-ray	D
	5000–20000 (class II)	X-ray	D
	10000–30000 (class III)	X-ray	D
	15000	radiowave	D
Aspect ratio	0.03–0.18	EUV	D
	0.1 (class I,II)	X-ray	D
	0.04 (class III)	X-ray	D
	0.075	microwave	D
Inclination of loop plane to vertical	7^o–25^o	EUV	D
Lifetime	hours (small loops)	visible	L
	days (large loops)	visible	L
	$> 6\ hr$	EUV	D
	$> 31\ hr$ (interconnecting)	EUV	D
	$> 10\ hr$ (class I)	X-ray	D
	hours-days (interconnecting)	X-ray	D
	hours-days	microwave	D
Temperature (K)	1-2.6 X 10^6	Visible	L
	2-2.2 X 10^6	EUV	D
	2-3.2 X 10^6	X-ray	D
	1.7-3 X 10^6	radiowave	D
Electron density (cm^{-3})	1.5-20 X 10^8	visible	L
	1.8-20 X 10^9	EUV	D
	8-60 X 10^8	X-ray	D
	5–25 X 10^8	radiowave	D
Gas pressure ($dyne/cm^2$)	0.5 (class I)	Visible	L
	0.7–16.6	EUV	D
	2.4 (class II)	X-ray	D
	2	radiowave	D
Nonthermal velocity (km/sec)	6–16	Visible	L
Total magnetic field (G)	130–200	radiowave	D

Table 1.3: *Properties of hot loops (Bray et al 1991).*

few measurements. Similarly, there are too few measurements of the total magnetic field to permit meaningful comment. In summary, hot loops tend to be thicker, longer, higher, and longer-lived than cool loops, with which they are not cospatial. however, our present knowledge appears to indicate that their other morphological and physical properties (except temperature) are similar.

1.4.4 Flare loops

In the two previous sections we have described in detail the morphological and physical properties of coronal loops which have nothing to do with the solar flare phenomenon. In this section we shall refer briefly in flare loops and their role in solar flares, since the coronal loop models constructed in this thesis have small relation with those in flares.

Flares appear to form two basic types, *simple-loop* flares and *two-ribbon* flares (Priest, 1984, 1985, Svestka 1981). Two-ribbon flares, which are highly dynamic events, are perhaps the more interesting since most large flares fall into this category so that – with a given spatial resolution – the structure is more easily observed, and because they contain numerous loops.

A simple-loop flare, also known as a compact flare or subflare, is a small flare which consists of a single loop or collection of loops which simply brightens and fades, without movement or change of shape (Priest 1984). It is observed both in Hα and in soft X-rays. Compact flares comprise some of the best flare observations obtained from Skylab. the main difference between compact and large two-ribbon flares is in the relative absence of continued heating and of a loop system growth of a compact flare during the decay phase.

Two-ribbon flares rank as the largest and most energetic of all solar flares. Photospheric magnetograms show that the two characteristic ribbons of bright Hα emission lie on either side of a line of zero longitudinal field strength treading the active region. Prior to the onset of the flare, this inversion line is usually occupied by a dark filament. Sometimes the two bright ribbons are straight, parallel and very similar in appearance. Often, however, the structure seen in Hα line is much more irregular. In such cases, however, the true two-ribbon nature of the flare can be established with the aid of maps of the longitudinal photospheric field, where the neutral line will be observed to separate the ribbons of flare emission.

The process of the onset of a two-ribbon flare, starts quite some time before, with changes in the photospheric magnetic field (Svestka 1981). On the occasions when the line, defined where the longitudinal field strength is zero, is marked by a filament, the rearrangement of the field is signalled by the activation and ultimately disruption of the filament. The disruption marks the appearance of newly-formed loops visible in Hα which form an arcade spanning the neutral line. The footpoints of the loops are located in the ribbons which constitute the Hα flare. As the flare proceeds, the two ribbons are often seen to move apart with a velocity of 2 to 10 km/sec. The number of Hα loops that are visible at any time varies, and the duration of their visibility is from 6 to 23 min (Heinzel et al 1992).

Early in the course of a flare a soft X-ray loop system is also observed; this system can outlast the optical event by many hours. As time proceeds new, progressively higher, Hα loops are formed, their footpoints remaining rooted to the ribbons. This process can last for hours, which explains why the Hα are often called post-flare loops. During the decay phase of the flare the X-ray loops are also formed as successively greater heights, greater than those of the Hα loops; the height of X-ray loops can extend to beyond 100000 km. The Hα and X-ray loop systems do not appear to consist

of single loops rising upwards but rather of newly formed or activated stationary loops appearing at successively higher levels. At heights similar to those of Hα and X-ray loops, loops are also observed in the EUV lines (Pneuman 1981).

The physical connection between the footpoints of the Hα loops and the chromospheric ribbons has been known for a long time. More recent observations show that the Hα footpoints are located on the insides of the ribbons, while the X-ray footpoints are rooted in the middle and outer portions of the ribbons. This is consistent with the concept of a system of hot loops (Pneuman 1981).

It is of considerable importance to out understanding of the role of loops in flares to establish the site of the primary energy release. MacCombie & Rust (1979) found that the tops of soft X-rays loops were considerably hotter and brighter than the legs, and that in each case the temperature difference was maintained for at least 8 hours, indicated a continual heating. Also, confidence for hard X-ray emission from the footpoints of loops has been presented. Nevertheless, the convectional view at the present time is that the primary energy release occurs at or near the tops of the flare loops, i.e. in the inner corona (Bray et al 1991).

The morphological, dynamical and physical properties of flare loops observed in different regions of the spectrum are summarized in Table 1.4. For many of the quantities there is a large range in values – due in part to real variations from flare to flare and from loop to loop. However a satisfactory degree of consistency is apparent in most, but not all, cases.

It is important to attempt a comparison between the Table 1.4 with the Tables 1.2 and 1.3 for cool and hot non-flare loops described in previous sections. Let us consider, firstly, the morphological and dynamical properties. In the case of Hα loops, we find that the properties of flare and non-flare loops are the same or nearly the same. However, compared with non-flare loops, Hα loop systems appear to be slightly higher and to last longer, as do individual flare loops. Hα loops must therefore be distinguished from non-flare loops by their other properties, including their other properties, including their closer association with flares, brightness, direction of material flow, and number of loops in a system.

The morphological and dynamical properties of EUV flare loops are also similar to those of EUV non-flare loops. EUV flare loops appear to lie somewhat lower, but the ranges of values overlap. The microwave data are inadequate to make a comparison between flare and non-flare loops meaningful (Heinzel et al 1992).

Finally, in soft X-rays both flare and non-flare loops reach very great heights, but the non-flare ones appear to reach greater heights. But again the ranges overlap. The footpoint separation for soft X-ray flare loops appears to be much smaller, but this particular quantity is very dependent on the geometry, which is usually unknown.

In general, therefore, we are led to the conclusion that the morphological properties of flares and non-flare loops are remarkably similar, regardless of the wavelength region in which they are observed.

The situation is very different when we compare physical conditions. For the hot not-flare loops we find that independent of the wavelength region, flare loops are approximately an order magnitude hotter than non-flare loops. Also, except in the EUV, the electron density is also an order of magnitude greater. Accordingly, we arrive at the important conclusion that the gas pressure in flare loops is approximately two orders of magnitude greater than in non-flare loops.

The value of the total magnetic field given by the microwave observations appears somewhat bigger for flare than for non-flare loops, but in both cases the results are sparse.

Finally, unlike hot flare loops, cool flare loops observed in Hα and other visible region lines yield similar values for the electron temperature and also of the non-thermal velocity to those of cool non-flare loops.

In summary, the extensive numerical data which has been derived for flare and non-flare loops leads to the conclusion that hot flare loops are distinguished from hot non-flare loops by their very different physical conditions rather than by morphological differences. By contrast, cool flare loops can be distinguished from their non-flare counterparts only by characteristics other than their morphological and physical properties.

1.5 Flows in solar atmosphere

Solar observations from Earth and satellites have established the fact that the solar atmosphere is not a static one but it is in *a continuous motion.* Apart from the well-known motions like granulation, spicules, Evershed effect e.t.c., many others have been discovered in the recent years. In this chapter we shall review some of these recent observations of systematic mass motions related with the subject of this thesis.

1.5.1 Supergranular flow

Supergranules are defined by photospheric horizontal flows diverging from the cell center and converging at the network-bordering adjacent cell. Magnetic knots are located at the foci of of converging flow and are associated with downflow of the order of 0.1 to 0.2 km/sec. Upflow occurs near the cell centers, but unlike the downflow it is not concentrated in small tubes and it is lower in amplitude. There is a continuity in the supergranule circulation from the photosphere to the middle chromosphere span-

Quantity	Value	Wavelength	Flare phase
Height, true (km)	45000–60000	Hα	3
	4200–13000	EUV	1,2
	<2000–50000	hard X-ray	2
	15000–50000	microwave	2
Height, projected (km)	60000–79000	Hα	3
	33000–67000	EUV	3
	15000	soft X-ray	1
	35000–180000	soft X-ray	3
Length true (km)	60000–100000	Hα	3
	23000–27000	EUV	1
	30000–65000	microwave	2
Length projected or estimated (km)	10000–20000	EUV	0,2
	15000	soft X-ray	1
	7250–100000	soft X-ray	2
	45000–250000	hard X-ray	2
Separation of the *footpoints*(km)	35000–55000	Hα	3
	30000	soft X-ray	1
Diameter (km)	< 1500–2200	Hα	3
	2500–14000	EUV	1,2,3
	3000	soft X-ray	1
	5000–20000	soft X-ray	2,3
	6000	hard X-ray	2
	2200–9400	microwave	2
Inclination of loop plane to vertical	1^o–45^o	visible	3
Tilt of axis of symmetry	5^o–14^o	visible	3
Lifetime	12 hr (loop system)	Hα	3
	0.25–1.5 hr (single loop)	Hα	3
	13 hr (single loop)	EUV	3
	< 72 hr(single loop)	hard X-ray	3
Axial flow speed (km/sec)	45–110	visible	3
	30 (downflow)	EUV	1,2,3
	200 (upflow)	EUV	2
Temperature (K)	7600–21000	Visible	–
	5×10^6	Visible	–
	$2\text{-}2000 \times 10^4$	EUV	–
	$5\text{-}50 \times 10^5$	EUV	3
	1.5×10^7	soft X-ray	2
	6.8×10^6	soft X-ray	3
	3×10^7	hard X-ray	2,3
	$3\text{-}7 \times 10^7$	microwave	2
Electron density (cm^{-3})	$1\text{-}7 \times 10^{10}$	Visible	–
	$2\text{-}30 \times 10^{11}$	EUV	0
	$8\text{–}2000 \times 10^8$	EUV	3
	4.7×10^{10}	soft X-ray	2
	1.7×10^{10}	soft X-ray	3
	$3\text{-}11 \times 10^{10}$	hard X-ray	–
	10^{10}	microwave	0
	$2\text{–}700 \times 10^8$	microwave	1,2
Gas pressure ($dyne/cm^2$)	55	Visible	–
	0.02–7	EUV	3
	195	soft X-ray	2
	138	microwave	2
Nonthermal velocity (km/sec)	3–16	Visible	–
Total magnetic field (G)	21–500	microwave	1,2
	120–176	microwave	3

Table 1.4: *Properties of flare loops (Bray et al 1991). The last column refers to the flare phase, 0 =preflare, 1 =rise, 2 =maximum, 3 =decay.*

ning approximently 1500 km and 10 scale heights. Although the sense of the flow is preserved over this extended height range, the detailed pattern changes markedly. At photospheric levels, the horizontal flow velocity of about 0.8 km/sec greatly exceeds the vertical flow velocity, whereas in the middle chromosphere the two are approximately equal and are increased to at least 3 km/sec (Athay 1980).

1.5.2 Flows in sunspots

The most-well known example of plasma flow is of course the *Evershed effect* (Alissandrakis et al 1988,1992, Dere et al 1990, Dialetis et al 1985, Kjeldseth-Moe et al 1993). It was J. Evershed in 1909 who showed that observations implied a mainly radial outflow in the penumbra at about 2 km/sec, although some evidence has also been given for substantial vertical and tangential components. The flow begins near the umbra/penumbra border, achieves maximum speed in the penumbra and decays within a spot diameter of the outer penumbral boundary.

The Evershed flow associated with large sunspots has both striking similarities and differences from supergranular flow. Among the similarities are the predominance of horizontal flow and the divergence from a well-defined center. Among the differences are the concentration of vertical magnetic flux at the center of divergence of horizontal flow (the sunspot umbra) rather than at the foci of convergence, and the reversal of the sense of flow between the photosphere and chromosphere.

Early observations indicated that the Evershed outflow was largest in the weakest photospheric lines, decreased progressively in stronger lines, and then reversed sing to increase with line strength as an inflow in chromospheric lines. This dependence upon line strength suggested a height variation. But more recent spectral in imaging observations at higher spatial resolution have shown that the interpretation is more complex, and the line strength dependence does not yet seem to have a widely accepted explanation.

One finding is that the photospheric outflow is observed only in the dark penumbral filaments, where it may be reach velocities up to 6 km/sec (Fig.1.30). The inward Evershed flow observed in Hα is clearly associated with rapid motions of chromospheric penumbra and extend well beyond it. It is possible that this Hα inflow is just coronal material falling into umbra along relatively much higher field lines and has little to do with the photospheric Evershed effect. Both flows are usually subsonic, but supersonic velocities also have observe in chromospheric altitutes near the the spot. In this area the velocity fields often deviate considerably from circular symmetry. It must be note that high spatial resolution observations are compatible with the fact that around sunspots the plasma flows along the magnetic field lines.

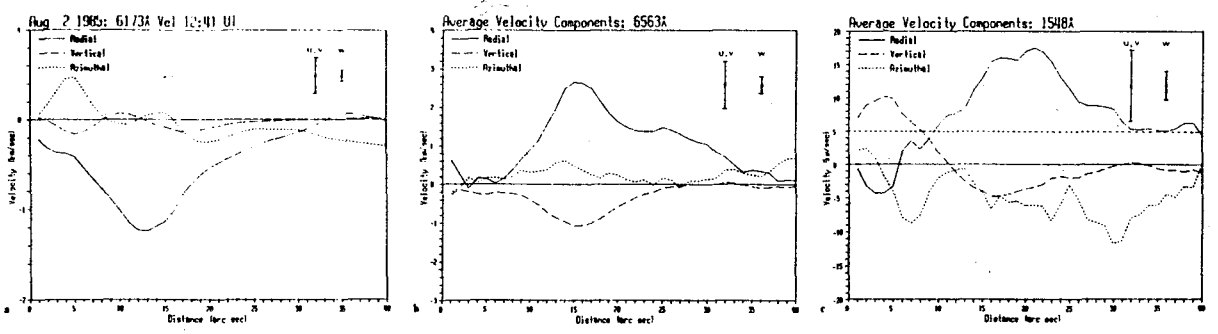

Figure 1.30: *Components of the velocity vector as a function of distance from the center of the spot. Positive radial component corresponds to inflow, positive vertical component to upflow and positive azimouthal component to clockwise motion. (a) photosphere (FeI 6173 Å). (b) chromosphere (Hα ± 0.3 Å). (c) transition zone CIV 1548,1550 Å(Dere et al 1990).*

In transition-region lines the situation is less clear, because the flows appear more complex. The velocity is, on average, directed into the sunspot with predominant vertical directions. If averaged over all position angles in the sunspot, velocities are modest and subsonic. In high spatial resolution observations are seen multiple velocity structure with velocities up to 100 km/sec. One or two distinctly supersonic velocity components may appear in addition to a component with subsonic speed. The regions with supersonic speeds may cover a large part of the entire sunspot region. Smaller areas of concentrated mass flux may occur within the regions. Also moderate upflows are also present in the transition region. Finally the flow pattern persist for long period, but show clear changes on time scales from minutes to days. Finally in active regions, downflow speeds of 70-100 km/sec are commonly observed in the "coronal rain" of plasma cooling from 10^6 K to 10^4 K, draining along fieldlines into sunspots.

1.5.3 Flows in filaments and prominences

The presence or not of systematic flows in filaments is a controversial subject. Downflows observed in prominences seen in the limb, while upflows in filaments in the disc. The concept of the existence of mean upward flow in a filament is generally accepted with an amplitude of 0.5 km/sec in Hα and of 5 km/sec in CIV. But strong downflows comparable in Hα and CIV are observed (< 10 km/sec) at footpoints at the end of a filament, lasting 1 to 10 h. Up and down motions (± 6 km/sec in Hα) are also observed at footpoints suggesting the existance of loops. It should be noted that the detection of Doppler speeds in Hα in filaments is difficult because of their transparency (Athay 1989, Chou & Zirin 1988, Georgakilas et al 1990, Schmieder 1987, Schmieder et al

1985).

Analysis of mass motions from center to limb observations in prominences shows the existance of an horizontal flow in and around the filament. Fast horizontal motions of 5 km/sec are inclined to the prominence axis with an angle of $\approx 20^o$. The direction of the velocity is the same as that of the magnetic field lines. Also observations in EUV lines shows the presence of horizontal motions with small velocities (< 20 km/sec). Also in some cases horizontal velocities are slightly less than the vertical one because of the presence of different structures, like bushs of small loops, aligned along the filament axis.

Finally, Athay et al (1983) studies CIV Doppler velocities in an active region, and found a velocity neutral line coincident with the magnetic neutral line. While their results may not apply to quiescent prominences, they do suggest a large-scale systematic flow (in loops perhaps), associated with a magnetic arcade.

1.5.4 Coronal rain

Coronal rain is a phenomenon observed over active regions at the limb. Bright condensations at coronal levels are observed to funnel into localized areas as trough the matter were channeled along magnetic lines of force above one pole of a dipole. This is different from the situation for post-flare loops in which matter is seen flowing in both legs of a closed loop system, i.e., into both poles of a dipole. Also, the flow trajectories for coronal rain typically have less curvature than in post-flare loops, and the focus of the inflow is less well defined than in the case of post-flare loops. Material velocities for the falling condensation in coronal rain are typically of the order of 100 to 200 km/sec. The motion appears to be subsonic in nearly all cases. In general, coronal rain is not identified with energetic phenomena related to flare activity (Athay 1980, Athay et al 1980, Bruner et al 1976, Withbroe & Noyes 1977).

1.5.5 Surges and sprays

Surge and spray prominences are associated with flare activity. Both consist of violent upheavals of major proportions. Also, both are associated closely with flare-like events at the seat of the ejection. It is possible that all true surges occur as expansions of flare material (Athay et al 1980).

Sprays, in general, are more violent events than surges and are more typically associated with larger flares. The ejection velocity in sprays exceeds that in surges criterion which used for the definition of sprays i.e., ejections for which the outward velocity exceeds the escape velocity. Also sprays can be defined in terms of their fragmented appearance. In this definition, a spray consists of small, discrete condensation

or droplets, whereas surges are more typically fibrous streams of ejected material which appear follows the magnetic field lines.

Surges have have typical velocities of 100 to 200 km/sec. Their upward motion of 10 to 20 minutes duration, and often along a curved trajectory, is usually followed by a retraction along more or less the same path. This is consistent with the conclusion that the magnetic field pattern remains the intact. If one considers sprays as those events for which the velocity exceeds the escape velocity, then spray ejecta are found to typically move in straight lines and never reverse direction. Spray velocities up to 1500 km/sec are observed (Athay 1980).

1.5.6 Flows in loops

In the recent years space observations shows the dominations of loop structures in the appearance of the active corona. Apart from the classification of section 1.3.5 we can distingouist in two district classes – a high-temperature one or hot loops, ($T > 10^6\ K$) for which equilibrium apparently prevails, and a low-temperature one or cold loops ($T < 10^6\ K$) characterized by large plasma flows. The time behavior of these two classes, even though not yet satisfactorily defined, seems to be qualitatively different, hot loops have longer durations and appear to be more stable than cool loops. Gerassimenko et al (1978) in examing the time behavior of three loops found less than a two percent variation over a 25-min period. Sheeley (1980) on the bases of FeXV observations, noted that a typical loop pattern lasts for several days, whereas the individual loops within the pattern evolve on a time scale of about 6 h. Levine & Withbroe (1977) reported a sizable decrease in NeVII emission from a loop observed by Skylab over a 16-min period, as well as a total loop disruption in less than 2.5 h. Contrasting evidence, however is shown by the cool loops studied by Foukal (1976), who found only little variation in a NeVII loop observed with a time separation of 5 h. Also temporal changes in loop morphology or emission pattern comprise indirect evidence for motions. For cool loops such evidence derives also from consideration of their overall visibility pattern at any instant, loop structures extending up to 50000 km above the limb are not uncommon, and observations show no evidence for density variation for the factor $10^3 - 10^4$ over this height range that would expect to characterize a plasma in hydrostatic equilibrium at $10^5\ K$.

But also direct observations suggest the existance of a family of coronal loops characterized by mass flow of the plasma inside the loop (Fig.1.31). Mass motions with velocity up to 100 km/sec have been observed in the chromosphere-corona transition region, particular in areas of intense vertical magnetic field (i.e., active regions), such as those where coronal loops are likely to be rooted. These conclusions coming from the

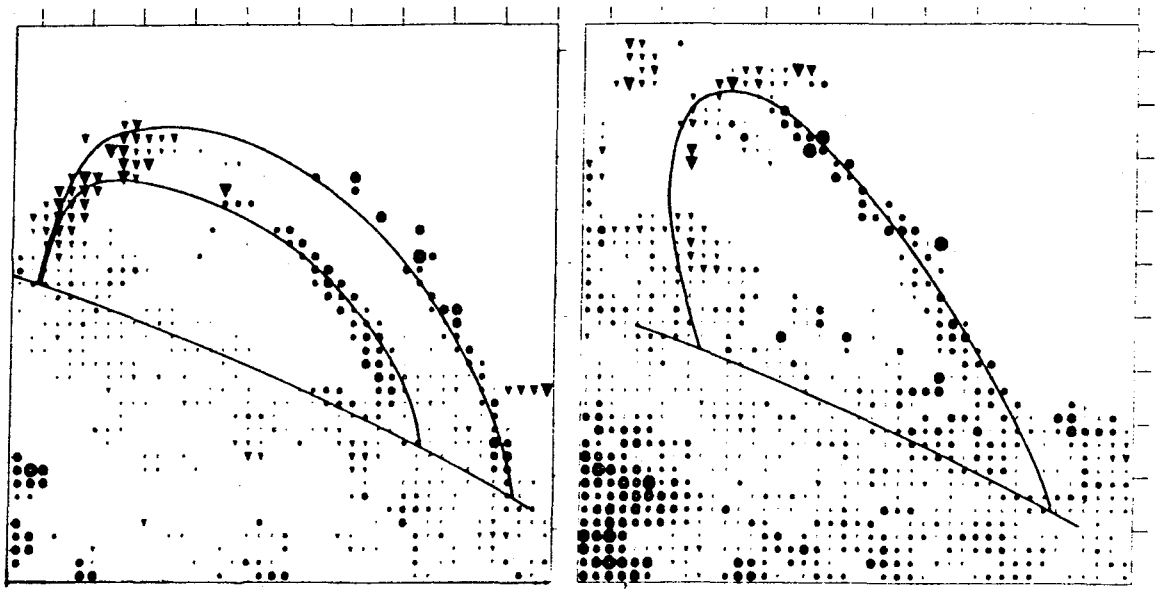

Figure 1.31: *Line of sight velocity maps in CIV (1548 Å) of a loop region observed at two different times. Filled circles (inverted triangles) correspond to positive (negative) velocities. i.e., to blueshifts (redshifts) and the size of the symbol plotted is proportional to the observed line of sight velocity. The superimposed curves are the semicircles that best represent the shape of the loop. Also is drawn the solar limb (Kopp et al 1985).*

general observed redshift broading of transition region profiles. The redshift velocity increase initially with temperature reaching a maximum at 10^5 K and after it decrease. In general this broadening is larger than the thermal or the expect turbulence broadening by an averaged excess velocity of 18 km/sec. The emission pattern appears to be steady for days and to be confined to areas of closed magnetic field. Finally, large flows along loop structures have been also observed in the corona (Athay 1981; Kopp et al 1985, Withbroe & Noyes 1977).

This catholic redshift emission is one of the most fascinating and puzzling results of the EUV observations of the Sun (Fig.1.32). The inferred mass flux at 10^5 K is sufficient to empty the corona in only a few minutes, it seems highly unlikely that a true net downward mass flux (which would also require plasma to cross closed magnetic fieldlines) is involved. More likely the apparent downflow results from a spatial and/or temporal averaging of the motion of material which is more visible (at EUV wavelengths) when descending than when ascending (i.e., motion along loop-like fieldlines). Although that the downflow mass flux rate is comparable to that of spicules, it is unlikely that the two mass flux rates refer to the same phenomenon, because in

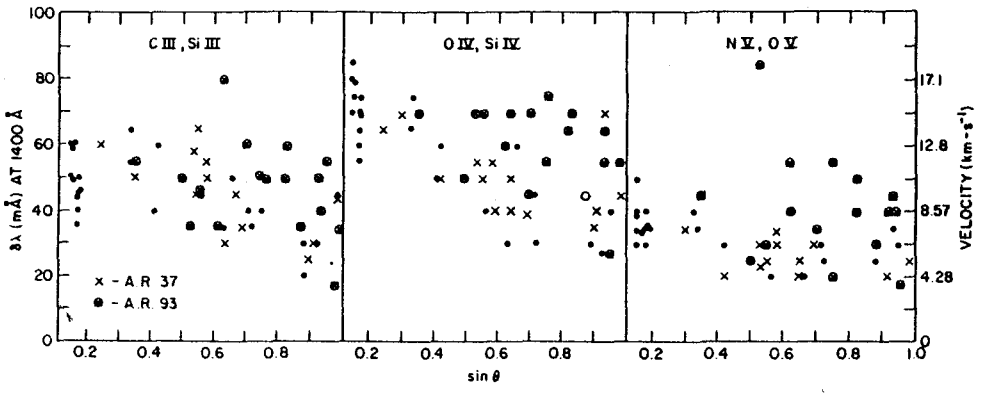

Figure 1.32: *Wavelength shifts in active region spectra and the corresponding Doppler line of sight velocities as a function of solar longitude, for lines CIII (1175 Å), SiIII(1294, 1296 Å), OIV (1401, 1407 Å) SiIV(1394 Å), NV (1239, 1243 Å) and OV(1218 Å). The solar limb corresponds to* $\sin\theta = 1$ *(Feldman et al 1982).*

active regions where the down flows are strongest, spicules appear to be suppressed.

There are also theoretical reasons for expecting such flows. Any pressure difference between the footpoints would induce a plasma flow along the loop (Glenross 1980, Loughhead et al 1984, Mariska 1984,1988). This should persist for a long time – if not disturbed – without canceling the pressure difference itself, given the large mass difference between coronal and chromospheric regions of a loop. It appears that loops can exist which are not in hydrostatic equilibrium; however, there are likely to be in a steady state since the free-fall time (10^3 *sec* for a loop of 10^5 *km* of height) and sound travel time (10^2 *sec*) are much shorter than the lifetime. Loops often appear to be stable for more than a day (Webb 1981). Finally Craig & McClymont (1986), McClymont & Craig (1987), McClymont (1989) tried to explain theoretically the presence of the redshift emission in transition region saying steady high-speed flows can exist only in cool loops so it gets out that only the downflow leg of the loop is visible; if the hot loops (with high densities) have flows would be dominated both the blueshifted emission in transition region temperatures and the Doppler-shift emission in coronal temperatures.

Thus we see that in many cases the plasma flows are present in solar structures. Especially in active regions the plasma is not a static one. Following Priest (1984), *is now known that the active-region plasma is dynamic with continual activity in the form of a wide range of flows along fieldlines, while the magnetic field of an active region probably evolves through a series of essentially stationary states, mainly force-free.* In fig.(1.33) we see a typical situation of the various flows presented by Priest (1984) discussed previously. In briefly, ground based observations reveal Evershed outflow (6

to 7 km/sec), inflow (20 km/sec), network downflow (0.1 to 2 km/sec), surges (20 to 30 km/sec) spicules (20 to 30 km/sec) and coronal rain (50 to 100 km/sec). Space observations show both transient, small scale, fast flows (0 to 150 km/sec), lasting for minutes or less, and persistent, large scale slower flows (2 to 10 km/sec), lasting for an hour or more (Priest 1984); also, in transition region lines (Doschek et al 1976, Feldman 1982), or X-ray coronal lines, systematic flows (50 - 100 km/sec) may be responsible for the observed nonthermal X-ray line broadening. Furthermore, if these flows occur along contorted magnetic field lines (Parker 1983), the derived excess velocities of 100 km/sec (Acton et al 1981), or 50 km/sec (Saba & Strong 1991), may represent a lower limit since the actual velocities could be several times larger, perhaps even comparable to the sound speed.

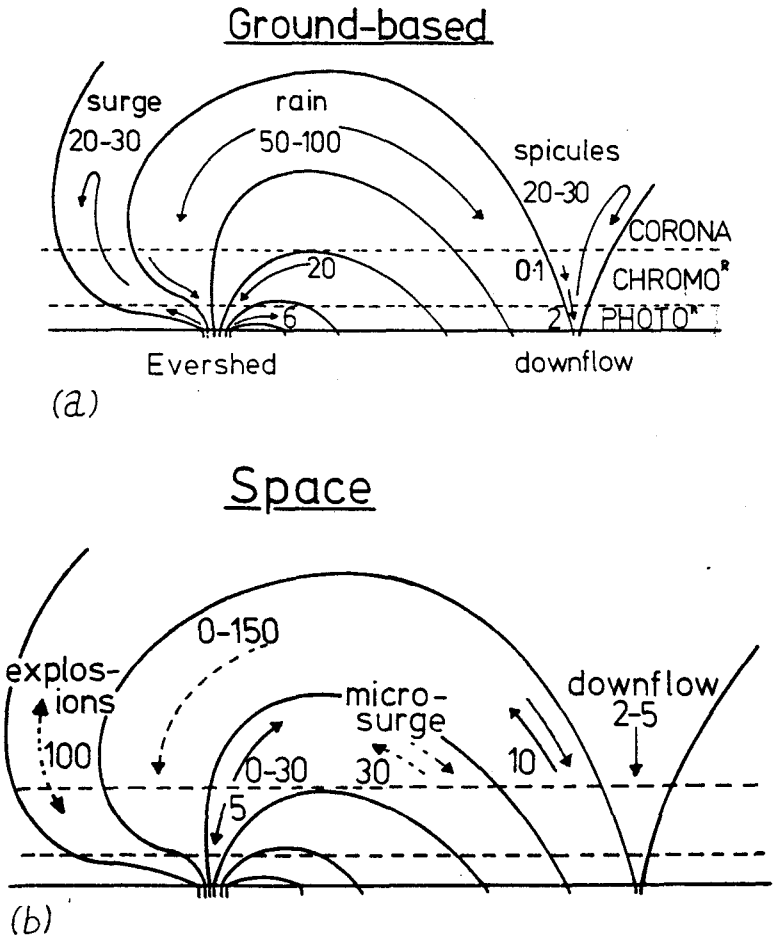

Figure 1.33: *Several types of active region flow from (a) ground-based observations. The schematic active region has preceding magnetic flux (left) concentrated as a sunspot and following flux (right) more diffuse. Heavy-headed arrows indicate the flow directions and the numbers give the typical speeds in km/sec. In (b) transient flows has dashed arrows, while large-scale steady flows are indicated by solid arrows (Priest 1984).*

Chapter 2

THEORY OF SOLAR PLASMAS

If the plasma moves in a magnetic field, electric fields are induced in it and electric currents flow. The magnetic field exerts forces on these currents which may considerably modify the flow. Conversely, the currents theirselves modify the magnetic field. Thus we have a complex interaction between the magnetic and the fluid-dynamic phenomena, and the flow must be examined by combining the field equations with those of fluid dynamics. In this chapter we shall derive the basic equations discrubing this interaction.

2.1 The reduction of Maxwell equations

Maxwell equations for an electric field $\mathbf{E}$ and magnetic field $\mathbf{B}$ in any inertial coordinate system in the presence of a net charge density δ and current density $\mathbf{J}$ are

$$\nabla \cdot \mathbf{E} = 4\pi\delta\,, \tag{2.1.1a}$$

$$\nabla \times \mathbf{E} = -\frac{\partial \mathbf{B}}{\partial t}\,, \tag{2.1.1b}$$

$$\nabla \cdot \mathbf{B} = 0\,, \tag{2.1.1c}$$

$$\nabla \times \mathbf{B} = \frac{4\pi}{c}\mathbf{J} + \frac{1}{c}\frac{\partial \mathbf{E}}{\partial t}\,, \tag{2.1.1d}$$

where c is the speed of light.

In a frame of reference moving with velocity $\mathbf{V}$ relative to the coordinate system, the electric field $\mathbf{E}'$ is (Jackon, 1975)

$$\mathbf{E}' = \gamma\left(\mathbf{E} + \frac{\mathbf{V}\times\mathbf{B}}{c}\right), \tag{2.1.2a}$$

$$\mathbf{B}' = \gamma\left(\mathbf{B} - \frac{\mathbf{V}\times\mathbf{E}}{c}\right), \tag{2.1.2b}$$

where $\gamma = (1 - V^2/c^2)^{-1/2}$ is the Lorentz factor. We assume now that the charged particles (electrons and ions) that produce these fields can be regarded as a neutral continuum (because the free electrons quickly neutralize any separated charges, so the charge densities of the electrons and ions are equal, $\delta = 0$), and the whole system can be approximated as a *fluid* which means that all physical quantities that characterize the fluid are averaged values of the real one. Such a description is possible in the case of cosmic plasmas when the Debye length, the cyclotron radius and the mean free path for Coulomb collisions are much smaller than a characteristic length of the plasma (Tsinganos 1992a).

Assuming next that the background fluid is a classical fluid with a large scalar electrical conductivity σ, in the frame of reference of the fluid the electrical current density $\mathbf{J}'$ is related to the electric field by Ohm's law (Parker 1979)

$$\mathbf{J}' = \sigma\mathbf{E}' . \tag{2.1.3}$$

Consider now the fact that most flows observing in the Sun and the most astrophysical flows are extremely nonrelativistic, i.e., $V/c << 1$ where V is a characteristic bulk flow speed. Then, in the view of the high conductivity, it follows that the displesment current $\partial\mathbf{E}/\partial t$ and the polarization current $\delta\mathbf{V}$ are both smaller by V^2/c^2 times to the electric current density $\mathbf{J}$. Thus, in those circumstances the plasma is electrically neutral and the only electrical fields that are present are the induced (Eq.2.1.1b). Thus, we have the Ampére law

$$\nabla\times\mathbf{B} = \frac{4\pi}{c}\mathbf{J}, \tag{2.1.4}$$

Also, neglecting second order terms in V/c we found that the magnetic field in the moving and fixed frames are equal, $\mathbf{B}' = \mathbf{B}$, so the current densities in the moving and fixed frames are equal, $\mathbf{J}' = \mathbf{J}$. This is easy to understood because the polarization current $\delta\mathbf{V}$ is negligible. It follows from Eqs.(2.1.3) and (2.1.4)

$$\mathbf{J} = \sigma\left(\mathbf{E} + \frac{\mathbf{V}\times\mathbf{B}}{c}\right). \tag{2.1.5}$$

Thus, using Eqs.(2.1.1b), (2.1.4) and (2.1.5) to eliminate **J** and **E** we obtain the magnetohydrodynamic (MHD) induction equation

$$\frac{\partial \mathbf{B}}{\partial t} = \nabla \times (\mathbf{V} \times \mathbf{B}) + \nabla \times (\eta \nabla \times \mathbf{B}), \tag{2.1.6}$$

where for converience we have defined the *resistive diffusion coefficient*

$$\eta = \frac{c^2}{4\pi\sigma}. \tag{2.1.7}$$

If η is independent of the position, as usually assumed, Eq.(2.1.6) reduces to

$$\frac{\partial \mathbf{B}}{\partial t} = \nabla \times (\mathbf{V} \times \mathbf{B}) + \eta \nabla^2 \mathbf{B}. \tag{2.1.8}$$

Writing Eq.(2.1.8) in dimmensionless form we see that the first right term dominates if

$$R_m = \frac{L_* V_*}{\eta} >> 1, \tag{2.1.9}$$

where R_m is the *magnetic Reynolds number* (L_*, V_* being characteristic length and velocity scales of the plasma). Using the Spitzer electrical conductivity $\sigma = 10^7 T^{3/2}$ one finds for the most solar structures $R_m \approx 10^{12}$ so the plasma is almost perfectly conducting ($\sigma \to \infty$) and Eq.(2.1.8) simplifies to

$$\frac{\partial \mathbf{B}}{\partial t} = \nabla \times (\mathbf{V} \times \mathbf{B}). \tag{2.1.10}$$

This limit of MHD is called ideal MHD. Following from the ideal limit, the 'frozen-in flux' theorem of Alfvén holds; namely *"In a perfect conducting plasma, field lines behave as if they move with the plasma"*.

2.2 Plasma Equations

The behavior of the magnetic field, which is described by the induction equation, is coupled to that of the plasma by the presence of the velocity term in this. The plasma motion is in turn governed by the equations of mass continuity, momentum and energy. When ρ and P are the plasma pressure and density,

$$P = \frac{k_B}{m} \rho T, \tag{2.2.1}$$

i.e. the perfect gas law holds for the plasma (where k_B is the Boltzmann constant and m is the mean particle mass; $m = m_p/2$ for a fully ionized H), the mass continuity equation can be written as

$$\frac{\partial \rho}{\partial t} + \nabla \cdot (\rho \mathbf{V}) = 0\,, \tag{2.2.2}$$

the equation of motion as

$$\rho \frac{\partial \mathbf{V}}{\partial t} + \rho(\mathbf{V} \cdot \nabla)\mathbf{V} = -\nabla P + \frac{\nabla \times \mathbf{B} \times \mathbf{B}}{4\pi} - \rho \nabla U\,, \tag{2.2.3}$$

and the energy equation

$$\frac{\rho^\gamma}{\gamma - 1}\left[\frac{\partial}{\partial t}\left(\frac{P}{\rho^\gamma}\right) + (\mathbf{V} \cdot \nabla)\left(\frac{P}{\rho^\gamma}\right)\right] = -\mathcal{L}\,. \tag{2.2.4}$$

where γ is the ratio of the specific heats of the plasma (For a fully-ionized hydrogen plasma $\gamma = 5/3$). In Eq.(2.2.3) U is the gravitational potential, usually known, because in the most cases the self-gravitation of the plasma is negligible. Also in Eq.(2.2.3) we have neglected viscous, and rotational forces because for the most solar applications are very small compared to the other inertial terms. Also in Eq.(2.2.4) $\mathcal{L}$ is the *energy function* and may be written as

$$\mathcal{L} = \nabla \cdot \mathbf{q} + L_r - H\,, \tag{2.2.5}$$

where $\mathbf{q}$ is the *heat flux* due to particle conduction; L_r is the *net radiation*, and H represents the sum of all other *heating sources* (i.e. from nuclear reactions, from viscous and wave heating, from ohmic dissipation heating etc).

Often, when the energetics of a process is not of prime consideration, the energy equation is approximated by the *polytropic approximation* which holds for each plasma element following its motion,

$$\frac{P}{\rho^\alpha} = const.\,, \tag{2.2.6}$$

where α is a constant. This approximation is simply meant to model temperature variations in a rough manner, but it may be derived from the full energy equation when the only contribution to L is the conduction term and the conductive flux q is proportional to the work done by the pressure. If $\alpha < \gamma$ we have a heated plasma; the opposite happens if $\alpha > \gamma$. Also the two extreme cases are important. When $\alpha = \gamma$ this means that $\mathcal{L} = 0$ and the plasma is thermally isolated and its variations are adiabatic. This is the case when the time-scale for changes in P, ρ and T much smaller than the time-scale for radiation, conduction and heating; this is often valid for rapid changes associated with wave motions or instabilities. From the other hand if $\alpha = 1$ this means that following the motion the temperature of each plasma element T is constant (Priest 1984).

2.3 Equations of ideal Magnetohydrodynamics

As discussed in the two previous sections, in the cases of a non-relativistic plasma with very large conductivity ($\sigma \to \infty$) and very low viscosity, in which a characteristic scale of the system is much larger than all the microscopic characteristic lengths of the plasma, the equations which governed the structure and the evolution of the plasma are those of the ideal magnetohydrodynamics (MHD)

$$\nabla\cdot\mathbf{B} = 0\,, \tag{2.3.1a}$$

$$\frac{\partial\rho}{\partial t} + \nabla\cdot(\rho\mathbf{V}) = 0\,, \tag{2.3.1b}$$

$$\frac{\partial\mathbf{B}}{\partial t} = \nabla\times(\mathbf{V}\times\mathbf{B})\,. \tag{2.3.1c}$$

$$\rho\frac{\partial\mathbf{V}}{\partial t} + \rho(\mathbf{V}\cdot\nabla)\mathbf{V} = -\nabla P + \frac{\nabla\times\mathbf{B}\times\mathbf{B}}{4\pi} - \rho\nabla U\,, \tag{2.3.1d}$$

$$\frac{\rho^\gamma}{\gamma-1}\left[\frac{\partial}{\partial t}\left(\frac{P}{\rho^\gamma}\right) + (\mathbf{V}\cdot\nabla)\left(\frac{P}{\rho^\gamma}\right)\right] = -\mathcal{L}\,. \tag{2.3.1e}$$

$$P = \frac{k_B}{m}\rho T\,, \tag{2.3.1f}$$

Thus, we have a system of nine partial differential equations with nine unknowns, namely the $\mathbf{B}$, $\mathbf{V}$, P, ρ and T. The solenoidal equation (2.3.1a) is used for posing conditions in the magnetic field configuration.

The properties and general behavior of the solutions of the set of Eq.(2.3.1) are not known due to its mathematical complexity. Thus, the time-dependent problem posed by Eqs.(2.3.1) is formidable and no progress has been made so far towards its solution.

To simplify the mathematical structure of MHD equations further, we make the assumption that all timescales are much larger that the Alfvén and the sound travel time. This is not an unreasonable assumption when modeling the solar atmosphere (at least to first order) where structures evolve fairly slowly (ranging from hours to months). Thus, all time-dependent terms are neglect and we have the following set of steady equations,

$$\nabla\cdot\mathbf{B} = 0\,, \tag{2.3.2a}$$

$$\nabla\cdot(\rho\mathbf{V}) = 0\,, \tag{2.3.2b}$$

$$\nabla\times(\mathbf{V}\times\mathbf{B}) = 0\,. \tag{2.3.2c}$$

$$\rho(\mathbf{V}\cdot\nabla)\mathbf{V} = -\nabla P + \frac{\nabla\times\mathbf{B}\times\mathbf{B}}{4\pi} - \rho\nabla U\,, \tag{2.3.2d}$$

$$\frac{\rho^{\gamma}}{\gamma-1}(\mathbf{V}\cdot\nabla)\left(\frac{P}{\rho^{\gamma}}\right)=-\mathcal{L}\,. \tag{2.3.2e}$$

$$P=\frac{k_B}{m}\rho T\,, \tag{2.3.2f}$$

Equilibrium states that satisfy Eqs.(2.3.2) may be used to study the macroscopic behavior of astrophysical plasmas such as sunspots, solar coronal loops and prominences, solar and stellar winds, jets, etc. But also and in this case there are not known exact solutions, except from the trivial equipartition solution $\mathbf{B}=\mathbf{V}/\sqrt{4\pi\rho}$, $\rho=const.$ and solutions for symmetric configurations. At this point we must say that there is a discussion (Grad 1967, Parker 1972,1976,1979, Yu 1973, Low 1975a,b, 1980, Edenstrasser 1980a,b, Rosner & Knobloch 1982, Tsinganos 1982a,b, Tsinganos et al 1984) on the question of the existance of solutions of MHD equilibrium without any symmetry. It seems that, except from the equipartition case, there are not other non-symmetric solutions and non-equilibrium is the result. The need for some symmetry arises from the mechanics of balancing the highly anisotropic Lorentz and inertial forces with pressure gradients and gravity, which are forces involving scalar potentials. The requirement of symmetry can be expressed mathematically in the form of a local compatibilility relation. In the most simple case this compatibility relation is express through the existance of one ignorable coordinate so the resulting solutions are 2-D. Because the only 3-D known solutions are magnetostatic (Borgan & Low 1986, Low 1980,1985,1992) and force-free (Low 1988), in the following we will present a method to generate families of symmetric solutions having an ignorable coordinate.

Starting our analysis from Eq.(2.3.2c) we conclude that the requirement of equilibrium excludes space filling ergodic lines; this property may formally be seen from the integral of this equation

$$\mathbf{V}\times\mathbf{B}=\nabla\Phi\,, \tag{2.3.3}$$

where Φ is the induction potential. An arbitrary hydromagnetic system in equilibrium should satisfy Eq.(2.3.2). However, this equation alone requires that magnetic lines and streamlines cannot be ergodic in 3-D space, since they are constrained to lie on 2-D surfaces (Tsinganos 1992b). This follows immediately from Eq.(2.3.3)

$$\mathbf{V}\cdot\nabla\Phi=\mathbf{B}\cdot\nabla\Phi=0\,, \tag{2.3.4}$$

so, magnetic fieldlines, together with streamlines are constrained to lie on the surfaces $\Phi=const.$. In the following, we shall derive a scalar differential equation that will define these surfaces under the assumption that the hydromagnetic system has a symmetry expressible through the existance of an ignorable coordinate.

The system of coordinates is (x_1,x_2,x_3) with line elements $h_1(x_1,x_2)$, $h_2(x_1,x_2)$, $h_3(x_1,x_2)$, wherein coordinate x_3 is ignorable. The general solution of Eqs.(2.3.2a,b)

can be written in terms of a vector potential x_3-component $A(x_1, x_2)$ and a stream function $\Psi(x_1, x_2)$ (which, as noted, are functions of x_1 and x_2 alone)

$$h_2 h_3 B_1 = \frac{\partial A}{\partial x_2} \qquad h_1 h_3 B_2 = -\frac{\partial A}{\partial x_1}, \tag{2.3.5}$$

$$h_2 h_3 \rho V_1 = \frac{1}{4\pi}\frac{\partial \Psi}{\partial x_2} \qquad h_1 h_3 \rho V_2 = -\frac{1}{4\pi}\frac{\partial \Psi}{\partial x_1}, \tag{2.3.6}$$

Lines of constant A are field lines of the meridional field, while lines of constant Ψ are stream lines of the meridional flow.

Following the formalism of Tsinganos (1982) we write the Eqs.(2.3.2c,d) in Jacobian notation,

$$\{f, g\} = \frac{\partial f}{\partial x_1}\frac{\partial g}{\partial x_2} - \frac{\partial f}{\partial x_2}\frac{\partial g}{\partial x_1}. \tag{2.3.7}$$

When $\{f, g\} = 0$, this means that ∇f and ∇g are parallel, f and g are both constants on the same lines in the x_1-x_2 plane.

The x_1 and x_2-components of the induction equation (2.3.2c), yield

$$\frac{\partial}{\partial x_2}\left(\frac{1}{4\pi\rho}\frac{1}{h_1 h_2 h_3}\{\Psi, A\}\right) = 0, \tag{2.3.8}$$

and

$$\frac{\partial}{\partial x_1}\left(\frac{1}{4\pi\rho}\frac{1}{h_1 h_2 h_3}\{\Psi, A\}\right) = 0, \tag{2.3.9}$$

and are equivalent to the single expression

$$\{\Psi, A\} = 0, \tag{2.3.10}$$

which its solution is

$$\Psi = \Psi(A). \tag{2.3.11}$$

Thus the magnetic and stream surfaces (magnetic and steam axes) coincide (Fig.2.1). Notice, however, that the streamlines do not coincide everywhere with the magnetic lines, since, in general, there is a nonuniform convection of the fields in the ignorable direction arising from the difference of the field components V_3 and B_3.

The x_3-component of the induction equation (2.3.2c) gives

$$\left\{\frac{V_3}{h_3}, A\right\} - \left\{\frac{B_3}{4\pi\rho h_3}, \Psi\right\} = 0, \tag{2.3.12}$$

or equivalently

$$V_3 - \frac{\Psi_A}{4\pi\rho} B_3 = h_3 \Phi_A = h_3 \Omega, \tag{2.3.13}$$

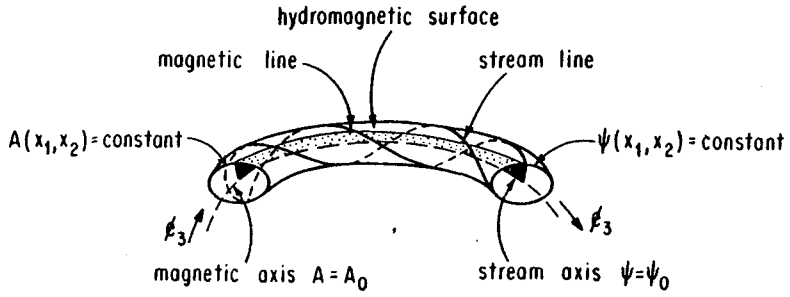

Figure 2.1: *Schematic drawing of a toroidal hydromagnetic surface. The fields are independent of the coordinate x_3 (Tsinganos 1982).*

where $\Omega(A)$ is a function of A relating to the induction potential $\mathbf{V} \times \mathbf{B} = \nabla\Phi$ and the subscript A in functions Ψ and Φ denotes the derivative with respect to their argument A.

From the x_3-component of the momentum balance equation we get

$$\{h_3 B_3 - h_3 \Psi_A V_3, A\} = 0\,, \tag{2.3.14}$$

which has the general solution

$$h_3 B_3 - h_3 \Psi_A V_3 = G(A)\,, \tag{2.3.15}$$

where $G(A)$ is another function of A.

From the Eqs.(2.3.13) and (2.3.15) we have the following expressions for the field and velocity components in the ignorable direction

$$\left(1 - \frac{\Psi_A^2}{4\pi\rho}\right) V_3 = h_3\Omega + \frac{G\Psi_A}{4\pi\rho h_3}\,, \tag{2.3.16}$$

$$\left(1 - \frac{\Psi_A^2}{4\pi\rho}\right) B_3 = h_3\Omega\Psi_A + \frac{G}{h_3}\,. \tag{2.3.17}$$

Notice the appearance of a "critical" surface from these two relations with the equations

$$\Psi_A^2 = 4\pi\rho \qquad G + h_3^2\Omega\Psi_A = 0\,. \tag{2.3.18}$$

It is easy to check that when the flow is field aligned, $\Omega = 0$. Then,

$$4\pi\rho\mathbf{V} = \Psi_A\mathbf{B}\,. \tag{2.3.19}$$

In the final step, integrate the remaining two components of momentum equation. We must distinguish two cases according to use either (i) the polytropic approximation

(Eq.2.2.6) or more general an equation of the form $P = P(\rho)$, or (ii) the detail energy equation (2.3.2e), together with the gas law (2.3.2f).

(i) In case when the pressure is a function of the density only the momentum balance equation can be written as

$$\nabla W = \frac{(\nabla \times \mathbf{B}) \times \mathbf{B}}{4\pi\rho} + \mathbf{V} \times \nabla \times \mathbf{V}\,, \tag{2.3.20}$$

where

$$W = \int \frac{dP}{\rho} + U + \frac{V^2}{2}\,. \tag{2.3.21}$$

and $U = U(x_1, x_2)$ is the gravitational potential. The Lorentz force has no component along the lines of magnetic force, so,

$$B \cdot \nabla W = \mathbf{B} \cdot (\mathbf{V} \times \nabla \times \mathbf{V})\,, \tag{2.3.22}$$

which can be manipulated into the form

$$\{W, A\} = \frac{1}{2h_3^2}\{h_3^2 V_3^2, A\} - \frac{1}{8\pi\rho h_3^2}\{h_3^2 B_3^2, A\}\,, \tag{2.3.23}$$

Transforming Eq.(2.3.23) to x_1-A coordinates after some algebra we find that,

$$\int \frac{dP}{\rho} + U + \frac{V^2}{2} - \frac{\Omega}{\Psi_A} h_3 B_3 = E(A)\,, \tag{2.3.24}$$

where $E(A)$ is a definite function of A and represents the energy flux density per unit of mass flux density. It is the sum of the thermal $\int dP/\rho$, kinetic $V^2/2$, potential U, and Poynting $\mathbf{B} \times (\mathbf{V} \times \mathbf{B})/4\pi\rho\mathbf{V}$ energy flux densities per unit of mass flux density. The invariance of E on each streamline is simply the consequence of the time independence of the equations.

Now the remaining x_1 and x_2-components of the momentum balance equation can be written

$$\frac{1}{h_1 h_2 h_3}\left(\frac{\partial}{\partial x_1}\frac{h_2}{h_1 h_3}\frac{\partial}{\partial x_1} + \frac{\partial}{\partial x_2}\frac{h_1}{h_2 h_3}\frac{\partial}{\partial x_2}\right)\frac{\partial A}{\partial x_i}$$

$$-\frac{\Psi_A}{h_1 h_2 h_3}\left(\frac{\partial}{\partial x_1}\frac{h_2}{h_1 h_3}\frac{\Psi_A}{4\pi\rho}\frac{\partial A}{\partial x_1} + \frac{\partial}{\partial x_2}\frac{h_1}{h_2 h_3}\frac{\Psi_A}{4\pi\rho}\frac{\partial A}{\partial x_2}\right)\frac{\partial A}{\partial x_i}$$

$$+4\pi\rho\frac{\partial W}{\partial x_i} = \frac{1}{2h_3^2}\left(4\pi\rho\frac{\partial(h_3^2 V_{x_3}^2)}{\partial x_i} - \frac{\partial(h_3^2 B_{x_3}^2)}{\partial x_i}\right)\,, \tag{2.3.25}$$

where $i = 1, 2$. If we write these equations in (x_j, A) coordinates respectively $(j = 2, 1)$ and transform the partial derivatives with respect to A to derivatives of suitable functions of A alone, they reduce to the following expression for $A(x_1, x_2)$ called transfield equation

$$\frac{1}{h_1 h_2 h_3}\left[\frac{\partial}{\partial x_1}\frac{h_2}{h_1 h_3}\frac{\partial A}{\partial x_1}+\frac{\partial}{\partial x_2}\frac{h_1}{h_2 h_3}\frac{\partial A}{\partial x_2}\right]$$
$$-\frac{\Psi_A}{h_1 h_2 h_3}\left[\frac{\partial}{\partial x_1}\frac{h_2}{h_1 h_3}\frac{\Psi_A}{4\pi\rho}\frac{\partial A}{\partial x_1}+\frac{\partial}{\partial x_2}\frac{h_2}{h_1 h_3}\frac{\Psi_A}{4\pi\rho}\frac{\partial A}{\partial x_2}\right]$$
$$+\frac{1}{1-\Psi_A^2/4\pi\rho}\left[\frac{1}{2h_3^2}\frac{dG^2}{dA^2}+2\pi\rho h_3^2\frac{d\Omega^2}{dA}+4\pi\rho\frac{d}{dA}\left(\frac{G\Omega}{\Psi_A}\right)\right]+$$
$$\frac{1}{(1-\Psi_A^2/4\pi\rho)^2}\left[\frac{G^2}{2\pi\rho h_3^2}+\frac{h_3^2\Omega^2}{2}+\frac{G\Omega}{\Psi_A}\right]\frac{d\Psi_A^2}{dA}+4\pi\rho\frac{dE}{dA}=0\,, \tag{2.3.26}$$

In the absence of flows, Eq.(2.3.26) is known as the Grad-Shafranov equation.

(ii) In the second case where the pressure is function both of the density and temperature, using the gas law (Eq.2.3.2f), the momentum balance equation can be written along each fieldline

$$\frac{\partial \ln P}{\partial x_i}+\frac{m}{k_B T}\frac{\partial \mathcal{F}}{\partial x_i}=0\,, \tag{2.3.27}$$

where $(i = 1, 2)$ and

$$\mathcal{F}=U+\frac{V^2}{2}+\frac{\Omega}{\Psi_A}h_3 B_3\,. \tag{2.3.28}$$

The general solution of Eqs.(2.3.27) is

$$P(A,S)=P_0(A)e^{-\int_{\mathcal{F}_0}^{\mathcal{F}}\frac{m}{k_B T(A,\mathcal{F}')}d\mathcal{F}'}\,, \tag{2.3.29}$$

where $P_0(A)$ is another arbitrary function of A and the integration with respect to $\mathcal{F}$ is to be performed along each fieldline $A(x_1, x_2) = const.$ This is an extension of the simple barometric law including flows. The unknown temperature function must be found from the energy equation (2.3.2e). although that these two equations are coupled each other together with the equation for the field lines which in this case is written

$$\frac{1}{h_1 h_2 h_3}\left[\frac{\partial}{\partial x_1}\frac{h_2}{h_1 h_3}\frac{\partial A}{\partial x_1}+\frac{\partial}{\partial x_2}\frac{h_1}{h_2 h_3}\frac{\partial A}{\partial x_2}\right]$$
$$-\frac{\Psi_A}{h_1 h_2 h_3}\left[\frac{\partial}{\partial x_1}\frac{h_2}{h_1 h_3}\frac{\Psi_A}{4\pi\rho}\frac{\partial A}{\partial x_1}+\frac{\partial}{\partial x_2}\frac{h_2}{h_1 h_3}\frac{\Psi_A}{4\pi\rho}\frac{\partial A}{\partial x_2}\right]+$$
$$\frac{1}{1-\Psi_A^2/4\pi\rho}\left[\frac{1}{2h_3^2}\frac{d\Omega^2}{dA^2}+2\pi\rho h_3^2\frac{d\Omega^2}{dA}+4\pi\rho\frac{d}{dA}\left(\frac{G\Omega}{\Psi_A}\right)\right]+$$

$$\frac{1}{(1-\Psi_A^2/4\pi\rho)^2}\left[\frac{G^2}{2\pi\rho h_3^2}+\frac{h_3^2\Omega^2}{2}+\frac{G\Omega}{\Psi_A}\right]\frac{d\Psi_A^2}{dA}+4\pi\frac{\partial P}{\partial A}\Big)_{\mathcal{F}}=0\,, \tag{2.3.30}$$

which, as expect, is the same as Eq.(2.3.26) except in the last term in which the partial derivative is taken keeping $\mathcal{F}$ constant.

2.4 Dimmensionless parameters

The derivations of the ideal MHD equations has been done under the assumptions of the very large conductivity, very low viscosity, and no rotating inertial effects. In the following we shall define some dimensionless parameters to have a more quantitative sense if these assumptions hold for the solar atmosphere.

As we seen in section 2.1, in terms of a typical plasma speed V_* and length-scale L_*, the magnitude of the convective term in Eq.(2.1.8) divided by that of the diffusive term is a dimensionless parameter

$$R_m=\frac{L_*V_*}{\eta}\,, \tag{2.4.1}$$

called *magnetic Reynolds number*. It is a measure of the strength of the coupling between the flow and the magnetic field. Typical in the solar atmosphere

$$R_m\approx 2\times 10^7\left(\frac{L_*}{10^4\ km}\right)\left(\frac{V_*}{1\ km/sec}\right)\left(\frac{T_*}{10^4\ K}\right)^{3/2}\,, \tag{2.4.2}$$

where T_* is a typical plasma temperature. Thus, in all cases (except if the plasma is in turbulent state, as for example in the central part of a solar flare, in which the conductivity is small and a reconnection process takes place) we have $R_m >> 1$ and the diffusive term in the induction equation (2.1.8) can be ignored.

The *Reynolds number*

$$R_e=\frac{L_*V_*}{\nu}\,, \tag{2.4.3}$$

known from the ordinary hydrodynamics gives the ratio of the size of the inertial forces to the viscous forces. In the above equation ν is the *coefficient of kinimatic viscosity* which depends of both the density and the temperature. Numerically we have

$$R_e\approx 10^{12}\frac{\left(\frac{L_*}{10^4\ km}\right)\left(\frac{V_*}{1\ km/sec}\right)}{\left(\frac{n_*}{10^{14}\ cm^{-3}}\right)\left(\frac{T_*}{10^4\ K}\right)^{5/2}}\,, \tag{2.4.4}$$

where n_* is a characteristic density of the plasma. Note that even for the low density and the high temperature of the corona, we still have $R_e >> 1$ so the viscous forces can be ignored.

The *Rossby number*

$$R_o = \frac{V_*}{L_*\Omega_*}, \tag{2.4.5}$$

is the ratio of the inertial forces to the Coriolis forces in the case where the plasma system rotates as a whole with angular velocity Ω_*. For the Sun we have $\Omega_* = \Omega_\odot \approx 10^6$ sec^{-1}, and

$$R_o \approx 10^2 \frac{\left(\frac{V_*}{1\ km/sec}\right)}{\left(\frac{L_*}{10^4\ Km}\right)}, \tag{2.4.6}$$

so the influence from the rotation of the Sun is in general small and can be ignored in a first approximation even for the largest structures observing in the Sun such as loops or prominences.

Apart from these dimensionless numbers which its values are such to say that the ideal MHD holds in the most parts of solar atmosphere there are also other three important definitions about the significant of the various terms in the momentum equation.

The *Mach number*

$$M = \frac{V_*}{V_s}, \tag{2.4.7}$$

measures the flow speed V_* relative to the sound speed

$$V_s = \sqrt{\gamma \frac{P_*}{\rho_*}}, \tag{2.4.8}$$

where P_* is the plasma pressure. The sound speed is the propagation velocity of a perturbation (acoustic wave) in a perfect gas. Also the Mach number is a measure of the ratio of the inertial forces to pressure gradient forces in momentum equation.

The *Alfvén number*

$$M_a = \frac{V_*}{V_a}, \tag{2.4.9}$$

gives the size of the flow speed in term of the Alfvén speed

$$V_a = \frac{B_*}{\sqrt{4\pi\rho_*}}, \tag{2.4.10}$$

which is the velocity of propagation of transverse waves (Alfvén waves) along the magnetic field B_* direction. Also is the ratio of the inertial forces to the Lorentz forces. If $M_a << 1$ the effects from the velocity terms can be ignored.

The *plasma* β

$$\beta = \frac{8\pi P_*}{B_*^2}, \tag{2.4.11}$$

is the ratio of the plasma pressure P_* to the magnetic pressure $B_*^2/8\pi$. If $\beta << 1$ the pressure gradients forces and the gravitational forces can be ignored.

It is easy to see that the above numbers satisfy the relation

$$M_a^2 = \frac{\beta M^2}{2}, \tag{2.4.12}$$

To see the importance of these parameters we write the momentum equation in the following symbolic form

$$\begin{pmatrix} \text{inertial forces} \\ M_a^2 \end{pmatrix} = \begin{pmatrix} \text{pressure forces} \\ \beta \end{pmatrix} + \begin{pmatrix} \text{Lorentz forces} \\ 1 \end{pmatrix} + \begin{pmatrix} \text{gravity forces} \\ U/V_a^2 \end{pmatrix}, \tag{2.4.13}$$

denoting the order of magnitude of each term with respect to the Lorentz term. In solar atmosphere in cases where the gravitational field can be treated as uniform ($U = gz$) the typical length-scale L_* of the system is comparable to the vertical scale height V_s^2/g so the ratio U/V_a^2 is of order of β. Thus for solar atmosphere we have the following extreme cases,

(i) $M_a << 1$. In this case the velocity terms are not important and the force balance of the system is described from the *magnetostatic equation*

$$0 = -\nabla \mathbf{P} + \frac{(\nabla \times \mathbf{B}) \times \mathbf{B}}{4\pi} - \rho \nabla U, \tag{2.4.14}$$

(ii) $M_a << 1$, and $\beta << 1$. In this case the Lorentz force must be zero, so the current density $\mathbf{J}$ must be parallel to the magnetic field $\mathbf{B}$,

$$(\nabla \times \mathbf{B}) \times \mathbf{B} = 0, \tag{2.4.15}$$

so we have the *force-free* case. In this case the presence of the plasma gas and the mass flows they have not significant influence in the magnetic structure. The particular case $\mathbf{J} = 0$ is the well known *potential-field.*

Chapter 3

CORONAL LOOP MODELS

As we saw in the first chapter, the solar atmosphere has no only vertical stratification produced by the force of gravity, but it is also compressible in the horizontal direction, and possesses a complex structure dominated by the magnetic field. As indicated by X-ray and EUV observations, the corona consists largely of loop structures that presumably outline the magnetic field. In this chapter we shall describe briefly some theoretical models for these coronal loops.

3.1 General remarks

Because ideal MHD holds in most structures at the Sun, a fully theoretical description would require appropriate solutions of the MHD equations. For the present time this is impossible even numerically, and to make some progress people simplified the ideal MHD system to one that is solvable either analytically or numerically. The term analytical includes also numerical solutions from ordinary differential equations because in this case it is easy to understand the behavior of the system (to check the boundary conditions, the dependence of the solutions on the various free parameters etc.). In fully numerical solutions this is very difficult and in most times impossible, so we have not a clear physical picture of the system. Also, fully numerical studies require very large computing power which is not available in most cases.

Until now people have tried to model coronal loops and other solar structures (prominences, sunspots, etc.) following usually two different ways. The first refers to the *thermal structure* and *energy balance* of them ignoring the *effects of flows* although in many cases are important, while the second focus on the flows only, neglecting in most cases the details of thermodynamics. In both approaches the magnetic configuration

is predescribed, because in many solar structures we have $\beta << 1$ so the plasma has negligible influence on the magnetic structure. For the magnetic configuration problem, most efforts that have been made are on the force-free case and only a few in the magnetostatic case.

3.2 Static energy-balance models

In the case of coronal loops, the construction of the static energy-balance models is made solving the energy equation (2.14) putting $\mathbf{V} = 0$. The heat flux term, is due to electron conduction which occurs mainly along the magnetic field lines and can be written

$$\nabla \cdot \mathbf{q} = \nabla_{\parallel} \cdot (\kappa \nabla_{\parallel} T) = (\hat{\mathbf{B}} \cdot \nabla)\Big[\frac{\kappa}{B}(\hat{\mathbf{B}} \cdot \nabla)T\Big], \tag{3.2.1}$$

or more simply, in terms of the distance s along a particular field line,

$$\nabla \cdot \mathbf{q} = B\frac{d}{ds}\left(\frac{\kappa}{B}\frac{dT}{ds}\right), \tag{3.2.2}$$

where B is the magnetic field strength and $\hat{\mathbf{B}}$ the unit vector along magnetic field-lines. The *thermal conduction coefficient* κ, for a fully ionized hydrogen plasma with temperature greater than $10^4\ K$, is

$$\kappa = \kappa_o T^{5/2} = 10^{-11} T^{5/2}\ \frac{W}{mK}. \tag{3.2.3}$$

The term L_r which is the net radiation loss, for an *optically thin* plasma such in the chromosphere and the corona, is due to bremsstrahlung, recombination and line radiation, and can be written as

$$L_r = \rho^2 Q(T), \tag{3.2.4}$$

where ρ is the density assuming fully ionized hydrogen plasma. The temperature dependence $Q(T)$ has been evaluated by a number of authors (Cox & Tucker 1969, Tucker & Koren 1971, McWhirter at al 1975, Raymond & Smith 1977) and is graphed in figure 3.2.1. It is accurate only to within about a factor of two, and so the detailed variations should not be taken too seriously; the most important features are the presence of a maximum around $10^5\ K$ and a minimum around $10^7\ K$. An analytic approximation is

$$Q(T) = \chi T^{\alpha}\ Wm^3, \tag{3.2.5}$$

with the temperature variation of the piecewise constants $\chi(T)$ and $\alpha(T)$ given in Table (3.1). For temperature range $10^5\ K < T < 10^7\ K$ a good approximation is

Range of T	α	χ
$10^{3.64}$–$10^{3.94}$	11.7	$10^{-29.30}$
$10^{4.00}$–$10^{4.30}$	6.15	$10^{-7.62}$
$10^{4.30}$–$10^{4.60}$	0	$10^{18.75}$
$10^{4.60}$–$10^{4.90}$	2	$10^{9.60}$
$10^{4.90}$–$10^{5.40}$	0	$10^{19.40}$
$10^{5.40}$–$10^{5.75}$	-2	$10^{30.2}$
$10^{5.75}$–$10^{6.30}$	0	$10^{18.66}$
$10^{6.30}$–$10^{7.00}$	-0.66	$10^{22.87}$

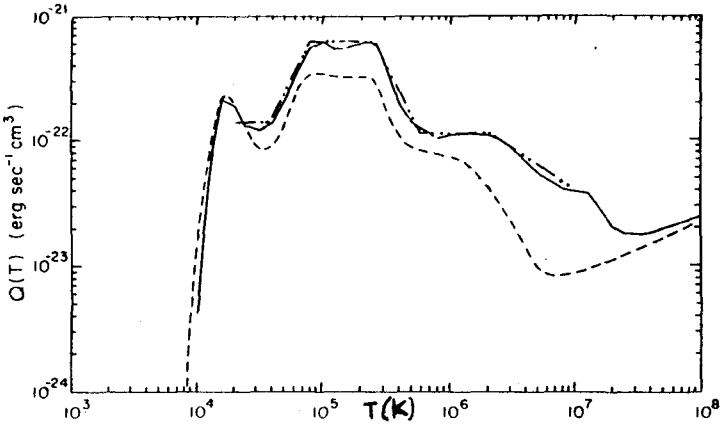

Table 3.1: *The variation with temperature T of α and χ in Eq.3.2.5. giving the loss function (Rosner et al 1978, Serio et al 1981). Plot of the radiative loss function derived by McWhirter at al (1975)* [– – ––], *and Raymond & Smith (1977)* [———], *together with the analytic fitting of Rosner et al (1978)* [· · – – ··].

$Q(T) = 10^{21.6}T^{-1/2}\ Wm^3$ with a departure from the accurate form less by a factor 1.4 (Priest 1984).

Thus for a loop in *hydrostatic equilibrium* and in *thermal equilibrium* between conduction, radiation and heating (of any kind), the temperature T and the density ρ, for fully-ionized hydrogen ($n_e = n_i$), satisfy

$$\frac{1}{\cos\theta}\frac{dP}{ds} = -\rho g\,, \tag{3.2.6a}$$

$$B\frac{d}{ds}\left(\frac{\kappa_o T^{5/2}}{B}\frac{dT}{ds}\right) = \chi\rho^2 T^\alpha - H\,, \tag{3.2.6b}$$

where the pressure is,

$$P = \frac{2k_B}{m_p}\rho T\,. \tag{3.2.6c}$$

For given forms of the magnetic field strength $B(s)$ of a symmetric loop length $2L$ at a distance s along it from the base, and the inclination $\theta(s)$ of the loop to the vertical, the above set of equations is to be solved given the temperature T_0 and pressure P_0 at the base ($s = 0$) and from the requirement that the temperature be symmetric about the summit so the temperature gradient (and the conductive flux also) must vanish at the loop summit ($s = L$). The first condition is entirely arbitrary. With T_0 given, the temperature profiles and, in particular the *summit temperature* T_L are determined by three parameters, namely the loop length $2L$, the base pressure P_0 and the heating rate H, so that $T_L = T_L(L, P_0, H)$. If we replace the condition for the pressure by the

condition that the temperature gradient vanishes at the loop base ($s = 0$) we have a *thermally isolated loop* (there is no energy flow from its ends). Thus, in this case, the summit temperature is a function of only two parameters $T_L = T_L(L, H)$ and of course must be $P_0 = P_0(L, H)$ by the remaining boundary conditions. The former case can be studied quite easily for the *low-lying loops* whose summits are much below a coronal scale height of roughly 80000 km. In these loops the pressure is uniform (assuming uniform cross-sectional area) so the summit temperature may be estimated in order of magnitude, using the fact that, whereas the relative sizes of the three terms in Eq.(3.2.6a) vary locally, their global (or integral) values are similar. Thus, equal each term in order of magnitude in the energy equation (3.2.6b), using the approximate form for the radiation loss, we get the following relations in mks units (Priest 1984, Rosner et al 1978, Serio et al 1981)

$$T_L \approx 10^4 (PL)^{1/3} \approx 10^3 H^{6/7} L^{5/7}\,, \tag{3.2.7a}$$

$$P \approx 3.7 \times 10^2 H^{2/7} L^{4/7}\,. \tag{3.2.7b}$$

From the above *scaling laws* it follows that both *the temperature and pressure are increased by either stretching a thermally isolated loop or enhancing its heating.*

The main features of the loop solutions can be seen in Fig.(3.1) which shows the result of the numerical integration of Eqs.(3.2.6) for a symmetric sercular loop of uniform cross-section and half-length $L = 3 \times 10^7\ m$. The heating is assumed to be constant throughout and is set equal to $H = 2 \times 10^{-4}\ W/m^3$. As expected, the pressure, which was set at 0.14 Pa at the footpoint where the temperature is 7000 K, drops only 20% up to the apex. Moreover, the temperature shows only a similar small variation over the upper 90% of the loop. At high temperatures the radiative loss rate ($\approx 10^{-4}$ W/m^3) is lower than the heating rate, but the conductivity is so high that conduction can convey the excess heat input to the lower part of the loop by means of a very shallow temperature gradient. This is the 'coronal' part of the loop. However, when the temperature drops below $10^6\ K$, the conductivity drops sharply and the temperature gradient steepens in order to maintain the conductive flux. This region of steep temperature gradient is known as the transition region. It is very thin compared to the pressure scale height and is therefore essentially isobaric.

Many authors (e.g. Antiohos 1984, Athay 1981, Brown 1991, Hood & Priest 1979, Mariska & Boris 1983, Poland & Mariska 1986, Priest & Smith 1979, Steele & Priest 1989; see also Demoulin 1993, Bray et al 1991, Priest 1980 and references therein) extend the above results solving Eqs.(3.2.6) numerically, in cases where the loop is large and not thermally isolated. They explain the observations for the active region loops that the shorter loops often appear brighter, and that different loops exhibit a relatively small variation in soft X-ray temperature but a much larger variation in pressure. From

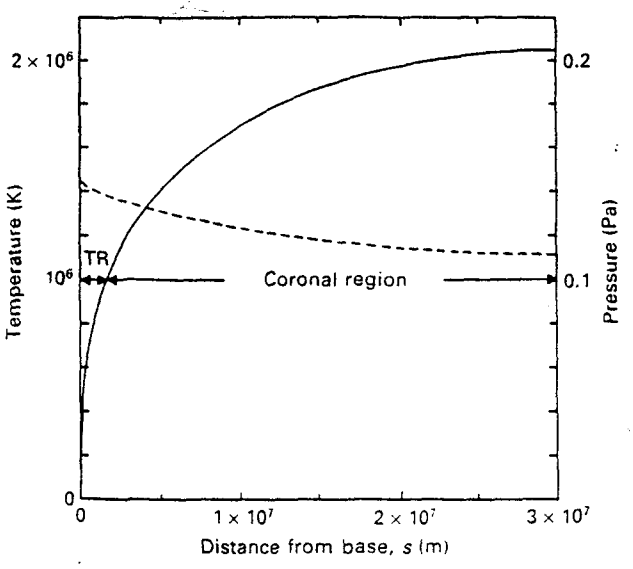

Figure 3.1: The one-dimensional structure of a for coronal loop of uniform cross section and uniform heating of $2\times10^{-4}\ W/m^3$. The full line shows the temperature, the dashed line the pressure as a function of distance from the base in which the temperature is 7000 K (Bray et al 1991).

the other side, the fact that the quit region loops which have temperatures and pressures lower than the active region ones, is attributed to a lower heating rate in them. But the most important result from these studies is that, if the pressure or the length of the loop increase, or the heating decrease, to a critical value, the loop becomes *thermally unstable*, and it cools reaching a new equilibrium at temperatures below $10^5\ K$. This may be an explanation for the observed cool cores in some coronal loops, although that these contains too much plasma to be in hydrostatic equilibrium; so flows are present and must taken to account. Also this cooling have been proposed as a mechanism for the formation of the active-region filaments or prominences.

3.3 Dynamic flow models

As we discussed in chapters 1 and 2, the interest in flows in loop structures has been stimulated by observations of various types of mass motions (up to 100 km/sec) over spots, plages and network, and also from the absence of hydrostatic equilibrium in some loops with cool cores.

There is a wide variety of possible cases for the flow patterns that are observed. The most well studied is the *siphon flow*, driven by a pressure difference that is maintained between the footpoints of a magnetic loop. Only for this mechanism, we shall give a

brief review for the proposed models, because in this direction is the contribution of this thesis.

The siphon flow was invoked by Meyer & Schmidt (1968) to explain Evershed motions along low-lying photospheric and chromospheric loops, but it may also occur along coronal loops. If one starts with a static loop and switches on a pressure difference, an *accelerated* flow will be driven from the high-pressure footpoint. But, if one starts with a loop containing a flow and then a small pressure difference is imposed in the opposition to the flow, it is possible for a *decelerated* flow to be set up towards the higher pressure. In general, this flow is unsteady, but if the footpoint pressures are constant and one waits several sound travel times, a steady flow may be established. There are several ways in which different footpoints pressures may be maintained. For example, the constancy of total base pressure (plasma plus magnetic) would imply that regions of high magnetic field strength possess a low plasma pressure. Also a converging photospheric flow could compress both magnetic field and plasma, and so enhance the pressure locally. Finally, the pressure at a loop footpoint may be increased by enhancing the heating there.

Until now, siphon flows have been analyzed in a number of studies, all in the slender flux tube approximation in which the loop is so narrow that its magnetic field is approximately uniform across its width; this means its magnetic flux at a distance s along the tube is simply the product of the area of the tube A, and the magnetic field strength B there; also the field strength at the surface of the tube (which is used in the surface boundary condition) does not therefore differ greatly from the value at the center of the tube. In a few words the above approximation is mathematically identical with the consideration of an individual field line by dropping out the details of the effect of the environment or taken a simplified description for the force balance across the field. Thus, in this case the steady MHD equations became ordinary differential equations (one-dimensional flow) since all the quantities depends only from the abscissa s along the loop.

The effects of the environment can be dropped out if the plasma β of the loop and the Alfvén number of the flow are both much less than unity. Then the flow may be regarded as taking place in a rigid tube of given shape and cross-section, because at that circumstances the magnetic structure does not influed by the flow. Thus the problem is the calculation of the flow in the context of ordinary hydrodynamics in a loop of given cross-section and shape. Cargill & Priest (1980) and Noci (1981) did that, for semi-secular loop in shape, in a uniform and in a spherically symmetric gravitational field U respectively. Thus, the equations of continuity, momentum and state, for steady,

inviscid flow of a fully-ionized plasma are

$$\frac{d}{ds}(\rho V S) = 0\,, \tag{3.3.1a}$$

$$\rho V \frac{dV}{ds} = -\frac{dP}{ds} - \rho \frac{dU}{ds}\,, \tag{3.3.1b}$$

$$P = \frac{2k_B}{m_p}\rho T\,, \tag{3.3.1c}$$

and in both studies they simplified the energy equation in the form

$$\frac{d}{ds}\left(\frac{P}{\rho^\alpha}\right) = 0\,. \tag{3.3.1d}$$

The boundary conditions in the above system is the value of the pressure P_0 and and temperature T_0 at the point where the fluid enters in the loop (at one footpoint) and the value of the pressure P_2 at the other where the fluid leaves the loop. If we eliminate P and ρ from Eq.(3.3.1b) we obtain

$$\left(V - \frac{V_s^2}{V}\right)\frac{dV}{ds} = \frac{V_s^2}{S}\frac{dS}{ds} - \frac{dU}{ds}\,, \tag{3.3.2}$$

where $V_s^2 = \alpha P/\rho$ is the sound speed. It should be noted that if V is replaced by $-V$ Eq.(3.3.2) in both two directions. For shocked flows, such a reversal is not possible because the entropy must increase across the shock wave. The reversal is possible if the position of the shock is in the other leg of the loop than previously. Another characteristic of the above differential equation is that it possesses a critical point (where dV/ds is undefined) where the speed is equal to the sound velocity ($V = V_s$) in locations that are determined from the zeros of the right part of Eq.(3.3.2). For simplicity let us suppose for the moment that gravity is absent, so we discuss about de Laval nozzles in ordinary tubes. In this case the critical point occurs in locations where the cross section has extreme, $dS/ds = 0$. Another differentiation of Eq.(3.3.2) gives ($U = 0$)

$$\left(\frac{dV}{ds}\right)^2 = \frac{V_s^2}{S(1+V_s^2)}\frac{d^2S}{ds^2}\,, \tag{3.3.3}$$

so if the tube has a minimum ($d^2S/ds^2 > 0$), two slopes for the fluid velocity dV/ds when the fluid velocity equals to the sound velocity ($V = V_s$) are possible (X-type critical point), while if the cross-section of the tube has an maximum ($d^2S/ds^2 < 0$), there no solutions with $V = V_s$ at the maximum cross-section (O-type critical point). For critical solutions, in the case of converging de Laval nozzles the velocity of fluid

increases continuously before and after the nozzle, while for diverging de Laval nozzles it decreases before the nozzle and increase after. Thus the main conclusion is that the velocity reached the sound velocity in the minimum cross-section. For the non-critical solutions, in tubes in which there is a minimum cross-section the velocity increases before the nozzle and decrease after, while the opposite happens in tubes with a maximum cross-section. Both cases are discuss again in section 4.5.2 in which diagrams of velocity versus distance are present (Fig.4.1). After the above small parenthesis about de Laval nozzles, it is evident from Eq.(3.3.2) that we can define an effective cross-section to include the influence of gravity, so the above discussion holds. Also, at this stage it is important to say that in general the presence of critical points on MHD equations is very important since they determine the topology of the solutions and the various types of flows that are possible to occur according to the boundary conditions (sections 6.2, 6.3).

Integrate Eq.(3.3.2) we obtain

$$\frac{1}{2}(V^2 - V_0^2) + \frac{V_{s_0}}{\alpha - 1}\left[\left(\frac{V_0}{V}\right)^{\alpha-1}\left(\frac{S_0}{S}\right)^{\alpha-1} - 1\right] + U = U_0\,, \tag{3.3.4}$$

where the subscript zero denotes a value at the footpoint from which s is measured. For a semi-circular loop in shape, length $2L$, in uniform gravity g we have

$$U(s) = gz(s) = g\frac{2L}{\pi}\sin\frac{\pi s}{2L}\,, \tag{3.3.5}$$

The simplest case, an isothermal loop ($\alpha = 1$) with uniform area, illustrates the basic ideas. The critical point is located at the loop summit (Fig.3.2) where the phase plane of Eq.(3.3.4) is shown.

For initial speeds $V_0 < V_0^*$ the flow is *subsonic* and symmetric about the top of the loop, so that the pressure ratio at the footpoints of the loop is unity. For $V_0 > V_0^*$ the results are unphysical. For $V_0 = V_0^*$ the flow becomes *sonic* at the loop summit. The whole situation is identical with converging de laval nozzles.

When there is no pressure difference between the ends of the loop ($P_2 = P_0$), any of the subsonic flows may occur. However, an imposed pressure difference forces the flow to became supersonic beyond the loop summit and then to be decelerated (and heated) at a shock wave, which is located at some position on the downflowing leg. This must be the case because the fluid can not reach the other footpoint at supersonic velocity; the value of the pressure there must determined the whole flow, and there is only one value of the pressure that corresponds to that case. If we impose other values of pressure, this information can not travel in the opposite direction of the flow since this moves with supersonic velocity (perturbations travel with the sound velocity), and

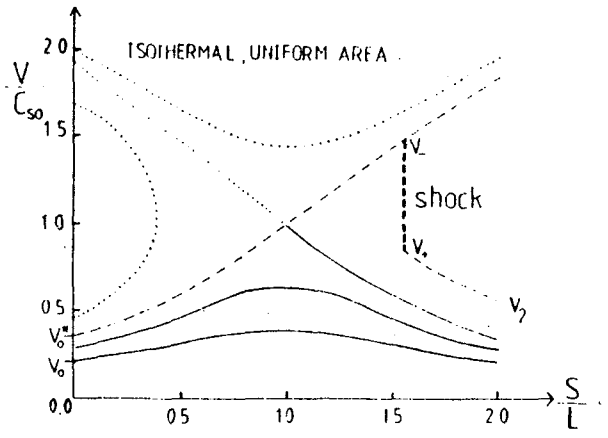

Figure 3.2: *The flow speed V at a distance s along a loop of half-length L. The loop has uniform cross-sectional area and the (unshocked) flow is isothermal with sound V_s. Subsonic flows (solid) have initial speeds V_0 less than V_0^*. Flows (dashed) with initial speed V_0^* become supersonic at the loop summit ($s = L$) and are slowed down from V_- to V_+ by a shock wave. Beyond the shock the flow has enhanced temperature T_+ and slows to V_2 at the footpoint. Dotted lines indicate unphysical or totally supersonic solutions (Cargill & Priest 1980).*

also in a first view it seems that there is no solution at this case. In order to do this a shock discontinuity appears at some position in the flow in which the fluid enders with supersonic velocity and comes out with subsonic. In the shock the entropy of the gas increased discontiniously and the comes out of the shock with greater temperature. All the quantities (P, ρ, T and V) in the shock are discontinuous but the flux mass, momentum, and energy must be continuous at the two sides of the shock. Thus we can write the shock conditions as follows (Rankine–Hugoniot relations)

$$[\rho V] = 0\,, \tag{3.3.6a}$$

$$[P + \rho V^2] = 0\,, \tag{3.3.6b}$$

$$\left[\int \frac{dP}{\rho} + \frac{V^2}{2}\right] = 0\,, \tag{3.3.6c}$$

where the brackets denote the difference between the values of the above expressions in the brackets on the two sides of the surface of the shock. Thus the effect of imposing different pressure differences is to change the location and the strength of the shock and the value of the downstream speed V_2. Of course the above discussion holds for any cross-sectional profile of the loop, and also can be generalized in any type of flow including also and magnetic effects.

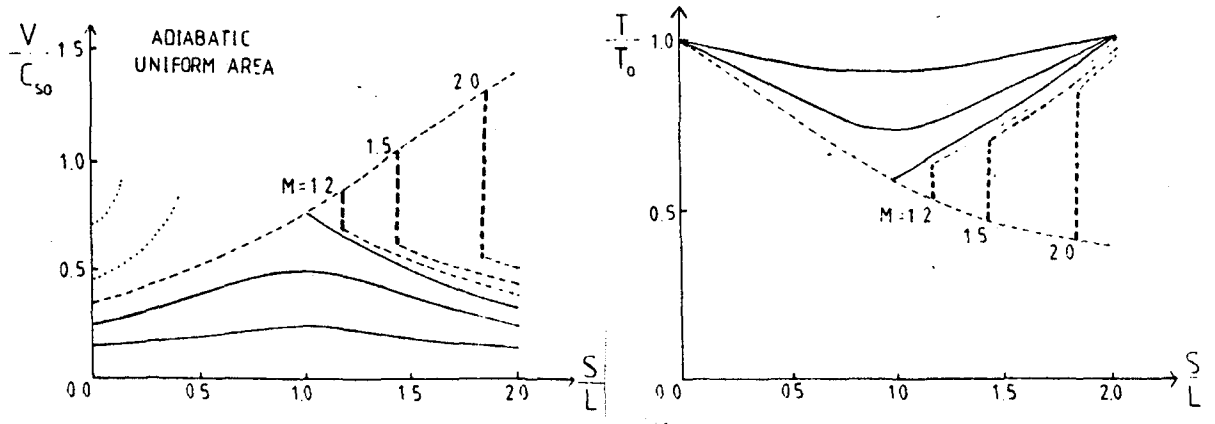

Figure 3.3: *The velocity (a), temperature (b), and the pressure (c) profiles for adiabatic flow in a loop with uniform cross-section. For the shocked solutions, the pre-shock Mach number, M, is indicated (Cargill & Priest 1980).*

The density has the inverse profile of that of velocity; it decreases up to the summit for subsonic flow and right up to the shock wave for a shocked flow. If the flow is adiabatic ($\alpha = 5/3$) rather than isothermal, this rarefraction of the plasma causes a fall in the summit temperature and pressure, too. This may possibly explain the cool cores that are found in some coronal loops (Fig.3.3).

If the cross-section is not uniform but it is symmetric having a maximum in the top of the loop, the sonic point still remains at the top, but the speed there is reduced. If the area-increase or the loop length are too large, the subsonic solutions cease to exist. Furthermore, for a moderate area-increase, several sonic critical points appear and greatly complicate the topology. One effect of a large enough area-increase is to make the flow speed decrease to a minimum before increasing and passing through the sonic point (Fig.3.4).

When the cross-sectional area is not constant or symmetric about the loop summit, the critical point no longer occurs at the loop summit. For a converging loop the sonic point is situated on the downflowing leg (after the summit), whereas for a diverging loop it is on the upflowing leg. At any case, for subsonic solutions, all the quantities at the two foot points are now unequal, which means that there is a non-zero pressure difference between them. Diverging loops give a phase plane for subsonic flows that may be obtained from that of a converging loop by rotating the solutions about the summit. Independent of the two above cases there are two possibilities; the flow can be accelerated towards to the low pressure footpoint where the cross-section is minimum, or to be decelerated as moving in the direction of increasing pressure where the cross-section is maximum. It can be seen that when the footpoint pressures are equal the

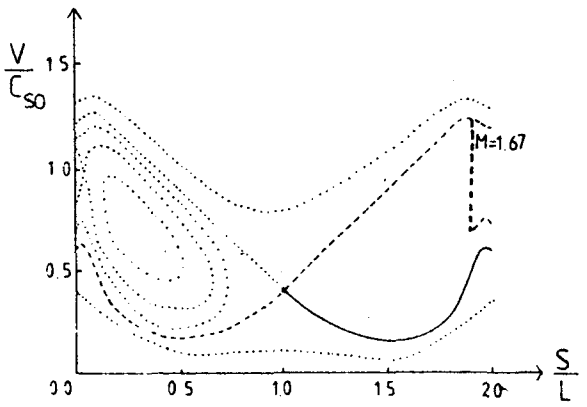

Figure 3.4: *The phase plane for adiabatic flow along a symmetric loop whose cross-sectional area varies as* $S = S_0(1 + 19 \sin \pi s/2)$. *Note that for physical subsonic or transonic flows the initial velocity must be less than 0.615. If the area increases very fast there are no solutions (Cargill & Priest 1980).*

solution is static (no flows). For accelerated (decelerated) flows as the final pressure at the minimum (maximum) cross-section decrease (increase) from the initial pressure at the other footpoint, the solutions at first yield subsonic flow, and further decreasing (increasing) has the result of a shocked flow. It must be noted that in the cases of a decelerated flow there are two solutions with the same boundary conditions; one subsonic and the other shocked. Also there is an accelerated shocked solution in loops where the flow is to the direction of decreasing cross-section (Fig.3.5).

On the other hand Noci (1981) has studied the properties of the steady siphon flow Eqs.(3.3.4) in the spherically symmetric gravitational field of the Sun for a semi-circular loop in shape, radius R, and constant cross-section for which

$$U(s) = -\frac{GM_\odot}{r} = -\frac{GM_\odot}{R_\odot}\left\{1 + 2\frac{R}{R_\odot}\left[1 - \left(\frac{R}{R_\odot}\right)\right]^{1/2} \sin\frac{s}{R}\right\}. \qquad (3.3.7)$$

He also puts $\alpha = 1.1$, since this value gives solar winds solutions in the inner corona that agree quite well with solutions to the full energy equations. The phase plane of the solutions are shown in Fig.(3.6a) and obviously are similar to that of the previous study of Cargill & Priest (1980). Apart from this, he investigated also the distribution of the brightness in some coronal UV lines along the loop, to see if the physical differences of the various types of flows which can occur in a loop can be seen in the observations. He found that the intensities for static and subsonic loops do not differ considerably, while those for static and shocked loops do differ greatly in the downflowing leg, especially when the shock is close to the footpoint. This suggests a definite observable signature

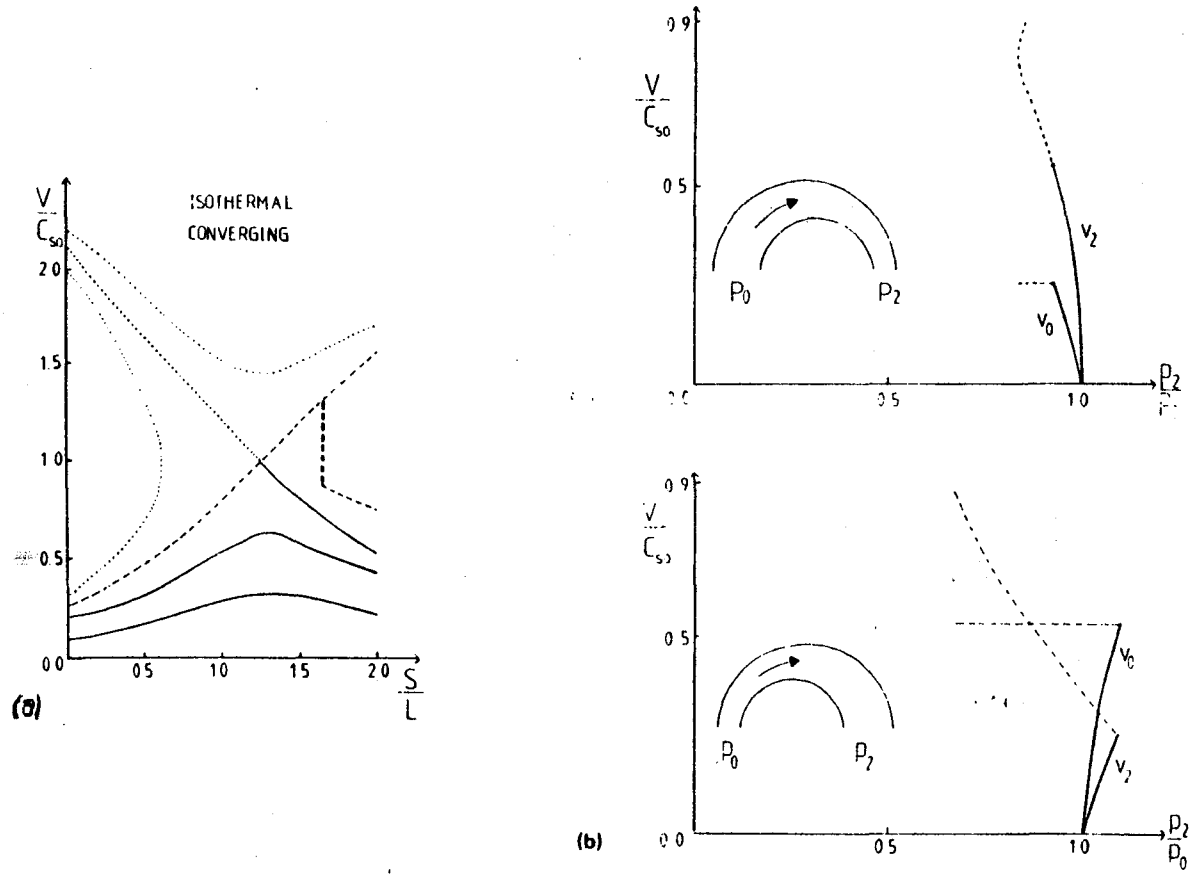

Figure 3.5: *(a) Phase plane $V(s)$ for isothermal flow in a converging loop with $S = S_0(1 - s/4L)$ for accelerated flows. For decelerated flows (diverging loop) the phase plane is found by rotation of the solutions about the summit. (b) The flow speeds V_0, V_2 at loop footpoint at a function of the imposed pressure ratio for an accelerated $(P_2/P_0 < 1)$ and a decelerated flow $(P_2/P_0 > 1)$ (Cargill & Priest 1980).*

for supersonic flows. Indeed, it may well be that some loops (observed to extend from one foot point and then disappear before reaching the second footpoint) possess this feature because of a subsonic-supersonic siphon flow (Fig.3.6a).

In the plasma β of the loop is not much less than unity, the influences of the pressure and weight of the gas, the flow, and the environment must be taken into account. Thus, the cross-section and the shape of the loop are not given but must be found from the requirement of the satisfying the force balance along and across the loop. Thomas and Montesinos dit that in a series of articles (Thomas 1988, Thomas & Montesinos 1989, 1991, Montesinos &Thomas 1989) in the thin flux tube approximation. The equations that describe the motion of the fluid inside the loop (force balance along the loop) in a uniform gravitational field g are again Eqs.(3.3.1), where now the cross-section of the loop $S(s)$ is not given but relates with the magnetic field $B(s)$ of the loop by the magnetic conservation law

$$\frac{d}{ds}(BS) = 0\,, \tag{3.3.8a}$$

while from the requirement that the total pressure (gas plus magnetic) must be continuous at the surface of the loop we have

$$P + \frac{B^2}{8\pi} = P_e\,, \tag{3.3.8b}$$

where P_e is the pressure of external gas atmosphere outside of the tube for which we assume that is in planar-stratified equilibrium in vertical direction

$$-\frac{dP_e}{dz} - \rho_e g = 0\,, \tag{3.3.9a}$$

and of course the equation of state is assumed to be the perfect gas law.

$$P_e = \frac{2k_B}{m_p}\rho_e T_e\,. \tag{3.3.9b}$$

Thus for given temperature distribution $T_e(z)$ we can determine the distributions of the pressure $P_e(z)$ and the density $\rho_e(z)$. For simplicity we can take a uniform temperature distribution; a more detailed consideration requires a full solution of this problem. It easy to see that Eqs.(3.3.1) and (3.3.8) formed a closed set if we predescribed the shape $B_z(s)$ of the loop. But if we want to solve the problem completely the shape of the loop must be found from the lateral force balance

$$\frac{\rho V^2}{\mathrm{R}} - \frac{B^2}{4\pi \mathrm{R}} + (\rho_e - \rho) g \cos\theta = 0\,, \tag{3.3.10a}$$

which express the fact that the centerfucal force plus the gradient of the pressure of the external atmosphere in the vertical direction of the loop are equal to the magnetic

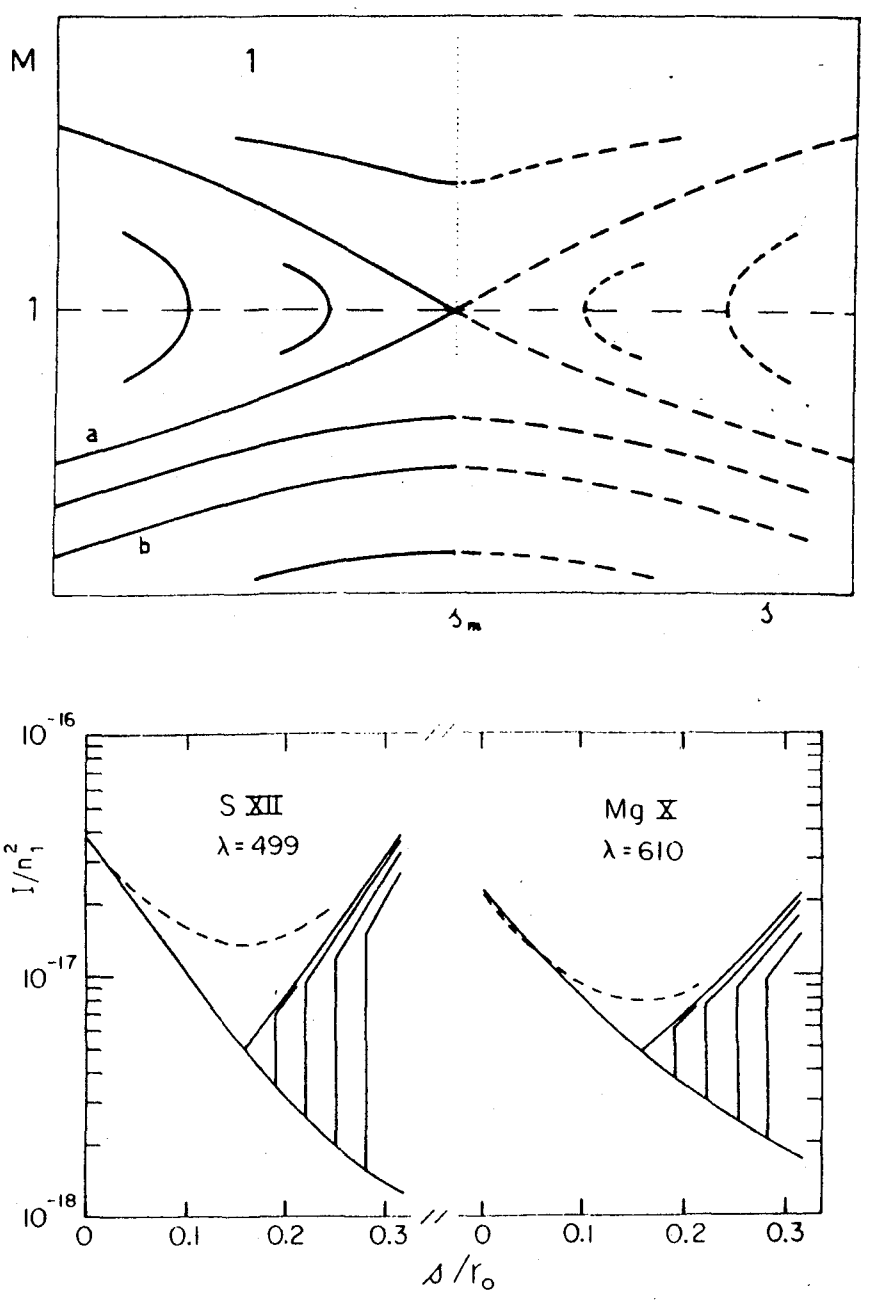

Figure 3.6: *(a) Phase plane of solutions for a symmetric loop in the Noci (1981) model where gravity drops as $1/r$. (b) Brightness variations (in c.g.s. units for two UV lines for a hot loop for subsonic and shocked. The loop width is one tenth of the loop radius. Dashed curves represent brightness variation for a static isothermal loop having the same temperature as the dynamic loop in the first footpoint. For the sake of clearness the dashed curve which is symmetric around the top is not completed.*

tension force plus the one component of the weight of the fluid in the tube. From basic geometrical arguments we can write the following expressions for the radius of curvature R at any point of the loop and its inclination angle θ or for its height z and horizontal distance x

$$\frac{dz}{dx} = \tan\theta\,, \tag{3.3.10b}$$

$$\frac{1}{\mathrm{R}} = \cos\theta\frac{d\theta}{dx}\,, \tag{3.3.10c}$$

We should point out that this decoupling of the problem is a direct consequence of the thin flux tube approximation; in a thick flux tube, the flow will not be one dimensional and the problem of determining the equilibrium path and the flow will be fully coupled.

As in the work of Cargill & Priest (1980) we can derive differential equations relating the area $S(s)$, velocity $V(s)$, and height $z(s)$ that are useful in determining the character of the flow independent of the shape of the loop is given or not. Thus from momentum equation using the conservation mass law we find

$$\left(1-\frac{V^2}{V_s^2}\right)\frac{dV}{V} = -\frac{dS}{S} + \frac{g}{V_s^2}dz\,, \tag{3.3.11}$$

which is the same as Eq.(3.3.2) and is known as the area-velocity-height relation. From this using the magnetic flux conservation and the lateral pressure balance we can eliminate the cross-section and we get

$$\left(1-\frac{V^2}{V_t^2}\right)\frac{dV}{V} = \left[1-\left(\frac{\rho_e-\rho}{\rho}\right)\frac{V_s^2}{V_a^2}\right]\frac{g}{V_s^2}dz\,, \tag{3.3.12}$$

and if we eliminate the velocity

$$\left(1-\frac{V^2}{V_t^2}\right)\frac{dS}{S} = \left(1-\frac{V^2}{V_1^2}\right)\left(\frac{\rho_e-\rho}{\rho}\right)\frac{g}{V_a^2}dz\,, \tag{3.3.13}$$

known as velocity-height and area-height relations respectively. In the above equations $V_s = (\alpha P/\rho)^{1/2}$, and $V_a = (B^2/4\pi\rho)^{1/2}$ are the sound and Alfvén velocity respectively, and

$$V_t = \sqrt{\frac{V_s^2 V_a^2}{V_s^2+V_a^2}}\,, \tag{3.3.14}$$

is the tube speed which is the velocity of propagation of axisymmetric distortions to the cross-sectional area of an isolated magnetic flux tube. In Eq.(3.3.13) V_1 is another characteristic speed defined by

$$V_1^2 = \left(\frac{\rho_e-\rho}{\rho}\right)V_s^2\,. \tag{3.3.15}$$

We can deduce some qualitative properties of the steady flows by examing just the velocity-height relation and the area-height relation. First, note that the tube speed V_t plays the role of the critical speed for the flow, replacing the role of the sound speed for a rigid flux tube. Thus and in this case we have subcritical ($V < V_t$), critical ($V = V_t$) and supercritical flows ($V > V_t$) instead of subsonic, sonic, and supersonic flows. For simplicity we consider the case that the temperature inside the tube is everywhere equal to the external temperature assuming uniform. The equality of temperatures arises from the rapid radiative cooling of the flux tubes in the solar photosphere. At this case we have always $V_1 < V_t$, and Eqs.(3.3.14) and (3.3.15) are written

$$\left(1 - \frac{V^2}{V_t^2}\right)\frac{dV}{V} = \frac{dz}{2L}, \tag{3.3.16}$$

$$\left(1 - \frac{V^2}{V_t^2}\right)\frac{dS}{S} = \left(1 - \frac{V^2}{V_1^2}\right)\frac{dz}{2L}, \tag{3.3.17}$$

where $L = V_s^2/g$ is the scale height in the external atmosphere. From Eq.(3.3.16) we see that the critical speed $V = V_t$ occurs always in the top of the loop and the situation is similar as in the rigid flux tube. But apart of this from Eq.(3.3.17) we see that at the points where $V = V_1$ the cross-section obtains a maximum; these points called bulge points. Thus for example, if the flow starts from the one foot point of the arc with velocity which is less from both the two characteristic speeds V_t, and V_1 we can have the cases of Figs.(3.7). The rest of the cases can be found easily from the former ones.

Thomas and Montesinos integrated the systems of equations in two cases; with the assumption that the shape of the loop is a parabolic arc (Thomas 1988, Montesinos & Thomas 1989), and without this assumption where the shape is an unknown quantity (Thomas & Montesinos 1990, 1991). Their results for the second case are seen in Figs.(3.8) (Thomas and Montesinos 1990). The difference between the two approaches are that in the second case the horizontal extension of the loop has a limited value (a expected result because it is known many years ago for the static loops), but near the top the two approaches coincide. Also, as it is expected, the effects of the increasing the flow causes the loop to became more steeper.

For a adiabatic consideration for the gas into the tube (assuming now that the flow speed is so great that there is no enough time for the internal gas to be heated by thermal conduction or radiation from the surroundings) the above qualitative results remains the same (Fig.3.9). The difference between the two considerations are that in the adiabatic case the arcs are more wide that in the isothermal case, and in some circumstances the path of the tube becomes periodic in the horizontal direction.

Apart from these elementary considerations many others generalized the above results. For example in the low β limit Cargill & Priest (1982a,b) and solved the hydro-

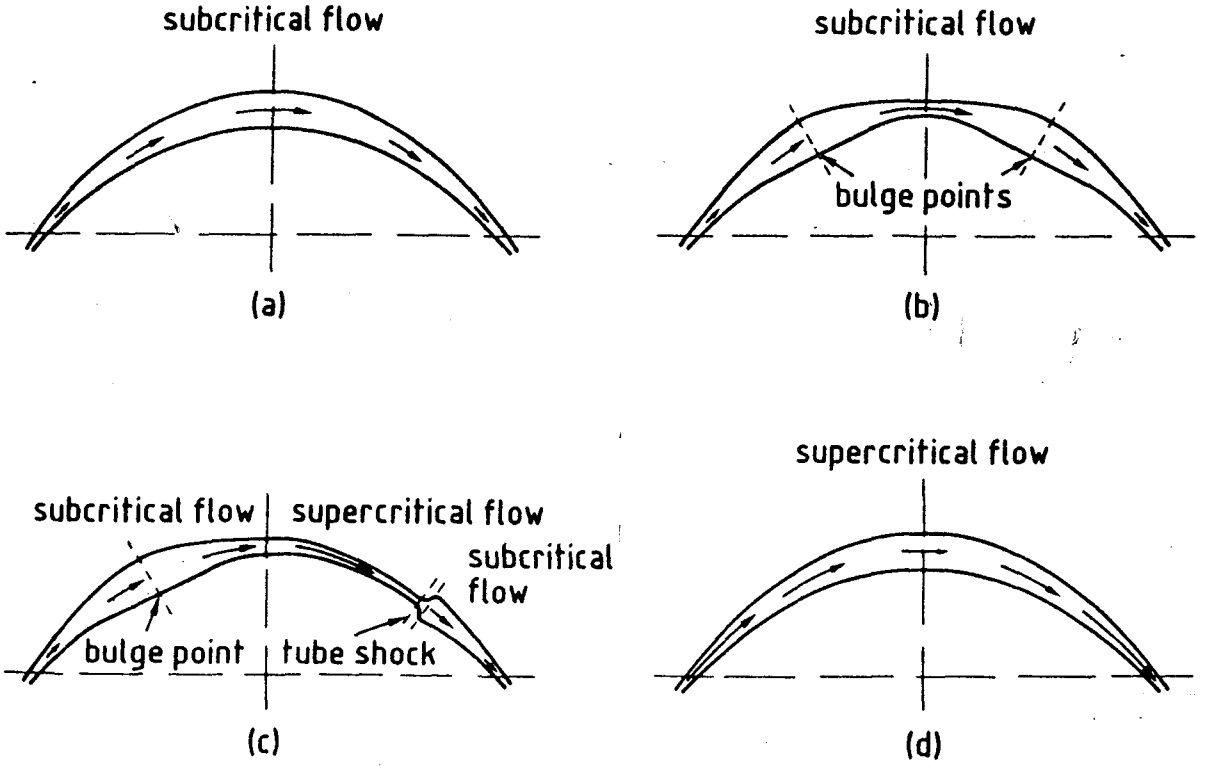

Figure 3.7: *Schematic diagrams of various types of steady flows in a symmetric, arched, isolated magnetic flux tube, showing the changes in flow velocity V (arrows) and the cross-sectional area S along the tube in each case. (a) Purely subsonic flow without bulge points ($V_{\rm top} < V_1 < V_t$). (b) Purely subcritical flow with upstream and downstream bulge points ($V_1 < V_{\rm top} < V_t$). (c) Critical ($V_{\rm top} = V_t$) undergoing a smooth transition from subcritical flow ($V_{\rm top} < V_t$) to supercritical flow ($V_{\rm top} > V_t$) at the top of the arch. The flow velocity is decelerated to subcritical speed at a standing "tube shock" somewhere in the downstream half of the arch. (d) Purely supercritical ($V > V_t$) flows, everywhere (Thomas 1988).*

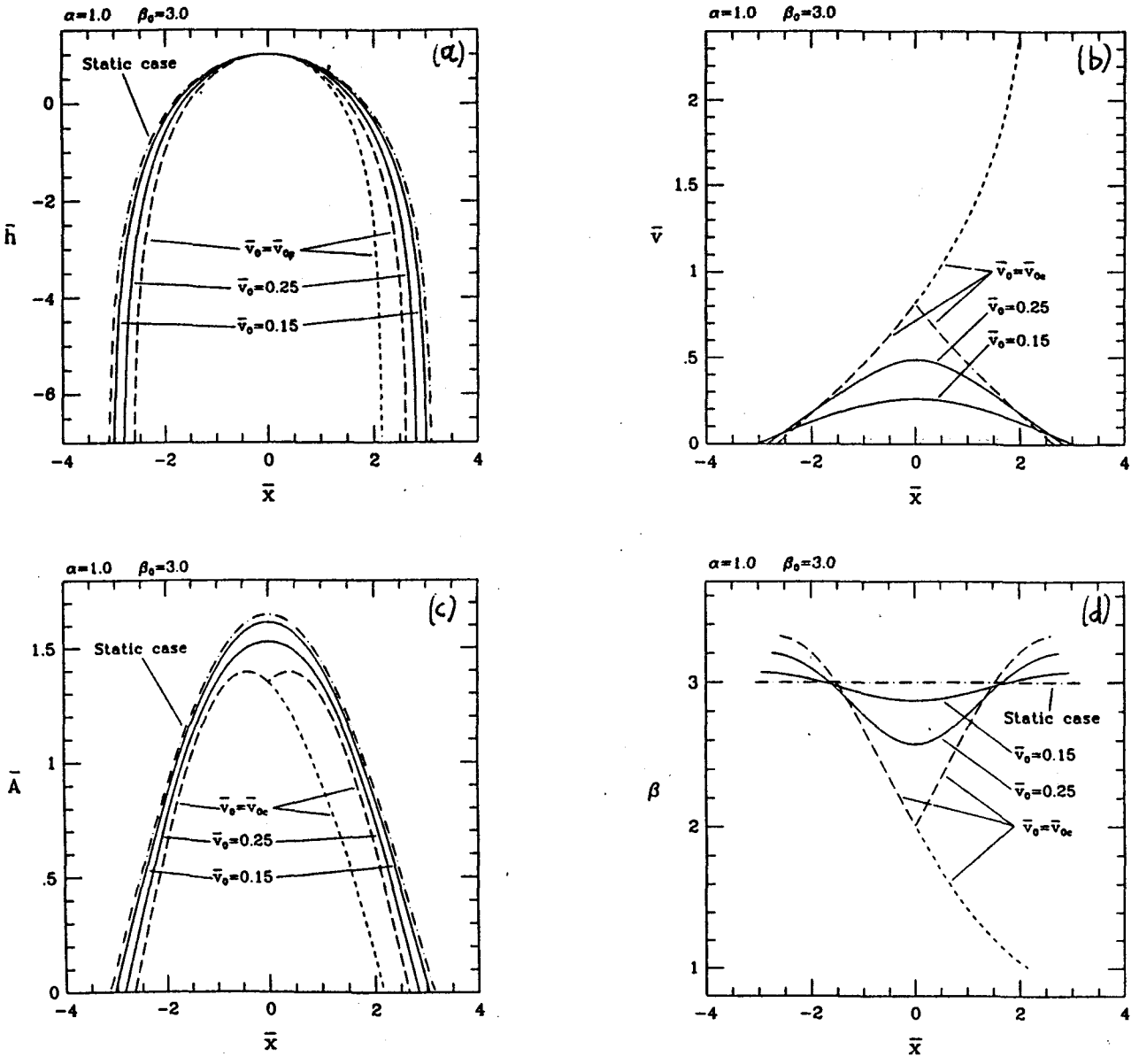

Figure 3.8: *Plots of (a) the equilibrium path $z(x)$, (b) the velocity $v(x)$, (c) the cross-sectional area $S(x)$, and (d) the plasma $\beta(x)$ for a thin tube with uniform temperature inside equals to the external temperature. The integration have started from $z = 0$ with $A = 1$ and $V = V_0$ (four values of 0 which corresponds to the static case 0.15 and 0.25 for subcritical flows and 0.303 for critical flows). The plasma β at the footpoints is equal to 3 and the height of the arch is 1 (all the lengths are normalized with the vertical scale height of the external atmosphere and the velocities are in units of V_1) (Thomas & Montesinos 1990).*

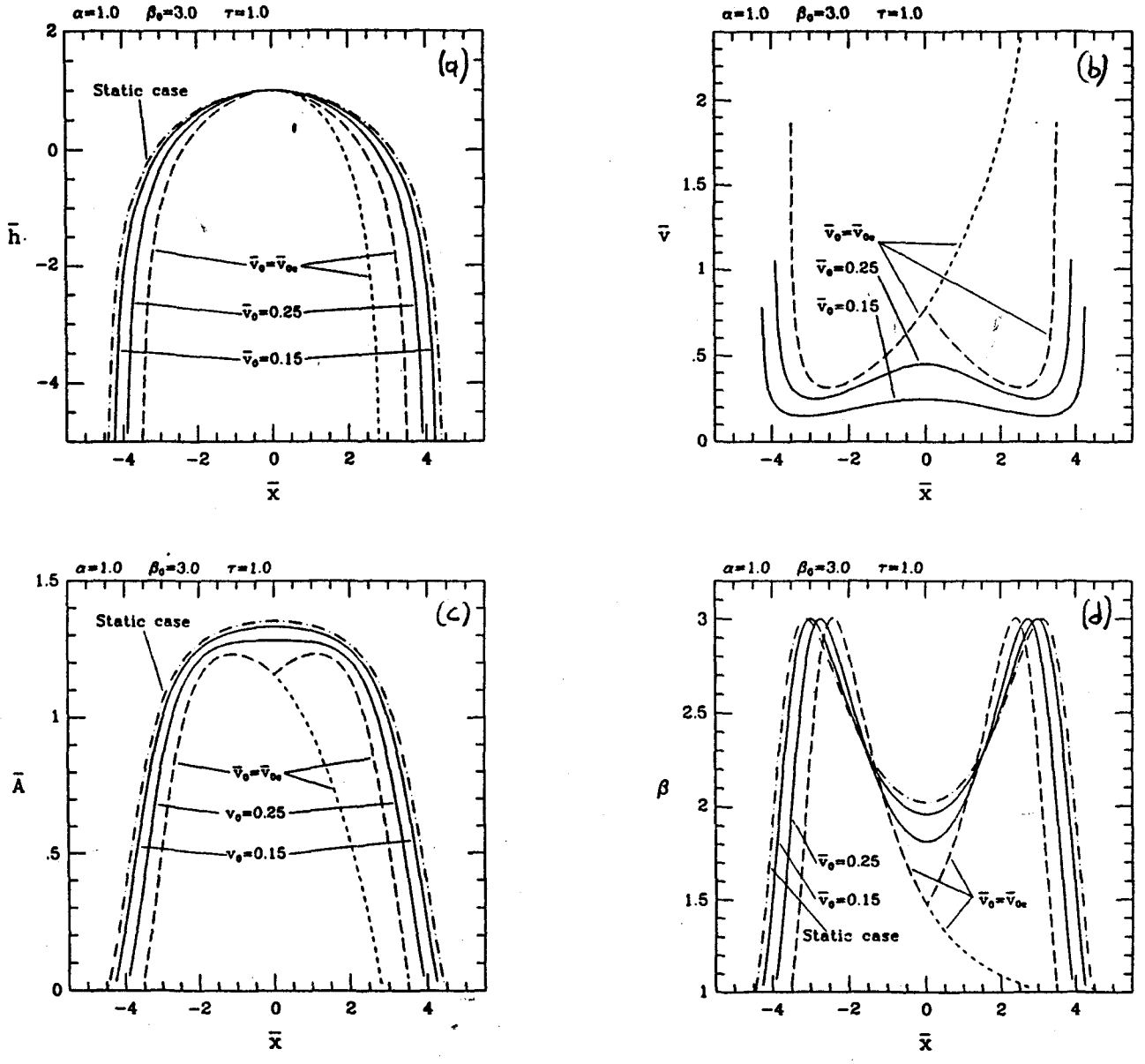

Figure 3.9: *The same as Fig.(3.8) but for adiabatic shock flows with the foot temperature equals to the external temperature. The other parameters are as in Fig.(3.8) except for the critical velocity which is now 0.316 (Thomas & Montesinos 1990).*

dynamic equations using the appropriate for the solar corona energy equation (2.17e) in order to produced more realistic models for coronal loops in order to compare with observations. In a number of studies (Antiohos 1984, Peres et al 1992, Mariska & Boris 1983, Mariska 1988, McClymont 1989, Craig & McClymont 1986, 1987) calculations of the intensities in the UV emission confirmed theoretically the presence of flows in some come coronal loops. Also from the other side for low β loops Montesinos & Thomas (1993) and Degenhardt (1989, 1991) present solutions for radiative flows using an appropriate energy equation for photospheric conditions including also the energy exchange between the tube and its environment which is a realistic external atmosphere in order to model photospheric flux tubes and the Evershed effect. In well defined cases a siphon flow is responsible for the normal Evershed effect (in these cases although that the external atmosphere has been taken horizontally stratified the tube is asymmetrical due to radiative exchange between the tube and the external atmosphere.

It is important to say that all the above discrubing approaches are one-dimensional because of the difficulty of the solution of the two-dimensional MHD equations with one ignorable coordinate (section 2.3). At this case the non-linear ordinary differential equations becomes non-linear partial differential equations which is difficult to solve even numerically. But except of the numerical approach there is an analytical approach to the problem by searching special classes of solutions which can be treated analytically. This will be the subject of the next three chapters which describing briefly in the next section. This approach started studied wind-type solutions in spherical geometry. For a modeling of the solar atmosphere structures (arcades, sunspots, prominences, open-field regions etc.) we must solve the MHD equations in cartesian or cylindrical geometry. de Ville & Priest (1990, 1991a,b,c) found a class of solutions field-aligned flows in cartesian and in cylindrical geometry assuming that the plasma is incompressible in each fieldline. In more details they considered the case

$$\rho = \rho(A)\,, \tag{3.3.18}$$

so, the density is constant along each field line. In this particular case from the momentum balance equation it is easy to see that

$$P + \frac{1}{2}\rho V^2 + \rho U = \Pi(A)\,, \tag{3.3.19}$$

where $\Pi(A)$ is a function of A only, playing similar role as $E(A)$. Of course making similar analysis like in section(2.3) we found that there are also three other free integrals $\Psi(A)$, $\Omega(A)$ and $G(A)$. Note that for field aligned flows we must have again $\Omega(A) = 0$. Now it easy to see that Eq.(2.3.25) is written now as $(i = 1, 2)$

$$\frac{1}{h_1 h_2 h_3}\left(\frac{\partial}{\partial x_1}\frac{h_2}{h_1 h_3}\frac{\partial}{\partial x_1} + \frac{\partial}{\partial x_2}\frac{h_1}{h_2 h_3}\frac{\partial}{\partial x_2}\right)\frac{\partial A}{\partial x_i}\,,$$

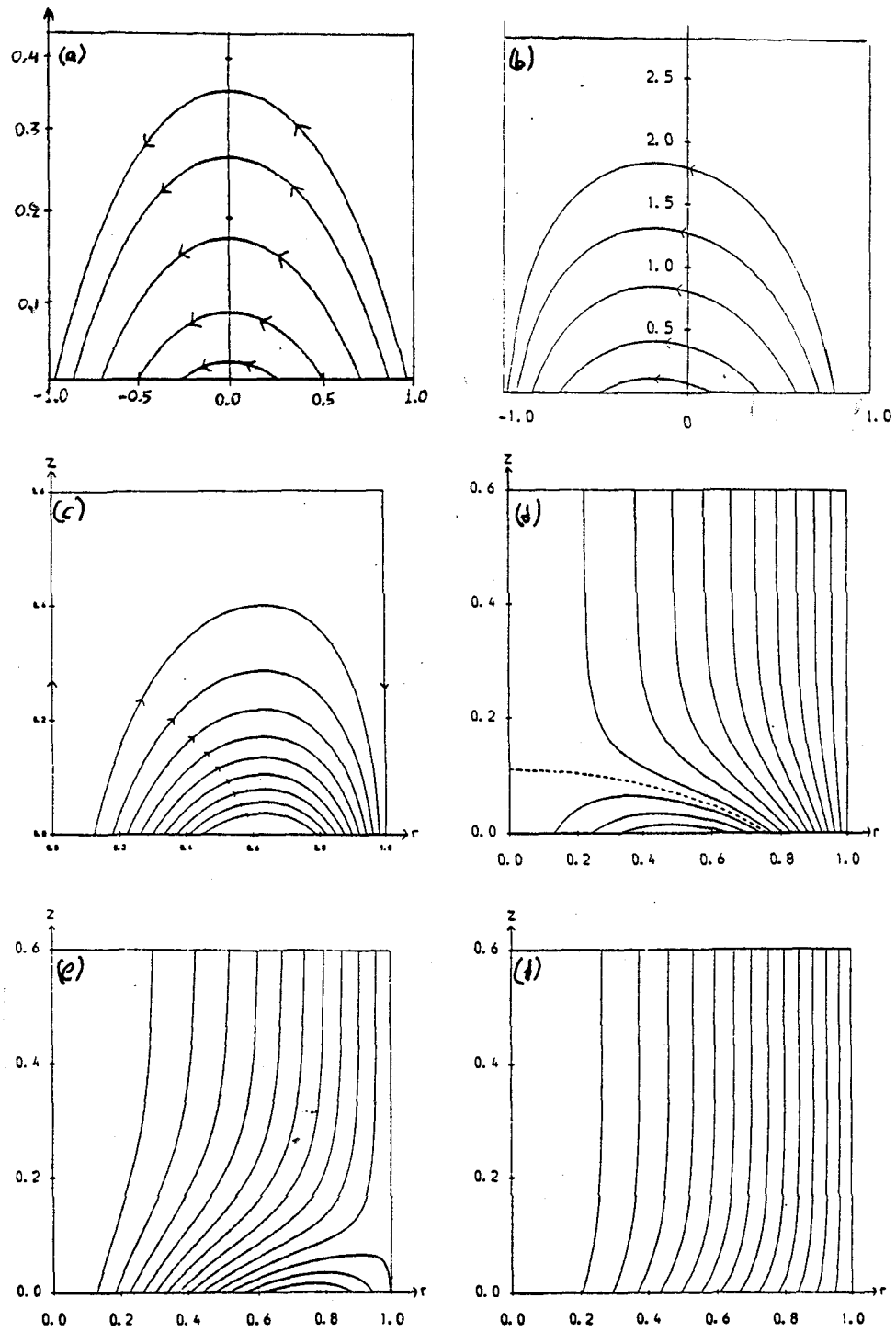

Figure 3.10: Possible magnetic topologies in cartesian coordinates, modeling (a) symmetric and (b) asymmetric arcades, and in cylindrical coordinates modeling (c) the sunspot field (closed fieldlines), (d) coronal streamers and (e) coronal holes (partially open fieldlines) and (f) emerging flux regions (open fieldlines) (de Ville 1990, 1991a,b,c).

$$-\frac{\Psi_A}{h_1h_2h_3}\left(\frac{\partial}{\partial x_1}\frac{h_2}{h_1h_3}\frac{\Psi_A}{4\pi\rho}\frac{\partial A}{\partial x_1}+\frac{\partial}{\partial x_2}\frac{h_1}{h_2h_3}\frac{\Psi_A}{4\pi\rho}\frac{\partial A}{\partial x_2}\right)\frac{\partial A}{\partial x_i}$$

$$+\frac{\partial \Pi}{\partial x_i}-\frac{V^2}{2}\frac{\partial \rho}{\partial x_i}-U\frac{\partial \rho}{\partial x_i}=\frac{1}{2h_3^2}\left(4\pi\rho\frac{\partial(h_3^2V_{x_3}^2)}{\partial x_i}-\frac{\partial(h_3^2B_{x_3}^2)}{\partial x_i}\right), \qquad (3.3.20)$$

and because the density is function of A only the transfield equation can be written as

$$\left(1-\frac{\Psi_A^2}{4\pi\rho}\right)\frac{1}{h_1h_2h_3}\left[\frac{\partial}{\partial x_1}\frac{h_2}{h_1h_3}\frac{\partial A}{\partial x_1}+\frac{\partial}{\partial x_2}\frac{h_1}{h_2h_3}\frac{\partial A}{\partial x_2}\right]$$

$$-\frac{1}{2h_3^2}\left[\frac{1}{h_1^2}\left(\frac{\partial A}{\partial x_1}\right)^2+\frac{1}{h_2^2}\left(\frac{\partial A}{\partial x_2}\right)^2\right]\frac{d}{dA}\left(\frac{\Psi_A^2}{4\pi\rho}\right)$$

$$+\frac{1}{2h_3^2}\frac{d}{dA}\left(\frac{G^2}{1-\Psi_A^2/4\pi\rho}\right)-U\frac{d\rho}{dA}+4\pi\rho\frac{d\Pi}{dA}=0, \qquad (3.3.21)$$

It is easy to see that the following choice, neglecting gravity ($U=0$),

$$\rho=\rho_0A^2 \qquad \Psi_A=\Psi_0A \qquad G=G_0A \qquad \Pi=\Pi_0A, \qquad (3.3.22)$$

reduces the above transfield equation to the linear elliptic equation

$$\frac{1}{h_1h_2h_3}\left[\frac{\partial}{\partial x_1}\frac{h_2}{h_1h_3}\frac{\partial A}{\partial x_1}+\frac{\partial}{\partial x_2}\frac{h_1}{h_2h_3}\frac{\partial A}{\partial x_2}\right]+k^2A=C, \qquad (3.3.23)$$

where ρ_0, Ψ_{A_0}, G_0, and Π_0 are constants, and

$$k=\frac{G_0}{1-M_{ao}^2}, \qquad C=-\frac{\Pi_0}{1-M_{ao}^2}, \qquad M_{a_o}^2=\frac{\Psi_0^2}{4\pi\rho}. \qquad (3.3.24)$$

Eq.(3.3.23) is easy to solve by separation of variables. de Ville and Priest did that in cartesian coordinates (de Ville & Priest 1990), modeling symmetric and asymmetric arcades (Figs.9a,b), and in cylindrical coordinates (de Ville & Priest 1991), modeling the magnetic structure of various features such as spots, plumes, coronal streamers (Figs.3.9c,d,e,f). Thus in cartesian coordinates the basic result is that the presence of a flow increases the summit height of the arcade compared with the static case. Increasing the flow speed will eventually cause the arcade to erupt. In the case of asymmetric arcades they can be model siphon flows driving by a non-zero footpoint pressure difference. In cylindrical geometry they found a wide range of possible magnetic topologies. The magnetic field may be closed, open (converging or diverging) or partially open (an arcade with an overlying field). The proportion of open fieldlines depends upon the flow of the plasma at the base of the region. Increasing the flow increases the number

of open fieldlines. Also increasing the twist component of the magnetic field imposed at the base results in the arcade of closed fieldlines rising, before it eventually erupts. From the other side the closed magnetic solutions could model the field above sunspot, with Evershed flow along fieldlines. Totally open magnetic field configurations can model emerging flux regions, while coronal streamers or coronal holes can be model using solutions consist of both open and closed regions of magnetic fieldlines. All the above solutions of course have the disavandange that the density is constant along fieldlines and the gravity is absent. Of course an obvious extension of this work is to include these parameters which we will do in the next chapters. Note that at least in cartesian coordinates, the influence of gravity can be taken into account leaving the above particular problem still analytically solvable.

We will close this chapter saying a few things about other causes of flows. For example downflows or upflows in both legs of a loop can be occur for example if for some reasons the heating or the length of the loop changed. From the scaling lows (3.2.7) we see that the summit density scales as $\rho_L \propto H^{4/7} L^{1/7}$ and if the heating or the length of the loop increases, this implies that the new equilibrium possess a higher density. To attain such equilibrium, extra material must be brought up or evaporated from below along the loop. Also if the heating or length are reduced in value, there is too much material in the loop for equilibrium, and some of it must drain down until the pressure gradient offsets gravity and all energy terms balance. The above mechanism has been invoked to describe the formation and the draining of some prominences. Other mechanisms which can be driven flows are the presence of various types of MHD waves and instabilities (Priest 1980,1984, Bray et al 1991).

Chapter 4

2-D LOW-β MHD EQUILIBRIA IN UNIFORM GRAVITY

4.1 Introduction

As we have discussed in the first chapter, it is known that the active region plasma is dynamic, with continual activity in the form of a wide range of flows, with very small Alfvén Mach numbers. At high temperatures *solar active regions* are seen to consist of *loops* with almost constant temperature, for a wide range of density. The magnetic field of an active region probably evolves slowly through a series of essentially stationary, mainly force-free states. As far as movement normal to the magnetic field is concerned, the plasma is completely dominated by the field, since the plasma β is usually much less than unity ($\approx 10^{-3}, 10^{-1}$) and the flow is subalfvénic. But, along the field, the plasma is observed to be in continuous motion rather than in a static state. Many type of flows are now observed, and are described in section 1.4.

However, as we saw in chapter 3, for the most part, the effect of the flow in the solar atmosphere has been neglected in theoretical models. From a theoretical point of view the flow in a loop can be regarded as a siphon flow which is driven by a pressure difference between the foot points. This was originally suggested by Meyer & Schmidt (1968) to explain Evershed motions, but it may also occur along coronal loops. If one starts with a static loop and switches on a pressure difference, then after several sound travel times a steady flow is established. In chapter 3 we discuss also how Cargill & Priest (1980) and Noci (1981) studied in detail the siphon flow, modeling the loop as a

rigid arch with a cross-sectional area that varies in a predescribed way. In this approach, which is valid in the limit $\beta \to 0$, lateral force-balance is neglected (no deformation of the field). Also, siphon flows in magnetic flux tubes has been investigated in the thin flux tube approximation by Thomas (1988), Montesinos & Thomas (1989), Thomas & Montesinos (1990,1991), and Degenhart (1991). Of course all these models are one-dimensional (all quantities depend only on the abscissa s along the loop) and do not take into account the lateral force balance between different streamlines. Finally, in an initial attempt to understand the role played by plasma flows in the equilibrium and stability properties of solar MHD structures, de Ville and Priest (de Ville 1990, de Ville & Priest 1991a,b,c) have recently presented exact solutions to the steady MHD equations in the absence of gravity. These solutions model incompressible flows along symmetric and nonsymmetric arcades of magnetic fieldlines.

In this chapter we study siphon flows in an isothermal magnetized atmosphere, taking into account the back reaction of the flow on the magnetic structure, and looking for as wide a class of boundary conditions as possible (Surlantzis et al 1993,1994). Since however, the solar situation is one of a small β plasma, we take advantage of the fact that the flow is subalfvénic but not necessarily subsonic to simplify the search for such solutions. In section 4.2 we present the equations of the model, and in sections 4.3 and 4.4 we discuss the properties of various solutions. Our main mathematical assumption is that there is an ignorable coordinate.

4.2 Low-β and low Alfvénic Mach number flows

In coronal loops and in chromospheric Evershed flow both the plasma β, and the Alfvén-Mach number M_a are less than unity. In this case the field is to the lowest order approximation force-free

$$(\nabla \times \mathbf{B_0}) \times \mathbf{B_0} = 0\,, \tag{4.2.1a}$$

$$\nabla \cdot \mathbf{B_0} = 0\,. \tag{4.2.1b}$$

The force-free structure is some sort of empty container which pressure, gravity and inertial forces perturb weakly. We expand the perfect MHD equations in β and M_a^2. The zeroth order gives Eq.(4.2.1a). Writing

$$\mathbf{B} = \mathbf{B_0} + \mathbf{B_1}\,, \tag{4.2.2}$$

where $\mathbf{B_1}$ is meant to be small, of order β or M_a^2 as compared to $\mathbf{B_0}$. In other words we have split the magnetic field as a sum of a force-free component $\mathbf{B_0}$, and a small

$\mathbf{B_1}$ component which is due to the influence (or back reaction) of the plasma. Thus, we get to first order, in these small plasma parameters

$$\nabla \cdot \mathbf{B_1} = 0\,, \tag{4.2.3a}$$

$$\nabla \cdot (\rho \mathbf{V}) = 0\,, \tag{4.2.3b}$$

$$\nabla \times (\mathbf{V} \times \mathbf{B_0}) = 0\,, \tag{4.2.3c}$$

$$\rho \mathbf{V} \cdot \nabla \mathbf{V} = -\nabla P + \frac{(\nabla \times \mathbf{B_0}) \times \mathbf{B_1}}{4\pi} + \frac{(\nabla \times \mathbf{B_1}) \times \mathbf{B_0}}{4\pi} + \rho \mathbf{g}\,. \tag{4.2.3d}$$

Thus, we have linearized the MHD equations with respect to the magnetic field, but not with respect to the flow variables, since we want to allow the field-aligned flow to be even strongly non linear. Of course this is a valid approach for $\beta << 1$ and the Alfvén number $M_a^2 << 1$. If the magnitude of the flow speed does not greatly exceed the sound speed V_s, $\beta << 1$ implies $M_a^2 << 1$ (note that $M_a^2 = \beta M^2/2$), so we shall refer to these conditions simply as $\beta << 1$.

Finally, we adopt an energy equation of the form

$$P = P(\rho)\,. \tag{4.2.3e}$$

So, Eqs.(4.2.3) constitute a closed system for P, ρ, $\mathbf{V}$ and $\mathbf{B_1}$. We stress again that the velocities are not so small as to ignore the left hand side term in Eq.(4.2.3d). We still have the plasma β, and the Alfvénic Mach number much less than unity.

4.3 Cartesian coordinates

We start our study by considering configurations with translational symmetry. The coordinate system is (x, y, z) wherein coordinate y is ignorable. The z-axis points in the opposite direction to the uniform acceleration of gravity $\mathbf{g}$. The general solution with translational symmetry of Eqs.(4.2.3a,b) can be written in terms of a vector potential y-component $A_1(x, z)$ and a stream function $\Psi(x, z)$ (which, as noted, are functions of x and z alone)

$$B_{1_z} = \frac{\partial A_1}{\partial x} \qquad B_{1_x} = -\frac{\partial A_1}{\partial z}\,, \tag{4.3.1}$$

$$\rho V_z = \frac{1}{4\pi}\frac{\partial \Psi}{\partial x} \qquad \rho V_x = -\frac{1}{4\pi}\frac{\partial \Psi}{\partial z}\,, \tag{4.3.2}$$

The general solution of Eq.(4.2.1b) is

$$B_{0_z} = \frac{\partial A_0}{\partial x}, \qquad B_{0_x} = -\frac{\partial A_0}{\partial z}\,. \tag{4.3.3}$$

where the vector potential y-component A_0 is also assumed to be function of x and z alone. Lines of constant $(A_0 + A_1)$ are field lines of the meridional field, while lines of constant Ψ are stream lines of the meridional flow. It is well known that the force-free condition (4.2.1a) can be written as

$$\nabla^2 A_0 + \frac{1}{2}\frac{dB_{0_y}^2(A_0)}{dA_0} = 0\,, \tag{4.3.4}$$

where $B_{0_y}(A_0)$ is the component of the magnetic field in the ignorable direction which must be a function of A_0 only.

Following the formalism of Tsinganos (1982) we write the Eqs.(4.2.3c,d) in Jacobian notation,

$$\{\Psi, A\} = \frac{\partial \Psi}{\partial z}\frac{\partial A}{\partial x} - \frac{\partial \Psi}{\partial x}\frac{\partial A}{\partial z}\,. \tag{4.3.5}$$

$\{\Psi, A\} = 0$ means that $\nabla\Psi$ and ∇A are parallel, Ψ and A being both constants on the same lines in the x-z plane.

The x and z-components of the induction equation (4.2.3c), yield after simple algebra

$$\{\Psi, A_0\} = 0 \qquad \Longleftrightarrow \qquad \Psi = \Psi(A_0)\,. \tag{4.3.6}$$

Then the mass flux can be written as

$$\rho\mathbf{V} = \left(-\frac{\Psi_{A_0}}{4\pi}\frac{\partial A_0}{\partial z}, \rho V_y, \frac{\Psi_{A_0}}{4\pi}\frac{\partial A_0}{\partial x}\right)\,, \tag{4.3.7}$$

where $\Psi_{A_0} = d\Psi/dA_0 = \Psi_{A_0}(A_0)$.

The y-component of the induction equation gives

$$\{V_y, A_0\} - \{B_{0_y}/4\pi\rho, \Psi\} = 0\,, \tag{4.3.8}$$

or equivalently

$$V_y - \frac{\Psi_{A_0}}{4\pi\rho}B_{0_y} = \Phi_{A_0} = \Omega(A_0)\,, \tag{4.3.9}$$

where $\Omega(A_0)$ is a function of A_0 related to the induction potential $\mathbf{V} \times \mathbf{B_0} = \nabla\Phi$ and the subscript A_0 in functions Ψ and Φ denotes the derivative with respect to their argument A_0. In cylindrical geometry Eq.(4.3.9) is usually referred to as the isorotation law (Ferraro, 1966). In translational symmetry it means that the motion in the symmetry direction is made of a field-aligned flow plus a translation of each magnetic surface in the invariant direction.

From the y-component of the momentum balance equation we get

$$\Psi_{A_0}\{V_y, A_0\} = \{B_{0_y}, A_1\} + \{B_{1_y}, A_0\}\,. \tag{4.3.10}$$

Note that

$$\{B_{0_y}, A_1\} = -\frac{dB_{0_y}}{dA_0}\{A_1, A_0\}\,, \tag{4.3.11}$$

so Eq.(4.3.10) is written as

$$B_{1_y} - \Psi_{A_0} V_y = \frac{dB_{0_y}}{dA_0} A_1 + G_1(A_0)\,. \tag{4.3.12}$$

where $G_1(A_0)$ is a function of A_0 only. Eq.(4.3.12) expresses force balance in the ignorable direction.

From Eqs.(4.3.9) and (4.3.12) we have the following expressions for the field and velocity components in the ignorable direction in terms of the perturbed potential

$$V_y = \Omega + \frac{\Psi_{A_0}}{4\pi\rho} B_{0_y}\,, \tag{4.3.13}$$

$$B_{1_y} = \frac{{\Psi_{A_0}}^2}{4\pi\rho} B_{0_y} + \Psi_{A_0}\,\Omega + \frac{dB_{0_y}}{dA_0} A_1 + G_1\,. \tag{4.3.14}$$

It is easy to see from Eqs.(4.3.7, 4.3.13) that when the flow is field aligned (with respect to the $\mathbf{B_0}$ field), we have $\Omega = 0$. Then,

$$4\pi\rho\mathbf{V} = \Psi_{A_0}\mathbf{B_0}\,. \tag{4.3.15}$$

Here we consider this case. Thus the function Ψ_{A_0} is simply the ratio of the mass flux to the magnetic flux. If Ω were not zero, magnetic surfaces would glide on each other in the direction of invariance.

The momentum balance equation can be written as

$$\nabla E = \frac{(\nabla \times \mathbf{B_0}) \times \mathbf{B_1}}{4\pi\rho} + \frac{(\nabla \times \mathbf{B_1}) \times \mathbf{B_0}}{4\pi\rho} - (\nabla \times \mathbf{V}) \times \mathbf{V}\,, \tag{4.3.16}$$

where

$$E = \int \frac{dP}{\rho} + gz + \frac{V^2}{2}\,. \tag{4.3.17}$$

Since the Lorentz force has no component along the lines of magnetic force and since $\mathbf{V}$ is parallel to $\mathbf{B_0}$ we have,

$$B_0 \cdot \nabla E = 0\,, \tag{4.3.18}$$

which can be written in Jacobian notation as $\{E, A_0\} = 0$ so,

$$\int \frac{dP}{\rho} + gz + \frac{V^2}{2} = E(A_0)\,, \tag{4.3.19}$$

where $E(A_0)$ is another function of A_0 denoting the energy flux density per unit of mass flux density. Eq.(4.3.19) is the Bernoulli equation for each stream line. Physically it expresses that the sum of the thermal (enthalpy per unit mass), kinetic and potential energy flux densities per unit of mass flux density is constant along each streamline, a result which is simply the consequence of the time independence of the equations.

Now the remaining x and z-components of the momentum balance equation can be written

$$\frac{\partial A_0}{\partial z}\left[\nabla^2 A_1 + \nabla^2 A_0 - \Psi_{A_0}\left(\frac{\partial}{\partial x}\frac{\Psi_{A_0}}{4\pi\rho}\frac{\partial A_0}{\partial x} + \frac{\partial}{\partial z}\frac{\Psi_{A_0}}{4\pi\rho}\frac{\partial A_0}{\partial z}\right)\right] + 4\pi\rho\frac{\partial E}{\partial z} = \left[2\pi\rho\frac{\partial V_y^2}{\partial z} - \frac{\partial(B_{0_y}B_{1_y})}{\partial z}\right], \tag{4.3.20}$$

together with a similar equation where x replaces z and vice-versa. Use is then made of Eqs.(4.3.4), (4.3.13), (4.3.14), (4.3.19). Writing these equations in (x,A_0) and (z,A_0) coordinates and transforming the partial derivatives with respect to A_0 to derivatives of suitable functions of A_0 alone, they reduce to the following equation for $A_1(x,z)$

$$\nabla^2 A_1 + \frac{1}{2}\frac{d^2(B_{0_y}^2)}{dA_0^2}A_1 = \Psi_{A_0}\left[\frac{\partial}{\partial x}\frac{\Psi_{A_0}}{4\pi\rho}\frac{\partial A_0}{\partial x} + \frac{\partial}{\partial z}\frac{\Psi_{A_0}}{4\pi\rho}\frac{\partial A_0}{\partial z}\right] - \frac{d(B_{0_y}G_1)}{dA_0} - \frac{1}{8\pi\rho}\frac{d(B_{0_y}^2\Psi_{A_0}^2)}{dA_0} - 4\pi\rho\frac{dE}{dA_0}. \tag{4.3.21}$$

This is a linear equation in A_1 of Poisson type, the right hand-side is known from A_0 (initial force-free field) wherein ρ is obtained from Bernoulli equation (4.3.19) for the zeroth order field. In other words Eqs.(4.3.19) and (4.3.21) describe respectively the field-aligned flow and the perturbed magnetic structure. Eq.(4.3.21) could be derived as well by performing a linearization in β and in M_a^2 on the general transfield equation which describes such flows. In appendix A we have done this in a general coordinate system. A number of the original equations have been absorbed into the first integrals represented by Ψ (which expresses mass conservation), B_{0_y} and G_1 (which stem from the force balance equation in the ignorable coordinate), and E which expresses energy conservation. These functions must be defined by consideration of the boundary conditions or criticality conditions as we shall see.

In summary the unperturbed magnetic field $\mathbf{B_0}$ is defined by the force-free equilibrium, Eq.(4.3.4). With this, the perturbed magnetic field $\mathbf{B_1}$ is found from the linearized transfield equation, Eq.(4.3.21), the velocity field from the mass flux conservation, Eq.(4.3.15), and the density from the Bernoulli equation (4.3.19). In practice, we solve first the Bernoulli equation (4.3.19) obtaining the density $\rho(x,z)$ and then we solve Eq.(4.3.21) which is linear in A_1.

4.4 Flows in Current-free Fields

As an example we analyze flows in an initial potential field $\mathbf{B_0}$ wherein $B_{0_y}(A_0) = 0$. In this case, the general form of A_0 (solution of $\nabla^2 A_0 = 0$ vanishing as $z \to \infty$) is written as

$$A_0 = \sum_{i=0}^{\infty} \left[c_i \cos\left(\frac{q_i x}{2L}\right) + d_i \sin\left(\frac{q_i x}{2L}\right) \right] e^{-\frac{q_i z}{2L}}, \tag{4.4.1}$$

where L is a typical scale height of the system.

We assume that each field line has a uniform temperature $T(A_0)$. This is because we want our assumptions to remain valid at large z. A consideration of the Bernoulli equation under Eq.(4.2.3e) shows that for the density to approach zero as $z \to \infty$ the specific enthalpy must scale like $\ln \rho$ which means that the gas should be isothermal at large heights.

Let $V_s(A_0)$ and $V_{s\infty}$ be respectively the sound speed on the field line A_0 and at infinity, and let $\tau(A_0) = T(A_0)/T_\infty$ be the dimensionless temperature. Then on each field line we have an isothermal equation of state,

$$P = V_s^2 \rho = \tau(A_0) V_{s\infty}^2 \rho . \tag{4.4.2}$$

We define the scale height $L = V_{s\infty}^2/g$ and the Mach number $M = V/V_s$. The Bernoulli equation (4.3.19) then writes,

$$\ln \frac{\rho}{\rho_*} + \frac{z}{\tau L} + \frac{M^2}{2} = \frac{E(A_0)}{V_s^2}, \tag{4.4.3}$$

where ρ_* is a characteristic density (see Eq.4.5.2).

We suppose that there is no electric field [if $\Omega = 0$ then $\mathbf{V}$ is given by Eq.(4.3.15)] which means that the flow is field aligned with respect to $\mathbf{B_0}$. Because $B_{0_y} = 0$, Eq.(4.3.21) for A_1 simplifies to,

$$\nabla^2 A_1 = \Psi_{A_0} \left[\frac{\partial}{\partial x} \frac{\Psi_{A_0}}{4\pi\rho} \frac{\partial A_0}{\partial x} + \frac{\partial}{\partial z} \frac{\Psi_{A_0}}{4\pi\rho} \frac{\partial A_0}{\partial z} \right] - 4\pi\rho \frac{dE}{dA_0}, \tag{4.4.4}$$

where the density is found from Eq.(4.4.3).

For Eq.(4.4.4) to have a well behaved solution for $z > 0$, the first-integrals $\Psi_{A_0}(A_0)$ and $E(A_0)$ cannot be arbitrary. We are restricted here to solutions wherein the density, pressure, velocity and the plasma β tend to zero at very large heights ($z \to \infty$). Thus the right hand side term of Eq.(4.4.4) should approach to zero at large z in order to have asymptotically a potential field.

Let $\xi = min[q_i]$, $i = 1, 2, 3, ...$ For $z \to \infty$, where $M \to 0$, the potential field goes with height like $A_0 \propto e^{-\frac{\xi z}{2L}}$, while the density from Eq.(4.4.3) goes like $\rho \propto e^{-\frac{\xi z}{L}}$. Thus, the plasma β behaves at large heights as

$$\beta = \frac{8\pi\rho V_s^2}{B_0^2} \propto e^{(\xi-1)z/L} . \tag{4.4.5}$$

Thus, we conclude that the stratification parameter for the magnetic field must be $\xi < 1$ for β to remain finite at large z, as assumed and as it seems to be the case in the corona. For $\xi > 1$, the magnetic field at large heights would not be strong enough to confine the plasma and a wind would be present.

4.5 Flows in a simple arcade.

Let us take the simplest current-free field as the unperturbed configuration in Cartesian coordinates zxy,

$$A_0(x, z) = A_* \cos\left(\frac{\xi x}{2L}\right) e^{-\frac{\xi z}{2L}} . \tag{4.5.1}$$

This is defined in the strip $|x| \leq \pi L/\xi, z \geq 0$, with $\xi < 1$. The field strength B_0, which depends in this special case only from the height z, is

$$B_0(x, z) = \frac{A_* \xi}{2L} e^{-\frac{\xi z}{2L}} . \tag{4.5.1b}$$

The temperature T_∞ (or equivalently the sound speed at infinity height $V_{s\infty}$) is taken as reference and equal to 1.6×10^6 K (typical for the quiet solar corona) and $L = 80,000$ km.

4.5.1 Adimensionalization.

It is convenient to define the following dimensionless variables in terms of the characteristic length L, temperature T_∞, Alfvén velocity V_a and the sound velocity V_s,

$$\mathrm{x} = \frac{\xi x}{L}, \quad \mathrm{z} = \frac{\xi z}{L}, \quad \varrho = \frac{\rho}{\rho_*}, \quad M = \frac{V}{V_s}, \quad M_A^2 = \frac{{\Psi_{A_0}}^2}{4\pi\rho} ,$$

$$B_* = \frac{A_* \xi}{L}, \quad V_* = \frac{\Psi_{A_0 *} B_*}{4\pi\rho_*}, \quad M_* = \frac{V_*}{V_{s\infty}}, \quad M_{A^*}^2 = \frac{{\Psi_{A_0 *}}^2}{4\pi\rho_*} ,$$

$$\alpha(a_0) = \frac{\Psi_{A_0}(A_0)}{\Psi_{A_0 *}(A_0^*)}, \qquad \epsilon(a_0) = \frac{2}{V_*^2} E(A_0), \qquad \tau(a_0) = \frac{T(A_0)}{T_\infty} ,$$

$$a_0(\mathrm{x},\mathrm{z}) = \frac{A_0(x,z)}{A_*}, \qquad b_0(\mathrm{x},\mathrm{z}) = \frac{B_0(x,z)}{B_*}, \qquad a_1(\mathrm{x},\mathrm{z}) = \frac{1}{M_{A^*}^2}\frac{A_1(x,z)}{A_*}, \quad (4.5.2)$$

where the superscript $*$ refers to fiducial values. Eqs.(4.4.3) and (4.4.4) can be written in dimensionless form

$$\tau \ln \varrho + \frac{\mathrm{z}}{\xi} + \frac{M_*^2\alpha^2 b_0^2}{2\varrho^2} = \frac{M_*^2}{2}\epsilon(a_0)\,, \quad (4.5.3)$$

$$\nabla^2 a_1 = \alpha\left[\frac{\partial}{\partial \mathrm{x}}\frac{\alpha}{\varrho}\frac{\partial a_0}{\partial \mathrm{x}} + \frac{\partial}{\partial \mathrm{z}}\frac{\alpha}{\varrho}\frac{\partial a_0}{\partial \mathrm{z}}\right] - \frac{\varrho}{2}\frac{d\epsilon}{da_0}\,. \quad (4.5.4)$$

This is a Poisson equation in the half strip $|\mathrm{x}| \leq \pi$, $\mathrm{z} \geq 0$ with homogeneous Dirichlet boundary conditions (because the magnetic flux distribution is supposed not to be altered at the boundary). The appropriate Green function is given in Appendix B. These two equations for ϱ and a_1 contain three free functions $\alpha(a_0)$, $\epsilon(a_0)$ and $\tau(a_0)$ which relate to the boundary conditions (section 4.5.3).

4.5.2 Topology of the solutions

Before solving Eqs.(4.5.3,4.5.4) it is useful to focus our attention to the Bernoulli equation which can be written for a given field line (a_0 = const.) in terms of the Mach number M of the flow

$$-\ln M + \frac{M^2}{2} + \left(\frac{1}{\xi\tau} - \frac{1}{2}\right)z = \text{constant}\,, \quad (4.5.5)$$

By taking the differential of the above equation we find that we have a critical point at $M = 1$ where $d\mathrm{z}/d\mathrm{x} = 0$ (at the top of the field line). The physical meaning of this critical point can be seen better, if we write Eq.(4.5.5) as

$$-\ln M + \frac{M^2}{2} - \left(1 - \frac{2}{\xi\tau}\right)\ln\left(\cos\frac{\mathrm{x}}{2}\right) = \text{constant}\,. \quad (4.5.6)$$

because to a first approximation the equation for each field line is $\mathrm{z} = 2\ln[\cos(\mathrm{x}/2)/a_0]$ (the unperturbed magnetic field $\mathbf{B_0}$). This equation is identical with the Bernoulli equation in ordinary tubes if the effective cross-section of which would vary with x as

$$S(\mathrm{x}) = 2\cos^{1-\frac{2}{\xi\tau}}\left(\frac{\mathrm{x}}{2}\right). \quad (4.5.7)$$

The term 1 of the power is due to the actual flux tube geometry, while the term $-2/\xi\tau$ is due to gravity. For $\xi\tau < 2$ the critical point is of the X-type (the effective cross section has a minimum) and for $\xi\tau > 2$ it is of the O-type (the effective cross section

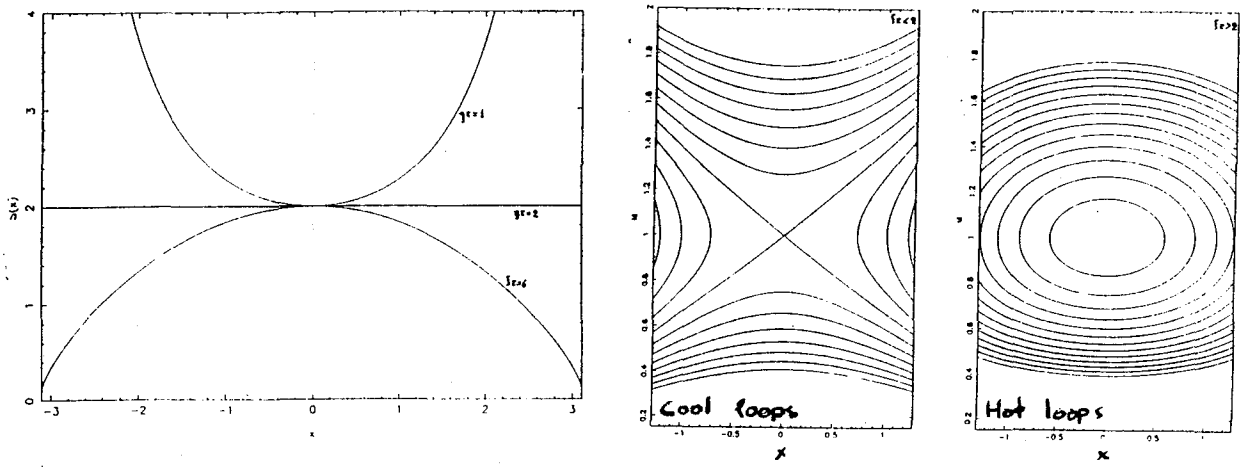

Figure 4.1: *(a) The variation of the effective cross section Eq.(4.5.7) with the horizontal distance* x *for three values of* $\xi\tau = 1, 2$ *and* 6. *(b) Topology of the Bernoulli equation (4.5.5) for* $\xi\tau = 1$ *and* 6.

has a maximum). If $\xi\tau = 2$ the effective cross section is constant along each field line (Fig.4.1a).

Thus, the whole discussion for de Laval nozzles (chapter 3) is valid and we have that for $\xi\tau > 2$ (*hot loops*) only subsonic solutions are possible, if boundary conditions forbid the flow to be supersonic at the base of the loop, which we assume. But for $\xi\tau < 2$ (*cool loops*) either subsonic or transonic solutions with shocks are allowed. When $\xi\tau = 2$ obviously the velocity is constant throughout the field lines (Fig.4.1b).

Because of the symmetry of the problem, in the subsonic cases the pressures at both foot points of the same field line are always equal. Only in the case of transonic solutions are the pressures unequal because of the presence of a shock (the plasma flows from the high pressure to the lower pressure foot point).

4.5.3 The integrals $\alpha(a_0)$, $\epsilon(a_0)$ and $\tau(a_0)$.

In order to solve Eqs.(4.5.3,4.5.4) we must prescribe the functional forms of $\alpha(a_0)$, $\epsilon(a_0)$ and $\tau(a_0)$. These functional forms correspond to the boundary conditions at the photospheric level (z = 0) of the system of Eqs.(2.3) for the mass flux, energy input and the temperature distribution. A solution of the Bernoulli equation must exist at all points of the strip for the chosen $\alpha(a_0)$, $\epsilon(a_0)$ and $\tau(a_0)$ functions. For $\xi\tau < 2$ (X-type topology), this is not so, if the resulting initial velocities (at z = 0) correspond to solutions having a turning point (the velocity has two possible values for a given

position x). For $\xi\tau > 2$ (O-type topology) the appropriate condition is that the velocity at z = 0 be always subsonic for any x (Fig.4.1). Finally the choose of the function $\tau(a_0)$ corresponds to the temperature distribution across field lines.

In the subsonic case, regarding Eq.(4.3.15) at z = 0 for given $\alpha(a_0)$, we see that if we give the boundary distribution of the density (or pressure) for example, automatically the velocity distribution is determined. In transonic cases, a shock is present and we have another free function which is the post-shock temperature (see section 4.5.5), or equivalently the distribution of the postshock pressure at z = 0.

4.5.4 Subsonic flows.

Having in mind that we want to construct solutions for coronal loops we split the functions $\alpha(a_0)$, $\epsilon(a_0)$, $\tau(a_0)$ in two components as follows

$$\alpha(a_0) = \alpha^{\rm in}(a_0) + \alpha^{\rm out}(a_0)\,, \tag{4.5.8a}$$

$$\epsilon(a_0) = \epsilon^{\rm in}(a_0) + \epsilon^{\rm out}(a_0)\,, \tag{4.5.8b}$$

$$\tau(a_0) = \tau^{\rm in}(a_0) + \tau^{\rm out}(a_0)\,, \tag{4.5.8c}$$

The functions with superscripts "in" refer to the region inside the loop (either with flows or not), and the functions with superscripts "out" define the values of its environment. (no flow). The choice of all functions must be such that the functions α, ϵ, τ and their first derivatives are continuous (because the first derivatives are present in Eq.4.5.4).

We can assume for the environment a uniform temperature $T^{\rm out}(a_0) = T_\infty = 1.6 \times 10^6\ K$ and magnetostatic equilibrium, $\alpha^{\rm out}(a_0) = 0$. The functional form of $\epsilon^{\rm out}(a_o)$ reflects the distribution of the environmental density at z = 0, since from Eq.(4.5.3) we have

$$\ln \varrho = \frac{M_*^2}{2}\epsilon^{\rm out}(a_0)\,. \tag{4.5.9}$$

For the internal loop structure we have assumed the following profiles

$$\alpha^{\rm in}(a_0) = \alpha^{\rm out} + \alpha^{\rm max}\sin^{N_\alpha}\left(\pi\frac{a_0 - a_{0f}}{a_{0i} - a_{0f}}\right), \tag{4.5.10a}$$

$$\epsilon^{\rm in}(a_0) = \epsilon^{\rm out} + \epsilon^{\rm max}\sin^{N_\epsilon}\left(\pi\frac{a_0 - a_{0f}}{a_{0i} - a_{0f}}\right), \tag{4.5.10b}$$

$$\tau^{\rm in}(a_0) = \tau^{\rm out} + \tau^{\rm max}\sin^{N_\tau}\left(\pi\frac{a_0 - a_{0f}}{a_{0i} - a_{0f}}\right), \tag{4.5.10c}$$

where a_{0i} and a_{0f} are the field lines defining the boundary of the loop. The first derivatives of the above functions are non singular only if $N_\alpha, N_\epsilon, N_\tau > 1$.

It is worth to compare the solution obtained with flow $[\alpha^{\rm in}(a_0) \neq 0]$ with a static solution $[\alpha^{\rm in}(a_0) = 0]$ having the same boundary conditions (temperature, density, pressure and vertical magnetic field component) at the base (z = 0). This implies that $a_0^{\rm static}(\mathbf{x},0) = a_0^{\rm flow}(\mathbf{x},0)$, $\tau^{\rm static}(a_0) = \tau^{\rm flow}(a_0)$ and that $\epsilon^{\rm static}(a_0)$ is given as function of $\epsilon^{\rm flow}(a_0)$ as follows. From Eq.(4.3.4) we have,

$$\ln \varrho^{\rm flow} + \frac{\mathrm{z}}{\xi\tau} + \frac{M^2}{2} = \frac{M_*^2 \epsilon^{\rm flow}(a_0)}{2}, \tag{4.5.11}$$

$$\ln \varrho^{\rm static} + \frac{\mathrm{z}}{\xi\tau} = \frac{M_*^2 \epsilon^{\rm static}(a_0)}{2}. \tag{4.5.12}$$

Then $\varrho^{\rm static} = \varrho^{\rm flow}$ at z = 0 if $\epsilon^{\rm static}(a_0) = \epsilon^{\rm flow}(a_0) - M_{\rm foot}^2/M_*^2$. At a given height z, the ratio between the densities becomes

$$\frac{\varrho^{\rm flow}}{\varrho^{\rm static}} = e^{-\frac{M^2 - M_{\rm foot}^2}{2}}. \tag{4.5.13}$$

In Figs.(4.2a,b) we present two typical loop structures for $\xi = 0.9$. In Fig.(4.2a) the flows are absent. We have chosen the parameters for the functions in Eqs.(4.5.10) such as to have equal densities at the foot points in each case (Eq.4.5.13). The maximum temperature inside the loop is 2.1×10^6 K ($\tau^{\rm max} = 0.3$) and we see that because throughout the loop $\xi\tau < 2$ the variation of the density along the field lines is larger in the loop with flows in Fig.(4.2b), so the density decrease is steeper than the classical exponential density decrease e^{-gz/V_s^2}. The ratio of the densities of the two loops at the same height is in the range $0.6 < e^{-(M^2 - M_{\rm foot}^2)/2} < 1$ because the gas accelerates towards the top of the loop ($M > M_{\rm foot}$). *Thus in cool loops, the flows cause the density to drop faster along fieldlines in comparison to the static case.*

If the loop temperature is very high this effect is reversed. In Figs.(4.3a,b) where the temperature is 7.2×10^6 K ($\tau^{\rm max} = 3.5$) the gas decelerates at the top ($M < M_{\rm foot}$), so the density falls off more slowly than in a static loop. The ratio of the densities at the same height are in the range $1 < e^{-(M^2 - M_{\rm foot}^2)/2} < 1.65$. There are cases, as in Fig.(4.3b) when the effects of flows are so strong that the maximum density is not at the foot points but at a certain height. There may exist sufficiently hot (or small) loops where the flows are strong enough to bring the maximum of the density at the loop top! *Thus in hot loops with flows the density drops slower or increases with height along fieldlines compare to the static case.*

Also, from Fig.(4.1b) we may be explain why strong flows are present only in cool loops (section 1.4). If we accept the extreme case that in the footpoints of the hot and cool loops (of the same geometrical properties) the velocities are the same, then in cool loops the flow speed increases with height reaching its maximum at the top (the

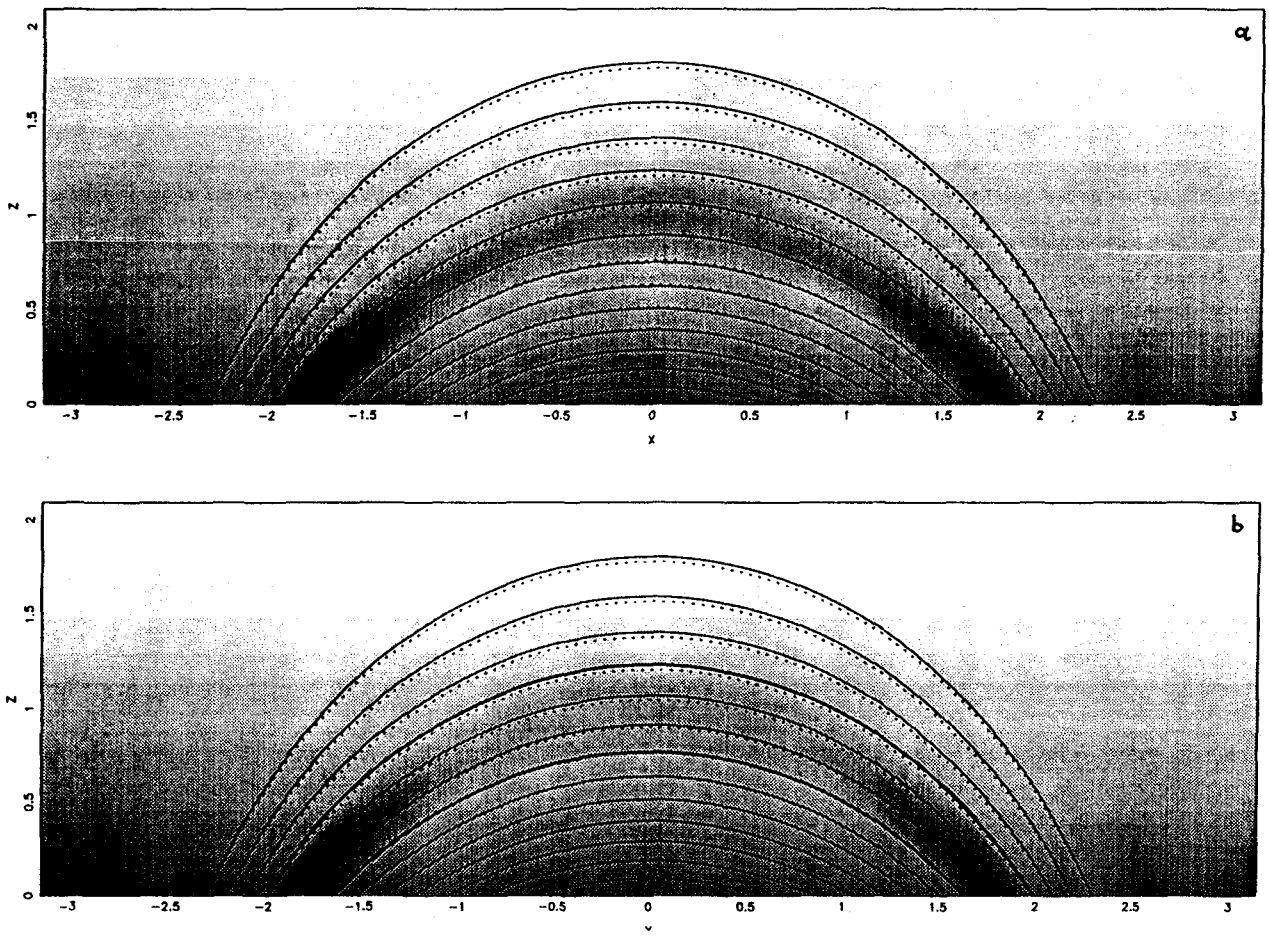

Figure 4.2: *Typical structure for a moderate hot loop ($\xi\tau < 2$) with an unperturbed magnetic field given by Eqs.(4.5.1). (a) static loop ($\alpha^{\max} = 0.$) and (b) loop with flows ($\alpha^{\max} = 1.1$, $\epsilon^{\max} = 0.6$). The profile of the functions α, ϵ, τ are given by Eqs.(4.5.8,4.4.10) with $N_\alpha = N_\epsilon = N_\tau = 1.1$ and $\tau^{\max} = 0.3$. The vertical field component, the temperature and the density are the same at the base (z = 0) in both cases. Continuous lines represent the field lines of the initial current-free configuration, while the doted lines the final magnetic structure. The grey levels are proportional to the density. In these solutions, where $\xi\tau < 2$ is satisfied everywhere, the density along the loop drops faster with height in the presence of flows as compared to the static case.*

left topology of the Fig.4.1), while in hot loops decreases (the right topology of the Fig.4.1). Thus, *in cool loops the flows will be appear stronger compare to the hot ones.*

In the static case the shape of field lines depends on the gradient of pressure which push either inwards or outwards. With flows, the centrifugal forces, which push outwards, are also present. Thus the field lines are pushed "locally" in order to balance the hydrodynamic and hydrostatic gas effects. These effects remain small when the Alfvénic Mach number is low.

4.5.5 Transonic flows.

For $\xi\tau < 2$ a pressure difference imposed at the foot points of each field line, forces the flow to become supersonic at the summit (where the effective cross section $S(\mathrm{x})$, Eq.(4.5.7), is minimum). In order to become subsonic again at the other foot point it must be decelerated through a shock that is located at some position downflow. But to first become supersonic, the flow must pass through a critical point on the field line (a_0), and the function $\alpha(a_0)$ must then be related to the function $\epsilon(a_0)$. Putting the partial derivative with respect to ϱ of the left hand side of Eq.(4.5.3) to zero, we see that the requirement $M = 1$ at the summit ($\mathrm{x} = 0, \mathrm{z} = -2\ln a_0$ where $S(\mathrm{x}) = S_{\min} = 2$) is equivalent to the following relation (criticality condition)

$$\epsilon(a_0) = \frac{2\tau}{M_*^2}\left[\frac{1}{2} + \ln\frac{M_* {a_0}^{1-\frac{2}{\xi\tau}}\alpha}{S_{\min}\sqrt{\tau}}\right]. \tag{4.5.14}$$

This condition imposed at the upstream foot point of a field line implies that the solution is transonic on it. It is physical to suppose the existence of subsonic flows in field lines around a 'transonic core'. In the transonic region, the temperature is $\tau_1(a_0)$ before the shock front. After, it is $\tau_2(a_0)$, a function determined by boundary conditions on the downstream foot point, mainly by the value of the pressure there. The boundary condition $\tau_2 = \tau_1$ must be also satisfied at those field lines that make the boundary between the transonic and subsonic layer. In the following we shall for simplicity prescribe the profile of the post-shock temperature $\tau_2(a_0)$ and deduce the associated pressure at the downstream footpoint.

The conditions at the shock front are that the mass flux, the energy flux, the normal component of the magnetic field, and the momentum flux must be continuous (Landau & Lifshitz 1960). Because we are in the ideal MHD context we must have also that the tangential component of the electric field from induction equation must be continuous. If we denote with indices n and t the directions normal and tangential to the vector which is perpendicular to the shock front we have

$$[\rho V_n] = 0\,, \tag{4.5.15a}$$

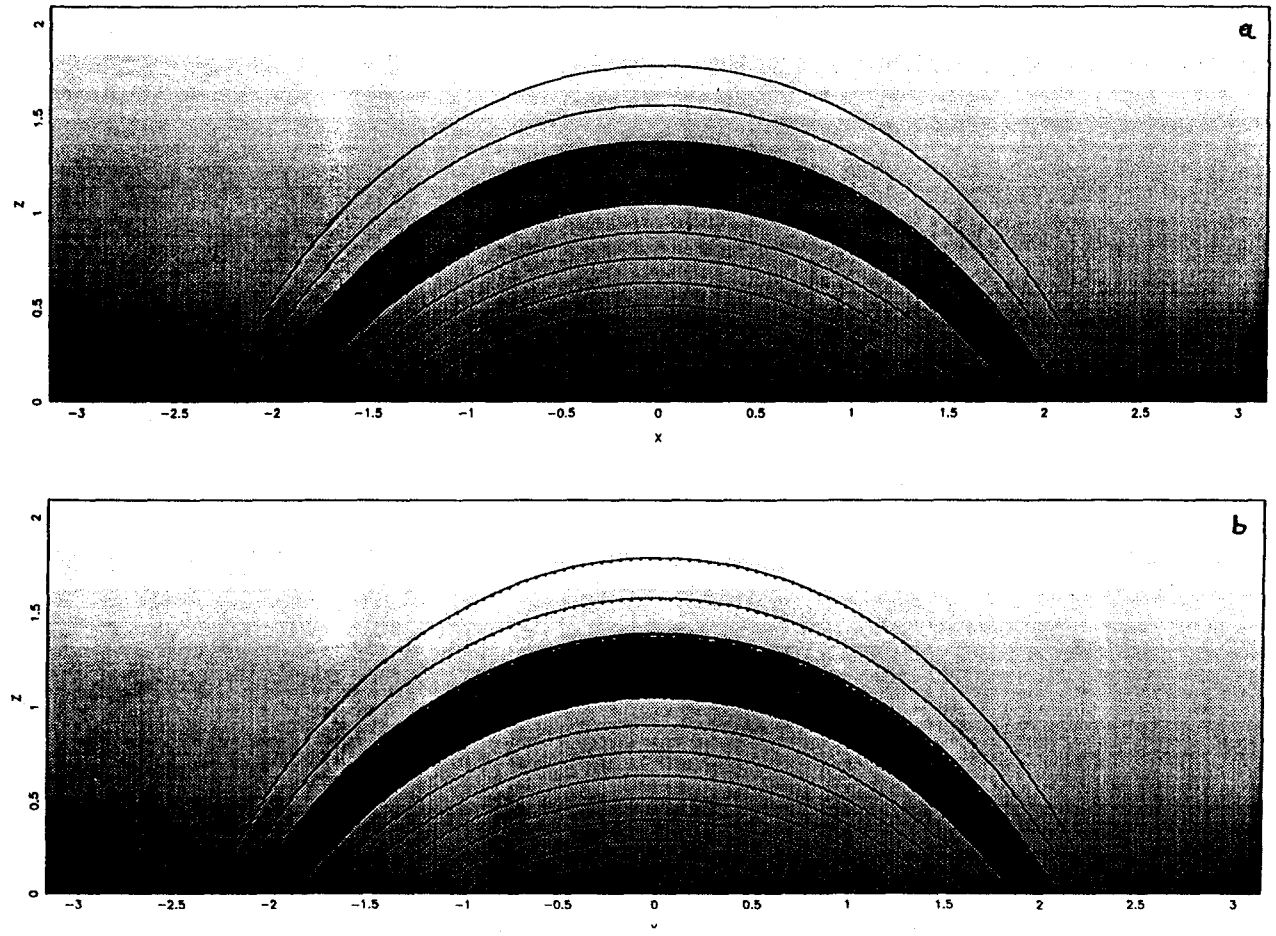

Figure 4.3: *Typical structure for a very hot loop ($\xi\tau > 2$) with an unperturbed magnetic field $\mathbf{B_0}$ given by Eqs.(4.4.1). (a) static loop ($\alpha^{\max} = 0.$) and (b) loop with flows ($\alpha^{\max} = 2.7$, $\epsilon^{\max} = 1.83$). The functions α, ϵ, τ are almost constant inside the loop, and its temperature is 7.2×10^6 K ($\tau^{\max} = 3.5$). The vertical field component, the temperature and the density are the same at the base (z = 0) in both cases. The drawing conventions are the same as in Figs.(4.2). In these solutions, where $\xi\tau > 2$ is satisfied in the region of strong flows, the density is larger in the presence of flows (b) than without (a). Then the maximum density is not at the foot points but above them.*

$$\left[\rho V_n\left(h+\frac{V^2}{2}\right)+\frac{V_n B^2}{4\pi}-\frac{B_n \mathbf{V}\cdot\mathbf{B}}{4\pi}\right]=0\,, \tag{4.5.15b}$$

$$[B_n]=0\,, \tag{4.5.15c}$$

$$\left[P+\rho V_n^2+\frac{B_t^2-B_n^2}{8\pi}\right]=0\,, \tag{4.5.15d}$$

$$\left[\rho V_n V_t-\frac{B_n B_t}{4\pi}\right]=0\,, \tag{4.5.15e}$$

$$[V_n B_t - V_t B_n]=0\,, \tag{4.5.15f}$$

where h is the enthalpy per unit mass and [ ] means the difference between the up- and down-stream values at the shock position. The two first conditions are automatically satisfied if the functions $\Psi_{A_0}(A_0)$ and $E(A_0)$ are identical before and after the shock front (the second because we assume that $\mathbf{V}//\mathbf{B_0}$ so the Poynting flux term is zero). Obviously, the continuity of the tangential component of the electric field is satisfied. The remaining three conditions yield to first order in β and M_a^2

$$[B_{1_n}]=0\,, \tag{4.5.16a}$$

$$\left[P+\rho V_n^2\right]+\frac{B_{0_t}}{4\pi}[B_{1_t}]=0\,, \tag{4.5.16b}$$

$$[\rho V_n V_t]-\frac{B_{0_n}}{4\pi}[B_{1_t}]=0\,, \tag{4.5.16c}$$

because both B_{0_n} are B_{0_t} are continuous. Using the continuity of ρV_n and $\mathbf{V}//\mathbf{B_0}$, Eq.(4.5.16c) becomes

$$\left[\rho V_t^2\right]-\frac{B_{0_t}}{4\pi}[B_{1_t}]=0\,. \tag{4.5.17}$$

Combining Eqs.(4.5.15b,d) we get

$$[P+\rho V^2]=0\,. \tag{4.5.18}$$

This equation gives the shape of the shock since it holds only at a single point on each field line. The Bernoulli equation, valid on both sides implies

$$\tau_i \ln \varrho_i+\frac{\mathsf{z}}{\xi}+\frac{M_*^2\alpha^2 b_0^2}{2\varrho_i^2}=\frac{M_*^2}{2}\epsilon(a_0)\,, \tag{4.5.19}$$

which gives the density $\varrho_i(\mathsf{x},\mathsf{z})$ before the shock ($i=1$) and after ($i=2$). Eq.(4.5.18) then indicates where the jump must be situated. Eq.(4.5.16c) can be written as

$$[B_{1_t}]=\frac{4\pi}{B_{0_n}}[\rho V_n V_t]\,. \tag{4.5.20}$$

This gives the surface current density $J_s = [B_{1_t}]$ along the shock. Note that, the flow being subalfvénic, such a shock is necessarily of the slow type.

In order to find the resulting structure of the loop we can use the superposition principle, adding the field created by distributed currents and by the surface current at the shock. We first solve for a_1 the Poisson equation (see Eq.4.5.4),

$$\nabla^2 a_1 = \alpha\left[\frac{\partial}{\partial \mathrm{x}}\frac{\alpha}{\varrho_i}\frac{\partial a_0}{\partial \mathrm{x}} + \frac{\partial}{\partial \mathrm{z}}\frac{\alpha}{\varrho_i}\frac{\partial a_0}{\partial \mathrm{z}}\right] - \frac{\varrho_i}{2}\frac{d\epsilon}{da_0}\,. \tag{4.5.21}$$

taking the density from the Bernoulli equation 4.5.19. The right-hand side of Eq.(4.5.21) is the distributed current. The potential A_{1_s} created by the surface current density J_s of the shock discontinuity is given by

$$\nabla^2 A_{1_s} = J_s = \frac{4\pi}{B_{0_n}}[\rho V_n V_t]\,. \tag{4.5.22}$$

Making similar adimensionalization in A_{1_S} as in A_1 we can write Eq.(4.5.22) as

$$\nabla^2 a_{1_s} = j_s = b_0\left[\frac{\cos\theta}{\varrho}\right] \tag{4.5.23}$$

where θ is the angle between the shock front and the initial magnetic field line a_0. The whole potential $a_{1_{\mathrm{total}}}$ is

$$a_{1_{\mathrm{total}}} = a_1 + a_{1_S}\,, \tag{4.5.24}$$

The conditions (4.5.16a) and (4.5.20) are satisfied by our way of constructing the solution.

In some cases, the above described construction of the solution would place the shock below the level $\mathrm{z} = 0$. This is obviously because our model does not properly describes the physics of the flow in the region of steep density gradient where the plasma passes from low to high β. The downwards supersonic flow is channeled in the low β region but not lower down. The situation is somewhat analogous to a flow exhausting from a nozzle into an open medium (Landau & Lifshitz 1966). Here however the open medium exhibits a steep gradient of pressure due to the stratification of the cold atmosphere by gravity. The very high values of the pressure which are obtained at even slightly negative altitutes are large enough to decelerate the supersonic downflow at some point in this steep gradient layer. This is made through a three dimensional shock of sonic nature. In practice then, when our construction fails to locate the decelerating shock in the low β region, the latter locates itself very near the photosphere.

In Fig.(4.4) we show a typical loop structure with shock. Note that the gas density in the pre-shocked area is almost constant because the flows are very strong ($M > 1$).

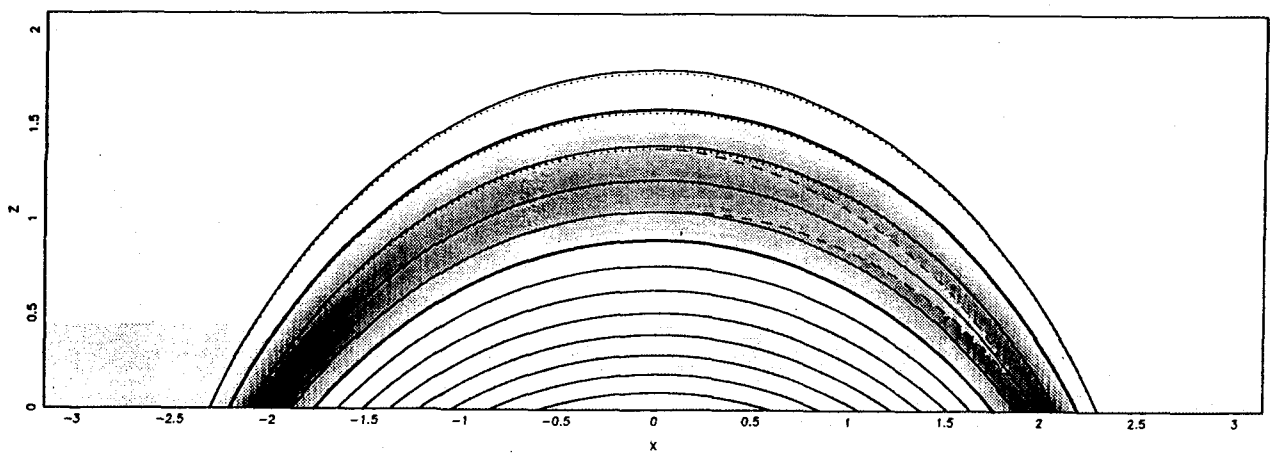

Figure 4.4: *Typical structure of a loop* ($\xi = 0.9$, $\alpha^{\max} = 30$, $N_\alpha = 2$) *with shock for the direction of the flow from left to right. The maximum temperature before (resp. after) the shock is* $\tau_1^{\max} = 0.3$ *(resp.* $\tau_2^{\max} = 0.4$*) and their profiles are given by Eqs.(4.4.8c) and (4.4.9c) with* $N_{\tau_i} = 2$*. The lines and the gray levels have the same meaning than in Fig.(4.2). The dashed line shows the shock position.*

In Fig.(4.5) we see another example applicable to cool loops. Cool loops are observed to have sizes comparable to the coronal scale height but are not in hydrostatic balance because their temperature is at least one order of magnitude lower than the coronal one, while their density is similar to that of the corona. Cool loops are surrounded by a hotter and denser medium. Foukal (1976) proposed that material enters in the cool loops at their top and flows down to the lower atmosphere. We modeled such a flow still keeping the isothermal assumption, although radiation losses may play a role. The result is shown in Fig.(4.5). Material has been assumed to be injected at the loop top with a sonic speed and its motion has then been calculated. The core temperature was taken to be 8×10^4 K. It is seen that the density profile is quite flat in the core before the material passes through the shock. The shape of the shock is not transverse to the field lines but tends to wrap around the cool core. We propose this as a possible explanation for the hot dense sheet observed around cool loops.

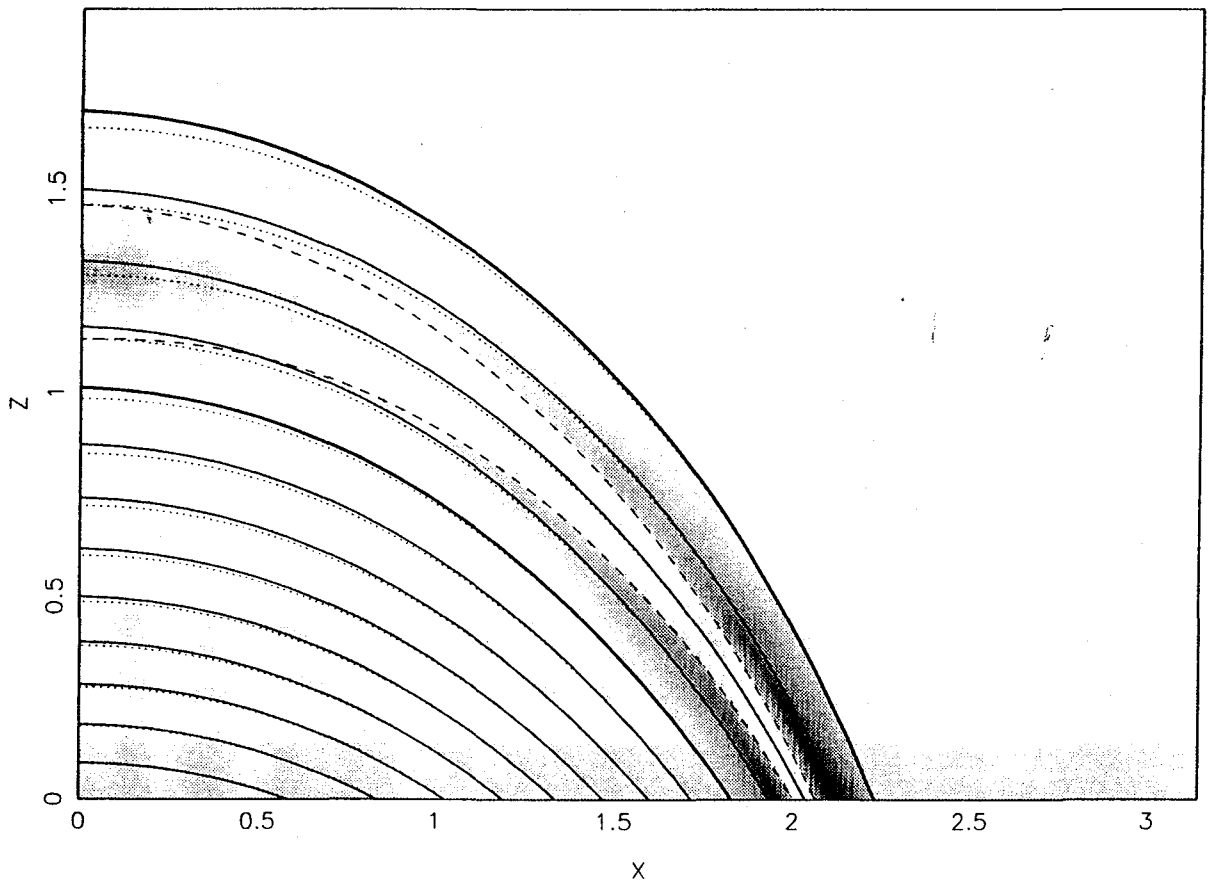

Figure 4.5: *Typical structure of the half of a loop* ($\xi = 0.5$, $\alpha^{\max} = 300$, $N_\alpha = 2$) *with shock having a cool core temperature of* 8×10^4 K ($\tau_1^{\max} = -0.95$, $\tau_2^{\max} = 0.4$). *The fluid inject at the loop summit with a sonic speed and then it flows down from both legs. In the pre-shock area the density is uniform because of the high Mach number of the flow, while the shock tends to wrap around the cool core. The shocked plasma forms a hot dense sheet around the cool core.*

4.6 Cylindrical geometry.

The most general magnetic current-free field in cylindrical coordinates $r\phi z$ is (Priest 1984)

$$A_0(r,z) = A_* \frac{\xi r}{2L}\left[\mathrm{Y}_1\left(\frac{\xi r_1}{2L}\right)\mathrm{J}_1\left(\frac{\xi r}{2L}\right) - \mathrm{J}_1\left(\frac{\xi r_1}{2L}\right)\mathrm{Y}_1\left(\frac{\xi r}{2L}\right)\right] e^{-\frac{\xi z}{2L}}, \qquad (4.6.1)$$

which can describe loop-like solutions with asymmetrical cross section. It is defined in the space between the two semi-open cylinders $r_1 \leq r \leq r_2$, $z \geq 0$ where r_2 is the first zero of Eq.(4.6.1) larger than r_1 and of course $r_1 \neq 0$. In limited cases for large $\xi r/L$ we can write approximently

$$A_0(r,z) \approx A_* \frac{2}{\pi}\sqrt{\frac{r}{r_1}} \sin\left[\frac{\xi(r_1 - r)}{2L}\right] e^{-\frac{\xi z}{2L}}, \qquad (4.6.2)$$

where $r_2 = r_1 + 2\pi$. The following simpler magnetic current-free configuration can be used as a first approximation for the magnetic field of a spot at chromospheric and coronal altitutes where the plasma $\beta << 1$,

$$A_0(r,z) = A_* \frac{\xi r}{2L}\mathrm{J}_1\left(\frac{\xi r}{2L}\right) e^{-\frac{\xi z}{2L}}. \qquad (4.6.3)$$

It is defined in $0 \leq r \leq 7.66341 L/\xi$, $z \geq 0$ [7.66341 is the first zero of $\mathrm{J}_1(x/2)$]. In both cases the magnetic field components are

$$B_{0_r} = -\frac{1}{r}\frac{\partial A_0}{\partial z}, \qquad B_{0_z} = \frac{1}{r}\frac{\partial A_0}{\partial r}. \qquad (4.6.4)$$

We assume the same energy equation (4.4.2) and make the same adimensionalization as in (4.5.3), except for the definition $\varpi = \xi r/L$ and $b_0 = A_* \xi^2/L^2$. Equations analogous to Eqs.(4.5.3) and (4.5.4) can be obtained from the general form of the transfield and Bernoulli equations presented in Appendix A. They can be written as

$$\tau \ln \varrho + \frac{\mathrm{z}}{\xi} + \frac{M_*^2 \alpha^2 b_0^2}{2\varrho^2} = \frac{M_*^2}{2}\epsilon(a_0), \qquad (4.6.5)$$

and

$$\frac{1}{\varpi}\left[\frac{\partial}{\partial \varpi}\frac{1}{\varpi}\frac{\partial a_1}{\partial \varpi} + \frac{\partial}{\partial \mathrm{z}}\frac{1}{\varpi}\frac{\partial a_1}{\partial \mathrm{z}}\right] = \frac{\alpha}{\varpi}\left[\frac{\partial}{\partial \varpi}\frac{1}{\varpi}\frac{\alpha}{\varrho}\frac{\partial a_0}{\partial \varpi} + \frac{\partial}{\partial \mathrm{z}}\frac{1}{\varpi}\frac{\alpha}{\varrho}\frac{\partial a_0}{\partial \mathrm{z}}\right] - \frac{\varrho}{2}\frac{d\epsilon}{da_0}. \qquad (4.6.6)$$

Thus, we have to solve Eq.(4.6.6) in the region $\varpi_1 \leq \varpi \leq \varpi_2$, $\mathrm{z} \geq 0$ when Eq.(4.5.1) holds and in $0 \leq \varpi \leq 7.66341$, $\mathrm{z} \geq 0$ in the other case. Boundary conditions are homogeneous Dirichlet ones. The appropriate Green function is given in Appendix B.

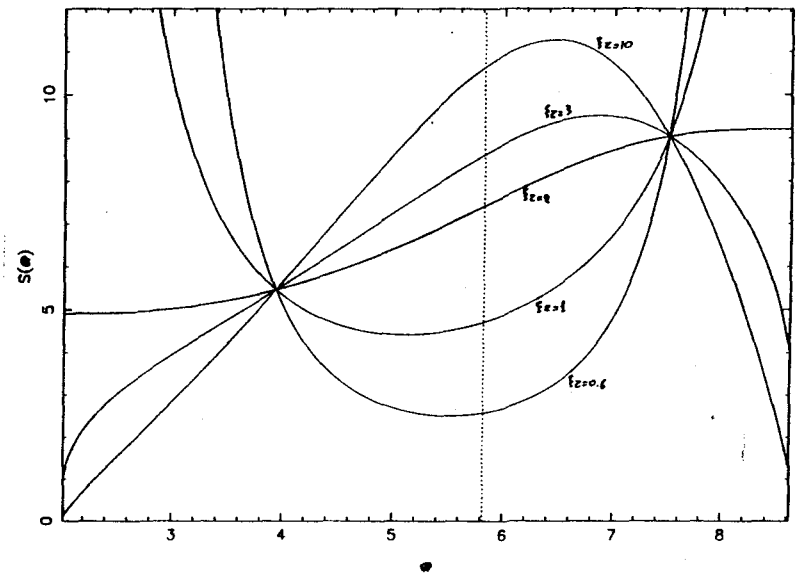

Figure 4.6: *The variation of the effective cross section Eq.(4.6.7) with the horizontal distance ϖ for five values of $\xi\tau = 0.6, 1, 2, 3$ and 10.*

Writing the Bernoulli equation for a given field line in terms of the horizontal coordinate ϖ we find that we can define the effective cross-section as

$$S(\varpi) = \frac{a_0^{1-\frac{2}{\xi\tau}}(\varpi, 0)}{b_0(\varpi, 0)}, \tag{4.6.7}$$

which has an extremum which depends on $\xi\tau$. In Fig.(4.6) we plot the function $S(\varpi)$ and we see that now the critical point of Eq.(4.4.3) is not at the top of the loop because the loop is not symmetric anymore because of the cylindrical geometry.

But the previous results still hold. For hot loops, where $\xi\tau > 2$, the critical point is of O-type (the effective cross section has a maximum after the loop summit), and only subsonic solutions are possible. For cold loops, where $\xi\tau < 2$, the critical point is of X-type (the effective cross section has a minimum before the loop summit) and both subsonic and transonic solutions are allowed. In the particular case where $\xi\tau = 2$ the effective cross section increases continuously as we move outwards, and only subsonic solutions are possible.

For subsonic flows the pressures at the two foot points of a same field line are now different. The solution is such that the higher is the magnetic field, the lower is the pressure; so the pressure at the outer foot point is higher than at the inner. This is a more general result than the usual static condition $P+B^2/8\pi = const.$ which holds only if the magnetic field is vertical. Note also that at the same altitude force balance along field lines requires equal densities and pressures in the absence of flows. Thus subsonic

flows are driven by small pressure differences. So the flow is accelerated towards the inner foot point. This siphon mechanism can explain naturally the reverse Evershed flow and the flow in asymmetrical coronal loops. Flows in the reverse direction would imply that the fluid move in the direction of increasing gas pressure, which calls for an additional driving mechanism, for example by Alfvén or magnetosonic waves, or a secular variation of the spot configuration.

For subsonic flows the ratio of the pressures at the two foot points of the same field line has a specific value which depends on $\alpha(a_0)$, $\tau(a_0)$ and $\epsilon(a_0)$. If boundary conditions happen to be different, the flow must be transonic and shocked solutions must occur. The criticality condition is given again by Eq.(4.5.14). The calculation of the structure with shocks proceeds in the same way as Cartesian coordinates.

In Fig.(4.7) we show a typical solution for the counter Evershed flow at chromospheric and coronal altitutes (section 1.5.2).

In Fig.(4.8) we show two typical loop structures. We see that the effect of flows causes the loop to become more asymmetrical than in the static case. We can imagine that there may exist loop structures in which the innermost part of the loop may not be visible.

In Fig.(4.9) we present two typical loop structures with shocks for the two possible directions of the flow.

4.7 Conclusion.

In this chapter we have constructed two-dimensional low-β, and subAlfvénic isothermal magnetic arcade solutions. Such stationary solutions are introduced in order to model flows in coronal loops and the Evershed effect in sunspots. We solved the MHD equations (in two coordinate systems) in the low-β and low Alfvén Mach number limit assuming that the magnetic structure is approximently force-free. Both the field-aligned dynamics and the cross-field force balance is solved. Our method of solution can be used in the presence of any boundary conditions and could allow modeling of other situations than the examples given in this paper. This is made possible because of the reasonable low-β assumption .

We assumed that the flows are always subsonic at the base of the structure. In cartesian coordinates, we analyzed the modifications brought about by flows in symmetrical magnetic configurations. When there is no pressure difference between the two foot points the flow is subsonic (we neglect the viscosity force) and the magnetic structure remains symmetric. When there is a pressure difference between the foot points and the loop is cool the flow becomes supersonic at the field line summit and after deceleration through a shock, the flow becomes subsonic again. In this case the

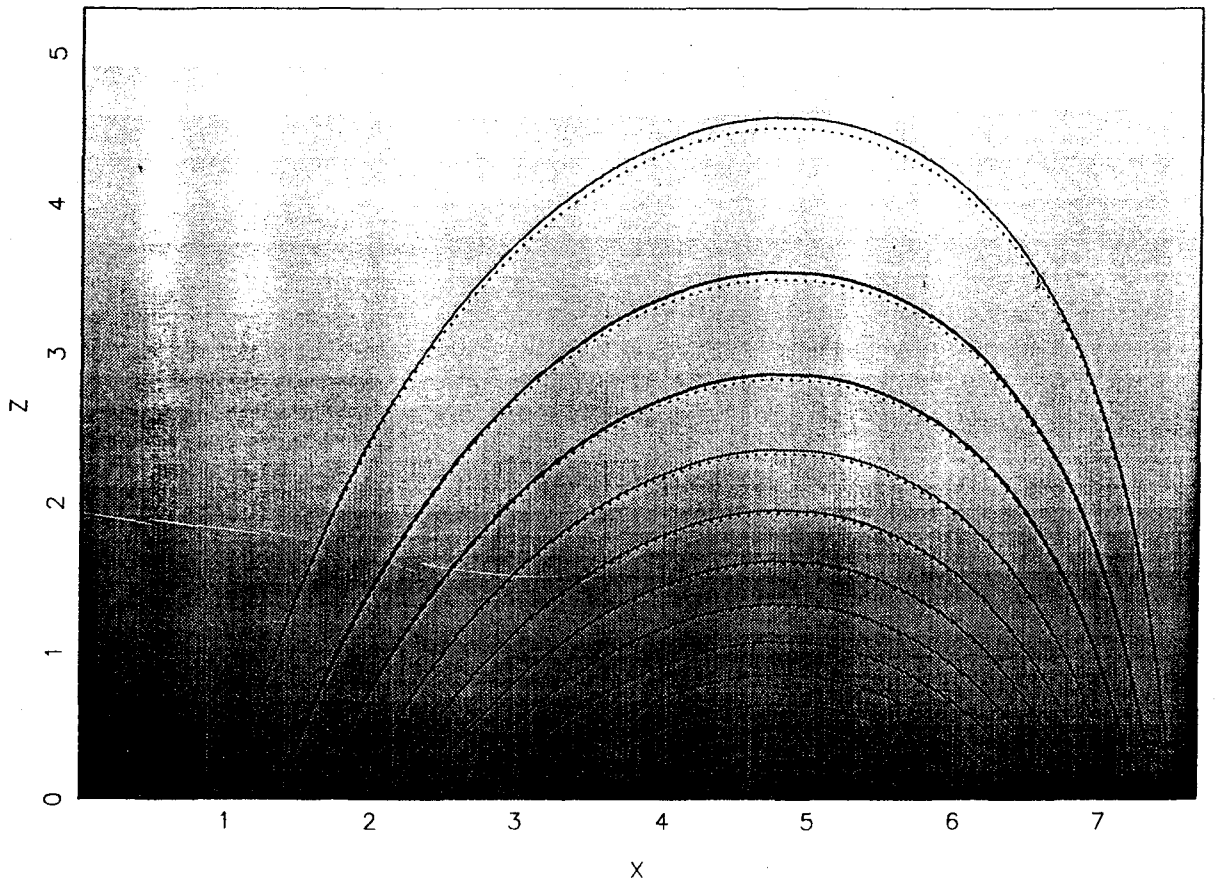

Figure 4.7: *Typical structure of a spot at chromospheric altitutes assuming isothermallity with a uniform temperature* 10^5 K *showing the counter-Evershed flow for* $\xi\tau = 4$ *and* $\alpha(a_0) = 0.8$.

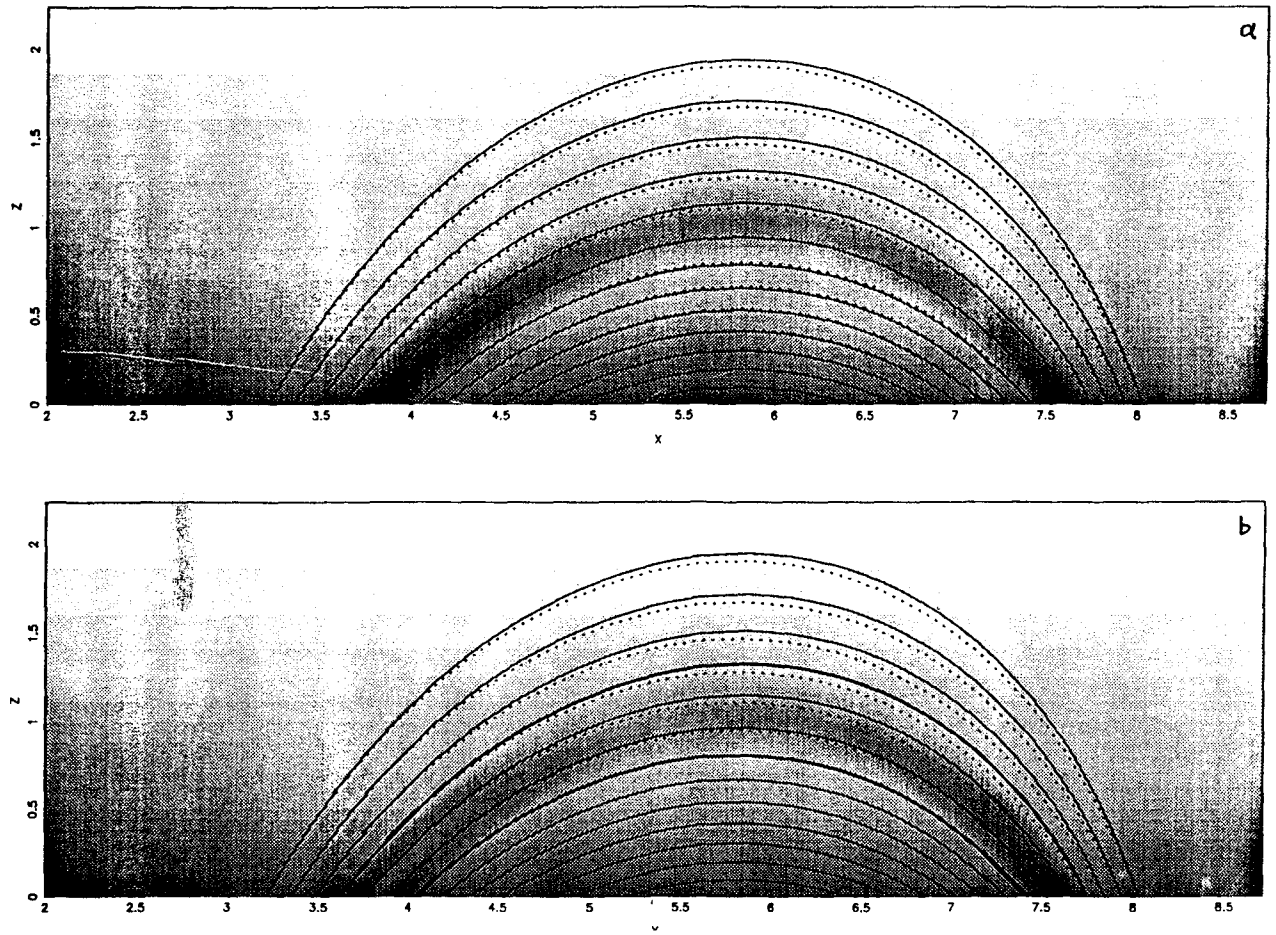

Figure 4.8: *Density structure of a static loop* ($\epsilon^{max} = 0.55$) *in* (a) *and density structure of a loop with flows in* (b) ($\alpha^{max} = 4.6$, $\epsilon^{max} = 0.7$). *Both have the same density at the outer foot. In both cases we have* $\xi = 0.8$ *and* $N_\alpha = N_\epsilon = N_\tau = 1.5$ *and* $\tau^{max} = 1$. *The flows decrease the density of the loop in the inner part and the loop becomes more asymmetrical than in the static case.*

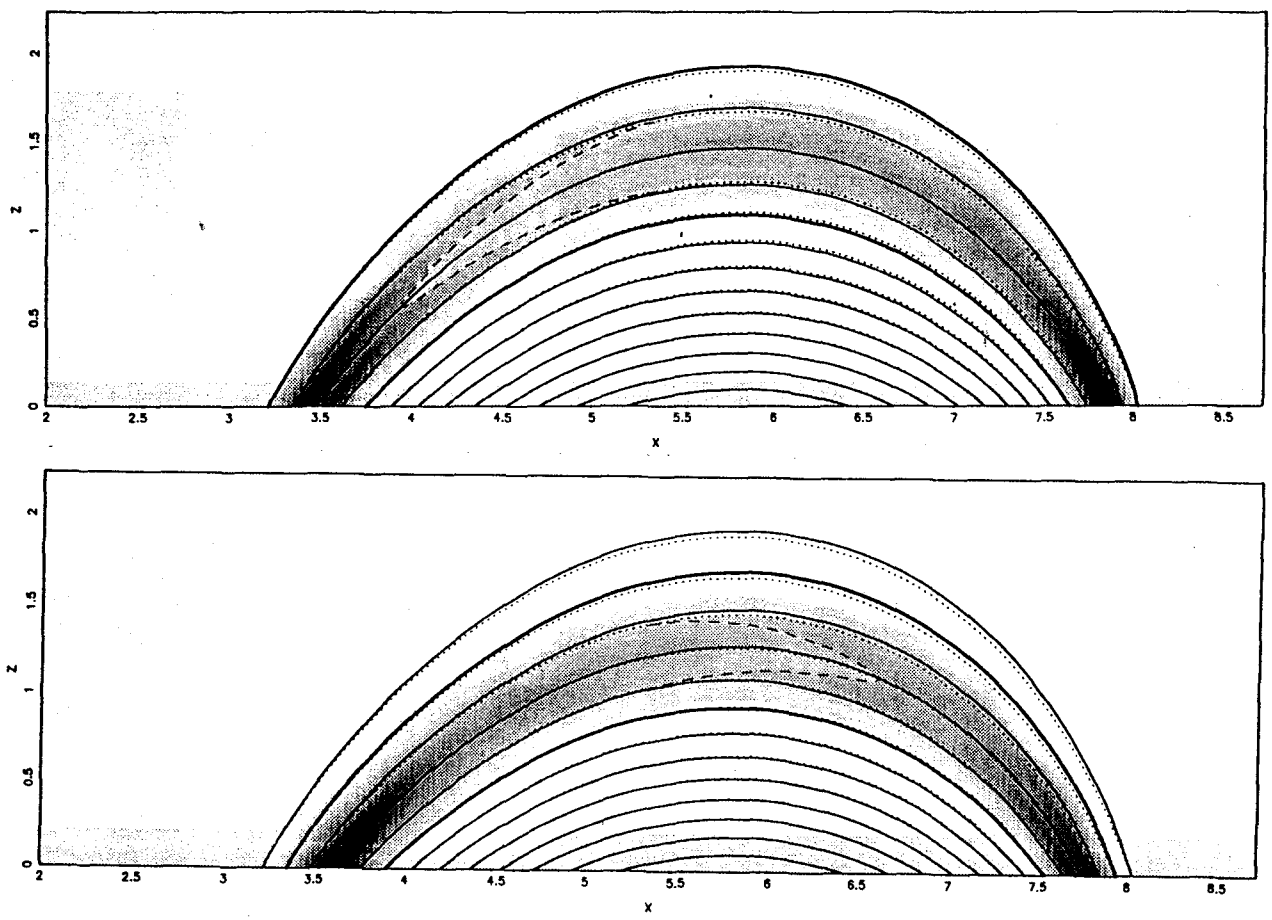

Figure 4.9: *Typical structures of two loops ($\xi = 0.8$, $\alpha^{\max} = 70$, $N_\alpha = 2$) with shocks for the two possible directions of the flow; from right to left in (a) and the opposite in (b).The pre-shock temperature is equal to the external coronal one and the the post-shock temperature has a "sinenosoidal" profile with $N_{\tau_2} = 2$ and its maximum is 1.1 times the external temperature.*

loop becomes asymmetrical. In extreme cases the shock may become very inclined to the magnetic field and the shocked material seems to wrap around a cool core. This might explain the situation observed sometimes in cool loops. In order for the density contrast to be visible against the surrounding, the energy flux inside the loop must be very different from its surrounding. In cool loops with temperature less than $\approx 10^6\ K$, the flows cause the density to drop faster along fieldlines compare to the static case, while in hot loops with temperature greater that $\approx 10^6\ K$ the flows causes the density drops slower and in some cases to increase with the height. Finally, in cool loops the flows will be appear stronger compare to the hot ones.

We also analyzed flows in asymmetric magnetic configurations by using cylindrical coordinates in order to apply both to asymmetrical loops and to sunspot configurations. We find that the counter-Evershed flow, detected in chromospheric and transition region temperature range, may be driven by a pressure difference (it flows from the low to the high field strength region). In the Evershed flow (observed at photospheric level) the plasma flows in the direction of increasing gas pressure. This requires another mechanism, may be time dependent, like the concentration of the sunspot magnetic field or wave pressure, to drive such flows. In asymmetrical loops the presence of flows increases the asymmetry of the density structure as compared to the static case. In some cases one leg of the loop may become poorly visible.

Chapter 5

1-D MHD EQUILIBRIA IN UNIFORM GRAVITY

5.1 Introduction

Until now, solar prominences (Priest 1989 and references therein) have been modelled as one-dimensional (Kippenhahn & Schlüter 1957, Poland & Anzer 1971), two-dimensional (Low 1975a, Low et al 1983, Hood & Anzer 1990), or, three-dimensional (Low, 1982, 1984, Wu & Low 1987, Demoulin 1989) magnetic structures in magnetostatic equilibrium, but without flows. Yet, Hα film observations and direct measurements of Doppler shifts indicate that even in quiescent prominences the plasma is not static, but it is instead in a continuous motion, suggesting therefore the ubiquitous presence of flows in almost all types of prominences (Mein 1977, Malherbe et al 1983; Martres et al,1981; Schmieder et al, 1985; Engvold et al, 1986).

As we have seen in chapter 1, magnetic loops and arcades on the other hand, have also been observed to have plasma flows. But from the previous chapters we see that such plasma flows have either been neglected altogether by studying the properties of those magnetic flux ropes as magnetostatic structures without flows, or, flows are allowed but the loops are described as rigid arches with a cross-sectional area that is allowed to vary in a prescribed way in the low-*beta* limit, or, as one-dimensional flexible loops, or, as incompresiple flows ignoring gravity (chapter 3).

The purpose of this and of next chapter is to proceed further by constructing a novel classes of steady MHD equilibria in the uniform gravitational field, without the critical approximation $\beta << 1$, that is approximated to exist in the low solar atmosphere. The construction is facilitated by the general reduction of the complete set of the symmetric,

but nonlinear and partial differential equations of ideal magnetohydrodynamics that we assume to describe – to zeroth-order – the interaction of compressible magnetofluids in the solar atmosphere. This is the crucial point that makes the difference in the solutions discrubing in the two later chapters from the existing ones; to solve the MHD equations for each field line. The only similar case to these solutions is the work of de Ville & Priest (1991a,b,c).

The most simpler and analytical class of equilibrium, is of course the one-dimensional MHD equilibria (Tsinganos 1992, Tsinganos & Surlantzis 1992). In sections 5.2 and 5.3 we review the 1-D static and hydrodynamic equilibria and in section 5.4 the one-dimensional planar MHD solution for an isothermal atmosphere is presented. This solution can be extended to the case that there exists a general polytropic relationship between pressure and density (section 5.5) and may be also constructed by a systematic method that generates analytically solutions of the full MHD equations with one ignorable coordinate (chapter 2). Finally, the main conclusions of the study are summarized in section 5.6.

5.2 Magnetostatic equilibrium

The simplest set of the integrals of the MHD equations, putting $\mathbf{V} = 0$ for the simple case of an isothermal atmosphere with a constant sound speed V_s, is

$$\Psi_A(A) = 0, \quad \Omega(A) = 0\,,$$

$$G(A) = 0, \quad E(A) = E_o + (g/B_o)A\,, \tag{5.2.1}$$

where B_o and E_o are constants. For this choice of the integrals, and an isothermal atmosphere, Eqs.(2.3.24, 2.3.26) yield the following two coupled equations for the pair of the two unknown variables $\rho(x,z), A(x,z)$,

$$\nabla^2 A + 4\pi\rho\frac{g}{B_o} = 0\,, \tag{5.2.2a}$$

$$V_s^2 \ln\frac{\rho}{\rho_o} + gz = E_o + \frac{g}{B_o}A\,. \tag{5.2.2b}$$

By eliminating A, we obtain a single equation for the dimensionless density $\varrho = \rho/\rho_o$, where ρ_o is the density at the origin $x = z = 0$,

$$\nabla^2 \ln\varrho + \frac{\beta}{2}\varrho = 0\ . \tag{5.2.3}$$

The differentiation in the above Laplacian is with respect to the dimensionless coordinates $\mathrm{x} = x/L$ and $\mathrm{z} = z/L$ (where $L = V_s^2/g$ is the scale height) while β is the familiar

plasma ratio at the origin, $\beta = 8\pi\rho_o V_s^2/B_o^2$. Thus, instead of solving the set of the coupled Eqs.(5.2.2) we need to solve this single equation for the dimensionless density ϱ (Low et al 1983). However, a detailed study of the various solutions of this nonlinear partial differential equation shall be postponed for the future. Here we shall confine our attention to the simplest possible solutions of this equation which correspond to 1-D equilibria similar to the Kippenhahn-Schlüter model for a quiescent prominence (Kippenhahn-Schlüter 1957) wherein the density is independent of z, $\varrho = \varrho(\mathrm{x})$ only. Indeed, the simplest such possible solution of Eq.(5.2.3) is

$$\varrho(\mathrm{x}) = \frac{1}{\cosh^2\left(\frac{\sqrt{\beta}\,\mathrm{x}}{2}\right)} . \tag{5.2.4}$$

From Eqs.(5.2.2) the resulting expression for the magnetic flux function A has the following form

$$A(x,z) = -B_o z + \int B_z(x)dx\,, \tag{5.2.5}$$

such that the magnetic field in the orthogonal coordinate system $x-y-z$ where the z-axis points toward the opposite direction of the uniform gravitational field g is,

$$B_x = -\frac{\partial A}{\partial z} = B_o \;\;,\;\; B_z = \frac{\partial A}{\partial x} = B_z(x) \;\;,\;\; . \tag{5.2.6}$$

Finally, the z-component of the magnetic field, $b_z(\mathrm{x}) = B_z(x)/B_o$, may be obtained by taking the derivative with respect to x of Eq.(5.2.2b),

$$b_z(\mathrm{x}) = \sqrt{\beta}\tanh\left(\frac{\sqrt{\beta}\,\mathrm{x}}{2}\right) . \tag{5.2.7}$$

Note that the following relations that hold between b_z-ϱ-x

$$b_z = \pm\sqrt{\beta(1-\varrho)}, \qquad \frac{db_z}{d\mathrm{x}} = \frac{\beta\varrho}{2}\,,$$

$$\pm d\mathrm{x} = \frac{d\varrho}{\varrho\sqrt{\beta(1-\varrho)}} . \tag{5.2.8}$$

are also obtained from Eqs.(5.4.19) in the limit of zero flows, M=0.

The dimensionless density ϱ and magnetic field b_z are expressed in terms of a single parameter, the plasma ratio β at the origin x = 0 where the density is maximum and the magnetic field lines are horizontal, $b_z = 0$. Notice that for given maximum density ρ_o the z-component of the magnetic field which supports the plasma weight against gravity is

$$b_z(\infty) = \pm\sqrt{\beta} = \pm\sqrt{8\pi\rho_o V_s^2/B_o^2}\,. \tag{5.2.9}$$

The minimum radius of curvature R_o of the field lines at the point of maximum density is then

$$\mathrm{R}_o = \frac{V_a^2}{g}\,. \tag{5.2.10}$$

Notice also that in this solution the total pressure $[P + B^2/8\pi]$ is constant everywhere, with the result that the plasma weight is supported against gravity by the tension of the magnetic lines alone. The density is maximum at the origin where the field lines have the greatest curvature and tension. The density tends asymptotically to zero at infinity, where the field lines become straight lacking any curvature and tension. Note that most of the plasma is confined horizontally within a few scale heights; and the extent of the volume containing most of the plasma is smaller the smaller is β. The solution (5.2.4), (5.2.7) forms the basis of the well known Kippenhahn-Schlüter model for a quiescent prominence (Kippenhahn-Schlüter 1957, Poland and Anzer 1971) and all we have done here is to show a novel way for deriving it from the Eqs.(2.3.24,2.3.26). This may be helpful in generating more solutions of Eq.(5.2.3) and also additional classes of solutions for more general expressions of the integrals in Eq.(5.2.1).

In the above Kippenhahn-Schlüter solution the atmosphere is compressible only in the horizontal direction. It is an interesting fact that this solution can exist in a plane-parallel stratified atmosphere as well (Low et al 1983). In that case the total density $\rho(\mathrm{x},\mathrm{z})$ is given by the expression,

$$\rho(\mathrm{x},\mathrm{z}) = \rho_\infty \mathrm{e}^{(-\mathrm{z})} + \frac{\rho_0}{\cosh^2\left(\frac{\sqrt{\beta}\,\mathrm{x}}{2}\right)}\,, \tag{5.2.11}$$

where $\rho_{||}$ is the density at $\mathrm{z} = 0$, $\mathrm{x} \to \pm\infty$.

5.3 Hydrodynamic equilibrium

It is instructive to consider for a moment the equilibrium of the similar, one-dimensional velocity field,

$$\rho\mathbf{V} = [\rho V_x, 0, \rho V_z] = [\rho(x)V_x(x), 0, \rho(x)V_z(x)]\,, \tag{5.3.1}$$

in the same isothermal atmosphere where we have put $\mathbf{B} = 0$. Then, the continuity equation is satisfied identically if $\rho(x)V_x(x) =$ constant, while the remaining force balance equations read,

$$\frac{d}{dx}\left[P + \rho V_x^2\right] = 0\,, \tag{5.3.2a}$$

$$\frac{d}{dx}\left[\rho V_x V_z\right] = -\rho g\,. \tag{5.3.2b}$$

Noting the analogy of Eqs.(5.3.2) to the corresponding equations of the previous case of magnetostatic equilibrium, integrate Eq.(5.3.2a) to obtain $\rho = const.$ Notice then that this result is drastically different from that expressed by Eq.(5.2.3), the streamlines of the flow are the familiar parabolic paths of a projectile fired against the uniform gravitational field instead of the sagged, under the plasma weight, magnetic field lines. None of the interesting features found in the one-dimensional magnetostatic equilibrium is found in this case of the one-dimensional hydrostatic equilibrium. This physical difference is better understood when we compare the Maxwell and Reynolds stress tensors (Parker 1979),

$$M_{ij} = -\left[P + \frac{B^2}{8\pi}\right]\delta_{ij} + \frac{B_i B_j}{4\pi}\,, \qquad (5.3.3a)$$

$$\varrho_{ij} = -P\delta_{ij} - \rho V_i V_j\,. \qquad (5.3.3b)$$

The non-uniform part of the Maxwell's stress tensor represents tension along a magnetic line while the non-uniform part of the Reynolds stress tensor represents compression along a stream line. The inevitable result is that magnetic lines are stretched tight whereas stream lines tend to buckle. It becomes of interest then to know which of the two stresses dominates when we have flows along the magnetic field lines.

5.4 1-D Hydromagnetic and Isothermal Equilibrium

The simplest cases of pure magnetostatic and hydrostatic 1-D equilibria in uniform gravity, respectively, was briefly discussed. In this section we proceed with a step by step construction of an analytic solution for the composite case of dynamical equilibrium ($\mathbf{V}, \mathbf{B} \neq 0$). It will be seen that this general case of MHD equilibrium, although it maintains the basic features of the simpler pure magnetostatic and hydrostatic equilibria to which it reduces in the extreme cases $\mathbf{V} = \mathbf{0}$ or $\mathbf{B} = \mathbf{0}$, respectively, is much more complex than each of them and reveals novel features.

5.4.1 Governing equations

Take the z-axis of the orthogonal system yzx to point in the opposite direction of the uniform acceleration of gravity $\mathbf{g}$. Search for solutions where the horizontal component of the magnetic field is uniform, the vertical component depends only on the horizontal distance x while the mass flux is parallel to the magnetic flux,

$$\mathbf{B} = [B_x, 0, B_z] = [B_o, 0, B_z(x)] \quad , \quad \rho\mathbf{V} = \lambda\mathbf{B}\,. \qquad (5.4.1)$$

The components of the momentum balance equations yield then,

$$\frac{d}{dx}\left[P+\frac{B_z^2}{8\pi}+\frac{\lambda^2 B_o^2}{\rho}\right]=0\,, \tag{5.4.2a}$$

$$\frac{d}{dx}\left[\frac{B_o B_z}{4\pi}\left(1-\frac{4\pi\lambda^2}{\rho}\right)\right]=\rho g\,. \tag{5.4.2b}$$

Assuming for simplicity an isothermal atmosphere, $P=V_s^2\rho$, Eq.(5.4.2b) can be integrated to give,

$$\rho V_s^2+\frac{B_z^2}{8\pi}+\frac{\lambda^2 B_o^2}{\rho}=\rho_o V_s^2+\frac{\lambda^2 B_o^2}{\rho_o}\equiv\rho_1 V_s^2\,, \tag{5.4.3}$$

where ρ_o is the density at the valleys of the equilibrium where $B_z=0$ and ρ_1 is a positive constant. Combining Eqs.(5.4.2b) and (5.4.3) we obtain

$$B_z(\rho)=\pm\sqrt{\frac{8\pi V_s^2}{\rho}(-\rho^2+\rho\rho_1-\delta^2)}\,, \tag{5.4.4a}$$

$$\frac{d}{d\rho}\left[\frac{B_o B_z(\rho)}{4\pi}\left(1-\frac{4\pi\lambda^2}{\rho}\right)\right]=\rho g\frac{dx}{d\rho}\,. \tag{5.4.4b}$$

where $\delta=\lambda B_o/V_s$. Eq.(5.4.4b) – with $B_z(\rho)$ substituted from Eq.(5.4.4a) – is then the final equation which gives the density ρ as a function of the horizontal distance x.

Finally, substituting Eq.(5.4.4a) in Eq.(5.4.4b) the following first order ordinary differential equation is obtained,

$$\pm\sqrt{\frac{8\pi g}{B_o^2}}dx=\frac{C(\rho)d\rho}{\rho^3\sqrt{\rho(-\rho^2+\rho\rho_1-\delta^2)}}\,, \tag{5.4.5a}$$

while $C(\rho)$ is the cubic,

$$C(\rho)=\rho^3+4\pi\lambda^2\rho^2-\rho(\delta^2+8\pi\lambda^2\rho_1)+12\pi\lambda^2\delta^2\,. \tag{5.4.5b}$$

The above expression can be readily integrated to give $x(\rho)$ in terms of the incomplete elliptic integrals of the first and second kind, $F(t,k)$ and $E(t,k)$, respectively (Appendix D). The solution $x(\rho)$ depends on three constants, namely λ, ρ_1 and δ. For any given set of these constants Eqs.(5.4.5) can be integrated to give $x(\rho)$. In reversing the function $x(\rho)$ to obtain $\rho(x)$ some caution is needed however, since, for a fixed sign in Eq.(5.4.5) the function $\rho(x)$ might not be single-valued if the cubic equation, $C(\rho)=0$ has roots ρ_i, $i=1,2,3$, which happen to be in the interval of the allowed density. Keeping that in mind, in the following we shall examine the solutions of Eq.(5.4.5) for all possible values of the constants λ, ρ_1, and δ.

Note that the above solution can be constructed by using the formulation developed in chapter 2 with the following choice of the free integrals $\Psi_A(A)$, $\Omega(A)$, $G(A)$, and $E(A)$,

$$\Psi_A(A) = 4\pi\lambda\,, \quad \Omega(A) = 0\,, \quad G(A) = 0\,, \quad E(A) = E_o + (g/B_o)A\,, \tag{5.4.6a}$$

where E_o is constant and the magnetic flux function A is given by

$$A(x,z) = -B_o z + \int B_z(x)dx\,. \tag{5.4.6b}$$

5.4.2 Relations among the characteristic speeds

In order to have a qualitative understanding of the solution, in this subsection we investigate the relation of the magnitudes of the three characteristic speeds, the sound speed V_s, the Alfvén speed $V_a^{\pm}$ and the flow speed $V_x^{\pm}$ at the valleys $(+)$ and the summits $(-)$ of the field and streamlines where the density is $\rho^{\pm}$ and the fieldlines are horizontal.

Relations at the valleys. The z-component of momentum balance, Eq.(5.4.2b), can be written,

$$\left[1 - \frac{V_x^+ V_x}{(V_a^+)^2}\right] \frac{d}{dx}\frac{B_o B_z}{4\pi} + \frac{B_o B_z}{4\pi}\frac{d}{dx}\left[1 - \frac{V_x^+ V_x}{(V_a^+)^2}\right] = \rho g \tag{5.4.7}$$

Noting that at the lowest point of each field line $B_z = 0$, $dB_z/dx > 0$ and $V_x = V_x^+$, Eq.(5.4.7b) yields

$$V_x^+ < V_A^+\,. \tag{5.4.8}$$

This result can be simply understood by writing the equilibrium equations of force balance at the lowest point of the field line

$$\frac{\rho^+(V_x^+)^2}{\mathrm{R}^+} + \rho^+ g = \frac{B_o^2}{4\pi \mathrm{R}^+}\,, \tag{5.4.9a}$$

where r^+ is the radius of curvature at this point. By multiplying by r^+ and dividing by ρ^+ we obtain

$$(V_a^+)^2 - (V_x^+)^2 = \mathrm{R}^+ g\,, \tag{5.4.9b}$$

from which the inequality (5.4.8) follows.

On the other hand, consider the derivative of the x-component of the momentum balance Eq.(5.4.2a),

$$\frac{d^2\rho}{dx^2}\left[V_s^2 - \frac{(\rho^+ V_x^+)^2}{\rho^2}\right] + \frac{2V_x^+}{\rho^+}\frac{d\rho}{dx} = -\frac{1}{4\pi}\left[\frac{dB_z}{dx}\right]^2 - \frac{B_z}{4\pi}\frac{d^2 B_z}{dx^2}\,. \tag{5.4.10}$$

Substituting $B_z = 0$, $d\rho/dx = 0$ at the position of maximum density where the field and streamlines are horizontal we obtain,

$$\frac{d^2\rho^+}{dx^2}\left[V_s^2 - (V_x^+)^2\right] = -\frac{1}{4\pi}\left[\frac{dB_z}{dx}\right]^2 < 0\,. \tag{5.4.11}$$

Since $\rho^+ = \rho_{\max}$, we have that $d^2\rho/dx^2 < 0$ and

$$V_x^+ < V_s\,. \tag{5.4.12}$$

It follows that the flow at the valleys of the field and stream lines where the density is maximum, is subsonic and subalfvénic. This result should not be surprising, since at these localities the equilibrium is dominated by the magnetic tension forces, and therefore we have a Kippenhahn-Schlüter, prominence-like solution with a weak flow along the sagging magnetic field lines.

Relations at the summits. Let ρ^-, V_x^-, V_A^- the density, flow speed and Alfvén speed at the summit of some loop-like, one-dimensional hydromagnetic equilibrium, where the magnetic and stream lines are horizontal. At this point $B_z = 0$, $dB_z/dx < 0$, and the z-component of the momentum balance equation – similarly to Eq.(5.4.7b) – yields the inequality,

$$V_x^- > V_A^-\,. \tag{5.4.13}$$

As before, this relation can be simply understood by writing the force-balance equation

$$\frac{\rho^-(V_x^-)^2}{\mathrm{R}^-} = \rho^- g + \frac{B_o^2}{4\pi \mathrm{R}^-}\,, \tag{5.4.14}$$

where r^- is the corresponding radius of curvature.

On the other hand, the x-component of momentum balance gives Eq.(5.4.11), as before. Since $\rho^- = \rho_{\min}$, we have $d^2\rho/dx^2 > 0$ and the above inequality yields

$$V_x^- > V_s\,. \tag{5.4.15}$$

The flow at the summits of the field and stream lines, where the density is minimum, is supersonic and superalfvénic. As before, this result should not come as a surprise, since the flow at these localities has to be strong enough such that the resulting centrifugal force balances both the plasma weight and the magnetic tension force for equilibrium.

Note that there exists a simple relationship between the Mach numbers M^+, and M^-, at the valleys and summits of the MHD equilibrium. By combining relations (5.4.1) and (5.4.3) applied to the valleys and summits,

$$\rho^+ V_x^+ = \rho^- V_x^-\,, \qquad \rho^+ V_s^2 + \frac{\lambda^2 B_o^2}{\rho^+} = \rho^- V_s^2 + \frac{\lambda^2 B_o^2}{\rho^-}\,, \tag{5.4.16}$$

we obtain for the ratio of the densities and product of the Mach numbers at the summits and valleys,

$$\varrho^- = \rho^-/\rho^+ = (M^+)^2 \quad , \quad M^- M^+ = 1 \,. \tag{5.4.17}$$

5.4.3 The solution

Let

$$M = M^+ = \frac{V_x}{V_s} = \frac{\lambda B_o}{\rho_o V_s}, \quad M_a = M_a^+ = \frac{4\pi\rho_o V_x}{B_o^2}, \quad \beta = \beta^+ = \frac{8\pi\rho_o V_s^2}{B_o^2}, \tag{5.4.18}$$

denote the gas and magnetic Mach numbers and the plasma ratio, respectively, at the valleys of the MHD equilibrium where the density is $\rho = \rho_o$. Then, Eqs.(5.4.4a), (5.4.5) for the dimensionless z-component of the magnetic field $b_z = B_z/B_o$, and the dimensionless density $\varrho = \rho/\rho_o$ can be written in terms of these constants M, M_a and β (which are reffered to the valleys and for simplicity we have dropped the index '+'),

$$b_z(\varrho) = \pm\sqrt{\frac{\beta[1-\varrho][\varrho - M^2]}{\varrho}}, \tag{5.4.19a}$$

$$\pm\sqrt{\beta}d\mathrm{x} = \frac{C(\varrho)d\varrho}{\varrho^3\sqrt{\varrho[1-\varrho][\varrho - M^2]}}, \tag{5.4.19b}$$

where

$$C(\varrho) = \varrho^3 + M_a^2\varrho^2 - [M^2 + 2M_a^2 + 2M^2M_a^2]\varrho + 3M^2M_a^2\,, \tag{5.4.19c}$$

while again we have defined $\mathrm{x} = x/L$ and $L = V_s^2/g$ is the scale height of the atmosphere. It is obvious that the density must be in the interval $I = [M^2, 1]$. At the valleys, $\varrho = 1$, $M = M^+ < 1$ while at the summits, the density is equal to $\varrho^- = M^2$ and $M^- = 1/M > 1$. It is interesting to note that this result of a bound density distribution is a novel feature of 1-D hydromagnetic equilibria in uniform gravitational fields. Apparently it can be regarded as an extension of the known property of 1-D magnetostatic equilibria in uniform gravity where the density is bounded above, $\rho < \rho_o$, ($\varrho < 1$), but otherwise unbounded below, except, of course, to have positive values. The additional restriction on the density seems to have a *hydrodynamic* origin, since it can be seen that the lower bound disappears when $\mathbf{V} \to 0$, or $M \to 0$ (or equivalently $\lambda, \delta \to 0$).

We may distinguish two cases of such equilibria. *First*, equilibria that contain both valleys and summits. In this case, at the summits we have $M_a^- = M_a/M \geq 1$ which requires the relation $M \leq M_a < 1$, between the two Mach numbers M and

M_a. The cubic $C(\varrho)$ has two roots in I, as it may be also seen from Fig.(5.1) for $M_a = 0.8 > M = 0.5$. In the *second* case wherein $M_a \leq M < 1$, the Alfvén Mach number M_a at the summits is not greater than one and the solution from a valley cannot extend to a summit; only solutions with a valley, or, a summit are allowed in this case. The cubic $C(\varrho)$ has one root in I, as it may be seen from Fig.(5.1) for $M_a = 0.16 < M = 0.5$.

In order that we obtain from Eq.(5.4.19b) a physical solution for $\varrho(x)$ for a given set of the parameters M_a and M, we need to examine if the function $\mathrm{x}(\varrho)$ is one-to-one; i.e., we need to check if the cubic $C(\varrho)$ has roots in the interval I. By checking the determinant of $C(\varrho)$ we find that it is negative and therefore $C(\varrho)$ has always three real roots. To check if they fall in the interval I simply note that

$$C(1) = [1 - M^2][1 - M_a^2] > 0\,, \tag{5.4.20a}$$

$$C(M) = -2MM_a^2[1 - M^2] < 0\,, \tag{5.4.20b}$$

$$C(M^2) = M^2[1 - M^2][M_a^2 - M^2]\,, \tag{5.4.20c}$$

In the case of a continuous solution with both valleys and summits, $M < M_a < 1$, $C(M^2) > 0$, and we have two roots in I, Fig.(5.1).

5.4.4 Plots and parametric dependence of the solutions

Plots of this dimensionless density $\varrho(\mathrm{x})$ are shown in Fig.(5.3b) for various values of β. Note that at the points ϱ_i where $C(\varrho_i) = 0$, we have that $d\mathrm{x}/d\varrho = 0$. However, since the function $\varrho(\mathrm{x})$ must be single-valued, the solutions shown in Fig.(5.3b) have been stopped at this root $\varrho_i < 1$ of $C(\varrho)$ which is closer to 1; and after ϱ_i we have taken the mirror symmetric of the curve $\mathrm{x}(\varrho)$ with respect to the line $\mathrm{x} = \mathrm{x}(\varrho_i)$. In doing so we actually take advantage of the $\pm$ signs in expressions (5.4.19).

Plots of the magnetic field lines for various values of the Mach number, from $M = 0$ (magnetostatic Kippenhahn-Schlüter solution) to $M = 0.75$ are shown in Fig.(5.2), while for various values of the plasma β, are shown in Fig.(5.3a). We see that by increasing the Mach number M, or the plasma β, the field lines become steeper and steeper as a result of the increased centrifugal forces. Note that the Alfvén Mach number $(M_a^+)^2 = \beta^+(M^+)^2/2$ (which represents the ratio of the centrifugal and magnetic tension forces) increases by increasing the flow speed or the plasma β^+ at the valleys and that is the reason why the fieldlines become steeper. Another qualitative way to understand this result may be seen from Eq.(5.4.9) which can be written at the valleys as

$$(M^+)^2 + \frac{\mathrm{R}^+}{L} = \frac{2}{\beta^+}\,, \tag{5.4.21}$$

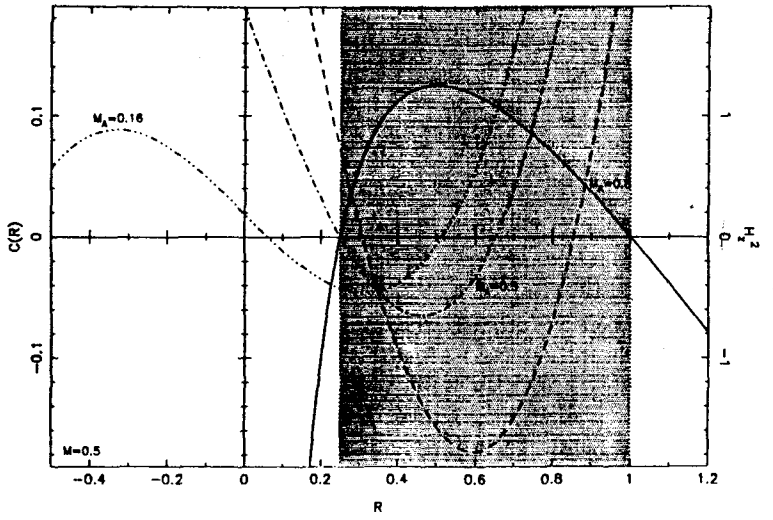

Figure 5.1: *Plot of the cubic $C(\varrho)$, Eq.(5.4.19c), for $M = 0.5$ and three values of the Alfvén Mach number M_a, $M_a = 0.8 > M$, $M_a = 0.5 = M$ and $M_a = 0.016 < M$, for the isothermal case, $\gamma = 1$. In the same plot $H_z^2(\varrho)$, Eq.(5.4.19a, solid curve), is shown for $M_a = 0.8$ and $M = 0.5$. Note that there always exist at least one root in the allowed interval of the density $I = [0.25, 1]$ (shaded area) and only in the case where we have two roots of the cubic in I it is possible to construct a continuous solution including both valleys and summits.*

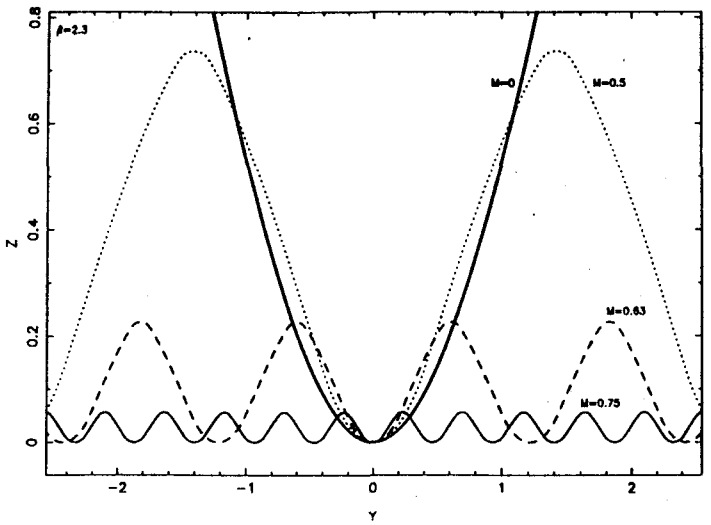

Figure 5.2: *Shape of the field and streamlines shape on the z-y plane for $\gamma = 1$, $\beta = 2.3$ and four values of the Mach number M: $M = 0$, (thick line, magnetostatic K-S solution), $M = 0.5$ (dotted line, magnetically dominated MHD solution), $M = 0.63$ (dashed line) and $M = 0.75$ (continuous line, hydrodynamically dominated MHD solution). Note that by decreasing M the separation of the peaks together with the height of the streamlines increases (converging toward the magnetostatic K-S case), while the opposite happens when M increases (converging toward the pure hydro, constant density and flow speed case).*

with L the scale height. For a constant β^+, an increase of the Mach number implies a decrease in the radius of curvature at the valleys which necessarily become steeper. Similarly, by increasing the plasma β at the valleys – keeping constant the Mach number – the radius of curvature there decreases. This is exactly the trend encountered in the plots of Figs.(5.2) and (5.3a).

In a steep valley the density varies also very fast – Fig.(5.3b) – while the magnitude of the z-component of the magnetic field and the total flow speed – Figs.(5.3c,d) are also greater than in a flatter valley. In these plots (5.2), (5.3a), (5.3b) and (5.3c) we also show by a thick line for comparison, the density, z-component of the magnetic field and the shape of the fieldlines for the static Kippenhahn-Schlüter solution.

At the summits of the equilibrium, we have similarly to Eq.(5.4.21),

$$(M^-)^2 = \frac{\mathrm{R}^-}{L} + \frac{2}{\beta^-}\,. \tag{5.4.22a}$$

Substituting $M^- = 1/M^+$ and $\beta^- = \beta^+(M^+)^2$, this relation becomes,

$$1 = \frac{(M^+)^2\mathrm{R}^-}{L} + \frac{2}{\beta^+}\,. \tag{5.4.22b}$$

Thus, increasing the Mach number M^-, or the plasma β^- at the summits, is equivalent to decreasing the Mach number M^+, or the plasma β^+ at the valleys, and this in turn leads to an increase of the radii of curvature R^- and R^+, Figs.(5.2), (5.3a). This happens despite the fact that the Alfvén Mach number $M_a^- = \beta^-(M^-)^2/2$, or, equivalently, the centrifugal force increase at the summits by increasing the flow speed there. This trend, is the opposite from what happens at the valleys and should be expected since the flow at the summits is hydrodynamically dominated and the role of the magnetic field is simply to reduce the height of the summit as compared to the pure hydrostatic case. Thus, the width and height of the summit together with the radius of curvature R^-, increase by increasing M^- and β^-.

Altogether, the solution at the valleys is magnetically dominated and the density is Kippenhahn-Schlüter type, while the solution is hydrodynamically dominated at the summits where the density is approximately constant.

5.5 1-D Hydromagnetic and Polytropic Equilibrium

In this section we briefly extend the previous results to the case of a polytropic atmosphere, with a constant polytropic index γ.

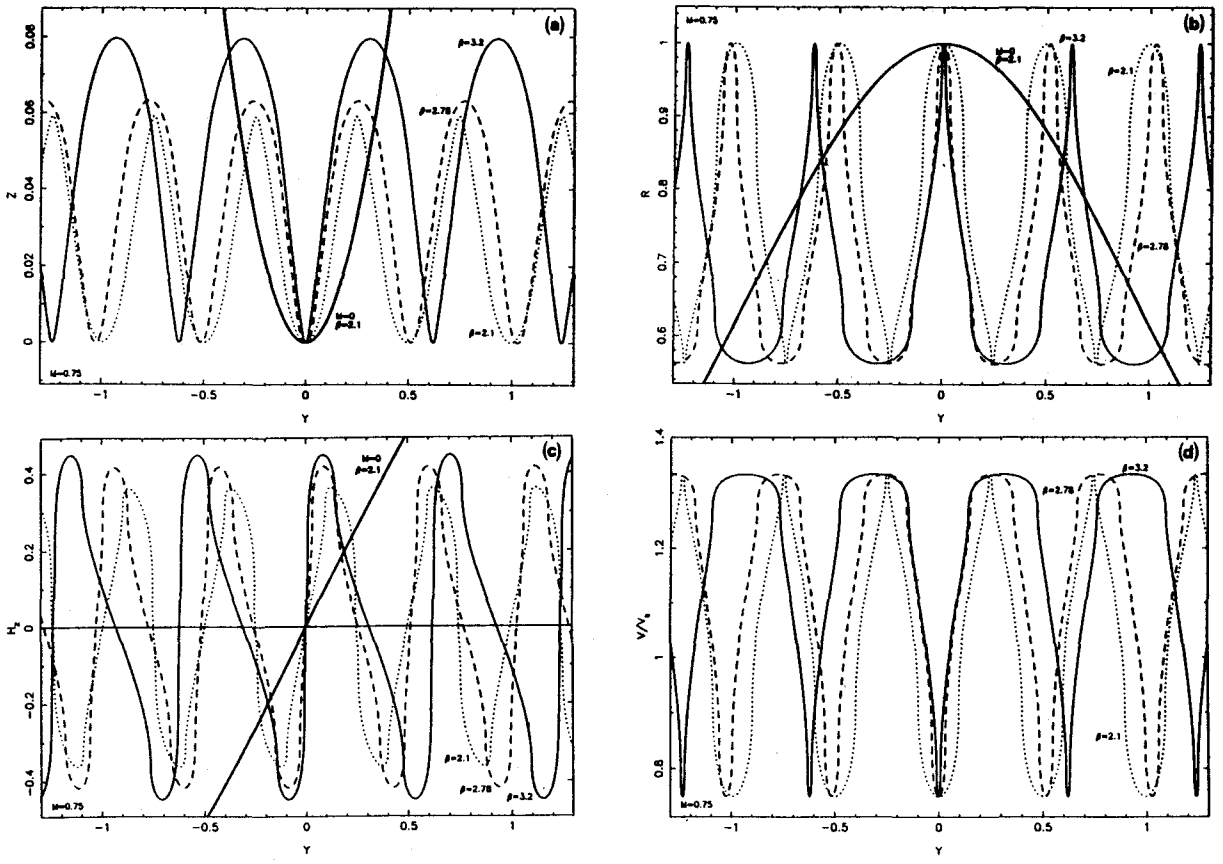

Figure 5.3: *Plot of the fieldline and streamline shape on the x-z plane in (a), the horizontal spatial dependence of the density in (b), the z-component of the magnetic field in (c) and the total flow speed in units of the constant sound speed in (d) for $\gamma = 1$, $M = 0.75$ and three values of the plasma β at the valleys: $\beta = 3.2$ (continuous line), $\beta = 2.78$ (dashed line) and $\beta = 2.1$ (dotted line). In the first three plots we have indicated with a heavy line the magnetostatic K-S solution corresponding to $\beta = 2.1$. Note that for $\beta = 2.78$ valleys and summits are almost symmetrical, by increasing β the summits become flatter than the valleys converging toward a hydro dominated case wherein density and flow speed are constant at the summits ($\beta \to \infty$). The opposite happens when we decrease β and the solution converges toward a K-S type magnetostatic equilibrium ($\beta \to 0$).*

In an atmosphere where a polytropic relationship $P = K\rho^\gamma$ holds, Eq.(5.4.2a) becomes

$$K\rho^\gamma + \frac{B_z^2}{8\pi} + \frac{\lambda^2 B_o^2}{\rho} \equiv K\rho_1^\gamma , \tag{5.5.1}$$

where K and ρ_1 are positive constants. Combining Eqs.(5.4.2b) and (5.5.1) we obtain

$$B_z(\rho) = \pm\sqrt{K[\rho_1^\gamma - \rho^\gamma] - \frac{\lambda^2 B_o^2}{\rho}} , \tag{5.5.2}$$

and equation (5.5.5b).

Let again ρ_o, $M = M^+ = \lambda B_o/\sqrt{\gamma\rho_o P_o}$ and $\beta = \beta^+ = 8\pi\rho_o V_s^2/\gamma B_o^2$ denote the density, Mach number and plasma ratio, respectively, at the valleys where the field lines are horizontal, ($B_z = 0$). Then, Eqs.(5.5.1) and (5.4.4b) give the following expressions for the dimensionless density $\varrho = \rho/\rho_o$ and magnetic field $b_z = B_z/B_o$,

$$b_z(\varrho) = \pm\sqrt{\frac{\beta[-\varrho^{\gamma+1} + (1+\gamma M^2)\varrho - \gamma M^2]}{\varrho}} , \tag{5.5.3a}$$

$$\pm\sqrt{\beta}d\mathrm{x} = \frac{D(\varrho)d\varrho}{\varrho^3\sqrt{\varrho[-\varrho^{\gamma+1} + (1+\gamma M^2)\varrho - \gamma M^2]}} , \tag{5.5.3b}$$

where

$$D(\varrho) = \varrho^{\gamma+2} + (2/\gamma - 1)M_a^2\varrho^{\gamma+1} - [M^2 + 2M_a^2/\gamma + M^2M_a^2]\varrho + 3M^2M_a^2 , \tag{5.5.3c}$$

As before, x denotes the dimensionless horizontal distance $\mathrm{x} = x/L$, with L the scale height in the atmosphere, $L = V_s^2/g$ where $V_s^2 = \gamma P_o/\rho_o$ is the square of the sound speed at the valleys of the equilibrium.

The square of the z-component of the magnetic field, $b_z^2(\varrho) = \beta[-\varrho^{\gamma+1} + (1 + \gamma M^2)\varrho - \gamma M^2]/\varrho$ has an obvious root at $\varrho = 1$ while other roots (Fig.5.4) can be found numerically. Continuous solutions exist only in the intervals where $H^2(\varrho) > 0$, as in the previous section. Also, in order that the density ϱ is a single-valued function of the horizontal distance x beyond the points ϱ_i where $D(\varrho_i) = 0$, the solution should be appropriately extended such as $\varrho(\mathrm{x})$ remains a single-valued function, similarly to the previous case examined in section 5.5.2. In Fig.(5.4), $D(\varrho)$ is plotted for $\gamma = 5/3$, $M = M^+ = 0.46$ and several values of the Alfvén number $M_a = M_a^+ = \gamma\beta\lambda^2/2$. Note that only those values of the Alfvén Mach number for which $(M_a^+)^2/\varrho^- > 1$, correspond to periodic solutions with valleys ($M_a^+ < 1$) and summits ($M_a^- = M_a^+/\varrho^- > 1$).

As in the previous case of an isothermal atmosphere, at the valleys the flow is subsonic and subalfvénic, while at the summits it is supersonic and superalfvénic. The

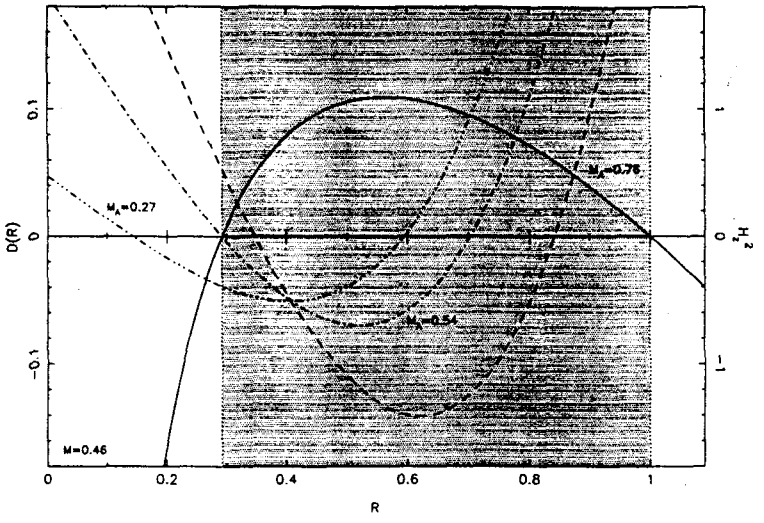

Figure 5.4: *Plot of the polynomial $D(\varrho)$, Eq.(5.5.3c), and the square of the z-component of the magnetic field H_z^2, Eq.(5.5.3a), (solid line) for $M = 0.46$, and three values of the Alfvén Mach number for the polytropic case with $\gamma = 5/3$. The dashed line corresponds to $M_a = 0.76$, the dot-dashed to $M_a = 0.54$ and the dot-dash-dotted line to $M_a = 0.26$. Note that always there exist at least one root in the allowed interval I of the density (shaded area). Also, only in the cases where there exist two roots of the polynomial $D(\varrho)$ in I it is possible to construct a continuous solution including both valleys and summits.*

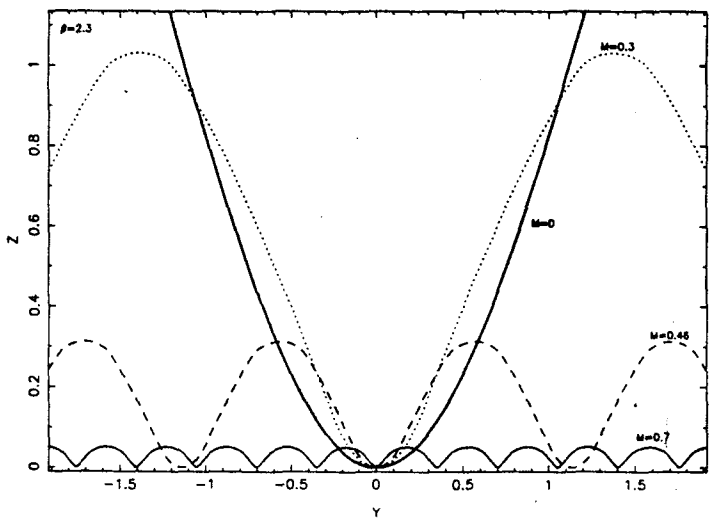

Figure 5.5: *Shape of the field and streamlines on the x-z plane for $\gamma = 5/3$, $\beta = 2.3$ and four values of the Mach number M, $M = 0$ (thick line, static K-S solution), $M = 0.3$ (dotted line, magnetically dominated MHD solution), $M = 0.46$ (dashed line) and $M = 0.7$ (continuous line, hydrodynamically dominated MHD solution).*

relation between the Mach numbers M^+ and M^- at the valleys and summits is now,

$$\varrho^- = \left[\frac{M^+}{M^-}\right]^{\frac{2}{\gamma+1}}, \qquad \frac{\gamma[M^-]^2 M^+ + M^+}{\gamma[M^+]^2 M^- + M^-} = \left[\frac{M^-}{M^+}\right]^{\frac{\gamma-1}{\gamma+1}}, \tag{5.5.4.}$$

which has as special case Eqs.(5.4.17) for $\gamma = 1$, as expected.

In Fig.(5.5) we plot the shape of the fieldlines on the plane x-z, for $\beta = 2.3$ and various values of M while in Figs.(5.6) the fieldline shape, density $\varrho(\mathrm{x})$, z-component of the magnetic field, $b_z(\mathrm{x})$ and total velocity $V(\mathrm{x})$ for $\gamma = 5/3$, and $M = 0.58$ and various values of β at the valleys. The solution has the same parametric dependence on M and β with the previous isothermal case [*cf.* Figs.(5.2), (5.3)]. Regarding the dependence on γ, it can be seen from a comparison of Figs.(5.5), (5.6) with Figs.(5.2), (5.3), that by increasing γ the valleys become steeper. This result is not surprising because for the same dependence of $\varrho(\mathrm{x})$, the gradient of the pressure is higher, the higher is the polytropic index and therefore the field gradients should be steeper in order to maintain force balance. Note also that by varying the polytropic index, the scale height varies too and identical values of the Mach numbers for different γ do not mean identical velocities.

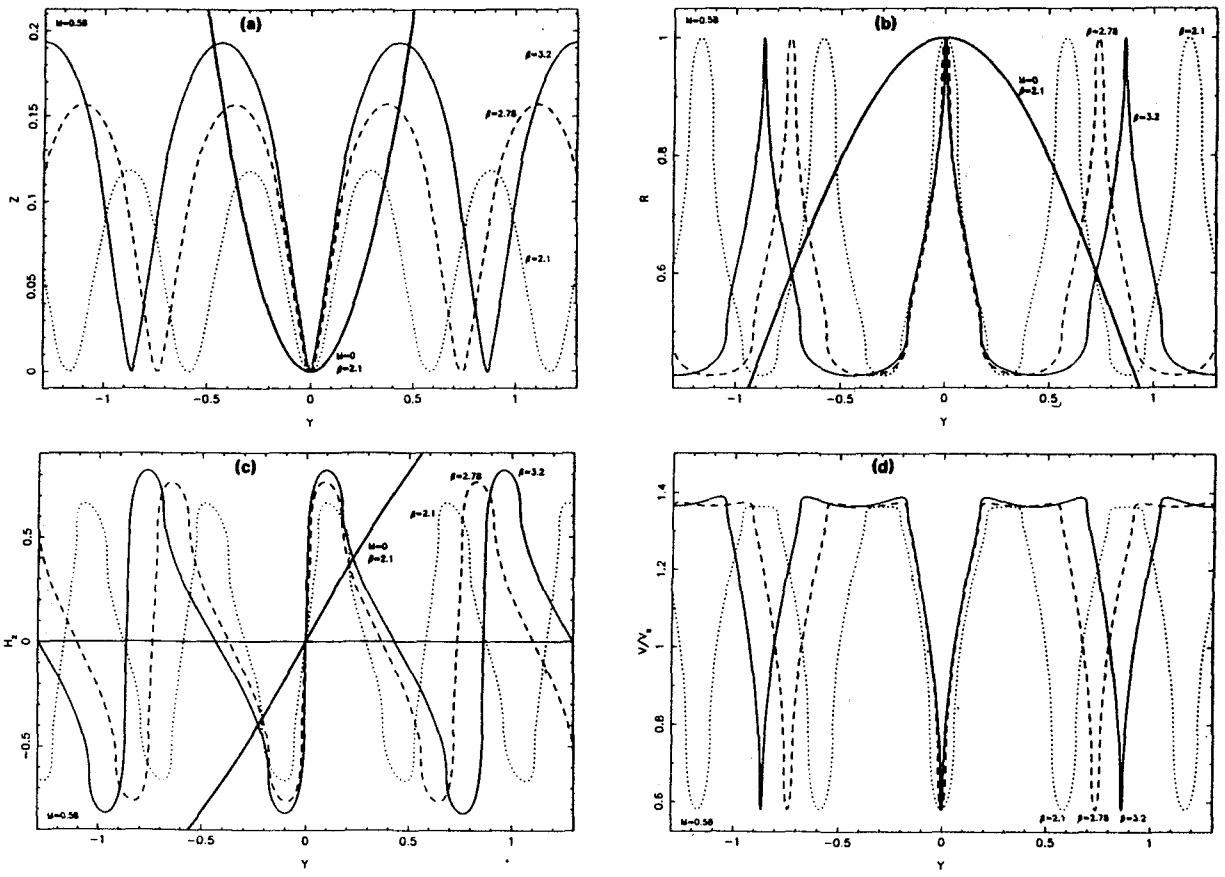

Figure 5.6: *Plots of the field and streamline's shape on the z-y plane in (a), of the horizontal spatial dependence of the density in (b), the z-component of the magnetic field in (c) and the total Mach number in (d) for* $\gamma = 5/3$, $M = 0.58$ *and three values of the plasma* β *at the valleys:* $\beta = 3.2$ *(continuous line),* $\beta = 2.78$ *(dashed line) and* $\beta = 2.1$ *(dotted line). In the first three plots we have plotted with a heavy line the magnetostatic K-S solution for* $\beta = 2.1$. *Note that for* $\beta = 2.78$ *valleys and summits are almost symmetric. On the other hand, by decreasing* β *the valleys become wider than the summits while their separation increases. The opposite happens when we increase* β. *The velocities and the scale height are the same as in the isothermal case. Comparing with the isothermal case (Fig.5.3), note that the valleys are steeper now because the gradient of the pressure is greater. On the other hand, at the summits density and velocity tend to be almost constant, as in pure hydrodynamic equilibrium.*

5.6 Summary and Conclusions

The purpose of this series of articles is twofold. *First*, to present some classes of exact solutions of the full 2-D MHD equations pertinent to prominence- and loop-like compressible MHD equilibria in a uniform gravitational field. And *second*, to examine the effects introduced by flows along magnetic fieldlines of solar MHD equilibria.

Regarding the *first* purpose, this first article of the series simply illustrated the possibilities that open by a systematic construction of symmetric compressible MHD equilibria through the method presented in chapter 2. Further solutions of Eqs.(5.2.2) (Low et al 1983) and Eqs.(2.3.24) may reveal more interesting classes.

Regarding the *second* purpose, we fused the well known Kippenhahn-Schlüter solution for magnetostatic equilibrium ($\mathbf{V} = \mathbf{0}$), with the corresponding hydrostatic equilibrium solution in a uniform gravitational field ($\mathbf{B} = 0$) producing our hydromagnetic solution; and this one-dimensional MHD solution was shown to have a periodic structure with prominence-like density enhancements (valleys) and loop-like density depletions (summits).

With these two extremes as reference cases, we studied the parametric dependence of the MHD solution by varying the only two parameters on which the solution depends, namely the Mach number M and the plasma β, both computed at the point of maximum density of the configuration. In particular, we found that the more we increase the magnitude of the flow speed at the valleys, M, or equivalently β by keeping M_a = constant, the more the solution departs from the characteristics of a K-S magnetostatic equilibrium solution and approaches the characteristics of a hydrodynamically dominated equilibrium solution. Thus, as M increases,

(i). The *density*, which is always confined in the interval $I = [M^2, 1]$ with $(M < 1)$, tends to beouvome more homogeneous, in particular around the summits of the fieldlines. This may be understood if we recall for comparison that in the K-S equilibrium the density is quite inhomogeneous being in the larger interval $I_m = [0, 1]$, while in the case of pure hydrostatic equilibrium it is homogeneous, everywhere. Thus, as M grows toward 1, the difference between the density at the denser valleys and the lighter summits reduces becoming asymptotically zero in the limit of a pure hydrodynamically dominated equilibrium. Also, in the neighbor of the summits the density tends to be more uniform with the horizontal distance, as M or, β increase, while in the neighbour of the valleys it changes rapidly with the horizontal distance (Figs.5.3b,5.6b).

(ii). The *wavelength* ℓ and *the height* h of the periodic field and stream lines decrease as M increases. For comparison, in the K-S equilibrium $(\ell, h) \to \infty$, while in the case of pure hydrostatic equilibrium $(\ell, h) \to 0$. At this point we are tempted to mention that the recently discovered and striking fibril structure of solar prominences (Ruzdjak

and Tandberg-Hanssen 1990), may be related to this feature of the solution. Noting that the wavelength ℓ of the configuration is related to the strength of the flow Mach number at the valleys, M, we obtain that for M sufficiently small, ℓ may become a very small fraction of the scale height L.

(iii). The *radius of curvature* of the magnetic fieldlines at the valleys decreases as M increases, in order to balance the increased centrifugal force there through an increased magnetic tension force. For the same reason by increasing M, the supporting z-component of the magnetic field, B_z, increases faster with the horizontal distance Y in comparison to the slower hyperbolic tangent increase of $B_z(x)$ in the K-S solution.

(iv). The *flow speed,* V tends to a constant value in a wide interval along the horizontal distance Y around the summits (Figs.5.3d,5.6d). This may be understood, if we recall for comparison, that in the case of pure hydrostatic equilibrium $V_x(x)$ is constant.

(v). All the above trends and properties of the solution are enhanced as *the polytropic index* γ increases from 1 to 5/3. For example, the valleys become steeper by increasing M for larger γ because with a higher polytropic index the pressure gradients are steeper and therefore steeper field gradients are required for support.

Another result is that the flow speed is always subsonic and subalfvénic at the denser and prominence-like magnetically dominated valleys, while it is always supersonic and superalfvénic at the depleted and loop-like summits. The regions of transition from magnetically dominated and subsonic/subalfvénic flows (valleys) to supersonic/superalfvénic and hydro dominated flows (summits), are separated by vertical sheets where the density gradient obtains locally very large values. It is well known that transonic solutions which emerge from nonlinear differential equations (see, Tsinganos and Trussoni 1991, Tsinganos and Sauty, 1991, 1992, 1994) have their subsonic and supersonic parts bordering at singular points. For example, in the classical solar wind theory, Parker (1963), this singular point is an x-type critical point where the flow speed becomes supersonic, while in MHD winds, Tsinganos and Trussoni, (1991) the critical point where the flow speed becomes superalfvénic is a higher order singularity. In our case, the two regimes are separated by two singular points, those wherein $C(\varrho) = 0$, where the density gradient becomes infinite, although the density remains everywhere continuous and finite everywhere.

Chapter 6

2-D MHD EQUILIBRIA IN UNIFORM GRAVITY

6.1 Introduction

High-resolution X-ray and EUV observations, describing in chapter 1, have revealed that the solar transition region and corona are not only radially stratified but also horizontally highly inhomogeneous, consisting of magnetized arcades and loops of various sizes and properties (Reeves et al. 1977; Vaiana & Rosner 1978). One basic aspect of the problem posed by the observation of these loops is the existence and role of plasma flows in them (section 1.5). For example, from the fact that many transition region loops extend over heights much larger than predicted by models without flows (Foukal 1976), indicate that flows play a role in determining their gross properties. Recently, Peres et al. (1992) compared the fitting of the intensities of some EUV transition region emission lines by loops with steady siphon flows relative to those without flows and concluded that siphon flow models of compact active-region loops are in better agreement with the observations.

The purpose of this chapter is to investigate analytically the physical problem, started in the previous chapter, posed by steady MHD flows along magnetic lines in the uniform gravitational field of a vertically stratified and horizontally compressible atmosphere in a somewhat general approach (Tsinagnos et al 1993a,b, Surlantzis & Tsinganos 1993), unconstrained by crucial assumptions such that one-dimensionality and $\beta << 1$. To that goal, we solve in section 6.2.1 by the method of separation of variables the coupled set of the two partial differential equations for the density and magnetic flux function that govern the equilibrium. Attention is focused on the

critical points of this system of coupled equations in section 6.2.2. The topologies of the corresponding solutions are then explored in some detail in section 6.3 in order to isolate the physically interesting cases. The form of the exact solutions with flow is briefly examined in the limit of the simpler similar configuration of magnetostatic equilibrium without flows in section 6.4.1, and the limit of very weak flows in section 6.4.2. In section 6.5.1 we choose the parameters of the solution to be in the same ranges as those inferred from observations of solar coronal loops and in section 6.5.2 explore the change of curvature and footpoint separation of the arcade as the magnitude of the flow at its summit changes. Finally, in section 6.6 the nature of the novel saddle critical point that determines the topologies of the solutions is investigated and the main results are summarized in section 6.7.

6.2 2-D MHD steady flows in uniform gravity

Consider a compressible plasma structure in magnetostatic equilibrium embedded in an isothermal atmosphere with a uniform sound speed V_s. Assume that the plasma is compressible in the horizontal and vertical directions, in a uniform external gravitational field $-g\hat{z}$. In other words, assume that all physical variables depend on the horizontal distance x and the vertical height z in the orthogonal system zxy with z pointing upwards. In the following we write in a convenient form the basic equations governing the equilibrium and examine their critical points, which control their topology.

6.2.1 Governing equations

For field-aligned flows, the equilibrium is governed by the familiar equations for the conservation of mass, magnetic flux and momentum,

$$\nabla \cdot \tilde{\rho}\mathbf{V} = 0\,, \tag{6.2.1a}$$

$$\nabla \cdot \tilde{\mathbf{B}} = 0\,, \tag{6.2.1b}$$

$$\tilde{\rho}(\mathbf{V}\cdot\nabla)\mathbf{V} = -V_s^2\nabla\tilde{\rho} + \frac{(\nabla\times\tilde{\mathbf{B}})\times\tilde{\mathbf{B}}}{4\pi} - \tilde{\rho}g\hat{\mathbf{z}}\,, \tag{6.2.1c}$$

where the gas pressure $\tilde{P}(z,x)$ is written as

$$\tilde{P} = V_s^2\tilde{\rho}\,. \tag{6.2.1d}$$

Assuming for simplicity that the field-aligned flow is in the zx–plane, define the magnetic field in terms of a magnetic flux function $\tilde{A}(z,x)$,

$$\tilde{B}_z = \frac{\partial\tilde{A}(z,x)}{\partial x}\,, \quad \tilde{B}_x = -\frac{\partial\tilde{A}(z,x)}{\partial z}\,. \tag{6.2.2a}$$

A free parameter of the equilibrium is the mass flux density per unit of magnetic flux density. This is formally described in terms of an arbitrary function of $\tilde{A}$, $\Psi_{\tilde{A}}(\tilde{A})$, such that

$$4\pi\tilde{\rho}\mathbf{V} = \Psi_{\tilde{A}}(\tilde{A})\tilde{\mathbf{B}}\,. \tag{6.2.2b}$$

With Eqs.(6.2.2), force balance across and along streamlines requires, respectively,

$$\nabla^2\tilde{A} - \Psi_{\tilde{A}}\left[\frac{\partial}{\partial z}\left(\frac{\Psi_{\tilde{A}}}{4\pi\tilde{\rho}}\frac{\partial\tilde{A}}{\partial z}\right) + \frac{\partial}{\partial x}\left(\frac{\Psi_{\tilde{A}}}{4\pi\tilde{\rho}}\frac{\partial\tilde{A}}{\partial x}\right)\right] + 4\pi\tilde{\rho}\frac{dE}{d\tilde{A}} = 0 \tag{6.2.3a}$$

$$V_s^2 \ln\left(\frac{\tilde{\rho}}{\tilde{\rho}_o}\right) + gz + \frac{V^2}{2} = E(\tilde{A})\,, \tag{6.2.3b}$$

where $\tilde{\rho}_o$ is a constant and $F(\tilde{A})$ an arbitrary function of $\tilde{A}(z,x)$ (Tsinganos 1982). The various possible functional forms of $\Psi_{\tilde{A}}(\tilde{A})$ and $E(\tilde{A})$ give all possible planar MHD equilibria. It occurred to us that an interesting class of novel MHD equilibria is obtained by choosing the two free functions $\Psi_{\tilde{A}}(\tilde{A})$ and $E(\tilde{A})$ as follows,

$$\Psi_{\tilde{A}}(\tilde{A}) = 4\pi k\tilde{A} \quad \text{and} \quad E(\tilde{A}) = V_s^2 \ln\left|\frac{\tilde{A}}{\tilde{A}_o}\right|^{\frac{2(\xi-1)}{\xi}}, \tag{6.2.4}$$

with k, $\tilde{A}_o$ and ξ constants. An interesting special subclass of the above equilibria described by Eqs.(6.2.3–6.2.4) is the one where all physical quantities $\mathcal{Q}(z,x)$ can be written as $\mathcal{Q}(z,x) = \mathcal{X}(x)\mathcal{Z}(z)$. In particular, it is physically interesting to search for MHD equilibria where the plasma and magnetic pressures fall exponentially with the vertical height z, i.e.,

$$\tilde{\rho}(z,x) = \rho(x)e^{-\frac{\xi z}{L}}\,, \quad \tilde{P}(z,x) = P(x)e^{-\frac{\xi z}{L}}\,, \tag{6.2.5a}$$

and

$$\tilde{A}(z,x) = A(x)e^{-\frac{\xi z}{2L}}\,, \quad \tilde{B}_i(z,x) = B_i(x)e^{-\frac{\xi z}{2L}}\,, \quad i = x,z \tag{6.2.5b}$$

where L is the constant scale height, $L = V_s^2/g$ and have introduced the positive parameter $\xi > 0$ which controls the decline of the density and magnetic field with the height z. By substituting the above z-dependence of $\tilde{\rho}$ and $\tilde{A}$ in Eqs.(6.2.3) we obtain for the x-dependent parts of the density and flux function, $\rho(x)$ and $A(x)$, respectively,

$$\left(1 - \frac{4\pi k^2A^2}{\rho}\right)\frac{d^2A}{dx^2} + \frac{\xi^2 A}{4L^2} - \frac{4\pi k^2A^2}{\rho}\left[\left(\frac{dA}{dx}\right)^2 - \frac{A}{\rho}\frac{dA}{dx}\frac{d\rho}{dx}\right] + \frac{8\pi\rho V_s^2(\xi-1)}{\xi|A|} = 0\,, \tag{6.2.6a}$$

$$\ln\left(\frac{\rho}{\tilde{\rho}_o}\right)+\frac{k^2A^2}{2V_s^2\rho^2}\left[\left(\frac{dA}{dx}\right)^2+\frac{\xi^2A^2}{4L^2}\right]=\frac{2(\xi-1)}{\xi}\ln\left|\frac{A}{A_o}\right| \tag{6.2.6b}$$

Differentiating Eq.(6.2.6b) we obtain,

$$\left\{\frac{1}{\rho}-\frac{k^2A^2}{V_s^2\rho^3}\left[\left(\frac{dA}{dx}\right)^2+\frac{\xi^2A^2}{4L^2}\right]\right\}\frac{d\rho}{dx}$$

$$+\frac{k^2A}{V_s^2\rho^2}\left\{\left(\frac{dA}{dx}\right)^2+A\frac{d^2A}{dx^2}+\frac{\xi^2A^2}{L^2}-\frac{2(\xi-1)}{\xi}\frac{V_s^2\rho^2}{k^2A^2}\right\}\frac{dA}{dx}=0\,, \tag{6.2.7}$$

and substituting d^2A/dx^2 from Eq.(6.2.6a) in the above equation, we find finally

$$\frac{\rho}{A}\frac{dA}{d\rho}=\frac{\left[\frac{2(\xi-1)}{\xi}\ln\left|\frac{A}{\tilde{A}_o}\right|-\ln\left(\frac{\rho}{\tilde{\rho}_o}\right)\right]+\frac{2\pi k^2A^2}{\rho}-\frac{1}{2}-\frac{\pi\xi^2k^4A^6}{2V_s^2L^2\rho^3}}{\left[\frac{2(\xi-1)}{\xi}\ln\left|\frac{A}{\tilde{A}_o}\right|-\ln\left(\frac{\rho}{\tilde{\rho}_o}\right)\right]-\frac{(\xi-1)}{\xi}-\frac{\pi\xi^2k^4A^6}{2V_s^2L^2\rho^3}}\,, \tag{6.2.8}$$

An integration of Eq.(6.2.8) gives the functional relation of A and ρ. However, to obtain some physical insight into the solution, in the following we shall express Eq.(6.2.8) in a more convenient form in terms of appropriate physical variables. Thus, define the Mach numbers associated with V_x and V_z as

$$M_x\equiv\frac{V_x}{V_s}=\frac{\xi k}{2LV_s}\frac{A^2}{\rho}\,,\qquad M_z\equiv\frac{V_z}{V_s}=\frac{kA}{\rho V_s}\frac{dA}{dx}\,, \tag{6.2.9a}$$

such that the square of the total Mach number is

$$M^2\equiv M_x^2+M_z^2=2\ln\left[\frac{\left(A/\tilde{A}_o\right)^{\frac{2(\xi-1)}{\xi}}}{\rho/\tilde{\rho}_o}\right]\,. \tag{6.2.9b}$$

Note that the magnitude of the Mach number M measures the effect of the flows in modifying magnetostatic equilibria. Thus, in the limit $M\to 0$, the above expression should reduce to the corresponding relation between the density and magnetic flux function in the case of magnetostatic equilibrium without flows, as we discuss in section 4.

Next, the square of the Alfvén number is

$$M_a^2=\frac{V^2}{B^2/4\pi\rho}=4\pi k^2\frac{A^2}{\rho}=\lambda M_x\,, \tag{6.2.10}$$

with λ a dimensionless constant,

$$\lambda \equiv \frac{8\pi k V_s L}{\xi} = \frac{V_x V_s}{V_a^2}\Big|_{B_z=0} = \frac{\beta_o M_o}{2} = \frac{M_{ao}^2}{M_o}, \tag{6.2.11}$$

where β_o, M_{ao} and M_o represent the plasma β, and the Alfvén and Mach numbers at the valleys and summits of a fieldline configuration where $B_z = V_z = 0$ and the field is horizontal. Note that since the Alfvén number represents the relative strength of fluid and magnetic effects, small values of λ correspond to magnetically dominated states while large values of λ give dynamically dominated states. On the other hand, the plasma β gives for field-aligned flows the ratio of the Alfvén and Mach numbers, $M_a^2 = \beta M^2/2$.

Using the variables M_a^2 and M^2 we can write Eq.(6.2.6b) in terms of the angle θ a fieldline makes with the horizontal,

$$\tan^2\theta(x) \equiv \left[\frac{B_z}{B_x}\right]^2 = \frac{\lambda^2 M^2 - M_a^4}{M_a^4}. \tag{6.2.12}$$

Evidently solutions exist only when $\lambda^2 M^2 - M_a^4 > 0$. On the other hand, Eq.(6.2.8) can be written as

$$\frac{\rho}{A}\frac{dA}{d\rho} = \frac{M^2 + M_a^2 - M_a^6/\lambda^2 - 1}{M^2 - 2 + 2/\xi - 2M_a^6/\lambda^2} \tag{6.2.13}$$

or,

$$\frac{2}{M_a^2}\frac{dM_a^2}{dM^2} = \frac{\xi(M^2/2 + M_a^2) - 1}{[\xi(M^2/2 + M_a^2) - 1] - [M^2 + M_a^2 - M_a^6/\lambda^2 - 1]}. \tag{6.2.14}$$

Using Eq.(6.2.14), we can write Eq.(6.2.12) as,

$$\pm\frac{M_a^2}{2}\frac{dM^2}{d\mathrm{x}} = \frac{[\xi(M^2/2 + M_a^2) - 1] - [M^2 + M_a^2 - M_a^6/\lambda^2 - 1]}{(M^2 + M_a^2 - M_a^6/\lambda^2 - 1)}\sqrt{\lambda^2 M^2 - M_a^4}, \tag{6.2.15}$$

where $\mathrm{x} = x/L$ and we have assumed that $M^2\lambda^2 - M_a^4 \geq 0$. Multiplying Eqs.(6.2.14)–(6.2.15) we may obtain a third equation,

$$\pm\frac{dM_a^2}{d\mathrm{x}} = \frac{\xi(M^2/2 + M_a^2) - 1}{M^2 + M_a^2 - M_a^6/\lambda^2 - 1}\sqrt{\lambda^2 M^2 - M_a^4}. \tag{6.2.16}$$

The above set of three equations (6.2.14)–(6.2.16) determines $M_a(\mathrm{x})$ and $M(\mathrm{x})$ for given values of the parameters ξ and λ. Two initial conditions are also needed, namely

the values of the Mach number M and Alfvén number M_a at a given horizontal position x_o. However, since x does not appear explicitly in equations (6.2.14)–(6.2.16), we are free to choose the initial value of x where M_a and M are prescribed, say, at $x_0 = 0$. Note also that Eq.(6.2.14) may be solved independently of the other two Eqs.(6.2.15)–(6.2.16) and its solution topology can be studied in the $M_a - M$ phase plane.

6.2.2 Critical Points

A topological analysis of Eqs.(6.2.14)–(6.2.16) shows that they have three critical points where their numerator and denominator vanish simultaneously. In the following we analyze in detail these critical points which control the topology of the solutions.

First, the vanishing of the numerator and denominator of Eq.(6.2.16) gives the following two relations between the squares of the two Mach numbers,

$$M_a^2 + \frac{M^2}{2} = \frac{1}{\xi}\,, \tag{6.2.17}$$

$$M^2 + M_a^2 - \frac{M_a^6}{\lambda^2} - 1 = 0\,. \tag{6.2.18}$$

Note that, when Eqs.(6.2.17) and (6.2.18) hold, the numerator and denominator of Eqs.(6.2.14) and (6.2.15) vanish simultaneously, since,

$$\xi\left[\frac{M^2}{2} + M_a^2\right] - \left[M^2 + M_a^2 - \frac{M_a^6}{\lambda^2}\right] = 0\,. \tag{6.2.19}$$

Therefore, the intersection of the two curves given by Eqs.(6.2.17) and (6.2.18) determines the square of the Alfvén number at the critical point, $M_a^{\star 2}$, through the following cubic for $M_a^{\star 2}$

$$M_a^{\star 2} + \frac{M_a^{\star 6}}{\lambda^2} = \frac{2-\xi}{\xi}\,, \tag{6.2.20}$$

i.e.,

$$M_a^{\star 2} = \left\{\frac{(2-\xi)\lambda^2}{2\xi}\right\}^{1/3}\left\{\left[1+\sqrt{1+\frac{4\lambda^2\xi^2}{27(2-\xi)^2}}\right]^{1/3} + \left[1-\sqrt{1+\frac{4\lambda^2\xi^2}{27(2-\xi)^2}}\right]^{1/3}\right\}.$$

Evidently, a critical point exists at finite $M_a^{\star 2} > 0$ only when $0 < \xi < 2$, while for $\xi > 2$ we have $M_a^{\star 2} < 0$, i.e., the critical point is in a physically uninteresting part of the phase plane (M_a^2, M^2). The *nature* of this critical point at $(M_a^\star > 0,\ M^\star > 0)$ can be analyzed by making the usual expansion in Eq.(6.2.14) $M_a = M_a^\star(1+\mu)$, $M = M^\star(1+\epsilon)$ with

$\mu, \epsilon << 1$. A second-order algebraic equation for $\mu/\epsilon \equiv s$ is obtained giving the slope at this critical point as

$$\frac{2M_a^{\star 2}}{M^{\star 2}}\left[1-\frac{1}{\xi}+\frac{3M_a^{\star 4}}{\xi\lambda^2}\right]s^2+\left[1-\frac{2}{\xi}-M_a^{\star 2}\right]s-\frac{M^{\star 2}}{2}=0 \qquad (6.2.21)$$

and for $0 < \xi < 2$ the critical point is of X-type.

The location of the critical point $(M_a^\star, M^\star)$ on the plane $M_a^2 - M^2$ is found as the intersection of the two curves (6.2.17) and (6.2.18). For a given ξ of the monoparametric family of lines expressed by Eq.(6.2.17), the critical point is on the straight line which intersects the two axes at $M^2 = 2/\xi$ and $M_a^2 = 1/\xi$. The smallest possible value of the Mach number on this line occurs at the largest allowed value of ξ, i.e., $M = 1$ for $\xi = 2$. On the other hand, the exact location of the critical point on this line depends on the value of λ, through the curves given by Eq.(6.2.18) which also form a monoparametric family depending now solely on λ. For a magnetically dominated state (small λ), $M_a^{\star 2} \to 0$, $M^{\star 2} \to 2/\xi$; and, for a dynamically dominated state (high values of λ), $M_a^{\star 2} \to 1/\xi$, $M^{\star 2} \to 0$. For $\xi \to 2$, $(M_a^\star, M^\star) \to (0, 1)$ while as $\xi \to 0$, $M_a^\star$ and $M^\star$ increase.

Second, the numerator of Eqs.(6.2.15) and (6.2.16) vanishes also when $\lambda^2 M^2 = M_a^4$, which when combined with the simultaneous vanishing of the denominator, Eq.(6.2.18), gives a second critical point at the sonic transition,

$$M_a^2 = \lambda\,, \quad M = 1\,. \qquad (6.2.22)$$

The electric current density $\mathbf{J} = \nabla \times \mathbf{B}$ and vorticity $\omega = \nabla \times \mathbf{V}$ have only y-components for these planar and symmetric fields, $\mathbf{J} = J_y \hat{\mathbf{y}}$, $\omega = \omega_y \hat{\mathbf{y}}$. In order to appreciate better the physical implications of the existence of the two critical points $(M_a^\star, M^\star)$ and $(M_a^2 = \lambda, M = 1)$, it is instructive to consider for a moment the expressions for J_y,

$$J_y = \frac{\xi^2 \tilde{A}}{2L^2}\frac{\lambda^2}{M_a^2}\left[\frac{(\lambda^2 M^2 - M_a^4)(M^2/2 + M_a^2 - 1/\xi)}{\lambda^2(1-M_a^2)(M^2 + M_a^2 - M_a^6/\lambda^2 - 1)} - \frac{(M^2/2 + M_a^2 - 1/\xi)}{(1-M_a^2)} - 1\right], \qquad (6.2.23a)$$

and ω_y,

$$\omega_y = \frac{\lambda^2}{8\pi k M_a^2}\left[\frac{(\xi(M^2/2 + M_a^2) - 1)(M_a^4 - \lambda^2)}{\lambda^2(M^2 + M_a^2 - M_a^6/\lambda^2 - 1)} + 1\right]. \qquad (6.2.23b)$$

J_y and ω_y diverge everywhere along the curve given by Eq.(6.2.18) with the exception of two points; *first*, at the intersection of this curve with the curve (6.2.17), i.e., at

the critical point $(M^\star, M_a^\star)$ and *second*, at the sonic point $M = 1$, $M_a^2 = \lambda$. In addition, J_y is finite at the second intersection of (6.2.18) with the curve determining the summits/valleys of the equilibrium where $M_a^2 = 1$ and $M = 1/\lambda$, but ω_y diverges there. In other words, the sonic point (6.2.22) and the critical point at $(M_a^\star, M^\star)$ are the only two positions where the electric current and the fluid vorticity are simultaneously finite along the curve given by Eq.(6.2.18). These two points coincide in the case $\lambda = (2-\xi)/2\xi$.

A *third* singularity of Eqs.(6.2.14) and (6.2.15) exists evidently at $M_a = M = 0$, i.e., at the origin of the (M_a^2, M^2)–plane. By writing again $M_a^2 = \mu$, $M^2 = \epsilon$ with $\mu, \epsilon << 1$ we find that for $\xi \neq 1$ the corresponding critical point at this singularity is of *nodal-type* where the two characteristic slopes are $s = \mu/\epsilon = -1/2$ and $s = 0$. On the other hand, when $\xi = 1$, the critical point at this singularity is of *star-type* and all slopes are allowed.

6.3 Solution Topologies

In Figs.(6.1), (6.2), (6.3) we show some representative topologies of the solutions of Eqs.(6.2.14)–(6.2.16) in the planes (M_a^2, M^2) and (M, X) for some sets of values of the two parameters ξ and λ of our model. Several groups of curves appear in these planes corresponding to different classes of physical solutions. However, the following analysis makes it clear that, out of this large set of mathematical solutions to Eq.(6.2.14), only a few are physically interesting. To that goal, and in order to analyze the properties of all solutions encountered in the plane (M_a^2, M^2), we proceed as follows,

First, we distinguish the two critical branches (those passing through the critical point $M_a^\star$, $M^\star$) and classify the rest of the other branches which are adjacent to the critical ones in four groups labeled as L (left), R (right), U (up) and D (down).

Second, we plot the two curves given by Eqs.(6.2.17) and (6.2.18), the intersection of which determines the critical point. In Figs.(6.1a,6.1c,6.1d) Eq.(6.2.17) corresponds to the straight dashed line while Eq.(6.2.18) to the parabolic dashed curve. As $\lambda \to 0$, the critical point moves toward the lower right end of the line (6.2.17) while for large λ it moves towards its upper left end. On the other hand, as $\xi \to 2$ the critical point moves towards the point $(M = 1, M_a = 0)$ (*e.g.*, Fig.6.2) and away from it as $\xi \to 0$. To avoid having a solution where the electric current and the fluid vorticity diverge, we shall select only those branches which do not intersect the curve given by Eq.(6.2.18). Only branches intersecting (6.2.18) at the sonic and critical points will be accepted as physically interesting solutions.

Third, we isolate the shaded area bounded by the curve $M^2\lambda^2 - M_a^4 = 0$ which determines the allowed part of the plane (M_a^2, M^2) where $M^2\lambda^2 - M_a^4 \geq 0$ [*c.f.* Eq.(6.2.12)].

Note that this curve also determines the locations where the field lines are horizontal. Thus, solutions which intersect this curve may have a valley, or a summit there. Branches with only one such intersection may correspond to loop-like solutions with one summit, or, prominence-like solutions with one valley only, while those with two intersections may correspond to periodic solutions.

Fourth, in order to decide if a solution starting at a point where $B_z = 0$ has a valley or a summit there, we shall use Eq.(6.2.10), which requires that along a streamline $\tilde{A}(x,z) =$ constant the density is inversely proportional to the square of the Alfvén Mach number M_a

$$\tilde{\rho}(x,z)\Big|_{\tilde{A}(x,z)=const.} \propto \frac{1}{M_a^2}\,. \tag{6.3.1}$$

Therefore, if M_a decreases as we move away from the curve $M_a^2 = \lambda M$, then the density increases along a given fieldline and we have a loop-like solution (summit) which is Rayleigh-Taylor stable in the gravitational field; conversely, the density should decrease and M_a should increase as we move away from a prominence-like solution (valley) for stability.

Finally, upper and lower bounds can be easily placed on the Mach and Alfvén numbers of the flow at the above locations where the magnetic field lines are horizontal, $B_z = 0$. For example, from the z-component of the momentum equation by substituting $V_z = V_x \tilde{B}_z/\tilde{B}_x$ we obtain the following relation for M_a at those points where $\tilde{B}_z = 0$,

$$\frac{2(1-M_a^2)}{\left[\xi + \dfrac{2(\xi-1)\lambda^2}{M_a^2}\right]} = -\frac{\tilde{B}_x}{\dfrac{\partial \tilde{B}_z}{\partial \mathrm{x}}}\,. \tag{6.3.2}$$

Thus, at the local minima of the fieldlines (valleys) where $[\tilde{B}_x \partial \tilde{B}_z/\partial \mathrm{x}] > 0$, we have

$$M_a^2 > 1 \qquad \text{if} \qquad \xi \geq 1\,, \tag{6.3.3a}$$

and

$$(M_a^2 - 1)\left(M_a^2 - \frac{2\lambda^2(1-\xi)}{\xi}\right) > 0 \quad \text{if} \quad \xi < 1\,. \tag{6.3.3b}$$

On the other hand, at the local maxima of the fieldlines (summits) where $[\tilde{B}_x \partial \tilde{B}_z/\partial \mathrm{x}] < 0$ we find instead

$$M_a^2 < 1 \qquad \text{if} \qquad \xi \geq 1\,, \tag{6.3.4a}$$

and

$$(M_a^2 - 1)\left(M_a^2 - \frac{2\lambda^2(1-\xi)}{\xi}\right) < 0 \quad \text{if} \quad \xi < 1\,. \tag{6.3.4b}$$

It follows that *the flow is always subalfvénic at the summits of the arcades and superalfvénic at the lower points of the valleys, if* $\xi \geq 1$.

On the other hand, by taking the derivative with respect to x in the x-component of the momentum balance equation we find at the points where $B_z = 0$ and $d\tilde{\rho}/dx = 0$,

$$(V_s^2 - V_o^2)\frac{\partial^2 \tilde{\rho}}{\partial \mathrm{x}^2} = -\frac{1}{4\pi}\left(\frac{\partial \tilde{B}_z}{\partial \mathrm{x}}\right)^2 - \xi \tilde{B}_x \frac{\partial \tilde{B}_z}{\partial \mathrm{x}}\left[\frac{1}{8\pi} + \frac{\tilde{\rho}V_x^2}{B_x^2}\right]. \tag{6.3.5}$$

It follows that at the locations where the field lines are horizontal and have a local minimum (valley-type) such that $\tilde{B}_x \partial \tilde{B}_z/\partial \mathrm{x} > 0$ the flow is subsonic, $V_o < V_s$, and $M_a^2 < \lambda$ if the density is locally maximum, $\partial^2 \tilde{\rho}/\partial \mathrm{x}^2 < 0$. If the density is locally minimum, $\partial^2 \tilde{\rho}/\partial \mathrm{x}^2 > 0$, the flow may or may not be supersonic. Note that in the absence of vertical stratification ($\xi \to 0$), Eqs.(6.3.2) and (6.3.5) give subalfvénic/subsonic flow at the valleys and superalfvénic flows at the summits, as discussed in the previous chapter. In the following section we make use of the above limits in order to select the physically interesting solutions of Eq.(6.2.14).

The analysis is simplified if we consider separately several cases, according to the value of the parameter ξ.

6.3.1 Arcades with scale height ξ in the interval $1 \leq \xi < 2$

In this case, all intersections of the various solutions with the bounding curve $M_a^2 = \lambda M$ correspond to valleys if this intersection is in the superalfvénic regime, because of constraint in Eq.(6.3.3a), and to summits if it is in the subalfvénic regime, because of constraint in Eq.(6.3.4a). Furthermore, note that for each value of ξ there is a characteristic value of λ

$$\lambda \equiv \lambda_{\mathrm{crit}} = \frac{2-\xi}{2\xi}, \tag{6.3.6}$$

for which the curve $M_a^2 = \lambda M$ (where $B_z = 0$) crosses the critical point and the two critical points are at the sonic transition. Therefore, we may distinguish three subcases according to the value of λ relative to λ_{crit}.

The critical case, $\lambda = \lambda_{\mathrm{crit}}$, Figs.(6.1a,6.1b). Consider first the two critical lines of positive and negative slope in the representative example of this class, namely Fig.(6.1a) plotted for $\xi = 1.7$, $\lambda = 0.08$. Since they are bounded by the curve $M_a^2 = \lambda M$ in the subalfvénic regime they correspond to solutions with a summit there [*c.f.* Eq.(6.3.4a)]. The critical point is at the sonic transition in this special case, $M^\star = 1$, while at this summit of loop-like fieldlines the Alfvén number reaches the value $M_a^\star = \sqrt{\lambda_{\mathrm{crit}}}$. In Fig.(6.1b) we have plotted with solid curves the Mach

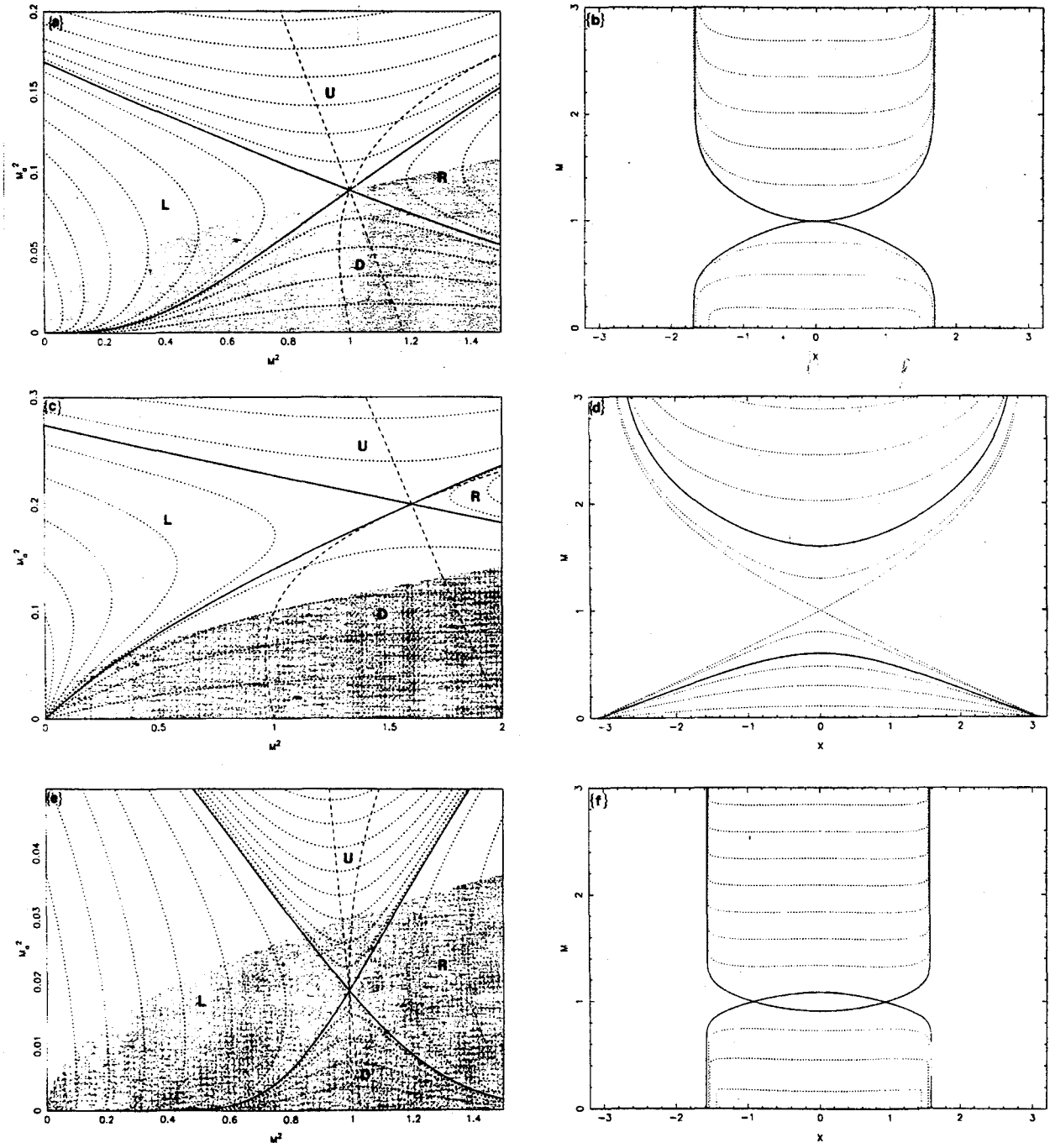

Figure 6.1: *Topology of solutions in* $(M_a^2 - M^2)$ *plane (left panels) and* (M, x) *plane (right panels). In (a-b)* $\xi = 1.7$ *and* $\lambda = 0.088$, *in (c-d)* $\xi = 1$ *and* $\lambda = 0.1$, *while in (e-f)* $\xi = 1.95$, $\lambda = 0.03$. *The new critical point in (a), (c) and (e) is at the intersection of the two dashed curves, while the shaded area corresponding to allowed solutions is bounded by the curve where the field is horizontal (summits or valleys). The classical sonic critical point at* $(M_a^2 = \lambda,\ M = 1)$ *can be seen in the* (M, x)*–plane of corresponding panels (b), (d), (f).*

number of the flow, $M(\mathrm{x})$, for these two critical solutions by arbitrarily setting $\mathrm{x} = 0$ at the positions where $B_z = 0$. Note that along the critical line of positive slope the flow is everywhere subsonic, while along the critical line of negative slope the flow is everywhere supersonic.

Two other physically interesting classes of solution can be constructed from the L and R-branches, and their Mach number $M(\mathrm{x})$ is also plotted in Fig.(6.1b) with dotted curves. These branches also correspond to loop-like solutions with the maximum flow speed at their summits everywhere subsonic in L-group and everywhere supersonic in R-group. Along those branches (L) and (R), as well as along the critical solutions, the density increases as we move away from the summit along the loop and down the gravitational field, because M_a decreases and therefore ρ increases in view of (6.3.1). This makes solutions (L) and (R) together with the two critical solutions Rayleigh-Taylor stable in the gravitational field. Note that of all R-branches only those which do not intersect the curve given by Eq.(6.2.18) where the electric current diverges (*c.f.* Eq. 6.2.22a) are acceptable.

Solutions (U) are not interesting because they do not belong to the physical domain where $\lambda^2 M^2 - M_a^4 \geq 0$ [shaded area in Fig.(6.1a)]. Finally branches (D), which have magnetic lines without any valley or summit, may be used only for shocked solutions. For instance, in a loop with nonsymmetric physical conditions about the plane $\mathrm{x} = 0$, the flow following the critical line of negative slope, and after crossing the critical point and becoming supersonic following the critical line of negative slope, may jump through a shock transition to one of the appropriate D-branches. Such shocked solutions, however, are outside the scope of this paper and will be considered in the future. Altogether then, we are left with the two critical branches as well as with L and R-branches as the potentially physically interesting loop-like solutions.

The subcritical case, $\lambda < \lambda_{\mathrm{crit}}$, Figs.(6.1c,6.1d). The picture changes slightly in the subcritical case, $\lambda < \lambda_{\mathrm{crit}}$. In the plots (6.1c,d) we show such a representative subcritical case with, say, $\xi = 1$, $\lambda = 0.1$, where the bounding curve $M_a^2 = \lambda M$ passes below the critical point in the (M_a^2, M^2) plane. The two critical curves are always bounded at $M_{ao} < 1$ and they correspond to loop-like solutions with a density minimum at their summits – the intersection of these branches with the curve $M_a^2 = \lambda M$. As may also be seen from Fig.(6.1d), the maximum speed is subsonic at the summit of the critical solution with positive slope and supersonic at the summit of the solution corresponding to a critical curve of negative slope (solid curves in Fig.6.2b).

Other physically interesting classes of solution correspond to L, R and D-branches, are plotted with dotted curves in Figs.(6.1c,6.1d). The group of branches (R), the supersonic curves of group (D) where J_y is finite and the critical solution of negative

slope, correspond to supersonic loop-like solutions. For group (L) and the subsonic curves of (D) wherein J_y is finite, together with the critical solution of positive slope, the density increases as we move away from the summit along the loop and down in the gravitational field. The electric current density J_y is finite everywhere along all these solutions. The last group of solutions (U) is not physically interesting because in the domain of branches (U) $\lambda^2 M^2 - M_a^4 < 0$. Note that shocked solutions also exist in this case through the only transonic branch of (D), i.e., the one tangent to the bounding curve $M_a^2 = \lambda M$ at $M = 1$.

The supercritical case, $\lambda > \lambda_{\rm crit}$, Figs.(6.1e,6.1f). Consider next a representative supercritical case, say, $\xi = 1.95$, $\lambda = 0.033$, where the bounding curve $M_a^2 = \lambda M$ passes above the critical point in the (M_a^2, M^2) plane. In this case the characteristic (critical) speed is always subsonic. The two critical curves are again bounded at $M_{ao} < 1$, which means that they correspond to loop-like solutions with a density minimum at their summits (the intersection of these branches with the curve $M_a^2 = \lambda M$). Contrary to the previous case of $\lambda \leq \lambda_{\rm crit}$ however, now the maximum speed is supercritical at the summit of the solution corresponding to the critical curve of positive slope and subcritical at the summit of the critical solution with negative slope, Fig.(6.1f) (two solid curves).

On the other hand, two other physically interesting classes of solution correspond again to the L and R-branches, also plotted with dotted curves in Fig.(6.1f). They too correspond to loop-like solutions with the maximum flow speed at their summits everywhere subcritical in L-group and everywhere supercritical in R-group. Along these branches (L) and (R), the density increases as we move away from the summit along the loop and down in the gravitational field, because M_a decreases and therefore ρ increases [*c.f.* Eq.(6.3.1)]. Similarly to the previous case $\lambda \leq \lambda_{\rm crit}$, the electric current density J_y is finite along branches (L) and (R), as well as in the two critical ones. Therefore, again the two critical branches together with those of the group (L) and (R) are physically acceptable.

Note that for each λ the family of subcritical solutions (L) exists up to a maximum value of the Alfvén number at their summit, $M_{ao}^{\rm max}$. Above this limit which does not exist if $\lambda \leq \lambda_{\rm crit}$, physical solutions do not exist and the loop may be disrupted by centrifugal forces. Thus, in the supercritical case, we are not completely free to choose the initial conditions at the top of the loop. In this context note that it has been shown that solar coronal mass ejections can be initiated by the dynamic evolution and shearing of the footpoints of a coronal magnetic field (Low 1981; Mikic 1988; Priest 1988). Here we have also shown that if the magnitude of the flow speed along the field in the arcade increases, the height of the arcade increases too and above a limit there

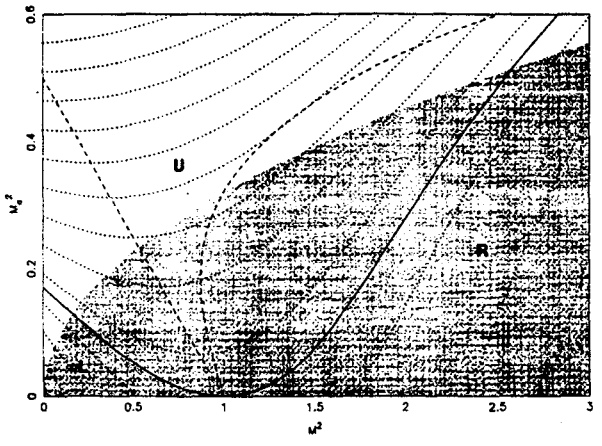

Figure 6.2: *Topology of solutions in* $(M_a^2 - M^2)$ *plane for the limiting value* $\xi = 2$ *and* $\lambda = 0.32$. *The critical point is at* $(M_a = 0, M = 1)$ *while the shaded area corresponds to allowed solutions.*

is no equilibrium with the possibility that the arcade erupts.

Finally, the other two groups of solution (U) and (D) are not physically interesting because branches (U) are bounded by the curve $M_a^2 = \lambda M$ at two successive summits, while in (D) the magnetic lines do not have any valley or summit at all (there are no intersections with the bounding curve $M_a^2 = \lambda M$). Branches (D) may be used only for shocked solutions, as in the critical case.

6.3.2 The case $\xi = 2$ and the strongly stratified case $\xi > 2$

In Fig.(6.2) we plot the topology of the solutions in the phase plane (M_a^2, M^2) for the limiting case $\xi = 2$. This is a degenerate case where the critical point is at $M_a = 0$, $M = 1$ while the two critical branches are joined and tangent to the axis $M_a = 0$ (solid line). Only this critical solution together with adjacent solutions (L) and (R) correspond to arcades with minimum density at their summits. However, note that these solutions have the peculiar property that the velocity monotonically increases along branches (L) - decreases along branches (U) - and at their footpoints $M_a = 0$ but $V_a \longrightarrow \infty$.

On the other hand, for $\xi > 2$, where the critical point has changed to a focus and moved to the $M_a^2 < 0$ subplane, acceptable solutions do not exist any longer. Thus, loop-like solutions can be found only for the limited range of the stratification parameter, $\xi \leq 2$.

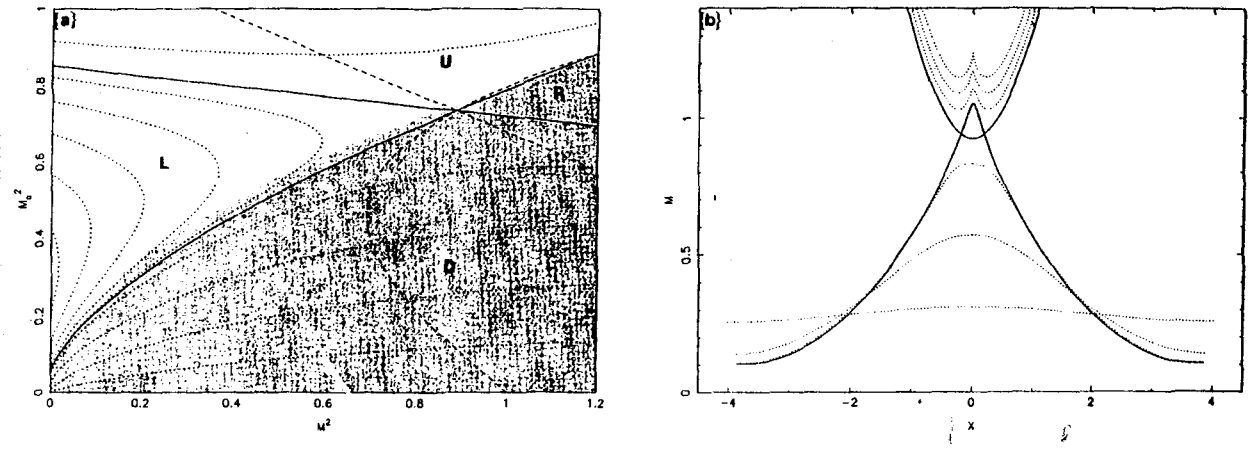

Figure 6.3: *Topology of solutions in $(M_a^2 - M^2)$ plane in (a) and (M, X) plane in (b), as in Fig.(6.1) but now for $\xi = 0.85$ and $\lambda = 0.77$. Note that periodic solutions – subsonic dotted L-branches in (b) and the critical branch of positive slope – have their valleys in (b) separated by more than 2π.*

6.3.3 The weakly stratified case $\xi < 1$

In all previous stratified atmospheres corresponding to $1 \leq \xi \leq 2$ we obtained loop-like solutions with moderate speeds as the only physically interesting solutions in the plane (M_a, M). In the rather weakly stratified atmospheres where $0 < \xi < 1$ we found that such low-speed loop solutions do not exist at all. In the place of arcades, only periodic solutions were found instead. Similar to the case $1 \leq \xi \leq 2$, for each value of ξ there are now two characteristic values of λ for which the curve $M_a^2 = \lambda M$ (where $B_z = 0$) crosses the critical point,

$$\lambda_{\rm crit}^{(1)} = \frac{2-\xi}{2\xi}\,, \quad \lambda_{\rm crit}^{(2)} = \sqrt{\frac{\xi}{2(1-\xi)}}\,. \tag{6.3.7}$$

As before, we may distinguish several subcases according to the value of λ relative to $\lambda_{\rm crit}^{(1)}$ and $\lambda_{\rm crit}^{(2)}$. For $2/3 < \xi < 1$ we have that $\lambda_{\rm crit}^{(1)} < \lambda_{\rm crit}^{(2)}$ and obtain periodic solutions which do not have points where the electric current density J_y diverges. Such a case is illustrated in Figs.(6.3) where we show the topology of the solutions in the (M_a^2, M^2) and (M, x) planes for $\xi = 0.85$ and $\lambda = 0.77$. Note that of all branches on this plane only the group of branches labeled (L) are physically acceptable as periodic solutions with a valley and a summit. Solutions labeled (R) are arcade-like solutions but the flow is supersonic and reaches large speeds along these arcades.

On the other hand, for $0 < \xi < 2/3$ all periodic solutions have two points where $J_y \longrightarrow \infty$. Thus, in the limit of $\xi \longrightarrow 0$ we recover the main features of the results

obtained in the previous chapter.

6.4 Useful limits of the Present Analysis

As is well known, fully two-dimensional exact MHD solutions for compressible and stratified plasmas with flows are not available in the literature to this day, because of the intrinsic mathematical difficulty of solving the coupled nonlinear equations governing this problem. On the other hand, the special and simpler cases of magnetostatic equilibrium without flows ($\lambda = 0$), or full MHD equilibrium in the approximation of low-M_a flows ($\beta << 1$), have received considerable attention because of their potential application to observed hydromagnetic structures in the active corona of the Sun.

In this analysis, we did not make any approximation about the magnitude and role of flows. Evidently, the results may apply to configurations of any β and M. Thus, in order to establish the connection of the present general analysis to other studies performed under mathematically simplifying assumptions, such as the above, in this section we briefly examine for comparison two such limiting cases. In the first, we set the magnitude of the flow equal to zero so that we have a situation of pure magnetostatic equilibrium without flows. And in the second, we examine the form of our solution when the plasma β is small, $\beta << 1$.

6.4.1 Magnetostatic Equilibrium, $M = 0$

For a planar magnetic field expressed in terms of a magnetic flux function $\tilde{A}(z, x)$ as in Eqs.(6.2.2) and an isothermal atmosphere with gas pressure $\tilde{P}(z, x) = V_s^2 \tilde{\rho}(z, x)$, force balance across the magnetic field lines is obtained from Eq.(6.2.3a) with $\Psi_{\tilde{A}} = 0$,

$$\nabla^2 \tilde{A}(x, z) + 4\pi \tilde{\rho} \frac{dE}{d\tilde{A}} = 0\,, \tag{6.4.1a}$$

while Eq.(6.2.3b) for force balance along the magnetic field lines reduces to

$$V_s^2 \ln\left(\frac{\tilde{\rho}}{\tilde{\rho}_o}\right) + gz = E(\tilde{A})\,, \tag{6.4.1b}$$

with $\tilde{\rho}_o$ a constant and $F(\tilde{A})$ again an arbitrary function of $\tilde{A}(x, z)$. The set of the coupled equations (6.4.1) determines all possible planar magnetostatic equilibrium states in a uniform gravity for the various functional forms of $F(\tilde{A})$, as is well known. In our case, the form of $F(\tilde{A})$ is again given by Eq.(6.2.10). Then, with the z-dependence of all physical quantities being exponential, as in Eqs.(6.2.5), force-balance along field

lines is obtained from Eq.(6.2.9b) in the limit $M \longrightarrow 0$,

$$\frac{\rho(x)}{\tilde{\rho}_o} = \left|\frac{A(x)}{\tilde{A}_o}\right|^{\frac{2(\xi-1)}{\xi}}, \tag{6.4.2a}$$

while force balance across field lines is obtained from Eqs.(6.2.6a) for $k = 0$ ($\lambda = 0$) as

$$\frac{d^2A}{dx^2} + \frac{\xi^2 A}{4L^2} + \frac{8\pi\tilde{\rho}_o V_s^2(\xi-1)}{\xi|A|}\left|\frac{A}{\tilde{A}_o}\right|^{\frac{2(\xi-1)}{\xi}} = 0\,. \tag{6.4.2b}$$

After multiplying Eq.(6.4.2b) by dA/dx and then integrating, we obtain a first-order differential equation for the dimensionless flux function $\alpha \doteq |A/\tilde{A}_o|$ in terms of the dimensionless horizontal distance $\mathrm{x} = x/L$,

$$\frac{4}{\xi^2}\left[\frac{d\alpha}{d\mathrm{x}}\right]^2 = 1 - \alpha^2 + \beta\left[1 - \alpha^{\frac{2(\xi-1)}{\xi}}\right], \tag{6.4.3}$$

where $\beta = 8\pi V_s^2\tilde{\rho}_o/(\xi^2\tilde{A}_o^2/4L^2)$ is the familiar plasma ratio at the origin $\mathrm{x} = 0$, where the field lines are horizontal and $B_z = 0$. For given values of ξ and β we can integrate numerically the nonlinear Eq.(6.4.3) to obtain the magnetic field and density distributions through Eqs.(6.2.2) and (6.4.2a). In the following we briefly review those properties of the solutions of Eq.(6.4.3) which are relevant to our study of MHD equilibrium with flows. The interested reader may find more details in Menzel (1951), where the above Eq.(6.4.3) has been originally derived, and in Hood and Anzer (1990), where Eq.(6.4.3) is discussed in the framework of modeling a solar prominence.

First, note that there exist three values of the parameter ξ, (1/2, 1, 2), where Eq.(6.4.3) may be solved analytically, in addition to the limiting case $\xi \to \infty$. Thus,

$$A(\mathrm{x}) = \tilde{A}_o\sqrt{\frac{1+\beta}{2} + \frac{1-\beta}{2}\cos\frac{\mathrm{x}}{2}} \qquad \text{for} \qquad \xi = \frac{1}{2}, \tag{6.4.4a}$$

$$A(\mathrm{x}) = \tilde{A}_o\cos\frac{\mathrm{x}}{2} \quad \text{for} \quad \xi = 1 \quad \text{(a potential field)}, \tag{6.4.4a}$$

$$A(\mathrm{x}) = \tilde{A}_o\left|-\frac{\beta}{2} + \frac{\beta+2}{2}\cos\mathrm{x}\right| \qquad \text{for} \qquad \xi = 2\,. \tag{6.4.4a}$$

Since the angle $\theta(\mathrm{x})$ that a field line makes with the horizontal is $\tan\theta(\mathrm{x}) \equiv B_z/B_x = [2L/\xi A(\mathrm{x})]dA(\mathrm{x})/d\mathrm{x}$, the field lines are horizontal at the positions x_o where $A(x)$ has an extremum, $dA(\mathrm{x})/d\mathrm{x}|_{\mathrm{x}=\mathrm{x}_o} = 0$. The first case $\xi = 1/2$, has $\theta = 0$ at $\theta = n\pi/2$, $n = 0, 1, 2, \ldots$ On the other hand, there are no positions where $\theta \to 90^o$ and the field is

vertical; in this case the fieldlines have a wavy shape, being periodic in the horizontal distance x. The second case $\xi = 1$, has $\theta = 0$ at $\mathrm{x}_o = n\pi$ and $\theta \to 90^o$ at $\mathrm{x}_{\max} = n\pi/2$. This is the typical geometry encountered in magnetic arcades. Similarly, in the case $\xi = 2$ we have horizontal fields at $\mathrm{x}_o = n\pi$ and $\theta \to 90^o$ at the horizontal positions $\mathrm{x}_{\max}$ where $\cos x_{\max} = \beta/(\beta + 2)$.

It is interesting to note that the general properties of these special analytical solutions are indicative of the corresponding properties for any value of ξ. For example, it is evident from Eq.(6.4.3) that it is not possible to have simultaneously $A = 0$ and $(dA/d\mathrm{x})^2 > 0$ when $\xi < 1$. In other words, for such values of the parameter ξ, locations where $B_x = 0$ and the field is vertical do not exist. We obtain then solutions with a wavy and periodic fieldline shape in the horizontal coordinate x for all $\xi < 1$. On the other hand, when $\xi \geq 1$, there exist values of A such that simultaneously $A = 0$ and $(dA/d\mathrm{x})^2 > 0$. Then, at these locations $B_x = 0$ and the field is vertical. These arcades of infinite height and finite width have fieldlines confined in a finite horizontal interval.

Second, consider the above class of solutions in the framework of modeling a prominence equilibrium. Inside the prominence the gas is cool and the scale height L_{prom} relatively small, $L_{\mathrm{prom}} \approx 180$ km, such that the pressure drops relatively fast. On the other hand, in the surrounding hotter corona the scale height L_{cor} is much larger, say, $L_{\mathrm{cor}} \approx 60,000\ km \approx 333\, L_{\mathrm{prom}}$ and the pressure drops more slowly. Therefore, in order to match the vertical variation of all physical quantities across the coronal boundary of the prominence, we need to employ two different values of ξ, ξ_{prom} for the prominence equilibrium and ξ_{cor} for the adjacent corona. For example, selecting $\xi_{\mathrm{cor}} = 1$ to have a potential equilibrium in the coronal environment, we need to have $\xi_{\mathrm{prom}} = \xi_{\mathrm{cor}}/333 = 0.003$. Then the pressure, density and magnetic field fall off at the same rate with vertical height both inside and outside the prominence. Hood & Anzer (1990) have used essentially this reasoning to construct an interesting model of a solar prominence.

Third, consider the equilibrium path of an isolated buoyant flux tube embedded in the polytropic solar convective zone (Parker 1975, 1979; Browning & Priest 1984, 1986). The curved flux tube may be held in equilibrium by its magnetic tension over horizontal distances of the order of the scale height L. Thus, in an isothermal atmosphere any flux tube needs to be anchored at points separated by no more than $2\pi L$, if it is going to be held in equilibrium by magnetic tension against the buoyancy forces. It is interesting that the equilibrium paths of the flux tubes described by Eqs.(6.4.4), although they are not treated as slender ones, obey the same limit. Thus, the arcade-type potential field (6.4.4b) has the footpoints of its fieldlines separated exactly by Parker's limit, 2π scale heights. On the other hand, the footpoints of the similar, arcade-type but non-potential fieldlines (6.4.4c) are separated by $2\mathrm{x}_{\max} = 2\cos^{-1}[\beta/(\beta+2)] < 2\pi$ scale

heights (with $x_{max} \to 0$ for large β). Also, the periodic field lines (6.4.4a) have a period $4\pi L > 2\pi L$ but they cannot be anchored. The curvature of the fieldlines (6.4.4) behaves analogously. The value of their radius of curvature R_o at their highest point is,

$$R_o \equiv -\frac{B_x}{dB_z/dx}\Big|_{B_z=0} = \frac{2}{\xi + (\xi-1)\beta_o}, \tag{6.4.5}$$

in units of H. It is evident that for the potential case (6.4.4b) we have $R_o = 2$, while for all $\xi > 1$, $R_o < 2$ with $R_o \to 0$ for large β_o. In the following sections we shall see that x_{max} and R_o depend also on the magnitude of the flows in the system.

6.4.2 Low-β solutions

In view of the usual practice to regard the solar corona as a rather low β plasma, it is useful to examine the limit of the general MHD solutions of section 2 when $\beta << 1$. Then, with $M_a^2 << M^2$, we can neglect terms of order M_a^2, or higher, in Eqs.(6.2.14–6.2.16). In this limit Eq.(6.2.14) simplifies considerably,

$$\frac{2}{M_a^2}\frac{dM_a^2}{dM^2} = \frac{\xi M^2/2 - 1}{(\xi/2-1)M^2}, \tag{6.4.6}$$

and has the solution,

$$\frac{M_a^2}{M_{ao}^2} = \left(\frac{M}{M_o}\right)^{\frac{2}{2-\xi}} e^{-\frac{\xi}{2(2-\xi)}(M^2-M_o^2)}. \tag{6.4.7}$$

On the other hand, Eq.(6.2.15) becomes, after neglecting powers of M_a^2 relative to M^2 (but not relative to $\lambda^2 M^2$)

$$\pm\frac{M_a^2}{2}\frac{dM^2}{dx} = \frac{(\xi/2-1)M^2}{M^2-1}\sqrt{\lambda^2 M^2 - M_a^4}, \tag{6.4.8}$$

and has the solution,

$$\frac{M}{M_o}e^{-\frac{\xi}{2(2-\xi)}(M^2-M_o^2)} = \cos\frac{\xi x}{2}, \tag{6.4.9}$$

Evidently, there are no solutions when $\xi > 2$. The flux function obtained from Eqs.(6.2.9b) and (6.2.10) is

$$\tilde{A} = \tilde{A}_0 \cos\frac{\xi x}{2} e^{-\frac{\xi z}{2}}, \tag{6.4.10}$$

representing a potential field with aligned flows, as expected.

Eq.(6.4.8) has a single critical point at the sonic transition, $M = 1$ and $M_a^2 = \lambda << 1$. In other words, the new critical point at $(M_a^\star, M^\star)$ obtained without assuming that

the magnitude of the Alfvén number is small, is lost in this limit of $\beta << 1$. Also, Eq.(6.4.10) represents magnetized arcades for any value of ξ and does not allow for the existence of periodic solutions, while by assumption the effects arising when the flows start to dominate the magnetic effects are not included.

The above solution can be obtained from the initial MHD Eqs.(6.2.1) through a perturbation analysis, if we require that the magnetic field is potential to zeroth order, $\nabla^2 \tilde{A} = 0$. The effect of flows along the field lines is obtained then from Bernoulli's integral, Eq.(6.2.3b), which, after being substituted into the transfield equation and so taking into account the feedback reaction of the flow, gives the perturbation to the potential magnetic field caused by the presence of the low Alfvén number flows. This case has been explored in detail in chapter 4. Note, however, that some properties arising from the non-linearity of the MHD equations are completely neglected and lost by this approach. For example,
(i) the novel critical speed which is different from the classical sound speed and does not appear in the low-M_a perturbation studies,
(ii) the fact that solutions do not exist for high Alfvén numbers, $M_a > M_{ao}^{\max}$, and the sonic speed cannot be reached in some cases (as in the supercritical case),
(iii) the existence of periodic solutions for $\xi < 1$ which do not exist in a low-M_a analysis.

We conclude therefore that a general treatment of the full MHD equations may be crucial *if* we are interested in novel physical properties of MHD equilibria in uniform gravity. And, *if* our interest is confined to modeling those magnetic structures of the solar corona where the magnetic field completely dominates over the plasma and its flows, we may use approximations like the above, or treat the magnetic lines as rigid pipes, or even neglect flows altogether. We should keep in mind, however, that in several instances in the lower quiet corona, in chromospheric loops and fibrils where the plasma β is the largest, in photospheric Evershed flows and also in the atmospheres of other stars where the magnetic field is less important locally, the present general analysis is much more appropriate.

6.5 Solar Arcade-like Solutions

A major feature that has naturally emerged here from a study of the topologies of the solutions of stratified MHD equilibria in a uniform gravity is the existence of loop-like solutions. On the other hand, since such magnetic field geometries are ubiquitously observed in the solar atmosphere, we are tempted briefly to consider the relation of such solutions to solar coronal arcades and loops.

6.5.1 Physical Parameters in Solar Coronal Loops

Our primary motivation in this paper is to build up the basic theory for the first time of compressible steady state MHD solutions in the presence of gravity, rather than to explain particular observations. In the following however, we outline briefly some potential applications, such as, Evershed flow; stellar loops where there is a greater variety of parameter values than on the Sun; and *some* solar chromospheric and coronal loops.

Let us consider briefly the applicability to the solar atmosphere, bearing in mind the *three main assumptions*, namely (i) of steady flow and (ii) of the plasma β being not too small and (iii) of Alfvén number M_α being not too small (say, of the order of 0.1).

First, write the plasma-β and the characteristic flow speeds as,

$$\beta = 0.35 \times \frac{n_{10} T_6}{B_1^2}, \tag{6.5.1}$$

$$V_a = 280 \times \frac{B_1}{\sqrt{n_{10}}} \text{ km/sec}, \qquad V_s = 150 \sqrt{T_6} \text{ km/sec}. \tag{6.5.2}$$

with n_{10} measured in units of 10^{10} cm^{-3}, T_6 in million degrees, and B_1 in units of 10 Gauss.

Second, note that there is a very wide variety of flows and structures in the solar atmosphere (Priest 1984) and even more on other stars. Flows include spicules, macrospicules and explosive events, but they are inherently nonsteady. However, they also include several types of flows to which our analysis may be relevant. For example, compact flares go through a quasi-steady phase for thousands of Alfvén times after an initially dynamic phase and the flow speeds may reach 100 km/sec or more, with the summit density and temperature reaching 10^{10} cm^{-3} and $10^7 - 10^8$ K, respectively. Also, there is Evershed outflow (6 to 7 km/sec) and Evershed inflow (20 km/sec) in sunspot regions (Dere et al. 1990). In addition, in surges streams of plasma are ejected upwards along curved paths at typically 20 to 30 km/sec though occasionally 100 to 200 km/sec and may last for up to half an hour; they too may show a quasi-steady phase after an initial dynamic start. Again coronal rain is cool plasma that flows downward along curved paths at speeds of 50 - 100 km/sec and it too may continue in a quasi-steady manner. From space observations steady large-scale flows over sunspots, the network and plage regions are found with a variety of speeds from 2 to 30 km/sec (Lites et al. 1976; Athay et al. 1980).

Third, consider *three* representative loop structures with flows observed in the photosphere, transition region and corona. In the *photosphere* and chromosphere and

in emerging flux areas, when a bipolar region with fairly low-lying loops is formed (an arch-filament system), the summits of those loops rise at up to 10 km/sec while plasma falls down near both ends with speeds up to 50 km/sec (Svéstka 1976). Higher up at *transition region* temperatures, the most prominent active- region loops are the sunspot loops which originate in sunspots. Foukal (1976) by analyzing the EUV emission of these sunspot-loops found that the observed material inside the loops has much higher scale-height than the one calculated by assuming hydrostatic balance. He then concluded that the material cannot be supported in the observed heights either hydrostatically or magnetohydrostatically, or by turbulent motions. In other words, pressure and energy balance of such loops is most simply understood if coronal material is falling downward under gravity, a conclusion reinforced recently by Peres et al. (1992). Strong downflows are also observed in cool H_α loops located below hot X-ray loops. Finally, in the *corona* systematic flows (50 - 100 km/sec) in loops of typical active region sizes may be responsible for the observed nonthermal X-ray line broadening if they occur along magnetic field lines which are contorted due to interweaving by footpoint motions (Parker 1983). In this case, if the derived excess velocities of 100 km/sec (Acton et al. 1981), or 50 km/sec (Saba & Strong 1991), represent the average line of sight component of flows through such twisted loops, the actual velocities could be *several times larger* than the deduced excess velocities, perhaps even comparable to the sound speed (Saba & Strong 1991).

Fourth, let us consider representative values of the plasma-β, V_a and V_s for such loops. If we adopt a temperature of 2.7×10^6 K, a density of 10^9 cm^{-3} and a magnetic field of 5 Gauss, we obtain a plasma beta of 0.4. In many parts of the solar atmosphere the temperature is indeed greater than this, especially in active regions where Yohkoh finds $5 - 6 \times 10^6$ K by comparison with the above lower quiet region temperature of 2.7×10^6 K (Hara et al. 1992). Also, the density can be greater by a factor of 10, especially low down or in coronal condensations. Thus, following Saba & Strong (1991) we may put in Eqs.(6.5.1–6.5.2) $n_{10} \approx 1$ while $T_6 \approx 6$ from the Yohkoh results. The strength of the magnetic field on the other hand is not well determined due to uncertainties arising from the assumption that it is potential with photospheric values used as boundary conditions (Poletto et al. 1975; Galeev et al. 1981). Assuming a value of the total field $B \approx 20$ Gauss in Eqs.(6.5.1–6.5.2) we find,

$$\beta \approx 0.5\,, \qquad V_\alpha \approx 550\ km/sec\,, \qquad V_s \approx 400\ km/sec\,, \tag{6.5.3}$$

Thus, provided we restrict ourselves to regions of low magnetic field, values of plasma-β and Mach and Alfvén numbers in excess of say 0.1 are common. However, active regions, say, with a field larger by a factor of 10, have β values that are lower by a factor of 100 and our analysis is certainly not relevant - at least high in the corona.

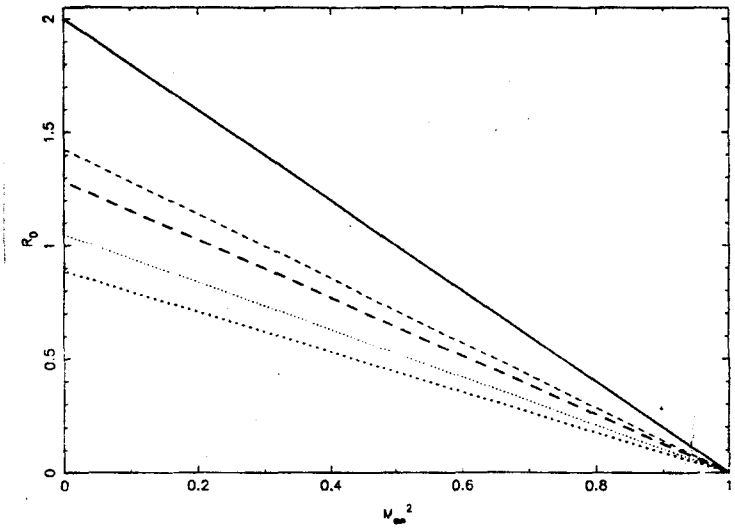

Figure 6.4: *Plot of radius of curvature* R_o *(in units of scale height L) for field lines at the summit* $x = 0$ *of the arcade as a function of the Alfvén Mach number* M_{ao} *there, for* $\xi = 1$ *(solid curve),* $\xi = 1.5$ *and* $\beta_o = 0.01$ *(thin dashes),* $\xi = 1.5$ *and* $\beta_o = 0.4$ *(thick dashes),* $\xi = 1.9$ *and* $\beta_o = 0.01$ *(thin dots),* $\xi = 1.9$ *and* $\beta_o = 0.4$ *(thick dots).*

Similarly, in those regions of strong magnetic field the Alfvén number is also small, although in parts of the quiet Sun it may also exceed 0.1. Our conclusion therefore is that in quiet Sun loops in the chromosphere or corona the conditions for our analysis to be relevant and to have significant effects are likely to be met.

Finally, within the assumptions of the analysis we have chosen to illustrate the solutions of the present study with typical values of the parameter λ of the order of 0.1 and corresponding values of the plasma-β of the same order. For example, in Fig.(6.1a) we have taken $\lambda = 0.088$ such that the Alfvén number at the loop summit reaches the value $M_{ao} \approx 0.3$ and the plasma-β in Fig.(6.1b) is $\beta_o = 0.17$. In Figs.(6.1c,d), $\lambda = 0.088$, $M_{ao} \approx 0.8$ and $\beta_o \approx 0.2$, while in Figs.(6.1e,f), $\lambda = 0.03$, $M_{ao} \approx 0.17$ and $\beta_o \approx 0.06$. Needless to say, an advantage of the analytical nature of our study is that any value of λ and β can be considered in the limits of the previous ambiguities in λ and β_o. The values chosen here, although for illustration purposes only, were within those limits. It is also important to note (in comparing with other studies performed under the assumption that $M_a << 1$ and neglecting the nonlinear effects) that as long as ξ is slightly larger than 1 the conclusions are similar to those of section 4.2 (field-aligned flows in a potential field). But as $\xi \to 2$ the non-linear effects become important.

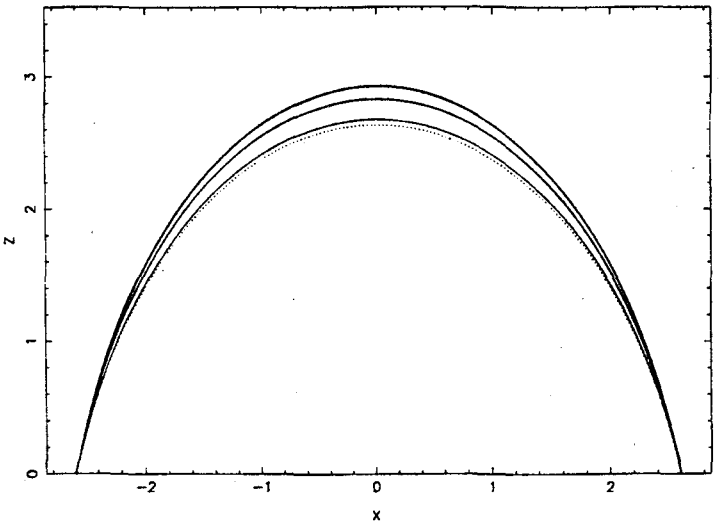

Figure 6.5: *For the solution with $\xi = 1$ and $\beta_o = 0.2$ we plot the shape of the field lines as the value of the Mach number M_o at the summit $x = 0$ increases from $M_o = 0$ (dotted curve), to $M_o = 0.3$ (lower thin curve), then to $M_o = 0.7$ and finally to $M_o = 0.9$ (upper thick solid curve).*

6.5.2 Change of Curvature and Footpoint Separation of Arcade

As discussed in the previous section 3, when $1 \leq \xi \leq 2$, we obtain loop-like solutions. In order to see in some more detail the effect of the flow in changing the properties of such arcades, in the following we discuss how the geometrical shape of the arcade changes as the Alfvén number M_{ao} at its summit increases.

Change of curvature at arcade summit with increasing strength of flow. The radius of curvature of the arcades at their top depends both on plasma β_o and the Alfvén number there, M_{ao}

$$R_o = \frac{2(1 - M_{ao}^2)}{\xi + (\xi - 1)\beta_o}, \tag{6.5.1}$$

In Fig.(6.4) we plot R_o as a function of M_{ao} for different values of the parameter ξ and plasma β_o. For given ξ and β, as the strength of the Alfvén number of the flow at the summit increases, the radius of curvature of the lines, R_o, decreases from the static value without flows (Eq. 4.5) to zero for flows which become Alfvénic at their summit, $M_{ao} = 1$. This trend is of course well understood, since in this case, by increasing the strength of the centrifugal force at the summit, the loop responds by becoming more curved in order that the increased centrifugal force is balanced by magnetic tension. Note that, in the special case of $\xi = 1$, the pressure gradient in

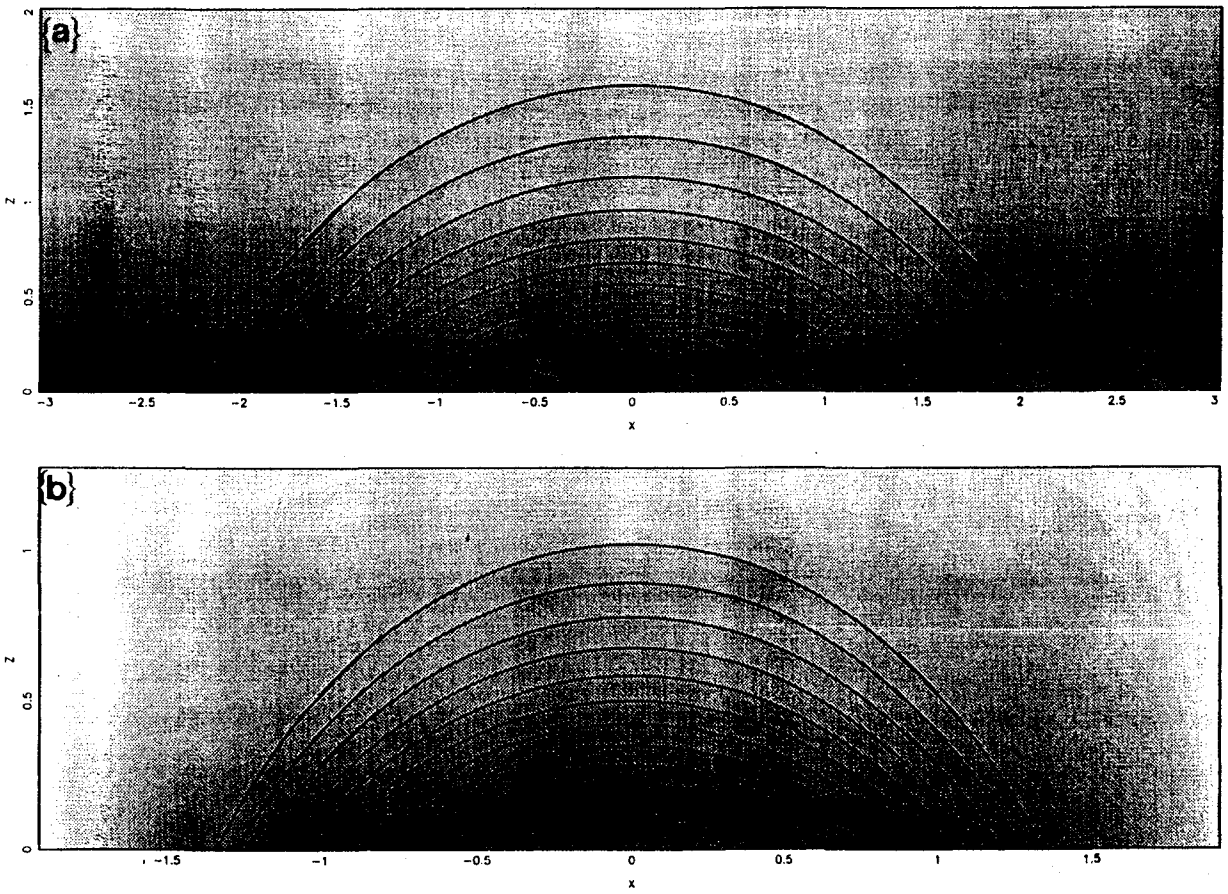

Figure 6.6: *The typical shape of the arcade in the vertical x-z–plane is plotted for $\xi = 1$ and $\beta_o = 0.2$ in (a) and in (b) for $\xi = 1.5$ and $\beta_o = 0.2$.*

the z-direction exactly balances the plasma weight, leaving the downward magnetic tension (in the z-direction) to balance the sum of the upward centrifugal force and upward z-component of the magnetic pressure gradient.

In Fig.(6.5b) we plot the various shapes of an arcade with fixed footpoints, as M_{ao} is progressively increased. It is evident, *first*, that all arcades with flows are already more curved than the corresponding static ones (dotted curve); and *second*, that the stronger are the flows (the higher is M_{ao} for fixed ξ and β_o) the more curved is the loop (progressively thicker curves). The shape of a typical such arcade is shown in Fig.(6.5a) together with the contours of constant density. For the special case $\xi = 1$ without flows, the density $\rho(\mathrm{x})$ is flat along a horizontal plane of $\mathrm{z} = const.$ intersecting the arcade, but in the presence of flows the density has a minimum at the vertical plane which goes through the summits of the arcade at $\mathrm{x} = 0$, for large M_{ao}. For $1 < \xi \leq 2$ the density is dropping fast as we reach the footpoints (Fig.6.6).

Change of footpoint separation with increasing flow strength at loop summit. As may be seen from Fig.(6.1d), by increasing the strength of the flow speed at the loop top (increasing M_{ao} for constant λ), there results a gradual decrease of the separation $2\mathrm{x}_{\max}$ of the loop footpoints. For $M_{ao} \longrightarrow 0$, we have $2\mathrm{x}_{\max} \longrightarrow 2\pi$, the Parker value for the separation of the footpoints of an anchored buoyant magnetic flux tube in an isothermal atmosphere.

6.6 Nature of Critical Points

In this section we *first* discuss the nature of the novel X-type critical point we have encountered in the $(M_a^2 - M^2)$–plane of the solution topologies by comparing it to the critical points that appear in the study of siphon flows in isolated slender flux tubes; and *second*, we compare the critical speed at this critical point to the characteristic speed for MHD wave propagation in a stratified medium. We conclude that the critical speed is not always equal to the sound speed. In addition, we find that for a rather highly stratified medium there are no loop-like solutions with field-aligned flows because MHD wave propagation occurs only above a cut-off speed in such a medium.

6.6.1 Siphon Flows in Isolated Thin Magnetic Flux tubes

Steady flows in the solar atmosphere have been studied either in the rigid flux tube approximation (Cargill & Priest 1980; Noci 1981) or in the approximation of a slender flux tube (Thomas 1988; Montesinos & Thomas 1989; Degenhardt 1989; Thomas &

Montesinos 1990, 1991). In this section we go briefly through the main results of these studies in order to compare them with the results of the present analysis.

Force balance along magnetic field lines in an isothermal MHD equilibrium in a uniform gravitational field g in the z-direction is expressed by

$$VdV + V_s^2 \frac{d\rho}{\rho} + gdz = 0\,. \tag{6.6.1}$$

For field-aligned MHD flows we also have

$$\frac{d\rho}{\rho} + \frac{dV}{V} - \frac{dB}{B} = 0\,. \tag{6.6.2}$$

Substituting $d\rho/\rho$ from Eq.(6.6.2) to Eq.(6.6.1) we obtain

$$\left[1 - \frac{V^2}{V_s^2}\right] \frac{dV}{V} = \frac{dB}{B} + \frac{dz}{L}\,. \tag{6.6.3}$$

To make more progress we need another relationship between B, V and z. This may be taken from magnetic flux conservation, where the cross-sectional area of the tube, $\sigma(z)$, is prescribed such that the magnetic field is obtained from $B(z) = F_B/\sigma(z)$, where F_B is the constant magnetic flux. This provides us with the required extra relationship between B, V and z such that the velocity $V(z)$ along the magnetic lines may be calculated in terms of z from (6.6.3), which now becomes (Cargill & Priest 1980; Noci 1981)

$$\left[1 - \frac{V^2}{V_s^2}\right] \frac{dV}{V} = \left[\frac{1}{B(z)} \frac{dB(z)}{dz} + \frac{1}{L}\right] \mathrm{d}z\,. \tag{6.6.4}$$

Note that there exists a critical point in the V–z plane at the sonic transition, $V = V_s$. In this approach, however, the tube is considered as rigid and lateral force balance is neglected altogether.

On the other hand, if lateral force balance is taken into account to yield $B = B(z, V)$, we have,

$$\left[1 - \frac{V^2}{V_s^2} - \frac{V}{B}\frac{\partial B}{\partial V}\Big|_z\right] \frac{dV}{V} = \left[\frac{1}{B}\frac{\partial B}{\partial z}\Big|_V + \frac{1}{L}\right] dz\,. \tag{6.6.5}$$

It follows that now the velocity at the critical point has shifted to $V_\star \neq V_s$, where

$$\frac{1}{V_\star^2} = \frac{1}{V_s^2} + \frac{1}{B^2}\frac{\partial B^2}{\partial V^2}\Big|_z\,. \tag{6.6.6}$$

For an equipartition flow where $B^2 = 4\pi\rho_o V^2$, lateral force balance is identically satisfied and the critical point occurs at the characteristic tube speed defined by (Roberts

1976)

$$V_t^2 = \frac{V_s^2 V_a^2}{V_s^2 + V_a^2} \,. \tag{6.6.7}$$

By comparison, if lateral force balance is taken into account within the framework of the restricted slender flux tube approximation where $P + B^2/8\pi = P_e$, we find

$$\frac{dB}{B} = \frac{V^2}{V_a^2}\frac{dV}{V} - \frac{dz}{2L} \,. \tag{6.6.8}$$

Combining Eqs.(6.6.5) and (6.6.8) we obtain the following equation for $V(z)$

$$\left[1 - \frac{V^2}{V_t^2}\right]\frac{dV}{V} = \frac{dz}{2L} \,, \tag{6.6.9}$$

and similarly for $B(z)$

$$\left[1 - \frac{V^2}{V_t^2}\right]\frac{dB}{B} = -\left[1 - \frac{V^2}{V_1^2}\right]\frac{dz}{2L} \,, \tag{6.6.10}$$

in terms of another characteristic speed V_1 defined by,

$$V_1^2 = \frac{V_s^2 V_a^2}{2V_s^2 + V_a^2} \,. \tag{6.6.11}$$

Note that V_1 is the speed above which the flow causes the tube to contract with height (Thomas 1988). Thus, the flow accelerates at the expanding initial portion of the thin flux tube through a density reduction as the plasma climbs along the expanding portion of the tube. Then, after the characteristic speed V_1 is reached at the location of maximum tube area and minimum field strength, the velocity continues to increase and the tube contracts with height because of a pressure reduction through the Bernoulli effect until the speed V_t is reached at the summit where the field is horizontal.

How can the above results be generalized if we do not keep the thin flux tube approximation? Let us first note that Eq.(6.6.6) can be written as

$$M^2 + \frac{V_\star^2}{B^2}\frac{\partial B^2}{\partial V^2}\Big)_z = 1 \,. \tag{6.6.12}$$

Also, when the flow speed equals the characteristic speed V_1 and the magnetic field attains an extremum, the Mach numbers M and M_a satisfy the relation

$$\frac{M^2}{2} + M_a^2 = 1 \,. \tag{6.6.13}$$

Eq.(6.6.12) implies that, in general, $M \neq 1$ at the critical point. And, evidently our Eq.(6.2.17) is an extension of Eq.(6.6.13) for $\xi \neq 1$, reducing to (6.6.13) when $\xi = 1$. This should be the case because we also obtained Eq.(6.2.17) from force balance along the fieldlines. However, we obtained an extra critical relationship between the two Mach numbers, namely Eq.(6.2.18) from force balance across the fieldlines; and the combination of Eqs.(6.2.17)–(6.2.18) determined the values of the Mach numbers at the critical point.

In the present study we also find that the critical point is not necessarily at the summit of the magnetic flux tube and that the speed at this critical point does not coincide with any known characteristic speed for MHD wave propagation in a uniform medium.

6.6.2 Wave Propagation and Characteristic Speeds

It is usually found that at critical points the flow speed equals some characteristic speed for wave propagation in the plasma. Thus, searching for a connection of the flow speed at the critical point of the present analysis with some characteristic speed for MHD wave propagation, we briefly discuss the various wave speeds that exist in magnetized media.

Consider first a *uniform* magnetic field $B\hat{z}$ filling all space. Then, MHD waves may propagate along the field as Alfvén waves, or, at any direction $\hat{k}$ as either of the so-called *slow* and *fast* magnetoacoustic waves with phase speeds $V = \omega/k$ where

$$\left(\frac{\omega}{k}\right)^4 - (V_s^2 + V_a^2)\left(\frac{\omega}{k}\right)^2 + V_s^2 V_a^2 \frac{k_z^2}{k^2} = 0\,, \tag{6.6.14}$$

For propagation along the magnetic field we thus find that the waves propagate with either the sound speed V_s or the Alfvén speed V_a.

On the other hand, consider how the phase speed of these waves is modified in the limit of squeezing the field in a *slender* magnetic flux tube. A straightforward normal mode analysis of the possible modes leads to the dispersion relation

$$k^2 V_t^2 = \omega^2\,, \tag{6.6.15}$$

i.e., the waves propagate at the reduced *tube-speed*, $V_t < \min(V_a, V_s)$ (Roberts 1976; Defouw 1976).

Consider next the effect of *stratification*, a situation corresponding to the present analysis. In the framework of the thin flux tube approximation, we may write for the z-dependence of the pressure, density, magnetic field strength and area, respectively,

$$P \sim e^{-\frac{\xi z}{H}}, \quad \rho \sim e^{-\frac{\xi z}{H}}, \quad B \sim e^{-\frac{\xi z}{2L}}, \quad \sigma \sim e^{\frac{\xi z}{2L}}\,, \tag{6.6.16}$$

such that both the Alfvén speed and the sound speed V_s are constants. Then a perturbation satisfying the conservation laws,

$$\delta P + \frac{B\delta B}{4\pi} = 0, \quad B\delta\sigma + \sigma\delta B = 0,$$

$$\delta P = V_s^2 \delta\rho, \quad \rho\frac{\partial \delta V}{\partial t} = -\frac{\partial \delta P}{\partial z} - g\delta\rho, \tag{6.6.17}$$

$$\sigma\frac{\partial \delta\rho}{\partial t} + \rho\frac{\partial \delta\sigma}{\partial t} + \delta V\frac{\partial(\rho\sigma)}{\partial z} + \rho\sigma\frac{\partial \delta V}{\partial z} = 0\,, \tag{6.6.18}$$

yields the differential equation

$$\frac{\partial^2 \delta P}{\partial z^2} + \frac{4-\xi}{2H}\frac{\partial \delta P}{\partial z} + \left[\frac{\omega^2}{V_t^2} + \frac{2-\xi}{2L^2}\right]\delta P = 0\,, \tag{6.6.19}$$

with the solution,

$$\delta P \sim e^{-\frac{(4-\xi)z}{4H}} e^{i(\omega t \pm kz)}\,, \tag{6.6.20}$$

where

$$\frac{k^2}{\omega^2} = \frac{1}{V_t^2} - \frac{\xi^2}{16L^2\omega^2}\,. \tag{6.6.21}$$

Propagation is possible only for frequencies above the cut-off frequency $\omega_o = \xi V_t/4H$, which is inversely proportional to the scale height H, as there exists a cut-off frequency in e-m wave propagation in a plasma. Thus, for very small scale heights H propagation is not possible. The situation is similar in our analysis. In our case, there is no critical point and critical speed for small scale heights, $\xi > 2$ and MHD flows along arcades are not possible. In other words, for $H \longrightarrow 0$, no wave propagation in a stratified medium is possible, consistent with our conclusion that for $\xi > 2$ no solutions for flows in arcades are found.

6.7 Summary and Discussion of Results

In Paper I we searched for exact 1-D MHD solutions in a uniform gravitational field. For simplicity we considered in that first step a variation of the physical quantities only with the horizontal coordinate X. Only periodic solutions were found including valleys and summits. The new element introduced in the present treatment is stratification in the vertical distance Z and therefore dependence of all physical quantities on both Z and X. As a result, a new feature has emerged naturally from this 2-D analysis, namely the existence of loop-like solutions not encountered in the previous unstratified treatments. Nevertheless, in the limit of the absence of stratification ($\xi \longrightarrow 0$) we

recover the results of the analysis for the unstratified case of Paper I. As with Paper I, the present study can be generalized to any nonisothermal atmosphere and also to include components of the fields in the symmetry-direction (y). The main conclusions of the present study can be summarized then as follows,

(1) Low Mach number *loop-like solutions exist only for a limited range of the stratification parameter* ξ, $1 \leq \xi \leq 2$, i.e., for the restricted case of a mildly stratified atmosphere where the density, pressure and magnetic field strength do not drop with height z faster than the classical scale height $H = V_s^2/g$. If this conclusion were shown to persist for other functional forms of the free integrals $\Psi_{\tilde{A}}(\tilde{A})$ and $F(\tilde{A})$, Eqs.(6.2.4), it would predict, for example, that in highly stratified coronae of stars and accretion disks, loops with flows do not exist. Note that this result is also in agreement with a perturbation analysis for MHD wave propagation in a stratified medium where there is a scale height–dependent cutoff frequency for the waves, Eq.(6.6.21).

(2) Topologies of the solutions in the (M_a, M)–plane for such loops are controlled by *a new critical point.* We have preliminarily explored the nature of this critical point and concluded that its appearance is strictly related to the vertical stratification. The flow speed at the critical point is then a generalization of the well-known *tube-speed*, V_t, encountered in wave propagation in slender flux tubes (Roberts 1976). The critical point is not necessarily, however, at the highest point of the tubes, as is the case in slender flux tube models with flows (Thomas 1988; Degenhart 1989; Thomas & Montesinos, 1990). Instead, the critical point seems to be similar to an analogous critical point that emerges from nonlinear solutions of the 2-D MHD equations explored in connection with astrophysical winds and jets (Tsinganos & Trussoni 1991; Tsinganos & Sauty 1992). In both these cases the new critical point appears when the two coupled partial differential equations which govern symmetric MHD equilibria – the transfield equation and the equation for force balance along the magnetic field and stream lines – are properly solved. Also, the critical point does not appear at the *fast* and *slow* MHD wave speeds, but at some other characteristic speed which evidently includes the *elasticity* of the fieldlines to changes in the flow magnitude.

(3) As the magnitude of the flow at the summit increases, the arcade responds by becoming more *curved* while the separation of its footpoints $2X_{\max}$ decreases. Always, however, $2X_{\max} \leq 2\pi$, with equality reached only in the limit of potential arcades without flows (Parker 1975, 1979). This conclusion is valid for arcades which in the absence of flows correspond to a potential magnetic field, $\xi = 1$, a case that may be relevant for some solar coronal magnetic fields. This property may explain the observational fact that most loops extend over heights much larger than predicted by static models without flows (Foukal 1976).

(4) Sometimes a limit exists on the magnitude of the flow speed at the summits beyond which steady solutions do not exist and we conjecture that *the arcades disrupt when the flow speed exceeds this limit.* Such high plasma motions are observed to occur in the solar corona and chromosphere. For example, transition region line profiles ($50,000 < T < 250,000$) are broadened almost everywhere beyond their thermal width (Brueckner et al. 1988). Our suggestion is that a consequence of such high plasma flows may be the disruption of the magnetic field lines which can be understood in terms of the failure of the magnetic tension force to continue to balance the centrifugal force. The required increased mass flows along the magnetic field lines may be due, for example, to appropriate changes in the footpoint pressure and other physical conditions at the base of the loops (Low 1981; Mikic 1988; Priest 1988).

(5) For asymmetric arcades there is the possibility of *a shock transition* that would connect the $M > 1$ branches with the $M < 1$ branches. The existence and location of this shock along the loop depends of course on the pressure difference between the two symmetric loop footpoints. Note that such shock transitions also appear in the subcases of rigid flux tube siphon flows, as well as in flows in slender flux tubes and attempts have been made to connect them with heating along the loops.

(6) *The density has a minimum at the summits* and increases as we move down in the gravitational field toward the footpoints. Also, the density has a minimum horizontally at the summit of the arcade.

(7) Finally, it is worth emphasizing that the present study is valid for *any* plasma β, small or large. And, although results obtained with the assumption of low β can be applied to solar active region loops if there $\beta << 1$, nevertheless such approximations are inappropriate for situations where the effects of the flow are important and a full solution of the MHD equations should be considered instead. Such situations arise, for example, in areas of magnetic flux emergence (Brueckner et al. 1988), or in compact flares with no eruption where the speeds are typically of the order of 100 km/s; similarly in high temperature X-ray loops (T $\approx$ 5-6 $\times$ 10^6 K) like those observed with Yohkoh (Hara et al. 1992). Similar considerations apply to chromospheric loops and fibrils where the plasma β is the largest and in the atmospheres of other stars where the magnetic field is less important locally. For the obvious application to photospheric Evershed flows in sunspots one needs to write the corresponding Eqs.(6.2.14-6.2.16) in cylindrical coordinates, this will be taken up in the future.

All the above conclusions are based on the particular form of the free integrals $\Psi_{\tilde{A}}(\tilde{A})$ and $F(\tilde{A})$, Eqs.(6.2.4). It is natural to wonder then whether the results of the present analysis are model-dependent and not extendable to other choices of $\Psi_{\tilde{A}}(\tilde{A})$ and $F(\tilde{A})$, or whether they indeed reveal some generic properties of MHD flows in a uniform gravity and in an atmosphere that is vertically stratified and horizontally

compressible. Unfortunately, to this day the set of expressions (6.2.4) for $\Psi_{\tilde{A}}(\tilde{A})$ and $F(\tilde{A})$ is the only one wherein it has been possible to examine analytically and display the general properties of such steady states. In this connection we briefly note that the expressions (6.2.5) for the z-dependence of the magnetic fields are quite appropriate for magnetic fields that exist high in the solar corona where they are regarded as approximately potential. On the other hand, for the mass flux per unit of magnetic flux we find that the simplest expression it can take is $\Psi_{\tilde{A}}(\tilde{A}) \propto \tilde{A}$, while for the energy flux, $F(\tilde{A}) \propto \ln\tilde{A}$. A Taylor expansion of these two free functions in $\tilde{A}$ will keep those terms at the lowest order. Therefore, we are inclined to accept the latter point of view that the above general trends are not purely accidental for the set (6.2.5) for $\Psi_{\tilde{A}}(\tilde{A})$ and $F(\tilde{A})$ alone. However, it remains a task for the future to show if other classes of such equilibria share the same properties and therefore that the previous trends have a general validity. We conclude then that more work is needed in order to understand some key properties of MHD steady flows in a uniform gravity and the related problem of MHD wave propagation in a nonuniform atmosphere. Such an understanding is necessary before we are able successfully to model the complex and nonlinear phenomenon of the MHD structure of solar and stellar atmospheres.

Chapter 7

SUMMARY AND FUTURE PERSPECTIVES

7.1 Summary

High-resolution X-ray images of the inhomogeneous solar atmosphere by satellites and rockets, seem to firmly establish the notion that the building blocks of the corona of the Sun are loops of various sizes and properties. In particular the role of magnetic field apparently emerges to be rather crucial in providing the confiment of the plasma in these higher density structures. On the other hand, a prelimary comparison of the fitting of the emission by these loops by static (without flows) or dynamic (with flows) models suggests that plasma flows play also an essential role in determining the physical and geometric characteristics of the loops. It is evident them, that a full MHD description is required in order to understand the basic physical properties of magnetized plasma loops. However, the construction of exact MHD models with flows for compressible magnetic loops has been so far halted by the nonlinear nature of the coupled MHD partial differential equations. This is the basic reason that all the models that we have for coronal loops are one-dimensional (in which the MHD partial differential equations becomes ordinary differential equations). Needless to say that self-consistent models of coronal loops may be the starting point for an examination of their stability properties, propagation of waves and subsequent heating.

With these considerations in mind, we have been studying some families of exact solutions of the MHD equations. We developed a method to solve in general the MHD equations in two dimensions in the low-β limit (i.e. that the plasma pressure is much less than the magnetic pressure) which an reasonable assumption for the solar

corona. In this limit the magnetic configuration is approximently force-free. Thus the influences of the plasma pressure, density and flows can be treated as perturbations to the initial force-free configuration. The resulting equations, describing the field-aligned dynamics and the cross-field force balance, which give the dynamics of the plasma and the change in the initial magnetic configuration can be solved for any boundary conditions assumed. As an example we examing in detail some configurations (symmetric and asymmetric) which model coronal loops, arcades and the sunspots. In more details in symmetrical magnetic configurations, when the distribution of pressure at the foot points is symmetrical, the flow is necessarily subsonic. Otherwise it can become supersonic at the summit of the magnetic field line and then passes through a shock. Such shocks can be very inclined to the magnetic field and the shocked material may form a dense hot sheet around a cooler core, a situation which seems to be observed in cool loops. For asymmetrical magnetic configurations, the flow accelerates towards the low gas pressure foot point and could be subsonic or transonic depending on the pressure difference between the foot points. Loops can have a significant density contrast against their environment only if their energy flux differs markedly from the background one. In asymmetrical loops one leg can be much less dense than the other and poorly visible. Near spots, the sign of the difference of pressure between the two foot points is such as to drive a reverse Evershed flow towards the spot and additional effects would be needed to drive a direct Evershed flow.

From the other hand, we tried to find MHD solutions without the crucial assumption that the plasma β is small. In this direction we have study two cases, starting from the generalization, in horizontally compressible atmosphere, of Kippenhahn-Schlüter model for the support of quiescences prominences. Adding flows along the fieldlines to this, we found that the resulting field structure has a periodic character, which is similar to the observed fine-scale fibril structure of solar prominences, with prominence-like valleys and arcade-type summits. At the valleys the density is maximum and the flow speed subsonic and subalfvénic while the opposite happens in the summits. But if in the above approach take to account the vertical stratification of atmosphere due to gravity the situation complicates and new characteristics emerge. The basic result for middly stratification, coronal loop models with flows along them comes out as the only solutions of the couple equations discrubing the force balance along and across fieldlines. The phase plane of this solutions controlled by a classical sonic and a novel saddle critical point, corresponding to a new characteristic speed for MHD wave propagation in this nonuniform medium. We also found that for strong stratification there no solutions at all, while for small stratification only periodic solutions arise which are totally subsonic and subalfvénic model the internal structure of prominences. We further compare some properties of these loops with those of force-free magnetic loops

in the low-β limit where loops are taking to be rigid. Among our results, is that an increase of the magnitude of the flow at the loop increases its height, in accordance with solar observations where some loops seem to extent over heights much higher than those predicted by static models. Finally, for strong flows there no equilibrium solutions and the loop is disrupted.

7.2 Suggestions for future work

The approach followed in this thesis is useful to construct more sofisticated models for various solar structures in the solar corona where the low-β assumption valid and comparing them with observations and to examine simple situations of the MHD equations in order to light some basic properties of them and to model in zeroth order situations where the low-β assumption is not valid. In the following we shall describe how we can extrapolate the works of chapters 4 and 6.

7.2.1 General low-β models

As we saw in the third chapter a magnetic structure in which the plasma β and the Alfvén Mach number M_a are both much less than unity (and also the scale of magnetic structures are much less than the Alfvénic scale height), is approximently force-free

$$(\nabla \times \mathbf{B_0}) \times \mathbf{B_0} = 0\,, \tag{7.2.1a}$$

$$\nabla \cdot \mathbf{B_0} = 0\,. \tag{7.2.1b}$$

while the influence of the plasma (density, pressure, flows and gravity) can be treated as perturbation of order β and M_a

$$\mathbf{B} = \mathbf{B_0} + \mathbf{B_1}\,, \tag{7.2.2}$$

writing in first order of these parameters

$$\nabla \cdot \mathbf{B_1} = 0\,, \tag{7.2.3a}$$

$$\nabla \cdot (\rho \mathbf{V}) = 0\,, \tag{7.2.3b}$$

$$\nabla \times (\mathbf{V} \times \mathbf{B_0}) = 0\,, \tag{7.2.3c}$$

$$\rho \mathbf{V} \cdot \nabla \mathbf{V} = -\nabla P + \frac{(\nabla \times \mathbf{B_0}) \times \mathbf{B_1}}{4\pi} + \frac{(\nabla \times \mathbf{B_1}) \times \mathbf{B_0}}{4\pi} + \rho \mathbf{g}\,. \tag{7.2.3d}$$

and closing the above system by the ideal gas law for fully ionized H

$$P = \frac{2k_B}{m_p}\rho T\,, \tag{7.2.3e}$$

and an energy equation

$$\frac{\rho^\gamma}{\gamma-1}(\mathbf{V}\cdot\nabla)\left(\frac{P}{\rho^\gamma}\right) = -(\hat{\mathbf{B}}_\mathbf{0}\cdot\nabla)\left[\frac{\kappa_o T^{5/2}}{B_0}(\hat{\mathbf{B}}_\mathbf{0}\cdot\nabla)T\right] - \chi\rho^2 T^\alpha + H\,. \qquad (7.2.3f)$$

where B_0 is the strength of the magnetic field. Thus Eqs.(7.2.3) constitute a closed system for P, ρ, T, $\mathbf{V}$ and $\mathbf{B_1}$.

For a magnetic configuration in coordinates (x_1, x_2, x_3) where x_3 is ignorable, defining the flux functions A_0 and A_1 from the solenoidal conditions Eqs.(7.2.1b,7.2.3a) it is easy to see that the discussion of section 4.3 still holds about the existance of free functions of A_0 like $\Psi(A_0)$, $\Omega(A_0)$ and $G_1(A_0)$ discrubing mass conservation and force balance in the ignorable direction (the integral $E(A_0)$ is not exist in this case). Of course the initial configuration satisfies the well-known 2-D force-free condition for A_0, and of course the function $G_0 = h^3 B_{0_{x_3}}$ is function of A_0 only. For field aligned flows $\Omega = 0$ we have

$$4\pi\rho\mathbf{V} = \Psi_{A_0}\mathbf{B_0}\,, \qquad (7.2.4a)$$

and the equations discrubing the hydrodynamic and thermal equilibrium of the plasma along each field line A_0 with abscissa s are

$$\rho V\frac{dV}{ds} = -\frac{dP}{ds} - \rho g\frac{B_{0_z}}{B_0}\,, \qquad (7.2.4b)$$

$$\frac{\rho^\gamma}{\gamma-1}V\frac{d}{ds}\left(\frac{P}{\rho^\gamma}\right) = -B\frac{d}{ds}\left(\frac{\kappa_o T^{5/2}}{B}\frac{dT}{ds}\right) - \chi\rho^2 T^\alpha + H \qquad (7.2.4c)$$

together with the ideal gas law. The above system can be solved for the unknowns P, ρ, T and $\mathbf{V}$. Finally the equation which gives the flux function A_1 end thus the correction in the x_1- and x_2-components of the magnetic field is

$$\frac{1}{h_1h_2h_3}\left[\frac{\partial}{\partial x_1}\frac{h_2}{h_1h_3}\frac{\partial A_1}{\partial x_1} + \frac{\partial}{\partial x_2}\frac{h_1}{h_2h_3}\frac{\partial A_1}{\partial x_2}\right] + \frac{1}{2h_3^2}\frac{d^2(G_0^2)}{dA_0^2}A_1 =$$

$$\frac{\Psi_{A_0}}{h_1h_2h_3}\left[\frac{\partial}{\partial x_1}\frac{h_2}{h_1h_3}\frac{\Psi_{A_0}}{4\pi\rho}\frac{\partial A_0}{\partial x_1} + \frac{\partial}{\partial x_2}\frac{h_2}{h_1h_3}\frac{\Psi_{A_0}}{4\pi\rho}\frac{\partial A_0}{\partial x_2}\right]$$

$$-\frac{1}{h_3^2}\frac{d(G_0G_1)}{dA_0} - \frac{1}{8\pi\rho h_3^2}\frac{d(G_0^2\Psi_{A_0}^2)}{dA_0} - 4\pi\frac{\partial P}{dA_0}\Big)_{\mathcal{F}}\,. \qquad (7.2.5a)$$

while the correction in $B_{1_{x_3}}$ is given by

$$B_{1_{x_3}} = \frac{\Psi_{A_0}^2}{4\pi\rho}B_{0_{x_3}} + + \frac{1}{h_3}\frac{dG_0}{dA_0}A_1 + \frac{G_1}{h_3}\,. \qquad (7.2.5b)$$

where the last partial derivative in the transfield equation is taken keeping the quantity $\mathcal{F} = gz + V^2/2$ constant, and is calculating numerically from the solution of the system of Eqs.(7.2.4).

The above formalism can be use to model in detail coronal loops, prominences, active regions etc., where the isothermally is not a realistic assumption.

7.2.2 Further study of the general 2-D MHD equations

Equilibrium states. The class of solutions studied in chapters 5 and 6 belongs to a more general class of solutions of MHD equations under the assumption that any quantity is separable. By this we seek solutions in the 2-D MHD equations in x_1,x_2 coordinates by writing every variable $\mathcal{Q}(x_1, x_2)$ in the separable form

$$\mathcal{Q}(x_1, x_2) = \mathcal{Q}_1(x_1)\mathcal{Q}_2(x_2)\,, \tag{7.2.6}$$

and asking which is the appropriate given form for $\mathcal{Q}_2(x_2)$, such that the MHD equations to became from a partial to ordinary differential equation system for the unknown functions $\mathcal{Q}_1(x_1)$. For the cartesian (x, y, z) or cylindrical (ϖ, ϕ, z) coordinates with y or ϕ being ignorable, it is easy to check that the most general z-dependence is given by Eqs.(6.2.5). Thus an obvious extension of the work of chapter 6 is the study of the solutions in cylindrical geometry and the study of non-planar solution assuming that the magnetic field and velocity have components and in ignorable direction. At this point we must note that in spherical coordinates (r, ϕ, θ) where ϕ is the ignorable coordinate there are already many models under this assumption discrubing solar and stellar winds and jets (Tsinganos & Trussoni 1990, 1991, Tsinganos & Sauty 1991, 1992, Sauty & Tsinganos 1994, Lima & Priest 1993a,b).

Critical points in the general transfield equation. Another crucial point that found in chapter 6 is this new critical point or a new characteristic speed, defining in Eq.(6.2.18) which can be written also using Eq.(6.2.10) as

$$M_a^2 + M^2 - M_a^2 M_x^2 - 1 = 0\,, \tag{7.2.7}$$

where M_a is the Alfvén number and M_x and M the Mach number of the x-component and of the total velocity. Of course for this critical point we have another more equation, i.e. Eq.(6.2.17) but this gives the position in the field line where Eq.(7.2.7) satisfies. From these results it is important to examing two things (Sauty 1993),
(i), if this critical point is due to the assumption of the separable variables, and
(ii) if it is a characteristic speed for wave propagation.

In general the study of wave propagation in non-uniform media, is of a great importance, but is only in its infancy. It is relating directly to the stability of equilibrium structures and to the classical problem of the heating of solar corona. To anwser the second question, Tsinganos et al (1994) showed that the case of the critical point defined in Eq.(7.2.7) can be written in the more familiar form (note that $M = V/V_s$, $M_a = V/V_a = V_x/V_{a_x}$

$$V - x^4 - V_x^2(V_s^2 + V_a^2) + V_s^2 V_{a_x}^2 = 0\,, \tag{7.2.8}$$

which means that the x-component of the flow speed along the critical curve (7.2.7) is equal to the characteristic speed of the fast/slow MHD waves propagating in the x-direction.

To answer to the first question we must examing some properties of the general MHD equations. In cartesian geometry for planar structures with translational symmetry and isothermal equation of state the MHD equations are the transfield equation

$$\nabla^2 A - \Psi_A\left[\frac{\partial}{\partial x}\frac{\Psi_A}{4\pi\rho}\frac{\partial A}{\partial x} + \frac{\partial}{\partial z}\frac{\Psi_A}{4\pi\rho}\frac{\partial A}{\partial z}\right] + 4\pi\rho\frac{dE}{dA_0} = 0\,. \tag{7.2.9a}$$

discrubing the force balance across fieldlines and the Bernoulli equation

$$V_s^2 \ln\left(\frac{\rho}{\rho_o}\right) + gz + \frac{\Psi_A^2}{32\pi^2\rho^2}\left[\left(\frac{\partial A}{\partial x}\right)^2 + \left(\frac{\partial A}{\partial z}\right)^2\right] = E(A)\,, \tag{7.2.9b}$$

discrubing the force balance along fieldlines. It is easy to see from Eq.(7.2.9b) that the density is function of A and z although that we can not found it explicitly. But its derivatives can be calculated explicitly and to substitute in the transfield equation which can be written

$$(1-M_a^2)\left[\frac{\partial^2 A}{\partial^2 x} + \frac{\partial^2 A}{\partial^2 z}\right] + M_a^2\left[\frac{1}{\rho}\frac{\partial\rho}{\partial x}\frac{\partial A}{\partial x} + \frac{1}{\rho}\frac{\partial\rho}{\partial z}\frac{\partial A}{\partial z}\right] - \frac{V_a^2}{2}\frac{d\Psi_A^2}{dA} + 4\pi\rho\frac{dE}{dA} = 0\,. \tag{7.2.10a}$$

where V_a is the Alfvén velocity. Thus from the Bernoulli equation we obtain

$$(M^2-1)\frac{1}{\rho}\frac{\partial\rho}{\partial x}\frac{\partial A}{\partial x} = \frac{M^2 M_{a_z}^2}{2M_a^2}\frac{d\Psi_A^2}{dA} + M_z^2\frac{\partial^2 A}{\partial^2 x} - M_x M_z\frac{\partial^2 A}{\partial x \partial z} - 4\pi\rho\frac{M_z^2}{M_a^2}\frac{dE}{dA}\,, \tag{7.2.10b}$$

$$(M^2-1)\frac{1}{\rho}\frac{\partial\rho}{\partial z}\frac{\partial A}{\partial z} = \frac{M^2 M_{a_x}^2}{2M_a^2}\frac{d\Psi_A^2}{dA} + M_x^2\frac{\partial^2 A}{\partial^2 z} - M_x M_z\frac{\partial^2 A}{\partial x \partial z} - 4\pi\rho\frac{M_x^2}{M_a^2}\frac{dE}{dA} - \frac{g}{V_s^2}\,, \tag{7.2.10c}$$

where M_z, is the z-component of the Mach number of the flow and M_{a_x} and M_{a_z} the $x-$ and z-components of the Alfvén number. Substitute them in the transfield equation

(7.2.10a) we get

$$[M^2 + M_a^2 - M_a^2 M_x^2 - 1]\frac{\partial^2 A}{\partial^2 x} - 2M_a^2 M_x M_z \frac{\partial^2 A}{\partial x \partial z} + [M^2 + M_a^2 - M_a^2 M_z^2 - 1]\frac{\partial^2 A}{\partial^2 z}$$
$$+\frac{V_a^2}{2}\frac{d\Psi_A^2}{dA} - 4\pi\rho M^2 \frac{dE}{dA} - \frac{g}{V_s}\Psi_A M_x = 0\,. \qquad (7.2.11)$$

The above equation is known in bibliography as 2-D quasi-linear partial differential equation because the higher derivatives of A is in linear form although that the coefficients of them depend from the A itself.

Now we recognize that the critical point appear in the analysis of chapter 6 is simply the coefficent of $\partial^2 A/\partial^2 x$. When this becomes zero all the other terms must became zero in order $\partial^2 A/\partial^2 x$ to be finite. The same also valid for the coefficient of $\partial^2 A/\partial^2 z$ but in the case studied in chapter 6 the z-dependence is dropped out from the beginning. Eq.(7.2.11) written first by Heinemann & Olbert (1978) in spherical geometry. It has the characteristic that is of mixed-type, in some points is elliptical ($D < 0$) while in others is hyperbolic ($D > 0$), where $D = b^2 - ac$ and a, b, c are the coefficients of the second order derivatives of A (Eq.7.2.11). Thus, appropriate boundary conditions must be used in each domain (i.e Laplace-type for the elliptic and wave-type in the hyperbolic domain), taking also to account that the solution must be continuous at the points of the line where $D = 0$. After a simple algebra we found that

$$D = (M^2-1)(M_a^2-1)(M^2+M_a^2-1) = (V^2-V_s^2)(V^2-V_a^2)(V^2-V_t^2)/V_s^4 V_a^4\,. \quad (7.2.12)$$

where V_t is the tube velocity which is smaller both from V_a and V_s. Define $V_{\min} = min[V_s, V_a]$ and $V_{\min} = min[V_s, V_a]$ we conclude that if $V < V_t$ or $V_{\min} < V < V_{\max}$ the transfield equation is of elliptic type, while if $V_t < V < V_{\min}$ or $V > V_{\max}$ is of hyperbolic type. Thus we see that in the points where the transfield equation changes character the fluid velocity is equals to a characteristic velocity which corresponds also to a characteristic wave propagation. But apart from this, it is interesting the fact that the velocities defined putting equal to zero the coefficients a, and c of the transfield equation are correspond to fast/slow MHD waves.

Wave propagation Because of the great importance of the the study of wave propagation in non-uniform media, we shall give in the following, the general equations discrubing this and a simple example.

Consider a force-free field $\mathbf{B_0}$ in a vertically stratified stationary isothermal plasma, under the influence of a uniform gravitational field g). Its density and pressure which behave like

$$\rho_0 = \rho_{00} e^{-\frac{z}{L}}, \qquad P_0 = P_{00} e^{-\frac{z}{L}}, \qquad (7.2.13)$$

where $L = P_{00}/\rho_{00}g$, and satisfy the hydrostatic equation $\nabla \mathbf{P_0} = \rho_0 \mathbf{g}$. Consider small departures from the equilibrium

$$\rho = \rho_0 + \rho_1, \qquad P = P_0 + P_1, \qquad \mathbf{B} = \mathbf{B_0} + \mathbf{B_1}, \qquad \mathbf{V} = \mathbf{V_1}, \tag{7.2.14}$$

and linearize the MHD equations (2.3.1) by neglecting squares and products of small quantities (denoted by subscript 1). The result is

$$\nabla \cdot \mathbf{B_1} = 0, \tag{7.2.15a}$$

$$\frac{\partial \rho_1}{\partial t} + \nabla \cdot (\rho_0 \mathbf{V_1}) = 0, \tag{7.2.15b}$$

$$\frac{\partial \mathbf{B_1}}{\partial t} = \nabla \times (\mathbf{V_1} \times \mathbf{B_0}), \tag{7.2.15c}$$

$$\frac{\partial P_1}{\partial t} + (\mathbf{V_1} \cdot \nabla) P_0 + \gamma P_0 (\nabla \cdot \mathbf{V_1}) = \mathcal{L}_1, \tag{7.2.15d}$$

$$\rho_0 \frac{\partial \mathbf{V_1}}{\partial t} = -\nabla P_1 + \frac{(\nabla \times \mathbf{B_1}) \times \mathbf{B_0}}{4\pi} + \frac{(\nabla \times \mathbf{B_0}) \times \mathbf{B_1}}{4\pi} + \rho_1 \mathbf{g}, \tag{7.2.15e}$$

where for the Eq.(7.2.15d) which describes the thermodynamics of the plasma we have linearized Eq.(2.3.1.d) writing

$$\mathcal{L} = \mathcal{L}_0 + \mathcal{L}_1, \tag{7.2.16}$$

where of course the energy function $\mathcal{L}_0$ has to do with the initial state and is such that isothermallity is holds in that. For simplicity the perturb energy function can be choose either zero $\mathcal{L}_1 = 0$, so adiabatic gas variations are studying, or such that that isothermallity relation holds for the perturb density and pressure. From technical point the second case can be found from Eq.(7.2.15d) putting again $\mathcal{L}_1 = 0$ but $\gamma = 1$.

The set of Eqs.(7.2.15) may be reduced to a single equation by differentiating the momentum equation and making the necessary substitutions. The result is a generalized wave equation for the disturbance velocity $\mathbf{V_1}$ (Priest 1984)

$$\rho_0 \frac{\partial^2 \mathbf{V_1}}{\partial t^2} = \gamma P_0 \nabla(\nabla \cdot \mathbf{V_1}) + (\gamma - 1)\rho_0 (\nabla \cdot \mathbf{V_1})\mathbf{g} + \rho_0 (\mathbf{g} \cdot \nabla)\mathbf{V_1}$$

$$+ \frac{[\nabla \times (\nabla \times \mathbf{V_1}) \times \mathbf{B_0}] \times \mathbf{B_0}}{4\pi} + \frac{[\nabla \times \mathbf{B_0}] \times [(\nabla \times \mathbf{V_1}) \times \mathbf{B_0}]}{4\pi}, \tag{7.2.17}$$

It is obvious from Eq.(7.2.17) that if the initial state was uniform the solution of this is easy to obtain by a Fourier transform (plane waves)

$$\mathbf{V_1} = \mathcal{V}_1 e^{i(\omega t - \mathbf{k}\cdot\mathbf{r})}. \tag{7.2.18}$$

Thus Eq.(7.2.17) reduces to algebraic equation for the dispersion relation $\omega = \omega(\mathbf{k})$ and the amplitude of the wave $\mathcal{V}_1$ is constant. This analysis cover from all text book in plasma physics. But for non-uniform initial states Eq.(7.2.17) becomes in general a partial differential equation for the amplitude $\mathcal{V}_1$ which is now a function of the spatial coordinates because the solution must be obey to certain boundary conditions. Note the Fourier analysis still holds for the time dependence and for coordinates in which the equilibrium configuration is invariance.

As an example we shall examing the propagation of waves in the most simple current-free planar magnetic configuration in cartesian coordinates

$$A_0 = 2LB_0 \cos\left(\frac{x}{2L}\right)e^{-\frac{z}{2L}}, \tag{7.2.19}$$

$$B_{0_x} = -\frac{\partial A_0}{\partial z} = B_0 \cos\left(\frac{x}{2L}\right)e^{-\frac{z}{2L}}, \qquad B_{0_z} = \frac{\partial A_0}{\partial x} = -B_0 \sin\left(\frac{x}{2L}\right)e^{-\frac{z}{2L}}.$$

in which the plasma β is constant everywhere. For simplicity we shall consider waves in which the x- and z-components of the disturbance velocity $\mathbf{V_1}$ are zero ($V_{1_x} = V_{1_z} = 0$). Thus we write for the remaining y-component

$$V_{1_y} = \mathcal{V}_{1_y}(x)e^{i(\omega t - k_y y - k_z z)}, \tag{7.2.20}$$

because the exponential z-dependence existing in the quantities of the equilibrium state drops out, and thus the amplitude $\mathcal{V}_{1_y}(x)$ satisfies an ordinary differential equation. It is easy to see that substitution of the above expression in the x- and z-components of the general wave equation gives

$$k_y = 0, \tag{7.2.21}$$

which means that there are no waves traveling in the invariance direction. From the other side the y-component of the wave equation (7.2.17) gives

$$\cos^2\mathrm{x}\frac{d^2\mathcal{V}_{1_y}}{d\mathrm{x}^2} + 2iK_z\cos\mathrm{x}\sin\mathrm{x}\frac{d\mathcal{V}_{1_y}}{d\mathrm{x}} + \left[iK_z + \Omega^2 - K_z^2\sin^2\mathrm{x}\right]\mathcal{V}_{1_y} = 0, \tag{7.2.22}$$

where we have define the dimensionless variables $\mathrm{x} = x/2L$, $K_z = 2Lk_z$, and $\Omega^2 = 2\beta\omega^2 L/g$. The above differential equation subject to the boundary conditions

$$\mathcal{V}_{1_y} = 0 \quad \text{at} \quad \mathrm{x} = \pm\frac{\pi}{2}, \tag{7.2.23}$$

will give the dispersion relation $\Omega = \Omega(K_z)$. Making the change of variable $\xi = \sin\mathrm{x}$ we rewrite Eq.(7.2.22) in the form

$$(1-\xi^2)^2\frac{d^2\mathcal{V}_{1_y}}{d\xi^2} + (2iK_z - 1)\xi(1-\xi^2)\frac{d\mathcal{V}_{1_y}}{d\xi^2} + (iK_z + \Omega^2 - K_z^2\xi^2)\mathcal{V}_{1_y} = 0, \tag{7.2.24}$$

In order to solve this we make the substitution

$$\mathcal{V}_{1_y} = (1-\xi^2)^q \mathcal{Y}, \tag{7.2.25}$$

which is leads to the differential equation

$$(1-\xi^2)\frac{d^2\mathcal{Y}}{d\xi^2} + (2iK_z - 1 - 4q)\xi\frac{d\mathcal{Y}}{d\xi} + (K_z^2 + 4iqK_z + 2q - 4q^2)\mathcal{Y} = 0\,, \tag{7.2.26}$$

where the exponent q is given from the condition

$$\Omega^2 + iK_z - K_z^2 - 4iqK_z + 4q^2 - 2q = 0\,, \tag{7.2.27}$$

Application of the Forbenious method in Eq.(7.2.26) gives that the boundary conditions (7.2.23) satisfied if

$$n(n-1) - (2iK_z - 1 - 4q)n - K_z^2 - 4iqK_z + 4q^2 - 2q = 0\,, \tag{7.2.28}$$

where $n = 0, 1, 2, ...$ From Eqs.(7.2.27,7.2.28) we get

$$iK_z - 2q = \frac{n^2 - \Omega^2 - iK_z}{2n}\,, \tag{7.2.29}$$

while Eq.(7.2.27) can be written as

$$(\Omega^2 + iK_z) + (iK_z - 2q)^2 - K_z^2 = 0\,, \tag{7.2.30}$$

Thus the dispersion relation written as

$$\left(\Omega^2 + iK_z + n^2\right)^2 = K_z^2\,. \tag{7.2.31}$$

Decoupling the wave number K_z in real and imagine parts we find from Eq.(7.2.31)

$$\mathrm{Re}(K_Z) = \mathrm{Im}(K_Z) = \frac{1}{2}(\Omega^2 + n^2)\,. \tag{7.2.32}$$

Thus we conclude that the amplitude of the wave increase with height as $e^{\mathrm{Im}(K_Z)Z}$ and the initial magnetic structure is unstable $\Omega^2 < 0$ for wavenumbers

$$\mathrm{Re}(K_Z) < \frac{n^2}{2}\,, \tag{7.2.33}$$

while the propagation velocity of the wave is (group velocity)

$$v_g = \frac{d\omega}{dk} = \frac{g}{\beta\omega}\,. \tag{7.2.34}$$

Appendix A

General transfield equation in low-β and M_a^2 limit

From the general transfield equation 2.3.36, in our case, in the lowest order approximation in β and M_a^2, $A = A_0$, $\rho = \Psi_{A_0} = \Omega = E = 0$, we get a force-free field configuration

$$\frac{1}{h_1 h_2 h_3}\left[\frac{\partial}{\partial x_1}\frac{h_2}{h_1 h_3}\frac{\partial A_0}{\partial x_1} + \frac{\partial}{\partial x_2}\frac{h_1}{h_2 h_3}\frac{\partial A_0}{\partial x_2}\right] + \frac{1}{2h_3^2}\frac{dG_0^2(A_0)}{dA_0} = 0\,, \qquad (A.1)$$

where $G_0(A_0) = h_3 B_{0_{x_3}}$ is a function of A_0.

Perturbations to first order in the small Alfvén-Mach numbers ($\Psi_{A_0}^2/4\pi\rho << 1$) give non-zero values for ρ, Ψ_{A_0}, E. We still impose $\Omega = 0$ because we deal with field-aligned flows. We write

$$A = A_0 + A_1\,. \qquad (A.2)$$

Instead of $G_0(A)$ introduce another function $G(A)$

$$G(A) = G_0(A) + G_1(A)\,, \qquad (A.3)$$

where $G_0(A) << G_1(A)$. Making a Taylor expansion we have

$$\Psi_{A_0}(A) = \Psi_{A_0}(A_0) + \frac{d\Psi_{A_0}}{dA_0}A_1 + ... \qquad (A.4a)$$

$$E(A) = E(A_0) + \frac{dE}{dA_0}A_1 + ... \qquad (A.4b)$$

$$G(A) = G_0(A_0) + \frac{dG_0}{dA_0}A_1 + G_1(A_0) + ... \qquad (A.4c)$$

Putting these expressions in the transfield equation and taking into account that the square of the Alfvén-Mach number is small and that in order of magnitude we have $\Psi_{A_0}^2/4\pi\rho \approx A_1/A_0$, we get the field-aligned flow condition Eq.(4.3.15), the Bernoulli Eq.(4.3.19) and

$$\frac{1}{h_1h_2h_3}\left[\frac{\partial}{\partial x_1}\frac{h_2}{h_1h_3}\frac{\partial A_1}{\partial x_1}+\frac{\partial}{\partial x_2}\frac{h_1}{h_2h_3}\frac{\partial A_1}{\partial x_2}\right]+\frac{1}{2h_3^2}\frac{d^2(G_0^2)}{dA_0^2}A_1 =$$

$$\frac{\Psi_{A_0}}{h_1h_2h_3}\left[\frac{\partial}{\partial x_1}\frac{h_2}{h_1h_3}\frac{\Psi_{A_0}}{4\pi\rho}\frac{\partial A_0}{\partial x_1}+\frac{\partial}{\partial x_2}\frac{h_2}{h_1h_3}\frac{\Psi_{A_0}}{4\pi\rho}\frac{\partial A_0}{\partial x_2}\right]$$

$$-\frac{1}{h_3^2}\frac{d(G_0G_1)}{dA_0}-\frac{1}{8\pi\rho h_3^2}\frac{d(G_0^2\Psi_{A_0}^2)}{dA_0}-4\pi\rho\frac{dE}{dA_0}. \qquad (A.8)$$

while the correction in $B_{1_{x_3}}$x is given by

$$B_{1_{x_3}}=\frac{\Psi_{A_0}^2}{4\pi\rho}B_{0_{x_3}}++\frac{1}{h_3}\frac{dG_0}{dA_0}A_1+\frac{G_1}{h_3}. \qquad (A.9)$$

Appendix B

Green functions for the linearized transfield equation.

For cartesian coordinates, the required Green function $G(x,z;x',z')$ of the Poisson equation which satisfies

$$\frac{\partial^2 G}{\partial x'^2}+\frac{\partial^2 G}{\partial z'^2}=\delta(x'-x)\delta(z'-z)\,, \tag{B.1}$$

and vanishes on $x'=a$, $x'=b$, $z'=0$, $z'\to\infty$. Such a solution can be expanded in the form

$$G(x,z;x',z')=\sum_{n=1}^{\infty}\sin[\gamma_n(x'-a)]Z_n(z')\,. \tag{B.2}$$

where

$$\gamma_n=\frac{n\pi}{b-a}\,. \tag{B.3}$$

Inserting this in Eq.(B.2) gives ordinary differential equations for Z_n. Solving these we get

$$G(x,z;x',z')=\frac{2}{b-a}\sum_{n=1}^{\infty}\frac{1}{\gamma_n}\sin[\gamma_n(x-a)]\sin[\gamma_n(x'-a)][e^{-\gamma_n|z-z'|}-e^{-\gamma_n(z+z')}]\,. \tag{B.4}$$

Using complex variables we can calculate the sum and we get

$$G(x,z;x',z')=$$

$$\frac{1}{2\pi}\ln\frac{1+e^{-2\gamma_1|z-z'|}-2\cos\gamma_1(x+x'-2a)e^{-\gamma_1|z-z'|}}{1+e^{-2\gamma_1|z-z'|}-2\cos\gamma_1(x-x')e^{-\gamma_1|z-z'|}}+$$

$$\frac{1}{2\pi}\ln\frac{1+e^{-2\gamma_1(z+z')}-2\cos\gamma_1(x-x')e^{-\gamma_1(z+z')}}{1+e^{-2\gamma_1(z+z')}-2\cos\gamma_1(x+x'-2a)e^{-\gamma_1(z+z')}}\,. \tag{B.5}$$

For the cylindrical coordinates, for the same boundary conditions, the required Green function $G(\varpi,z;\varpi',z')$ satisfies

$$\frac{\partial^2 G}{\partial\varpi'^2}+\frac{1}{\varpi'}\frac{\partial G}{\partial\varpi'}+\frac{G}{\varpi'^2}+\frac{\partial^2 G}{\partial z'^2}=\frac{1}{\varpi'}\delta(\varpi'-\varpi)\delta(z'-z) \tag{B.6}$$

and is given by

$$G(\varpi,z;\varpi',z')=$$

$$\sum_{n=1}^{\infty}\frac{1}{L_n\gamma_n}[\mathrm{Y}_1(\gamma_n a)\mathrm{J}_1(\gamma_n\varpi)-\mathrm{J}_1(\gamma_n a)\mathrm{Y}_1(\gamma_n\varpi)][\mathrm{Y}_1(\gamma_n a)\mathrm{J}_1(\gamma_n\varpi')-\mathrm{J}_1(\gamma_n a)\mathrm{Y}_1(\gamma_n\varpi')]$$

$$\times[e^{-\gamma_n|z-z'|}-e^{-\gamma_n(z+z')}] \tag{B.7}$$

where γ_n is found from the following condition

$$\mathrm{Y}_1(\gamma_n a)\mathrm{J}_1(\gamma_n b)=\mathrm{J}_1(\gamma_n a)\mathrm{Y}_1(\gamma_n b)\,, \tag{B.8}$$

and

$$L_n=\frac{b^2}{2}[\mathrm{Y}_1(\gamma_n a)\mathrm{J}_0(\gamma_n b)-\mathrm{J}_1(\gamma_n a)\mathrm{Y}_0(\gamma_n b)]^2-\frac{a^2}{2}[\mathrm{Y}_1(\gamma_n a)\mathrm{J}_0(\gamma_n a)-\mathrm{J}_1(\gamma_n a)\mathrm{Y}_0(\gamma_n a)]^2\,, \tag{B.9}$$

which is the square of the normalization factor of these eingefunctions. In the special case $a=0$, $b=7.66341$ (the first zero of $\mathrm{J}_1(\varpi/2)$ the Green function takes the simpler form

$$G(\varpi,z;\varpi',z')=\sum_{n=1}^{\infty}\frac{1}{L_n\gamma_n}\mathrm{J}_1(\gamma_n\varpi)\mathrm{J}_1(\gamma_n\varpi')[e^{-\gamma_n|z-z'|}-e^{-\gamma_n(z+z')}] \tag{B.10}$$

where

$$L_n=\frac{7.66341^2}{2}\mathrm{J}_0^2(7.66341\gamma_n)\,, \tag{B.11}$$

and γ_n satisfies

$$7.66341\gamma_n=j_{1,n}\,, \tag{B.12}$$

where $j_{1,n}$ is the n-zero of $\mathrm{J}_1(\varpi/2)$.

Appendix C

Numerical techniques.

Although that we know explicitly the appropriate Green functions it was convenient to use a standard routine that solves a partial elliptic differential equation in order to find the solution of the linearized transfield equations. Such a routine discretizes a given equation on a rectangular domain $a \leq x_1 \leq b$, $c \leq x_2 \leq d$, with $n_{x_1} \times n_{x_2}$ grid points. In our case, where $c = 0$, we have chosen instead of $d \to \infty$ the value $d = 4(b-a)$. Thus the rectangular domain was $-\pi \leq \mathrm{x} \leq \pi$, $0 \leq z \leq 8\pi$ in cartesian coordinates and $0. \leq \varpi \leq \varpi_2$, $0 \leq \mathrm{z} \leq 4\varpi_2$ (with $\varpi_2 = 7.66341$) in cylindrical coordinates; for the largest z, the right hand side of Eqs.(4.4.4) and (5.3b) is lower than $e^{-4\pi}$ which is smaller by two orders of magnitude than the routine errors $\left(\frac{b-a}{n_{x_1}}\right)^4 + \left(\frac{d-c}{n_{x_2}}\right)^4 \approx 2.10^{-4}$ for $n_{x_2} = 4n_{x_1} = 2^8$ for the grid. For each grid point the density has been obtained numerically from the Bernoulli equation keeping the larger (smaller) root for subsonic (supersonic) flows. Note that the various space partial derivatives of the density can be obtained analytically. The resulting linear system for the values of a_1 at each grid point is multi-diagonal and it can be solved by a cyclic reduction algorithm (in our case the generated system is always diagonally dominant).

In transonic cases, we first mark the grid points, there are three types of grid points, depending on the choice of solutions in Bernoulli equation, (i) those which are in the static (no-flows) and pre-shock (pre-critical) subsonic domain, (ii) those which are in pre-shock supersonic domain, and (iii) those which are in the post-shock subsonic domain. The character of a grid point comes from the information of the sonic and shock position for each field line on which the given grid point lies. Thus we are able to solve by the same method Eqs.(4.4.16) in the whole rectangular domain in order to find a_1 associated with the diffuse current. But to find the field a_{1_s} produced by the

shock surface current density j_s we use the Green functions (Appendix B) writing

$$a_{1_S}(x_1, x_2) = \int_C G(x_1, x_2; x_1^{\rm sh}, x_2^{\rm sh}) j_s(s) ds\,, \qquad (C.1)$$

where the integration takes place only along the shock front curve C given from the Eq.(4.4.14) and where $x_i^{\rm sh}(s)$ $i = 1, 2$ are the coordinates of the shock front. Because $s = s(a_0)$, we can transform Eq.(C1) in a_0 variable, so

$$a_{1_S}(x_1, x_2) = \int_C G(x_1, x_2; x_1^{\rm sh}, x_2^{\rm sh}) j_s(a_0) s'(a_0) da_0\,, \qquad (C.2)$$

where the prime denotes derivation and can be calculated analytically from the shock front shape and the equation for the field lines. Thus we can integrate Eq.(C.2) numerically finding first the shock position and then the surface current density.

Appendix D

Analytical form of Eq.(5.4.19)

In Eq.(5.4.19) X can be expressed as a function of R through the elliptic integrals. Thus, we may write Eq.(5.4.19) as

$$\pm\sqrt{\beta}X = \int_1^R \frac{dR}{\sqrt{R(1-R)(R-M^2)}} + M_a^2 \int_1^R \frac{dR}{R\sqrt{R(1-R)(R-M^2)}}$$

$$-(M^2 + 2M_a^2 + 2M^2M_a^2) \int_1^R \frac{dR}{R^2\sqrt{R(1-R)(R-M^2)}}$$

$$+3M^2M_a^2 \int_1^R \frac{dR}{R^3\sqrt{R(1-R)(R-M^2)}}. \qquad (D.1)$$

or,

$$\pm\frac{\sqrt{\beta}}{2}Y = \int_0^t \frac{dt}{\sqrt{(1-t^2)(1-k^2t^2)}} + M_a^2 \int_0^t \frac{dt}{(1-t^2)\sqrt{(1-t^2)(1-k^2t^2)}}$$

$$-(M^2 + 2M_a^2 + 2M^2M_a^2) \int_0^t \frac{dt}{(1-t^2)^2\sqrt{(1-t^2)(1-k^2t^2)}}$$

$$+3M^2M_a^2 \int_0^t \frac{dt}{(1-t^2)^3\sqrt{(1-t^2)(1-k^2t^2)}}. \qquad (D.2)$$

where $k^2 = 1/(1-M^2)$ and $t = \sqrt{(1-R)/(1-M^2)}$. It is evident then that $X(R)$ may be expressed in terms of the elliptic integrals of the first and second kind, $F(t,k)$ and $E(t,k)$, respectively and the Jacobian elliptic functions sn$u$, cn$u$, dn$u$, in the following

way (Byrd and Friedman 1971),

$$I_0 = \int_0^t \frac{dt}{\sqrt{(1-t^2)(1-k^2t^2)}} = F(t,k) = u\,, \qquad (D.3)$$

$$I_1 = \int_0^t \frac{dt}{(1-t^2)\sqrt{(1-t^2)(1-k^2t^2)}} = \frac{E(t,k) - k^2 \mathrm{sn}u\mathrm{cn}u/\mathrm{dn}u}{1-k^2}\,, \qquad (D.4)$$

$$I_2 = \int_0^t \frac{dt}{(1-t^2)^2\sqrt{(1-t^2)(1-k^2t^2)}} = \frac{2(2-k^2)I_1 - u - k^2\mathrm{sn}u\mathrm{cn}u/\mathrm{dn}^3u}{3(1-k^2)}\,, \qquad (D.5)$$

$$I_3 = \int_0^t \frac{dt}{(1-t^2)^3\sqrt{(1-t^2)(1-k^2t^2)}} = \frac{4(2-k^2)I_2 - 3I_1 - k^2\mathrm{sn}u\mathrm{cn}u/\mathrm{dn}^5u}{5(1-k^2)}\,, \qquad (D.6)$$

Note that sn$u$ (the inversion of the integral in D.3), cn$u$ $= \sqrt{1-\mathrm{sn}^2u}$ and dn$u$ $= \sqrt{1-k^2\mathrm{sn}^2u}$.

Bibliography

[1] Acton L.W., Culhane, J. L., Cabriel, A. H., et al. (1981), ApJ **244**, L137

[2] Alissandrakis, C. E., Georgakilas, A.A. Dialetis, D.,(1992), Sol. Phys. **138**, 93

[3] Alissandrakis, C. E., Dialetis, D., Mein, P., Schmieder, B., Simon, G. (1988), A&A, **201**, 339

[4] Antiochos, S.K.,(1984), ApJ **280**, 416

[5] Athay, R.G.,(1976), *The Solar Chromosphere and Corona, Quiet Sun*, D. Reidel, Dordrecht, Holland.

[6] Athay, R.G.,(1980), in *Solar Active Regions*, ed. F. Orrall, Colo. Ass. Univ. Press, p.83

[7] Athay, R.G.,(1981), A&A **249**, 340

[8] Athay, R.G.,(1989), Sol. Phys. **119**, 135

[9] Athay, R.G., Gurman, J.B., Henze, W., (1983), ApJ **269**, 706

[10] Athay, R.G., Gurman, J.B., Henze, W., Shine, R.A., (1982), ApJ **261**, 684

[11] Athay R.G., White O.R., Lites B.W., Bruner E.C., (1980), Sol. Phys. **66**, 357

[12] Berton , R., Sakurai, T.,(1985), Sol. Phys. **96**, 93

[13] Bogdan, T.J., Low, B.C.,(1986), ApJ **306**, 271

[14] Bommier , V., Leroy, J.L., Sahal-Bréchot, S., (1981), A&A **100**, 231

[15] Börner, P., Kneer, F. (1992), A&A, **259**, 307

[16] Bray, R.J., Loughhead, R. E.,(1983), Sol. Phys. **85**, 131

[17] Bray, R.J., Cram, L.E., Durrant, C.J., Loughhead, R.E., (1991) in *Plasma loops in Solar corona*, Cambridge University Press.

[18] Brown, S.F.,(1991), A&A **249**, 243

[19] Browning P.K., Priest E.R., (1984), Sol. Phys. **92**, 173

[20] Browning P.K., Priest E.R., (1986), Sol. Phys. **106**, 335

[21] Brueckner G.E., Bartoe J.-D. F., Cook J. W., Dere K.P., Socker D., Kurokawa H., McCabe M., (1988), ApJ **335**, 986

[22] Bruner, E.C., Chipman, E.G., Lites, B.W., Rottman, G.J., Shine, R.A., Athay, R.G., White, O.R.,(1976), ApJ **210**, L97

[23] Bruzek, A., Durrant, C.J., (1977), *Illustrated Glossary of Solar and Solar-Terrestrial Physics*, D. Reidel, Boston

[24] Bumda, V., Kleczek, J., (1961), Observatory, **81**, 141

[25] Byrd, P.F. and Friedman, M.D., (1971), *Handbook of Elliptic Integrals for Engineers and Scientists*, p. 58, p. 194, Springer-Verlag.

[26] Cargill, P.J., Priest, E.R., (1980), Sol. Phys. **65**, 251

[27] Chase, R.C., Krieger, A.S., Svestka, Z., Vaiana, G.S.,(1976), Space Recearch **XVI**, 917

[28] Chen, C.-L., Loughhead, R.E.,(1983), in *Proceedings of the Astronomical Society of Australia*, **5**, 204

[29] Cheng, C.-C.,(1980a), Sol. Phys. **65**, 347

[30] Cheng, C.-C.,(1980b), A&A **238**, 743

[31] Cheng, C.-C., Smith, J.B., Tandberg-Hanssen, E.,(1980), Sol. Phys. **67**, 259

[32] Chiuderi, C.,(1981), in *Solar phenomena in Stars and Stellar Systems* ed. R.M. Bonnet and A.K. Dupree.

[33] Chou, D-.Y., Zirin, H.,(1988), ApJ **333**, 420

[34] Craig, I.J.D., McClymont, A.N.,(1986), ApJ **307**, 367

[35] Culhane, J.L, Acton, L.W.,(1974), A&A **12**, 359

[36] Defouw R.J., (1976), ApJ **209**, 266

[37] Degenhart D., (1989), A&A **222**, 297

[38] Degenhart D., (1991), A&A **248**, 637

[39] Degenhart D., Deinzer, W.,(1993), A&A **278**, 288

[40] Davis, J.M., Krieger, A.S.,(1982), Sol. Phys. **45**, 393

[41] Dere, K.P.,(1982), Sol. Phys. **75**, 189

[42] Dere K.P., Schmieder B., Alissandrakis C.E., (1990), A&A **233**, 207

[43] de Ville A., Priest E.R., (1989a), ApJ **340**, 529

[44] de Ville A., Priest E.R., (1989b), ApJ **347**, 1167

[45] de Ville, A. (1990), *Ph.D. Thesis*, Univ. of St Andrews, UK

[46] de Ville A., Priest E.R., (1991a), ApJ **359**, 560

[47] de Ville A., Priest E.R., (1991b), Geophys. Astrophys. Fluid Dynamics **59**, 253

[48] de Ville A., Priest E.R., (1991c), Geophys. Astrophys. Fluid Dynamics **61**, 225

[49] de Jager, C., (1959), Handbuch der Physik, **52**, 80

[50] Degenhardt, D. (1989), A&A, **222**, 297

[51] Degenhardt, D. (1991), A&A, **248**, 637

[52] Degenhardt, D., Lites, B., (1993), ApJ, **404**, 383

[53] Degenhardt, D., Lites, B., (1993), ApJ, **416**, 875

[54] Degenhardt, D., Solanski, S.K., Montesinos, B., Thomas, J.H. (1994), A&A, (in press)

[55] Demoulin, P. (1989), *Ph.D. Thesis*, Université de Paris VII, France.

[56] Demoulin, P.,(1991) in *Advances in Solar system Magnetohydrodynamics*, ed. E.R. Priest and A.W. Hood, Cambridge Univ. Press, p.257

[57] Demoulin, P.,(1993), Adv. Space Res. **13**, (9)95

[58] Dialetis, P., Mein, P., Alissandrakis, C.E.,(1985), A&A **147**, 93

[59] Doschek G.A., Feldman U., Bohlin J.D., (1976), ApJ **205**, L177

[60] Dulk, G.A., Gary, D.E.,(1983), A&A **124**, 103

[61] Dunn, R.B, (1971), in *Physics of the Solar Corona* ed. C.J. Macris, Reidel, Dordrecht.

[62] Ellison, M.A., (1944), MNRAS **104**, 22

[63] Engvöld, O., Malville, J.M., Rustad B.M., (1976), Sol. Phys. **48**, 137

[64] Feldman, U., Cohen, L., Doschek, G.A.,(1982), ApJ **255**, 325

[65] Ferraro V.C.A.,(1966), *An introduction to magnetofluid mechanics* Oxford, Clarendon Press, p.24

[66] Foukal, P.,(1975), Sol. Phys. **43**, 327

[67] Foukal P.,(1976), ApJ **210**, 575

[68] Foukal, P.,(1978), ApJ **223**, 1046

[69] Foukal, P.,(1990), *Solar Astrophysics*, John Wiley & Sons.

[70] Freidberg, J. P. (1982) Rev. Mod. Phys. **54**, 801

[71] Galeev A.A., Rosner R., Serio S., Vaiana G.S., (1981), ApJ **243**, 301

[72] Georgakilas, A.A., Alissandrakis, C.E., Zachariadis, T.G.,(1990), Sol. Phys. **124**, 277

[73] Gerassimenko, M., Solodyna, C.V., Notle, J.T.,(1978) Sol. Phys. **57**, 103

[74] Glenross, W.M.,(1980), **83**, 65

[75] Golub, L., Noci, G., Poletto, G., Vaiana, G.S.,(1982), ApJ **259**, 359

[76] Gurman, J.B.,(1992) in *The Sun: A laboratoty for Astrophysics* eds. J. Schmeltz and S.F. Brown, p.221

[77] Habbal, S.R., Roman, R., Withbroe, G.L.,(1985), Sol. Phys. **98**, 323

[78] Hara H., Tsuneta S., Lemen J.R., Acton L.W., McTiernan J.M., 1992, PASJ 44, L135

[79] Heinemann, M., Olbert, S.,(1978), J. Geophys. Resear. **83**, 2457

[80] Heinzel, P., Schmieder, B., Mein, P., (1992), Sol. Phys. **139**, 81

[81] Heyvaerts, J., Norman C. A. (1989) ApJ, **347**, 1055

[82] Hood, A.W., Anzer, U., (1990), Sol. Phys. **126**, 117

[83] Hood, A.W., Priest, E.R.,(1979), A&A **77**, 233

[84] Howard, R., Svestka, Z.,(1977) Sol. Phys. **54**, 65

[85] Kjeldseth-Moe, O., Brynildsen, N, Brekke, P., (1988), ApJ **334**, 1066

[86] Kjeldseth-Moe, O., Brynildsen, N, Brekke, P., Maltby, P., Brueckner, G.E., (1993), Sol. Phys. **145**, 257

[87] Kippenhahn, R., Schlüter, A, (1957), *Zs. f. Ap.*, **43**, 36

[88] Kleczek, J.,(1963), in *Bulletin of the Astronomical Institutes of Czechoslovakia*, **14**, 167

[89] Klimchuk, J.A., et al (1992), **44**, L181

[90] Kopp R.A., Poletto G., Noci G, Bruner M., (1985), Sol. Phys. **98**, 91

[91] Krieger, A.S., de Feiter, L.D., Vaiana, G.S.,(1976), Sol. Phys. **47**, 117

[92] Kundu, M.R., Schmahl, E.J., Gerassimenko, M.,(1980), A&A **82**, 265

[93] Landau L., Lifshitz E. (1966) *Fluid mechanics* Pergamon Press, Chapter 8.

[94] Landau, L.D., Lifshitz, E.M., (1960), *Electrodynamics of Continuous Media*, Pergamon, New York.

[95] Lang, K.R., Wilson, R.F.,(1982), ApJ. **255**, L111

[96] Lang, K.R., Wilson, R.F., Rayrole, J.,(1982), ApJ. **258**, 384

[97] Lategan, A.H., Jarrett, A. H.,(1982) Sol. Phys. **76** 323

[98] Levine, R.H.,(1976), Sol. Phys. **46**, 159

[99] Lima, J.J.G., Priest, E.R.,(1993), A&A **268**, 641

[100] Lites B.W., Bruner, E. C., Chipman, E. G., et al. (1976), ApJ **210**, L111

[101] Lites B.W., Shine, R.A., Chipman, E. G., et al. (1978), ApJ **222**, 333

[102] Loughhead, R.E., Bray, R.J., (1984), ApJ **283**, 392

[103] Loughhead, R.E., Chen, C.-L., Wang, J.-L.,(1984), Sol. Phys. **92**, 53

[104] Low, B.C., (1975a), ApJ **197**, 251

[105] Low, B.C., (1975b), ApJ **198**, 211

[106] Low B.C., (1981), ApJ **251**, 352

[107] Low, B.C., (1982), ApJ **263**, 952

[108] Low, B.C., (1984), ApJ **277**, 415

[109] Low, B.C., (1985), ApJ **293**, 31

[110] Low, B.C., (1990), ARA&A **28**, 491

[111] Low, B.C., (1991), ApJ **370**, 427

[112] Low, B.C., (1992), ApJ **399**, 300

[113] Low, B.C., Hundhausen, A.J., Zweibel, H.G., (1983), *Phys. Fluids*, **26**, 2731

[114] Low, B.C., Tsinganos, K., (1986), ApJ **302**, 163

[115] McAllister, A., et al (1992), PASJ **44**, L205

[116] McClymont, A.N.,(1989), ApJ **347**, L47

[117] McClymont, A.N., Craig, I.J.D.,(1987), ApJ **312**, 402

[118] MacCombie, W.J. Rust, D.M.,(1979), Sol. Phys. **61**, 69

[119] McIntosh , P.S., Krieger, A.S., Nolte, J.T., Vaiana, G.,(1976), Sol. Phys. **49** 57

[120] Makhmudov, M.M., Nikolsky, G. M., Zhugzhda, Y. D.,(1980) Sol. Phys. **66**, 89

[121] Mariska J.T.,(1984), ApJ **281**, 435

[122] Mariska J.T.,(1988), ApJ **334**, 489

[123] Mariska J.T., Boris, J.P.,(1983), ApJ **267**, 409

[124] Martin, S.F., (1973) Sol. Phys. **31**, 3

[125] Martres, M.J., Mein, P., Schmieder, B., Soru-Escaut, I. (1981), Sol. Phys. **69**, 301

[126] Mein, P. (1977), Sol. Phys. **54**, 45

[127] Menzel D., (1951), in, *Proc. Conf. on Dynamics of Ionized Media*, University College, London

[128] Meyer F., Schmidt H.U. (1968), Z. Angew. Math. Mech. **48**, 218

[129] Mikic, Z. Barnes D.C., Schnack D.D., (1988), ApJ **328**, 830

[130] Montesinos B., Thomas J.H., (1989), ApJ **337**, 977

[131] Montesinos B., Thomas J.H., (1993), ApJ **402**, 314

[132] Muller R.,(1973), Sol. Phys. **32**, 409

[133] Noci, G.,(1981), Sol. Phys. **69**, 63

[134] Noci, G., Spadaro, D., Zappala, R.A., Antiochos, S.K., (1989), ApJ **338**, 1131

[135] Ogawara, Y.,(1992), PASJ 44, L41

[136] Pallavicini, R., Sakurai, T., Vaiana, G.S.,(1981), A&A **98**, 316

[137] Pallavicini, R., Vaiana, G.S., Tofani, G., Felli, M.,(1979), ApJ **229**, 375

[138] Pallavicini, R., Peres, G., Serio, S., Vaiana, G.S., Golub, L., Rosner, R., (1981), ApJ **247**, 692

[139] Parker, E.N., (1963), *Interplanetary Dynamical Processes*, Interscience.

[140] Parker E.N., (1979), Cosmical Magnetic Fields, Clarendon Press, Oxford, p. 141

[141] Parker E.N., (1983), ApJ **64**, 642

[142] Peres G., Spadaro D., Noci G., (1992), ApJ **389**, 777

[143] Pneuman, G.W.,(1981), in *Solar Flare Magnetohydrodynamics*, ed. E.R. Priest, Cordon and Breach, New York.

[144] Poland, A.I., Anzer, U., (1971), Sol. Phys. **19**, 401

[145] Poland, A.I., Mariska, J.T.,(1986), Sol. Phys. **106**, 303

[146] Poletto G., Vaiana G.S., Zombeck M.V., Krieger A.S., Timothy A.F. (1975), Sol. Phys. **44**, 83

[147] Priest, E.R. (1978), Sol. Phys. **58**, 57

[148] Priest, E.R.,(1980), in *Solar Active Regions*, ed. F. Orrall, Colo. Ass. Univ. Press, p.213

[149] Priest E.R., (1984), *Solar Magnetohydrodynamics*, D. Reidel, Dordrecht.

[150] Priest, E.R.,(1985), Transactions of the International Astronomical Union, **XIX A**, 90

[151] Priest E.R., (1988), ApJ **328**, 848

[152] Priest, E.R. (ed.), (1989), *Dynamics and Structure of Quiescent Solar Prominences*, Kluwer Academic Publishers, Dordrecht

[153] Priest, E. R., Smith, E. A., (1979) Sol. Phys. **64**, 267

[154] Ray, A., van Hoven, G.,(1982), Sol. Phys. **79**, 353

[155] Reeves E.M., Huber, M.C.E., Timothy, J.G. (1977), Appl. Opt. **16**, 837

[156] Roberts B., (1976), ApJ **204**, 268

[157] Rosner, R., Tucker, W.H., Vaiana, G.S.,(1978), ApJ **220**, 643

[158] Rust, D.M., Webb, D.F.,(1977), Sol. Phys. **54**, 403

[159] Ruzdjak, V. and Tandberg-Hanssen, E. (eds.), (1990), IAU Colloquium No. 117, *Dynamics of Quiescent Solar Prominences*, Hvar 25.-23 S. 1989.

[160] Saba J.L.R., Strong, K.T. (1991), ApJ **375**, 789

[161] Sakurai, T.,(1985), A&A **152**, 121

[162] Sakurai, T., Uchida, Y.,(1977), Sol. Phys. **52**, 397

[163] Sarris, E.T., Krimigis, S.M.,(1982), Geophys. Research Lets. **9**, 167

[164] Sauty, C. (1993), *Ph.D. Thesis*, Université de Paris VII, France.

[165] Sauty, C., Tsinganos , K.,(1994) A&A (in press)

[166] Schmahl, E.J., Mouradian, Z., Martes, M.J., Soru-Escaut, I.,(1982), Sol. Phys. **81**, 91

[167] Schmieder, B.,(1987) in *Dynamics and structure of Solar Prominences* ed. J.L. Ballester, and E.R. Priest, Universitat de les Illes Balears, p.5

[168] Schmieder, B., Malherbe, J.M., Poland, A.I., Simon, J., (1985), A&A **153**, 64

[169] Serio, S., et al (1978), Sol. Phys. **59**, 65

[170] Serio, S., Peres, G., Vaiana, G.S., Golub, L., Rosner, R.,(1981), ApJ **243** 288

[171] Sheeley, N.R.,(1980), Sol. Phys. **66**, 79

[172] Sheeley, N.R., et al (1975a), Sol. Phys. **40**, 103

[173] Sheeley, N.R., et al (1975b), Sol. Phys. **45**, 377

[174] Shibata, K., et al (1992), PASJ **44**, L173

[175] Shimizu, T., et al (1992), PASJ **44**, L147

[176] Spruit, H.C.,(1981), in *The Physics of Sunspots*, eds. L.E. Cram and J. Thomas, p.345

[177] Steele, C.D.C., Priest, E.R.,(1989), Sol. Phys. **119**, 295

[178] Surlantzis G., Démoulin P., Heyvaerts J., Sauty C., (1994), (in press).

[179] Surlantzis, G., Demoulin, P., Heyvaerts, J., Sauty, C., (1993) in *Physics of Solar and stellar coronae,* eds. J. F. Linsky and S. Serio, p.629

[180] Surlantzis, G., Tsinganos, K.,(1993), in *Proceedings of the first Panhellenic Astronomical Meeting,* eds. P. L. Laskaridis, National Astronomical Committee, p.385

[181] Svestka, Z., (1976), *Solar Flares*, Reidel, Dorhrecht.

[182] Svestka, Z., (1981), in *Solar Flare Magnetohydrodynamics*, ed. E.R. Priest, Cordon and Breach, New York.

[183] Tandberg-Hanssen, E.,(1974), *Solar Prominences*, Reidel, Dordrecht.

[184] Tandberg-Hanssen, E.,(1977), in *Illustrated Glossary for Solar and Solar-Terrestial Physics* ed. A. Bruzek and C. J. Durrant, Reidel, Dordrecht.

[185] Tandberg-Hanssen, E., Malville, J.M.,(1974), Sol. Phys. **39**, 107

[186] Thomas J.H.,(1981), in *The Physics of Sunspots*, eds. L.E. Cram and J. Thomas, p.345

[187] Thomas J.H., (1988), ApJ **333**, 407

[188] Thomas J.H., Montesinos, B., (1990), ApJ **359**, 550

[189] Thomas J.H., Montesinos, B., (1991), ApJ **375**, 401

[190] Tousey, R., et al (1973), Sol. Phys. **33**, 265

[191] Tsinganos, K.,(1981), ApJ **245**, 764

[192] Tsinganos, K.,(1982a), ApJ **252**, 775

[193] Tsinganos, K.,(1982b), ApJ **259**, 832

[194] Tsinganos, K.,(1991) in *Advances in Solar system Magnetohydrodynamics*, ed. E.R. Priest and A.W. Hood, Cambridge Univ. Press, p.257

[195] Tsinganos, K.,(1992a) in *The Sun: A laboratoty for Astrophysics* eds. J. Schmeltz and S.F. Brown, p.139

[196] Tsinganos, K.,(1992b) in *The Sun: A laboratoty for Astrophysics* eds. J. Schmeltz and S.F. Brown, p.155

[197] Tsinganos, K., Low, B.C. (1989), ApJ **342**, 1028

[198] Tsinganos, K., Distler, J., Rosner, R.,(1984), ApJ **278**, 409

[199] Tsinganos, K., Sauty, C. (1992a), A&A bf 255, 405

[200] Tsinganos, K., Sauty, C. (1992b), A&A bf 257, 790

[201] Tsinganos K., Surlantzis G., (1992), A&A **259**, 585

[202] Tsinganos K., Surlantzis, G., (1993) in *Physics of Solar and stellar coronae,* eds. J. F. Linsky and S. Serio, p.623

[203] Tsinganos, K., Surlantzis, G., Priest, E. (1993a), A&A, **275**, 613

[204] K. Tsinganos, K., Surlantzis, G., Priest, E.R.,(1993b) in *Physics of solar and stellar coronae,* eds. J. F. Linsky and S. Serio, 623

[205] Tsinganos, K., Trussoni, E. (1991), A&A **249**, 156

[206] Tsinganos, K., Distler, J., Rosner R. (1984), ApJ **278**, 409

[207] Tsiropoula, G., Alissandrakis, C., Bonnet, R.M., Gouttebroze, P.,(1986), A&A **167**, 35

[208] Ushida, Y.,et al (1992), PASJ, 44, L155

[209] Ushida, Y.,(1993), in *Physics of solar and stellar coronae* eds. J.F. Linsky and S.Serio, p.51

[210] Vaiana, G.S., Krieger, A.S., Timothy, A.F.,(1973), Sol. Phys. **32**, 81

[211] Vaiana, G.S., Krieger, A.S., Timothy, A.F., Zombeck, M.,(1976), Astrophysics and Space Science **39**, 75

[212] Vaiana G.S., Rosner R., (1978), ARA&A **16**, 393

[213] Vrsnak, B., (1984), Sol. Phys. **94**, 289

[214] Walker, A.B.C.,(1972), Space Science, Reviews, **13**, 672

[215] Webb, D.F., Krieger, A.S., Rust, D.M.,(1976), Sol. Phys. **48**, 159

[216] Webb, D.F., Davis, J.M., Kundu, M.R., Velusamy, T.,(1983), Sol. Phys. **85**, 267

[217] Wier, E., & Stellmacher, G. (1989), A&A, **225**, 528

[218] Withbroe, G.L., Noyes, R.W.,(1977), ARA&A **15**, 363

[219] Wu, F., Low, B.C. (1987), ApJ **312**, 431

[220] Zhang, H., Ai, G., Wang, H., Zirin, H., Patterson, A.,(1992), Sol. Phys. **140**, 307

[221] Zirin, H.,(1988), *Astrophysics of the Sun*, Cambridge University Press.

[222] Zirker, J.B.,(1989), Sol. Phys. **119**, 341

[223] Zombeck, M.V., et al (1978), ApJ Sup. Ser. **38**, 69

Η ΜΑΓΝΗΤΟΥΔΡΟΔΥΝΑΜΙΚΗ ΔΟΜΗ ΤΗΣ ΗΛΙΑΚΗΣ ΑΤΜΟΣΦΑΙΡΑΣ

Μοντέλα μαγνητικών βρόγχων πλάσματος με ροές

ΠΕΡΙΛΗΨΗ

Το Ηλιακό στέμμα παρατηρούμενο στις ακτίνες-Χ παρουσιάζει μια έντονα ανομοιογενή δομή. Οι δομικοί της λίθοι είναι μαγνητισμένοι βρόγχοι των οποίων η θερμοκρασία μπορεί να είναι μικρότερη ή μεγαλύτερη από την μέση θερμοκρασία του Ηλιακού στέμματος. Πρόσφατα απλοποιημένα μοντέλα αυτών των βρόγχων με ροές κατά μήκος των δυναμικών γραμμών είναι σε καλύτερη συμφωνία με τα παρατηρησιακά δεδομένα από ότι στατικά μοντέλα χωρίς ροές. Οι παρατηρήσεις αυτές μας οδηγούν στη μελέτη μοντέλων ηλιακών βρόγχων που αναδύονται σαν οι φυσιολογικές λύσεις των εξισώσεων της μαγνητοϋδροδυναμικής. Στις περιπτώσεις βρόγχων όπου η μαγνητική πίεση είναι πολύ μεγαλύτερη από την θερμική πίεση του πλάσματος λύσεις μπορούν να επιτευχθούν για ευρύ πεδίο συνοριακών συνθηκών. Στην περίπτωση των ψυχρών (θερμών) βρόγχων με ροές βρίσκεται ότι η πυκνότητα ελαττώνεται πιο γρήγορα (πιό αργά ή αυξάνεται) με το ύψος κατά μήκος των μαγνητικών δυναμικών γραμμών από ότι στην στατική περίπτωση. Επίσης όταν οι ροές είναι ισχυρές ένα κύμα κρούσης εμφανίζεται που αλλάζει δραματικά τις φυσικές και μορφολογικές ιδιότητες των βρόγχων. Το ίδιο συμβαίνει αν το σχήμα τού βρόγχου είναι ασύμμετρο, με συνέπεια ένα τμήμα του να μήν είναι ορατό. Αν όμως η μαγνητική πίεση είναι συγκρίσημη με την θερμική πίεση του πλάσματος, μαγνητοϋδροδυναμικές λύσεις μπορούν να επιτευχθούν μόνο για ορισμένες συνοριακές συνθήκες. Σε αυτή την περίπτωση έχει μελετηθεί η ισορροπία πλάσματος μέσα σε μια ισόθερμη ατμόσφαιρα που είναι οριζόντια συμπιεστή και κατακόρυφα στρωματοποιημένη, στο ηλιακό πεδίο βαρύτητας. Η τοπολογία των ακριβών αυτών λύσεων καθορίζεται από ένα σαγματικό κρίσιμο σημείο. Οι λύσεις τύπου μαγνητικών βρόγχων εμφανίζονται μόνο για μια ήπια στρωματοποιημένη ατμόσφαιρα, ενώ όταν η στρωματοποίηση είναι μεγάλη, δεν υπάρχουν λύσεις. Από το άλλο μέρος όταν η στρωματοποίηση είναι πολύ μικρή, υπάρχουν μόνο λύσεις πού αντιστοιχούν σε ηλιακές προεχοχές. Οταν το μέγεθος της ροής αυξάνει, το ύψος των βρόγχων αυξάνει και για πολύ ισχυρές ροές δεν υπάρχουν λύσεις ισορροπίας και εικάζεται ότι οι βρόγχοι εκρήγνυνται.

THE MAGNETOHYDRODYNAMIC NATURE OF THE SOLAR ATMOSPHERE
Models for magnetized plasma loops with flows

SUMMARY

High-resolution X-ray images of the inhomogeneous solar atmosphere by satellites and rockets, seem to firmly establish the notion that the building blocks of the corona of the Sun are magnetized plasma loops of various sizes and properties in which plasma flows seem to play an essential role in determining the physical and geometric characteristics of the loops. In this thesis, there were studied some families of exact solutions of the magnetohydrodynamic equations. They have been developed in order to solve them in two dimensions in the limit where the plasma pressure is much lower than the magnetic pressure – a reasonable assumption for the solar corona – for any boundary conditions imposed. In particular, in symmetrical magnetic configurations, when the distribution of pressure at the foot points is symmetrical, the flow is necessarily subsonic. For cool loops the flows cause the density to drop faster along fieldlines as compared with the static case, while in hot loops with flows the density can drop slower or even increases with the height. If the pressures at the two footpoints are unequal the flow becomes supersonic at the summit of the magnetic fieldline and then passes through a shock. In asymmetrical loops with flows one leg can be much less dense than the other and poorly visible as compared with the situation where flows are absent. However, if the gas pressure is comparable to the magnetic one, MHD solutions can be found for specific boundary conditions. In this case they have studied plasma equilibrium in a horizontaly compressible and vertical stratified atmosphere due to gravity, in which new characteristics emerge. The basic result for mild startification, is that, coronal loop models with flows along them, emerge as the only solutions of the coupled equations discribing the force balance along and across fieldlines. The phase plane of this solutions is controlled by a classical sonic and a saddle critical point, corresponding to a characteristic speed for hydromagnetic wave propagation, which it may be a common characteristic of other configurations as well. It was also found that for strong stratification there are no solutions at all, while for small stratification only periodic solutions arise which are totaly subsonic and subalfvénic and model the internal structure of prominences. Comparisons are made of the properties of these loops with those of force-free magnetic loops in the low-β limit where loops are taken to be rigid. Among the results is that an increase of the magnitude of the flow at the loop increases its height, in accordance with solar observations where some loops seem to extent over heights much higher than those predicted by static models. Finally, for strong flows there are no equilibrium solutions and the loop is disrupted.